

## Copyright Undertaking

This thesis is protected by copyright, with all rights reserved.

**By reading and using the thesis, the reader understands and agrees to the following terms:**

1. The reader will abide by the rules and legal ordinances governing copyright regarding the use of the thesis.
2. The reader will use the thesis for the purpose of research or private study only and not for distribution or further reproduction or any other purpose.
3. The reader agrees to indemnify and hold the University harmless from and against any loss, damage, cost, liability or expenses arising from copyright infringement or unauthorized usage.

If you have reasons to believe that any materials in this thesis are deemed not suitable to be distributed in this form, or a copyright owner having difficulty with the material being included in our database, please contact [lbsys@polyu.edu.hk](mailto:lbsys@polyu.edu.hk) providing details. The Library will look into your claim and consider taking remedial action upon receipt of the written requests.

# **THEORETICAL STRESS ANALYSES FOR ROCK SPHERES AND CYLINDERS UNDER THE POINT LOAD STRENGTH TEST**

XUEXIA WEI

B. Sc., M. Sc.

A thesis  
submitted to  
Department of Civil and Structural Engineering  
for the degree of  
Doctor of Philosophy  
The Hong Kong Polytechnic University  
March 1999



**Pao Yue-Kong Library**  
**PolyU • Hong Kong**

## STATEMENT OF SOURCES

To the best of my knowledge and belief, the work presented in the thesis 'Theoretical Stress Analyses for Rock Spheres and Cylinders under the Point Load Strength Test' is original unless otherwise acknowledged in the text. The material, either in whole or in part, has not been submitted for a degree in this or any other institutes.

Signed

---

Xuexia WEI

**To**  
**My Parents**

Fruitful intuition, a great mind for synthesis, and an informed sense of reality, are the essential qualities characterizing the creative scientist.

R. Taton, Reason and Chance in Scientific Discovery 1957, translated  
by A. J. Pomerans  
New York: Philosophical Library

Abstract of the thesis entitled:

**THEORETICAL STRESS ANALYSES FOR ROCK SPHERES AND  
CYLINDERS UNDER THE POINT LOAD STRENGTH TEST**

Submitted by Xuexia WEI

for the degree of Doctor of Philosophy at the Hong Kong Polytechnic University

in March, 1999

## ABSTRACT

The Point Load Strength Test (PLST) is an extremely convenient and useful method for rock classification and strength estimation. Although the PLST has been extensively studied by experimental approach, there are relatively few theoretical studies for the PLST. Analytic studies for the PLST include analyses of isotropic spheres under the diametral PLST by Hiramatsu and Oka (1966), finite cylinders under the axial PLST by Wijk (1978) and by Peng (1976), and finite cylinders under the diametral PLST by Wijk (1980) and Chau (1998a).

However, the exact stress field within a cylinder under the axial or diametral PLST has not been solved analytically. The only analytic results are the approximate solutions by Wijk (1978, 1980), in which the interaction between the indentors and the surfaces of the cylinder was idealized by two point forces. The finite element method has been applied to the axial PLST (e.g. Peng, 1976), but the contact problem between the indentors and the end surfaces was not considered either. The analytic solution by Chau (1998a) is for finite isotropic cylinders with zero shear displacement on the two end surfaces under the diametral PLST. Moreover, all of these analyses are restricted to considering rock as isotropic solids, there is no analytic solution for anisotropic rocks under the PLST.

Therefore, this dissertation presents a series of exact analytic solutions for anisotropic spheres and finite isotropic cylinders under the PLST. More specifically, the dissertation presents: (I) an exact analytic solution for spherically isotropic spheres under the diametral PLST; (II) an exact analytic solution for finite isotropic cylinders under the axial PLST; (III) an exact analytic solution for finite isotropic cylinders under

the diametral PLST; and (IV) a general analytic solution for finite isotropic cylinders under arbitrary surface load. In addition, a series of the PLST experiments have also been done on plaster, a kind of artificial rock-like material, to verify the theoretical solutions.

The method of solution for spheres uses the displacement potential approach together with the Fourier-Legendre expansion for the boundary loads. The solution reduces to the classical solution by Hiramatsu and Oka (1966) in isotropic case. Numerical results show that the maximum tensile stress along the axis of loading is very sensitive to the anisotropy in Young's modulus, Poisson's ratio and shear modulus, while the pattern of the stress distribution is relatively insensitive to anisotropy of rocks. The method for finite isotropic cylinders under the axial or diametral PLST expresses displacement functions in terms of series of the Bessel and modified Bessel functions; and the contact problem between the surfaces of the cylinder and the indentors, through which the point loads are applied, is considered. Numerical results show that the tensile stress distribution along the axis of loading within isotropic cylinders, either under the axial or diametral PLST, similar to that within isotropic spheres under PLST, is not uniform, tensile stress concentrations are developed near the point loads, the maximum tensile stress increases with the decrease of Poisson's ratio and the size of loading area. The theoretical prediction for the size and shape effects of the specimen on the PLST agrees well with experimental results. More importantly, if the sizes of the specimens are comparable (ISRM, 1985), the tensile stress distributions along the axis of loading in a sphere, in a cylinder under the axial or diametral PLST, have the similar pattern. This



conclusion indicates that the PLST is insensitive to the exact shape of the specimen, thus we provide the first theoretical basis for irregular lumps under the PLST.

In addition, by generalizing the method of solution for axisymmetric problem of the axial PLST and for non-axisymmetric problem of the diametral PLST, a new analytic framework for analyzing stresses for finite isotropic solid cylinders under arbitrary surface load is also presented.

## ACKNOWLEDGMENTS

I wish to express my sincere thanks to my chief supervisor Dr. K. T. Chau for his constant, incomparable guidance, patience and encouragement. I am impressed with his knowledge as well as his attitude to research, and I benefited most from his intuitive thinking, the rigorous reasoning and persistence in the pursuit of knowledge. Particular thanks are also given to my co-supervisor Dr. R. H. C. Wong for her guidance and encouragement. The mental support from both of my supervisors is especially crucial to carry me through difficult times in these two years.

I would like to thank Prof. J. Mizrahi for serving as the Chair of the final examination committee. Special thanks to Prof. L. M. Keer of the Northwestern University and Prof. C. F. Lee of Hong Kong University for reviewing my thesis and for serving as External Examiners.

My studies in Hong Kong would not be possible without the generous financial support, in terms of the research studentship, provided by the Research Grants Council (RGC) of the Hong Kong SAR Government under the Competitive Earmarked Research Grant (CERG) No. PolyU 70/96E through Dr. K. T. Chau. In addition, I wish to thank Prof. J. M. Ko, head of the Department of the Civil and Structural Engineering, for providing all the facilities and support in this Ph.D project. The encouragement from Prof. M. Anson, dean of the Faculty of Construction and Land Use, is also appreciated.

Grateful acknowledgments should be given to Ms. Anson for her care, concern and encouragement, especially for her whole effort in improving my English in these two years.

I want to thank Mr. H. Chui for his help when I did experiments in the Rock Mechanics Laboratory of the Department of Civil and Structural Engineering in the Hong Kong Polytechnic University.

Special thanks to Prof. H. R. Yu, Prof. T. D. Miao, Prof. Y. B. Wang and all other teachers in Lanzhou University for their encouragement and support. The help from my officemates Dr. H. Y. Liu, Mr. K. S. Chan, Mr. J. G. Zhu, and Miss M. Y. Chiu is also appreciated.

At last, but not least, I am truly indebted to my husband, Mr. J. S. Qin, and my lovely son, Z. Y. Qin, for their sacrifice and support. Without support from my husband, my study in Hong Kong would not have been possible. My endless love to my son gives me great strength to continually step my effort. I am also deeply indebted to the incomparable love, the concern, the support and the sacrifice given by my parents, my sister and brothers during these years, and I am really grateful to the whole support from my father.

## LIST OF PUBLICATIONS

1. Chau K.T. and Wei X.X. (1999), "Spherically isotropic, elastic spheres subject to diametral point load strength test", *International Journal of Solids and Structures*, **36**(29), 4473-4496.
2. Wei X.X., Chau K.T. and R. H. C. Wong (1999), "A new analytic solution for the axial point load strength test on solid circular cylinders", submitted to *Journal of Engineering Mechanics, ASCE* (accepted).
3. Chau K.T. and Wei X.X. (1999), "A new analytic solution for the diametral point load strength test on finite solid circular cylinders", submitted to *International Journal of Solids and Structures*.
4. Chau K.T. and Wei X.X. (1999), "Finite solid circular cylinders subjected to arbitrary surface load: part I. Analytic solution", submitted to *International Journal of Solids and Structures*.
5. Wei X.X. and Chau K.T. (1999), "Finite solid circular cylinders subjected to arbitrary surface load: part II. Application to double-punch test", submitted to *International Journal of Solids and Structures*.
6. Wei X.X. and Chau K.T. (1999), "Some new theoretical developments on point load strength test for rocks", *13th ASCE Engineering Mechanics Division Conference, Baltimore, June 13-16, 1999*.
7. Wei X.X. and Chau K.T. (1998), "Spherically isotropic spheres subject to diametral point load test: analytic solutions", *International Journal of Rock Mechanics and Mining Science* 35: 4-5, paper No. 006, 1998.

8. Wei X.X. and Chau K.T. (1998), "Analytic solution for the point load strength test on anisotropic rocks" , *International Conference on Geomechanics/ Ground Control in Mining and Underground Construction*, Australia. Vol. 1, pp147-156, 1998.
9. Wei X.X. and Chau K.T. (1998), " Similarities of tensile stress concentrations in solid cylinders and spheres under Point Load Strength Test (PLST): a new theoretical basis for testing irregular rock specimens using PLST", *Sixth Pan American Congress of Applied Mechanics PACAM VI*, Rio de Janeiro, Brazil. January pp1071-1082.

## LIST OF TABLES

<b>Table 4-1</b> The first ten roots of $J'_{2n}(\lambda_n) = 0$ for $n$ from 0 to 7	129
<b>Table 4-2</b> Comparison of the theoretical predictions of the normalized tensile stress, $\sigma_{center}/(P/D^2)$ , at the center of a solid circular cylinder under the diametral PLST given by Wijk (1980) and by the present study. Note that the results by Wijk (1980) were re-calculated to 4 significant digits.	130
<b>Table 4-3</b> Summary of some of the observed failure patterns. The T-mode and S-mode are depicted in Fig. 4-14 and $\theta_1$ and $\theta_2$ are defined as the two minimum angles between the cracks and the transverse line joining the two applied point loads.	131
<b>Table 6-1</b> The definitions for boundary conditions BC $ij$ ( $i,j=1,2,3$ ).	132
<b>Table 6-2</b> The $\theta$ - and $z$ -dependencies for superscripts $l$ ( $=1,2$ ) and $k$ ( $=1,2,3,4$ ) used for the displacement functions $\Psi$ and $\Phi$ given in Equations (6.23)-(6.24).	133
<b>Table 6-3</b> The $\theta$ - and $z$ -dependencies in (6.25)-(6.30) used for the stresses for superscripts $l$ ( $=1,2$ ) and $k$ ( $=1,2,3,4$ ). The symbols used are: E1=sin, E2=cos, cosh, zsinh; O1=sin, O2=sin, sinh, zcosh	

**Table 6-4** The definitions of  $\alpha_k$  ( $i=1,2,3$ ) and  $\Omega_{mn}^{(r)}$  used in (6.50) for  $k=1,2,3$ , and 4.

**Table 6-5** The definitions of  $\beta_k$  ( $i=1,2$ ) and  $\Omega_{mn}^{(s)}$  used in (6.52) for  $k=1,2,3$ , and 4.

**Table 6-6** The definitions of  $\kappa_k$  ( $i=1,2$ ) and  $\Omega_{mn}^{(t)}$  used in (6.55) for  $k=1,2,3$ , and 4.

## LIST OF FIGURES

**Fig. 2-1** Test specimens used for the Point Load Strength Test (from the left): sphere, cylinder under the axial point loads, irregular lump, cylinder under the diametral point loads

138

**Fig. 2-2** The spherical polar coordinate system used

139

**Fig. 2-3** A sphere under the Point Load Strength Test is modeled by uniform radial stress applied over two small spherical areas subtending an angle of  $2\theta_0$

140

**Fig. 2-4** The normalized stresses  $2\pi R^2 \sigma_{rr} / F$  and  $2\pi R^2 \sigma_{\theta\theta} / F$  versus the normalized radial coordinate  $r/R$  (along z-axis or with  $\theta = 0^\circ$ ) for various values of Poisson's ratio of isotropic spheres (i.e.  $\bar{\nu} = \nu' = \nu$ ) for  $\theta_0 = 3^\circ$

141

**Fig. 2-5** The normalized stresses  $2\pi R^2 \sigma_{rr} / F$  and  $2\pi R^2 \sigma_{\theta\theta} / F$  versus the normalized radial coordinate  $r/R$  (along z-axis or with  $\theta = 0^\circ$ ) for various values of  $\theta_0$  for isotropic spheres with  $\bar{\nu} = 0.1$

142

**Fig. 2-6** The normalized tangential Stress  $-\pi R^2 \sigma_{\theta\theta} / F$  versus the horizontal axis  $r/R$  (with  $\theta = \pi/2$ ) for isotropic sphere with  $\bar{\nu} = 0.48$ . The line with squares is the experimental result by Frocht and Guernsey (1953), the line with open circles is



the solution by Sternberg & Rosenthal (1952), and the solid line is our prediction for  $\theta_0 = 5^\circ$

143

**Fig. 2-7** Comparisons of the present solutions and the experimental results by Frocht and Guernsey (1953) for the normalized stresses  $\pi R^2 \sigma_{rr} / F$  and  $\pi R^2 \sigma_{\theta\theta} / F$  versus the normalized radial coordinate  $r/R$  (along  $z$ -axis or with  $\theta = 0^\circ$ ) for  $\bar{\nu} = \nu = 0.48$ . Our predictions for  $\theta_0 = 5^\circ$  and  $\theta_0 = 15^\circ$  are given in lines with circles and solid lines respectively, while the experimental results are given in lines with squares.

144

**Fig. 2-8** The normalized stresses  $2\pi R^2 \sigma_{rr} / F$  and  $2\pi R^2 \sigma_{\theta\theta} / F$  versus the normalized radial coordinate  $r/R$  (along  $z$ -axis or with  $\theta = 0^\circ$ ) for various values of modulus ratio  $\beta (=E/E')$  of anisotropic spheres with  $\alpha = 1.0$ ,  $\bar{\nu} = 0.2$ ,  $\xi = 1.0$  and  $\theta_0 = 3^\circ$

145

**Fig. 2-9** The normalized stresses  $2\pi R^2 \sigma_{rr} / F$  and  $2\pi R^2 \sigma_{\theta\theta} / F$  versus the normalized radial coordinate  $r/R$  (along  $z$ -axis or with  $\theta = 0^\circ$ ) for various values of  $\alpha$  ( $=\nu'/\bar{\nu}$ ) for anisotropic spheres with  $\beta = 1.5$ ,  $\bar{\nu} = 0.2$ ,  $\xi = 1.0$  and  $\theta_0 = 3^\circ$

146

**Fig. 2-10** The normalized stresses  $2\pi R^2 \sigma_{rr} / F$  and  $2\pi R^2 \sigma_{\theta\theta} / F$  versus the normalized radial coordinate  $r/R$  (along  $z$ -axis or with  $\theta = 0^\circ$ ) for various values of  $\xi$  ( $=A_{44}/A_{66}$ ) for anisotropic spheres with  $\beta = 1.0$ ,  $\bar{\nu} = 0.2$ ,  $\alpha = 1.0$  and  $\theta_0 = 3^\circ$

**Fig. 2-11** The normalized radial and tangential stresses along the line between the center of the sphere and one of the point loads under the action of uniform stress and contact stress for  $E = 18\text{GPa}$ ,  $\nu = 0.1$ ,  $D = 50\text{mm}$  and  $P = 15\text{kN}$

**Fig. 2-12** The normalized radial and tangential stresses along the line between the center of the sphere and one of the point loads under the action of uniform stress and contact stress for  $E = 18\text{GPa}$ ,  $\nu = 0.3$ ,  $D = 50\text{mm}$  and  $P = 15\text{kN}$

**Fig. 2-13** The normalized radial and tangential stresses along the line between the center of the sphere and one of the point loads under the action of uniform stress and contact stress for  $E = 70\text{GPa}$ ,  $\nu = 0.3$ ,  $D = 50\text{mm}$  and  $P = 15\text{kN}$

**Fig. 3-1** A sketch for the axial Point Load Strength Test for a cylindrical rock core of radius  $R$  and length  $2h$ . The origin and  $z$ -axis of the coordinates is set at the center of the cylinder and the axis of revolution

**Fig. 3-2** The normalized stresses  $\sigma_r / \sigma_0$  and  $\sigma_z / \sigma_0$  versus the normalized distance  $z/h$  along the  $z$ -axis for various values of Poisson's ratio  $\nu$  for  $H/D=1$ ,  $D=2R=50\text{mm}$ , and  $R_0 = 0.05R$

**Fig.3-3** The normalized stresses  $\sigma_r / \sigma_0$  and  $\sigma_z / \sigma_0$  versus the normalized distance  $z/h$  along the  $z$ -axis for various diameter  $R_0$  of the contact area for  $H/D=1.1$ ,  $D=2R=50\text{mm}$ , and  $\nu = 0.25$

153

**Fig. 3-4** Stresses  $\sigma_{\theta\theta}$  and  $\sigma_z$  versus the normalized distance  $z/h$  along the  $z$ -axis for four specimens of  $H/D=1.1$ ,  $D=56\text{mm}$ ,  $\nu = 0.25$  under the critical load  $P$

154

**Fig. 3-5** Comparisons of the theoretical predictions and the experimental results for the Point Load strength Index  $I_p$  versus diameter for a fixed length/diameter Ratio  $H/D=1.1$ , and  $\nu = 0.25$

155

**Fig. 3-6** Comparisons of the theoretical predictions and the experimental results for the Point Load Strength Index  $I_p$  versus length/diameter Ratio for a fixed diameter  $D=56\text{mm}$ , and  $\nu = 0.25$

156

**Fig 3-7** Theoretical predications for the Point Load Strength Index  $I_p$  versus length/diameter ratio for various diameters for Poisson's ratio  $\nu = 0.25$

157

**Fig. 3-8** A sketch showing the failure pattern of a solid cylinder of plaster material under the axial PLST if the specimen breaks into two pieces along a flat surface

**Fig. 3-9** A sketch showing the failure pattern of a solid cylinder of plaster material under the axial PLST if the specimen breaks into three pieces

**Fig. 3-10** Theoretical predictions for the hydrostatic stress versus the normalized distance  $z/h$  along the  $z$ -axis for different diameters for Poisson's ratio  $\nu = 0.25$ , together with the crushing pressure interpreted from Zhang et al. (1990)

**Fig. 4-1** A cylindrical rock specimen subjected to the diametral Point Load Strength Test (PLST)

**Fig. 4-2** The normalized stresses  $\sigma_{\theta\theta}/\sigma_0$ , and  $\sigma_r/\sigma_0$  versus  $r/R$  for various values of  $r_0/R$  and for  $\nu=0.25$ ,  $L/D=1.4$  and  $R_2=5\text{mm}$

**Fig. 4-3** The normalized stresses  $\sigma_{\theta\theta}/\sigma_0$ , and  $\sigma_r/\sigma_0$  versus  $r/R$  for various values of  $r_0/R$  and for  $\nu=0.25$ ,  $L/D=1.4$  and  $R_2=5\text{mm}$

**Fig. 4-4** A typical stress distribution of the normalized stresses  $\sigma_{\theta\theta}/\sigma_0$ ,  $\sigma_z/\sigma_0$  and  $\sigma_r/\sigma_0$  versus  $r/R$  for  $\nu=0.25$  and  $r_0/R = 0.039$

**Fig. 4-5** The normalized stresses  $\sigma_{\theta\theta} / \sigma_0$ , and  $\sigma_r / \sigma_0$  versus  $r/R$  for various values of  $\nu$  and  $r_0 / R = 0.039$

165

**Fig. 4-6** The normalized stresses  $\sigma_{\theta\theta} / \sigma_0$ , and  $\sigma_r / \sigma_0$  versus  $r/R$  for various values of  $R_2$  and  $r_0 / R = 0.039$

166

**Fig. 4-7** The normalized stresses  $\sigma_{\theta\theta} / \sigma_0$ , and  $\sigma_r / \sigma_0$  versus  $r/R$  for various values of  $D$  and  $r_0 / R = 0.039$

167

**Fig. 4-8** The normalized tensile stresses  $\sigma_{\theta\theta} / \sigma_0$ , and  $\sigma_z / \sigma_0$  versus  $L/D$  for various values of  $\nu$  and for  $D=50\text{mm}$  and  $r_0 / R = 0.039$ . The dotted and solid lines are for the axial and hoop stresses respectively

168

**Fig. 4-9** The maximum tensile stress envelopes versus  $L/D$  for various values of  $\nu$  and for  $D=50\text{mm}$ . The dotted and solid lines are for axial and hoop stresses respectively

169

**Fig. 4-10** The maximum tensile stress envelopes versus  $L/D$  for various values of  $D$  and for  $\nu=0.25$ . The dotted and solid lines are for axial and hoop stresses respectively

170

**Fig. 4-11** The theoretical stress distributions for  $\sigma_{\theta\theta}$ ,  $\sigma_{rr}$  and  $\sigma_{zz}$  versus  $r/R$  for three plaster specimens of size  $D=56\text{mm}$  ( $\nu=0.25$  and  $E=17.5\text{GPa}$ )

171

**Fig. 4-12** The theoretical and experimental point load strength index ( $I_p=P/D^2$ ) versus the geometric ratio  $D/L$  for the rock-like plaster material and for  $D=56\text{mm}$

172

**Fig. 4-13** The theoretical and experimental point load strength index ( $I_p=P/D^2$ ) versus the diameter  $D$  for the rock-like plaster material for  $L/D=0.7$

173

**Fig. 4-14** A sketch of the two failure modes (T-mode and S-mode) of cylinders under the diametral point load strength test ( $\theta_1$  and  $\theta_2$  are defined as the two minimum angles between the cracks and the transverse line joining the two applied point loads)

174

**Fig. 5-1** The normalized tensile stress  $\sigma_t D^2 / F$  and compressive stress  $\sigma_c D^2 / F$  versus the normalized distance  $r/R$  or  $z/h$  for cylinders and spheres under the axial and diametral PLST for  $D=50\text{mm}$

175

**Fig. 5-2** The normalized tensile stress  $\sigma_t D^2 / F$  and compressive stress  $\sigma_c D^2 / F$  versus the normalized distance  $r/R$  or  $z/h$  for cylinders and spheres under the axial and diametral PLST for  $D=60\text{mm}$

176

**Fig. 5-3** The normalized tensile stress  $\sigma_t D^2 / F$  and compressive stress  $\sigma_c D^2 / F$  versus the normalized distance  $r/R$  or  $z/h$  for cylinders and spheres under the axial and diametral PLST for  $D=75\text{mm}$

177

**Fig. 5-4** The normalized mean values of the maximum tensile stress  $\sigma_m D^2 / F$  versus different diameter  $D$

178

**Fig. 6-1** A sketch of a finite solid circular cylinder of length  $2L$  and radius  $R$  subjected to arbitrary tractions on the curved and end surfaces

179

**Fig. 7-1** A cylinder under the Brazilian Test

180

**Fig. 7-2** A cross-section of a cylinder under the modified Brazilian Test

181

## **TABLE OF CONTENTS**

<b>STATEMENT OF SOURCES</b>	ii
<b>ABSTRACT</b>	v
<b>ACKNOWLEDGMENTS</b>	ix
<b>LIST OF PUBLICATIONS</b>	xi
<b>LIST OF TABLES</b>	xiii
<b>LIST OF FIGURES</b>	xv
<b>Chapter 1 INTRODUCTION</b>	
1.1 Background and Motivation	1
1.2 A Brief Review of the Previous Work	2
1.3 Outline of the Present Research	5
<b>Chapter 2. SPHERICALLY ISOTROPIC, ELASTIC SPHERES SUBJECTED TO THE DIAMETRAL POINT LOAD STRENGTH TEST</b>	
2.1 Introduction	8
2.2 Governing Equations	12
2.2.1 Hook's law	12
2.2.2 Equilibrium equations	14
2.2.3 Boundary conditions	14
2.3 Displacement Functions	15
2.4 General Solutions for the Displacement Functions	18
2.5 Characteristic Roots for Solid Spheres	20
2.5.1 Case I: Two real roots	23



2.5.2 Case II: Two complex conjugate roots	23
2.6 The Method of Solutions	24
2.6.1 The general solutions of stresses	24
2.6.2 Determination of unknown coefficients	26
2.6.3 Final solutions for stresses	27
2.7 Numerical Results and Discussions	28
2.7.1 Stresses in isotropic spheres and comparisons with experiments	28
2.7.2 Stresses in anisotropic spheres	31
2.8 Point Loads Modeled by the Hertz Contact Stress	32
2.9 Conclusion	36
<b>Chapter 3. AN EXACT ANALYTIC SOLUTION FOR THE AXIAL POINT LOAD STRENGTH TEST ON SOLID CIRCULAR CYLINDERS</b>	
3.1 Introduction	38
3.2 Governing Equations	41
3.3 Method of Solution	44
3.4 Appropriate Form of the Displacement Potential	45
3.5 Determination of Unknown Coefficients	46
3.6 Numerical Results and Discussions	51
3.7 Experiments and Comparison with the Theoretical Predictions	53
3.9 Conclusion	58

**Chapter 4. AN EXACT ANALYTIC SOLUTION FOR THE DIAMETRAL  
POINT LOAD STRENGTH TEST ON FINITE SOLID CIRCULAR  
CYLINDERS**

4.1 Introduction	60
4.2 Governing Equations	63
4.3 Method of Solution	67
4.4 Series Expression for the Displacement Functions	68
4.5 General Solutions for Stresses	69
4.6 Determination of the Unknown Coefficients	71
4.7 Numerical Results and Discussion	76
4.8 Experimental Validation	82
4.9 Conclusion	85

**Chapter 5. THEORETICAL BASIS FOR TESTING IRREGULAR LUMPS  
UNDER THE POINT LOAD STRENGTH TEST**

5.1 Introduction	87
5.2 Isotropic Spheres Under the Diametral PLST	89
5.3 Solid Circular Cylinders Under the Axial PLST	90
5.4 Solid Circular Cylinders Under Diametral PLST	92
5.5 Numerical Comparison of Stress Distribution Within Spheres and Cylinders	93
5.6 Conclusion	96

**Chapter 6. EXACT STRESS ANALYSIS OF FINITE CIRCULAR CYLINDERS  
SUBJECTED TO ARBITRARY SURFACE LOAD**

6.1 Introduction	97
6.2 Governing Equations	101
6.3 Method of Solution	102
6.4 Series Expressions for the Two Displacement Functions	104
6.5 General Expressions for Stresses	106
6.6 Determination of the Unknown Coefficients	109
6.7 Special Cases	119
6.8 Characteristic of Roots of the Derivative of the Bessel Function	120
6.9 Conclusion	122
<b>Chapter 7. CONCLUSION</b>	
7.1 Summary of Results	124
7.2 Further Studies	126
<b>TABLES</b>	129
<b>FIGURES</b>	138
<b>REFERENCES</b>	182
<b>APPENDICES</b>	193
<b>CURRICULUM VITAE</b>	203

## **Chapter 1**

### **INTRODUCTION**

#### **1.1 Background and Motivation**

The Point Load Strength Test (PLST) is an extremely convenient and useful method for rock classification and strength estimation (e. g. Broch and Franklin, 1972; Guidicini et al., 1973; Bieniawski, 1974). Since the required apparatus for the PLST is light and portable, the testing procedure is extremely simple and quick, and little or no sample preparation is needed, the PLST has long been extensively used both in the field and in the laboratory. Samples with various shapes have been used as specimens for the PLST, such as spheres, rock cores (with the point loads applied axially or diametrically), or even an irregular lump picked up in situ. The testing procedure has been standardized by the International Society for Rock Mechanics (ISRM, 1985). In addition to rock testing, PLST has also been employed to estimate both tensile and compressive strength of concrete (Robins, 1980; Richardson, 1989) and reinforced concrete (Robins and Austin, 1985).

One typical feature of the PLST is that, each specimen is applied with a pair of vertical concentrated loads so as to induce a horizontal tensile stress, it is this tensile stress that splits apart the specimen along a plane or planes paralleling to the direction of load application. Though specimens may be splitted apart into two or three parts, and the failure planes may be along any directions, all failure planes pass through or approximately pass through the line joining two point loads. This observed failure pattern indicates that the stress distribution, especially the tensile stress distribution

along the line joining the two point loads, is of critical important to the PLST (Hiramatsu and Oka, 1966; Wijk, 1978, 1980). Photoelastic experiments (Hiramatsu and Oka, 1966) showed that the stress state, in the vicinity of the line joining two point loads in a sphere, a cube, a rectangular prism or an irregular lump with a comparable size is roughly the same. This stress analysis is considered to have provided a very important experimental basis for irregular lumps under the PLST, but so far there is not any theoretical basis for it. Even though extensive experimental studies have been done on the PLST, there are fewer theoretical studies for it. Cylinders are the most commonly used specimens for the PLST, but the stress fields within cylinders, which are induced by point loads, have not been solved analytically.

In addition, all of the previous theoretical studies are restricted to considering rock as isotropic solids, there is no analytic solution for anisotropic rocks under the PLST, though in reality, most of rocks are, to a certain extent, anisotropic in nature.

Therefore, it is really imperative to do a thorough theoretical investigation for the PLST. A brief literature review will be given in the next section.

## **1.2 A Brief Review of the Previous Work**

Specimens subjected to point loads were originally studied as an interesting research topic by Sternberg and Rosenthal (1952), D'Andrea et al. (1965), McWilliams (1966), Hiramatsu and Oka (1966), Reichmuth (1963, 1968), Franklin (1970) and Fookes et al. (1971). It was not until Broch and Franklin (1972) proposed the point load strength test to be a standard indirect tensile strength index test for rocks, PLST has been extensively studied by experimental approaches (e.g. Guidicini et al., 1973; Bieniawski, 1974, 1975; Pells, 1975; Carter and Sneddon, 1977; Hassani et al., 1980; Lajtai, 1980; Brook, 1977,

1980; Read et al., 1980; Greminger, 1982; Forster, 1983; Lumb, 1983; Irfan and Powell, 1985; and many others) and fewer theoretical studies (e.g. Peng, 1976; Wijk, 1978, 1980; Chau and Wong, 1996; Chau, 1998a). In particular, for theoretical studies, Sternberg and Rosenthal (1952) and Hiramatsu and Oka (1966) used two different methods and independently derived exact analytic solutions for isotropic spheres subjected to point loads. But the latter discussed in detail the stress distribution along the line joining the two point loads and thus provided the classical theoretical basis for the PLST. Wijk (1978, 1980) obtained approximate solutions which estimate the tensile stress at the center of cylinders under the axial and diametral PLST, and speculated that the tensile stress at the center of the cylinder under the diametral PLST is larger than that of a sphere under the diametral PLST but smaller than that of a finite circular plate under the axial PLST. The approximate solution for cylinders under the axial PLST has been used by Chau and Wong (1996) to estimate the index-strength conversion factor theoretically. Finite Element Method (FEM) has been applied to the axial PLST (e.g. Peng, 1976), but the interaction between the indentors and the surfaces of the cylinder, as same as Wijk (1978,1980), was idealized by two point forces. Chau (1998a) first solved the contact problem between the curved surface of the cylinder and the indentors, and provided an exact analytic solution for finite cylinders with zero shear displacement under the diametral PLST.

In addition, the stress analysis of elastic isotropic spheres and cylinders under various boundary conditions has been one of the most fundamental problems in theoretical elasticity and has long been studied by many researchers. In particular, for spheres, when isotropic spheres are compressed between two rigid blocks, analyses have been done by Frocht and Guernsey (1953), Durelli and Daniel (1961), Durelli and Chen

(1973), and Chen and Durelli (1973), Tatara (1991) and Tarata et al. (1991); when the loads are transferred to the elastic isotropic spheres through displacement boundary conditions, the problem was analyzed by Abramian et al. (1964). For cylinders, Pochhammer (1876) and Chree (1889) independently obtained the general analytic solution for an infinite circular isotropic cylinder subjected to arbitrary surface load. Dougall (1914) used three displacement functions and derived an analytic solution for circular isotropic cylinders. Filon (1902) presented analytic solutions for finite isotropic cylinders subjected to certain axisymmetric loads, particularly provided the notable solution which considered the effect of friction on the end surfaces on the nonuniform stress distribution within the cylinder for the uniaxial compressive test. Saito (1952, 1954) derived general analytic solutions for finite isotropic cylinders subjected to axisymmetric load. Ogaki et al. (1983) employed two stress functions and analyzed the stress field in a circular isotropic cylinder subjected to the parabolic distributed load on the end surfaces. Watanabe (1996) obtained an analytic solution for axisymmetric finite isotropic cylinders constrained part of the radial displacement of the loading ends under unconfined and confined compressive tests. Chau (1998a) derived an analytic solution for finite isotropic cylinders with zero shear displacement under the diametral PLST. It should be noted that, except the analytic solution by Chau (1998a), all of these closed-form solutions are for 2-dimensional problems for isotropic cylinders. Very fewer solutions for 3-dimensional problems for finite isotropic cylinders have been obtained because the boundary conditions on the curved surface and on the end surfaces are very difficult to satisfied exactly.

It is necessary to mention that other works have also been employed to analyze the stresses in isotropic cylinders (Pickett, 1944; Edelman, 1948, 1949; Horvay and

Mirabal, 1958; Balla, 1960, Kotte *et al.*, 1969; Knowles and Horgan , 1969; Bordia , 1970; Brady, 1971; Peng, 1971; Al-chalabi and Huang, 1974; Al-chalabi et al., 1974; Wijk, 1978, 1980; Robert and Keer, 1987a, 1987b; Herczynski and Folk , 1989).

However, there is no analytic solution for finite isotropic cylinders under the axial PLST, diametral PLST or under arbitrary surface load. Moreover, all of the previous theoretical analyses are restricted to considering rock as isotropic solids, there is no analytic solution for anisotropic rocks under the PLST. Though in experiment, the point load strength anisotropic index  $I_a$ , which is defined as the ratio of the greatest point load strength index  $I_t$  to the least one in different directions, has long been used to characterize the effect of anisotropy of rock on the PLST (e.g. Hassani et al., 1980; Lajtai, 1980; Read et al., 1980; Greminger, 1982; Forster, 1983; Broch, 1983; ISRM, 1985).

### **1.3 Outline of the Present Research**

The main objective of the dissertation is to obtain a series of exact analytic solutions for anisotropic spheres and finite isotropic cylinders under the PLST. Hopefully, by analyzing the stress fields within anisotropic spheres and finite isotropic cylinders under the PLST, we can provide a thorough understanding of the failure mechanism of rocks under the PLST.

More specifically, Chapter 2 presents an exact analytic solution for spherically isotropic spheres under the diametral PLST (this chapter is essentially the same as two papers by Chau and Wei, 1999a, International Journal of Solids and Structures; and by Wei and Chau, 1998, International Journal of Rock Mechanics and Mining Science 35:4-5, paper No. 006). The method of solution uses the theory for spherically isotropic



solids proposed by Ding and Ren (1991), which is modified from the general theory by Hu (1954). In particular, the displacement functions proposed by Hu (1954) will be applied to uncouple three equations of equilibrium, then a change of variables proposed by Ding and Ren (1991) is used such that closed-form solutions for the roots of the characteristic equation of the governing equations can be found. Displacement functions are further expressed in terms of spherical harmonics, and in turn all stress components can also be expressed in terms of spherical harmonics. To obtain the final solutions, applied load on the spherical surface is also expanded in terms of Fourier-Legendre series (as employed by Hiramatsu and Oka, 1966) and matches with the boundary values of the normal stresses of the spheres. The solution reduces to the classical solution by Hiramatsu and Oka (1966) in isotropic case. Moreover, the effect of the contact stress on the stress distribution along the line joining the two point loads is also considered. Chapter 3 presents an analytic solution for the stress field within an elastic circular solid cylinder under the axial PLST (The content of the Chapter has been submitted for publication, Wei et al, 1999). The “displacement potential approach” is also used to uncouple the equations of equilibrium, then both of the displacement potential and the contact stress on the end surfaces are expanded in terms of Fourier-Bessel expansion , so that, the unknown constants in expressions of stresses can be uniquely determined. In addition, a series of the axial PLST have been done on plaster to verify the analytic solution. Chapter 4 presents an exact analytic solution for an finite isotropic cylinders under the diametral PLST (The content of the Chapter has been submitted for publication, Chau and Wei, 1999b). The method of solution generally follows the approach by Chau (1998a). But new expressions of two displacement functions are introduced in terms of the Bessel function of first kind, trigonometric

functions and hyperbolic functions, such that the boundary conditions on the curved surface and the boundary conditions on the end surfaces are satisfied exactly. All coefficients can be determined by using the Fourier expansion or the Fourier-Bessel expansion technique. In addition, the contact problem between the surfaces of the cylinder and the indentors, through which the point loads are applied, is considered. Chapter 5 uses all of the solutions obtained in Chapters 2, 3 and 4, and compares the stress distribution along the line joining the two point loads in isotropic spheres and cylinders under the diametral PLST and that in isotropic cylinders under the axial PLST, so as to provide a theoretical basis for testing irregular lumps under the PLST.

In addition, Chapter 6 generalizes the method of solution for isotropic cylinders for axisymmetric problem of the axial PLST and for non-axisymmetric problem of the diametral PLST, and provides a new analytic framework for analyzing stresses for finite isotropic solid cylinders under arbitrary surface load. (The content of the Chapter has been submitted for publication, Chau and Wei, 1999c).

Finally, Chapter 7 summarizes the whole dissertation and gives recommendations for further research.

## **Chapter 2**

# **SPHERICALLY ISOTROPIC, ELASTIC SPHERES SUBJECT TO THE DIAMETRAL POINT LOAD STRENGTH TEST**

### **2.1 Introduction**

The Point Load Strength Test (PLST) is a convenient and inexpensive method for rock classification and strength estimation (e.g. Broch and Franklin, 1972; Guidicini et al., 1973; Bieniawski 1974). The required apparatus for the PLST is light and portable (Boisen, 1977). The point load strength test can be applied to rock cores (either axially or diametrically), to spheres, or to irregular lumps as shown in Fig. 2-1. The testing procedure has been standardized by the International Society for Rock Mechanics (ISRM, 1985). In addition to rock testing, the PLST has also been applied to estimate both tensile and compressive strengths of concrete (Robins, 1980; Richardson, 1989) and reinforced concrete (Robins and Austin, 1985).

Extensive experimental studies have been done on the PLST (see the review by Chau and Wong, 1996), but there are relatively few theoretical studies for PLST. Analytic studies for the PLST include the analyses of isotropic spheres subjected to a pair of diametrical point loads by Hiramatsu and Oka (1966), finite cylinders subjected to the axial point loads by Wijk (1978) and Chau and Wong (1996), and finite cylinders subjected to the diametral point loads by Wijk (1980) and Chau (1998a).

All of these analyses are restricted to considering rock as isotropic solids, there is no analytic solution for anisotropic solids under the PLST. However, in reality most

of rocks are, to a certain extent, anisotropic in nature. The PLST has also been commonly applied in testing the strength of anisotropic rocks (e.g. Hassani et al., 1980; Lajtai, 1980; Read et al., 1980; Greminger, 1982; Forster, 1983; Broch, 1983).

Therefore, in this chapter we will investigate the effect of material anisotropy on the tensile stress concentration within rock specimens under the PLST by considering the simplest problem for anisotropic materials: a spherically isotropic elastic sphere subject to the diametral PLST. The solution to be presented here can be considered as an extension of the classical solution for isotropic spheres obtained by Hiramatsu and Oka (1966). The spherically isotropic solid, which was first introduced by Saint-Venant in 1865 (see the historical account by Love, 1944), is the simplest type of anisotropic solids and contains five independent material constants. In order to cover the classical solution by Hiramatsu and Oka (1966), The diametral point loads are modeled by a uniform distributed radial stress applied on two finite regions of the spherical surface, which are further expanded into Fourier-Legendre series. However, in real PLST, the diametral point loads are applied to the rock specimens through steel cones with spherical heads (e.g. ISRM, 1985). Therefore, the actual boundary condition of the applied loads should be more realistically modeled by contact between the spherical rock and the steel cones, as proposed by Chau (1998a). Therefore, we also consider the effect of this contact stress on the tensile stress distribution within isotropic spheres subjected to the diametral PLST.

Although most of the rock specimens available for the PLST are either cylindrical (i.e. rock cores) or irregular (i.e. rock lumps), the solution for the tensile stress concentration in spheres under the diametral point loads has been found very

meaningful for the PLSTs. It provides not only a theoretical basis for the testing of irregular lumps of rocks (Hiramatsu and Oka, 1966), but also an upper bound of the tensile stress concentration within a cylindrical specimen under the diametral PLST (e.g. see Wijk, 1980). More specifically, Wijk (1980) obtained an approximation for the tensile stress concentration at the center of a cylinder under diametral point loads, which is found intermediate between the solutions of the same problem for a circular plate and for a sphere. The tensile stress distribution along the diameter of a cylinder under the diametral PLST can be approximated by interpolating the solutions for circular plates given by Wijk (1978) and for spheres given by Hiramatsu and Oka (1966) (see for example Fig. 2 of Wijk, 1980). Therefore, the solution for spheres does shed light on the stress analysis of the diametral PLST for cylindrical rock cores.

The compression of isotropic spheres by either force or displacement control is one of the most fundamental problems in the mathematical theory of elasticity and has been considered by various authors. Sternberg and Rosenthal (1952) first solved the problems of isotropic spheres under concentrated diametral loads by using the Boussinesq stress-function in dipolar coordinates, and their solutions have been verified by comparison to the experiments by Frocht and Guernsey (1953). When the diametral point loads are distributed over two finite areas on the spherical surface, the problem was solved by Hiramatsu and Oka (1966), and the analysis was motivated by the PLST for irregular lumps. Experiments and stress analyses for large deformations of spheres compressed between two rigid blocks have been done by Frocht and Guernsey (1953), Durelli and Daniel (1961), Durelli and Chen (1973),

and Chen and Durelli (1973), Tatara (1991) and Tarata et al. (1991). When the loads are transferred to the elastic spheres through displacement boundary conditions, the problem was analyzed by Abramian et al. (1964). However, all of these analyses are restricted to isotropic spheres, no stress analysis has been done on anisotropic spheres under diametral point loads.

Actually, with the exception of the theoretical analyses by Nowinski (1959), Eason (1962), Chen (1966), Hata (1993), Ding and Ren (1991) and Chau (1995, 1998c) for spherically isotropic spheres, not many analytical solutions exist for spherically isotropic materials or spheres.

The method of solution used here follows the general theory for spherically isotropic solids proposed recently by Ding and Ren (1991), which is modified from the general theory by Hu (1954). In particular, the displacement functions proposed by Hu (1954) will be applied to uncouple the equations of equilibrium, and a change of variables proposed by Ding and Ren (1991) will be used such that closed-form solutions for the roots of the characteristic equation of the governing equations can be found. Displacement functions are expressed in terms of spherical harmonics, and in turn all stress components can also be expressed in these terms. To obtain the final solutions, applied loads on the spherical surface are expanded in terms of Fourier-Legendre series (as employed by Hiramatsu and Oka, 1966) and match with the boundary values of the normal stresses of the spheres. Finally, a closed form solution can be obtained for the stress concentration. As expected, the isotropic limit of our solution recovers the classical solution by Hiramatsu and Oka (1966), and compares

well with the experimental observations obtained by Frocht and Guernsey (1953) using the method of photoelasticity.

It is also relevant to mention here that the contact problem between two identical transversely isotropic spheres has been solved by Keer and Mowry (1979). The actual contact problem between the steel cone and the anisotropic rock specimen and the study on inelastic crushing of the rock at the contact are complicated problems and out of the scope of the present study. We refer to Zhang et al. (1990) and Shah and Wong (1996, 1997) for some recent developments. The main focus in this chapter will be on the effect of material anisotropy on the tensile stress concentration within the spherical rock specimen.

## 2.2 Governing Equations

### 2.2.1 Hooke's law

Consider a spherical polar coordinate system  $(r, \theta, \varphi)$  with the origin locating at the center of the sphere, as shown in Fig. 2-2. The spherical rock specimen is assumed to be linear elastic and spherically isotropic, and the stress and strain components are related by the following generalized Hooke's law

$$\begin{aligned} \varepsilon_{\theta\theta} &= \frac{\sigma_{\theta\theta}}{E} - \frac{\bar{\nu}\sigma_{\varphi\varphi}}{E} - \frac{\nu'\sigma_{rr}}{E'} , & \varepsilon_{\varphi\varphi} &= -\frac{\bar{\nu}\sigma_{\theta\theta}}{E} + \frac{\sigma_{\varphi\varphi}}{E} - \frac{\nu'\sigma_{rr}}{E'} , \\ \varepsilon_{rr} &= -\frac{\nu'}{E'}(\sigma_{\theta\theta} + \sigma_{\varphi\varphi}) + \frac{\sigma_{rr}}{E'} , & \varepsilon_{\theta\varphi} &= \frac{(1+\bar{\nu})}{E}\sigma_{\theta\varphi} , \quad \varepsilon_{r\alpha} = \frac{\sigma_{r\alpha}}{2G'} , \end{aligned} \quad (2.1)$$

where  $\alpha = \theta, \varphi$ . The Cauchy stress tensor is denoted by  $\sigma$  and the strain tensor by  $\varepsilon$ . Physically,  $E$  and  $E'$  are the Young's moduli governing axial deformations on the planes of isotropy (i.e. any tangential plane on a spherical surface drawn from the

origin) and along direction perpendicular to it (i. e. the radial direction) respectively. The Poisson's ratios  $\bar{\nu}$  and  $\nu'$  characterize transverse reductions in the plane of isotropy under tension in the same plane and under radial tension respectively. The shear modulus  $G'$  governs the shear deformation of on the planes with unit normals perpendicular to the radial direction.

In order to make our Hooke's law compatible with others (e.g. Hu 1954; Ding and Ren 1991), (2.1) is inverted to give

$$\begin{aligned}\sigma_{\theta\theta} &= (2A_{66} + A_{12})\varepsilon_{\theta\theta} + A_{12}\varepsilon_{\varphi\varphi} + A_{13}\varepsilon_{rr}, \\ \sigma_{\varphi\varphi} &= A_{12}\varepsilon_{\theta\theta} + (2A_{66} + A_{12})\varepsilon_{\varphi\varphi} + A_{13}\varepsilon_{rr}, \\ \sigma_{rr} &= A_{13}(\varepsilon_{\theta\theta} + \varepsilon_{\varphi\varphi}) + A_{33}\varepsilon_{rr}, \quad \sigma_{\theta\varphi} = 2A_{66}\varepsilon_{\theta\varphi}, \quad \sigma_{r\alpha} = 2A_{44}\varepsilon_{r\alpha}\end{aligned}\tag{2.2}$$

where

$$\begin{aligned}A_{12} &= -\frac{E(\bar{\nu}E' + \nu'^2 E)}{(1 + \bar{\nu})\bar{E}}, \quad A_{13} = -\frac{\nu' E' E}{\bar{E}}, \quad A_{33} = -\frac{E'^2 (1 - \bar{\nu})}{\bar{E}} \\ A_{66} &= \frac{E}{2(1 + \bar{\nu})}, \quad A_{44} = G', \quad \bar{E} = E'(\bar{\nu} - 1) + 2\nu'^2 E\end{aligned}\tag{2.3}$$

For small deformation and small strain, the relations between the strain and displacement components in spherical polar coordinate are expressed as

$$\begin{aligned}\varepsilon_{rr} &= \frac{\partial u_r}{\partial r}, \quad \varepsilon_{\theta\theta} = \frac{1}{r} \frac{\partial u_\theta}{\partial \theta} + \frac{u_r}{r}, \quad \varepsilon_{\varphi\varphi} = \frac{1}{r \sin \theta} \frac{\partial u_\varphi}{\partial \varphi} + \frac{u_r}{r} + \frac{u_\theta}{r} \cot \theta, \\ \varepsilon_{r\varphi} &= \frac{1}{2} \left( \frac{1}{r \sin \theta} \frac{\partial u_r}{\partial \varphi} - \frac{u_\varphi}{r} + \frac{\partial u_\varphi}{\partial r} \right), \quad \varepsilon_{r\theta} = \frac{1}{2} \left( \frac{1}{r} \frac{\partial u_r}{\partial \theta} - \frac{u_\theta}{r} + \frac{\partial u_\theta}{\partial r} \right), \\ \varepsilon_{\theta\varphi} &= \frac{1}{2} \left( \frac{1}{r} \frac{\partial u_\varphi}{\partial \theta} - \frac{u_\varphi}{r} \cot \theta + \frac{1}{r \sin \theta} \frac{\partial u_\theta}{\partial \varphi} \right)\end{aligned}\tag{2.4}$$

where  $u_\theta, u_\varphi$  and  $u_r$  are displacements in  $\theta, \varphi$  and  $r$  directions, respectively.



### 2.2.2 Equilibrium equations

For the present problem of spheres under diametral compression, body forces can be neglected. Hence, the equations of equilibrium can be simplified to

$$\begin{aligned}
\frac{\partial \sigma_{rr}}{\partial r} + \frac{1}{r \sin \theta} \frac{\partial \sigma_{r\varphi}}{\partial \varphi} + \frac{1}{r} \frac{\partial \sigma_{r\theta}}{\partial \theta} + \frac{2\sigma_{rr} - \sigma_{\theta\theta} - \sigma_{\varphi\varphi} + \sigma_{r\theta} \cot \theta}{r} &= 0 \\
\frac{\partial \sigma_{r\varphi}}{\partial r} + \frac{1}{r \sin \theta} \frac{\partial \sigma_{\varphi\varphi}}{\partial \varphi} + \frac{1}{r} \frac{\partial \sigma_{\theta\varphi}}{\partial \theta} + \frac{3\sigma_{r\varphi} + 2\sigma_{\theta\varphi} \cot \theta}{r} &= 0 \\
\frac{\partial \sigma_{r\theta}}{\partial r} + \frac{1}{r \sin \theta} \frac{\partial \sigma_{\theta\varphi}}{\partial \varphi} + \frac{1}{r} \frac{\partial \sigma_{\theta\theta}}{\partial \theta} + \frac{3\sigma_{r\theta} + (\sigma_{\theta\theta} - \sigma_{\varphi\varphi}) \cot \theta}{r} &= 0
\end{aligned} \tag{2.5}$$

Substituting (2.2) and (2.4) into (2.5), we obtain

$$\begin{aligned}
-2(A_{12} + A_{66}) \frac{\varepsilon}{r} + A_{13} \left( \frac{\partial \varepsilon}{\partial r} + \frac{2\varepsilon}{r} - \frac{2\varepsilon_{rr}}{r} \right) + A_{33} \left( \frac{\partial \varepsilon_{rr}}{\partial r} + \frac{2\varepsilon_{rr}}{r} \right) + A_{44} \left[ \frac{1}{r^2} \nabla_1^2 u_r + \frac{\partial}{\partial r} \left( \varepsilon - \frac{2u_r}{r} \right) \right] &= 0 \\
\frac{A_{12}}{r \sin \theta} \frac{\partial \varepsilon}{\partial \varphi} + 2A_{66} \left( \frac{1}{r \sin \theta} \frac{\partial \varepsilon_{\varphi\varphi}}{\partial \varphi} + \frac{1}{r} \frac{\partial \varepsilon_{\theta\varphi}}{\partial \theta} + \frac{2 \cot \theta}{r} \varepsilon_{\theta\varphi} \right) + \frac{A_{13}}{r \sin \theta} \frac{\partial \varepsilon_{rr}}{\partial \varphi} + 2A_{44} \left( \frac{\partial \varepsilon_{r\varphi}}{\partial r} + \frac{3\varepsilon_{r\varphi}}{r} \right) &= 0 \tag{2.6} \\
\frac{A_{12}}{r} \frac{\partial \varepsilon}{\partial \theta} + 2A_{66} \left[ \frac{1}{r \sin \theta} \frac{\partial \varepsilon_{\theta\varphi}}{\partial \varphi} + \frac{1}{r} \frac{\partial \varepsilon_{\theta\theta}}{\partial \theta} + \frac{\cot \theta}{r} (\varepsilon_{\theta\theta} - \varepsilon_{\varphi\varphi}) \right] + \frac{A_{13}}{r} \frac{\partial \varepsilon_{rr}}{\partial \theta} + 2A_{44} \left( \frac{\partial \varepsilon_{r\theta}}{\partial r} + \frac{3\varepsilon_{r\theta}}{r} \right) &= 0
\end{aligned}$$

where

$$\varepsilon = \varepsilon_{\theta\theta} + \varepsilon_{\varphi\varphi} \tag{2.7}$$

$$\nabla_1^2 = \frac{\partial^2}{\partial \theta^2} + \cot \theta \frac{\partial}{\partial \theta} + \frac{1}{\sin^2 \theta} \frac{\partial^2}{\partial \varphi^2} \tag{2.8}$$

### 2.2.3 Boundary conditions

For the diametral compression of spheres of radius  $R$ , the pair of point forces of magnitude  $F$  are modeled by uniform radial stress  $p$  applied over two opposite

spherical areas (on  $r = R$ ), which subtend an angle of  $2\theta_0$  from the origin symmetrically with respect to the  $z$ -axis, as shown in Fig. 2-3. All other tractions are zero on  $r = R$ . Mathematically, this boundary condition can be expressed as:

$$\sigma_{rr} = \begin{cases} -p & \text{for } 0 \leq \theta \leq \theta_0 \text{ and } \pi - \theta_0 \leq \theta \leq \pi \\ 0 & \text{for } \theta_0 < \theta < \pi - \theta_0 \end{cases} \quad (2.9)$$

$$\sigma_{r\varphi} = \sigma_{r\theta} = 0 \quad (2.10)$$

on  $r = R$ , where  $p$  can be expressed in terms of  $F$ ,  $R$  and  $\theta_0$  as (Hiramatsu and Oka 1966):

$$p = F / [2\pi R^2 (1 - \cos \theta_0)] \quad (2.11)$$

Now, our problem is to solve the equilibrium equations (2.6) subject to boundary conditions (2.9) to (2.10). The technique of displacement function and the method of solutions are considered next.

### 2.3 Displacement Functions

It was proposed by Hu (1954) that the displacements under consideration can be resolved into two parts: the first displacement field corresponds to both the radial displacement and the dilatation equal to zero; and the second field corresponds to the radial component of the curl of the displacements equal to zero. More specifically, the displacements are decomposed into (Hu, 1954):

$$\begin{aligned} u_r &= u_r^I + u_r^{II} = 0 + w \\ u_\theta &= u_\theta^I + u_\theta^{II} = -\frac{1}{r \sin \theta} \frac{\partial \psi}{\partial \varphi} - \frac{1}{r} \frac{\partial G}{\partial \theta} \\ u_\varphi &= u_\varphi^I + u_\varphi^{II} = \frac{1}{r} \frac{\partial \psi}{\partial \theta} - \frac{1}{r \sin \theta} \frac{\partial G}{\partial \varphi} \end{aligned} \quad (2.12)$$

where  $\psi$  and  $G$  are displacement functions. Substitution of (2.12) into (2.6) leads to the following partial differential equations

$$\frac{2(a+b)}{r^3} \nabla_1^2 G - \frac{d}{r^2} \nabla_1^2 \frac{\partial G}{\partial r} + \frac{2g}{r^2} w + \frac{c}{r^2} \frac{\partial}{\partial r} (r^2 \frac{\partial w}{\partial r}) + \frac{h}{r^2} \nabla_1^2 w = 0 \quad (2.13)$$

$$\frac{1}{r} \frac{\partial B}{\partial \theta} + \frac{1}{r \sin \theta} \frac{\partial A}{\partial \varphi} = 0 \quad (2.14)$$

$$\frac{1}{r} \frac{\partial A}{\partial \theta} - \frac{1}{r \sin \theta} \frac{\partial B}{\partial \varphi} = 0 \quad (2.15)$$

in which  $A$  and  $B$  are functions expressed in terms of  $w$ ,  $G$ , and  $\psi$

$$A = -\frac{a}{r^2} \nabla_1^2 G + \frac{2b}{r^2} G - h \frac{\partial^2 G}{\partial r^2} + \frac{2(a+b)}{r} w + d \frac{\partial w}{\partial r} \quad (2.16)$$

$$B = (h-b) \left( \frac{1}{r^2} \nabla_1^2 \psi + \frac{2\psi}{r^2} \right) + h \left( \frac{\partial^2 \psi}{\partial r^2} - \frac{2\psi}{r^2} \right) \quad (2.17)$$

$$\begin{aligned} a &= A_{12} + 2A_{66}, \quad b = A_{44} - A_{66}, \quad d = A_{13} + A_{44}, \\ c &= A_{33}, \quad h = A_{44}, \quad g = d + h - 2(a+b) \end{aligned} \quad (2.18)$$

As shown in Section V of Hu (1954), without loss of generality, both  $A$  and  $B$  can be set to zero; that is,

$$A = B = 0 \quad (2.19)$$

The proof of this result is outlined briefly in Appendix I. In order to obtain a more tractable form of the solution for (2.13) and (2.19), the following change of variables similar to those proposed by Ding and Ren (1991) is introduced,

$$r = R \exp(\eta), \quad \psi = RZ \exp(\eta), \quad G = RF \exp(\eta), \quad w = -r \frac{\partial H}{\partial r} = -\frac{\partial H}{\partial \eta} \quad (2.20)$$

where  $Z$ ,  $F$ , and  $H$  are new displacement functions in terms of the new dimensionless radial variable  $\eta$ , and  $R$  is the radius of the sphere. When  $R = 1$ , the change of

variables introduced in (2.20) reduces to those of Ding and Ren (1991), but with the introduction of  $R$  into (2.20) no ambiguity in dimension will be resulted, as compared to the analysis by Ding and Ren (1991). The main reason for introducing the change of variables in (2.20) is that, as it will be shown later in this paper, the roots for the characteristic equations for the governing equations can be obtained explicitly, as compared to the implicit form given in equation (33) of Hu (1954).

Substitution of (2.20) into (2.16), (2.17), (2.19) and (2.13) leads to the following three partial differential equations for  $Z$ ,  $F$ , and  $H$ :

$$A_{44}(\frac{\partial^2 Z}{\partial \eta^2} + \frac{\partial Z}{\partial \eta}) + A_{66}\nabla_1^2 Z - 2(A_{44} - A_{66})Z = 0 \quad (2.21)$$

$$[h(\frac{\partial^2}{\partial \eta^2} + \frac{\partial}{\partial \eta}) + a\nabla_1^2 - 2b]F + [d\frac{\partial^2}{\partial \eta^2} + 2(a+b)\frac{\partial}{\partial \eta}]H = 0 \quad (2.22)$$

$$[(h-g)\nabla_1^2 - d\nabla_1^2\frac{\partial}{\partial \eta}]F - [c(\frac{\partial^3}{\partial \eta^3} + \frac{\partial^2}{\partial \eta^2}) + h\nabla_1^2\frac{\partial}{\partial \eta} + 2g\frac{\partial}{\partial \eta}]H = 0 \quad (2.23)$$

To uncouple the governing equations (2.22) and (2.23) for  $F$  and  $H$ , another new displacement function  $\phi$  is introduced such that

$$F = [d\frac{\partial^2}{\partial \eta^2} + 2(a+b)\frac{\partial}{\partial \eta}]\phi \quad (2.24)$$

$$H = -[h(\frac{\partial^2}{\partial \eta^2} + \frac{\partial}{\partial \eta}) + a\nabla_1^2 - 2b]\phi \quad (2.25)$$

Then, (2.22) is satisfied identically by (2.24) and (2.25). Substitution of (2.24) and (2.25) into (2.23) yields a single governing equation for  $\phi$ , which can be further simplified to the following form if another new potential  $\Phi$  is introduced

$$\{(\frac{\partial^2}{\partial \eta^2} + \frac{\partial}{\partial \eta})^2 + 2D(\frac{\partial^2}{\partial \eta^2} + \frac{\partial}{\partial \eta}) + M\nabla_1^2(\frac{\partial^2}{\partial \eta^2} + \frac{\partial}{\partial \eta}) - 4L + 2(N-L)\nabla_1^2 + N\nabla_1^2\nabla_1^2\}\Phi = 0 \quad (2.26)$$

where

$$D = \frac{hg - bc}{ch}, \quad L = \frac{bg}{ch}, \quad M = \frac{ac + h^2 - d^2}{ch}, \quad N = \frac{a}{c} \quad (2.27)$$

and  $\Phi$  is defined as

$$\Phi = -\frac{\partial \phi}{\partial \eta} \quad (2.28)$$

Subsequently, only two displacement potentials  $Z$  and  $\Phi$  remain and satisfy (2.21) and (2.26) respectively. Expressed in terms of these displacement functions, the displacement components become

$$\begin{aligned} u_\theta &= -\frac{1}{\sin \theta} \frac{\partial Z}{\partial \varphi} + \left[ d \frac{\partial}{\partial \eta} + 2(a+b) \right] \frac{\partial \Phi}{\partial \theta}, \quad u_\varphi = \frac{\partial Z}{\partial \theta} + \frac{1}{\sin \theta} \left[ d \frac{\partial}{\partial \eta} + 2(a+b) \right] \frac{\partial \Phi}{\partial \varphi}, \\ u_r &= -\left[ h \left( \frac{\partial^2}{\partial \eta^2} + \frac{\partial}{\partial \eta} \right) + a \nabla_i^2 - 2b \right] \Phi \end{aligned} \quad (2.29)$$

Substitution of (2.29) into (2.4) and (2.2) yields the strain and stress components in terms of  $Z$  and  $\Phi$ . The attractive feature of this displacement function approach is that our governing equations are reduced to two *uncoupled* partial differential equations, which are much easier to solve than coupled partial differential equations. But, as a trade off the governing equation (2.26) is of order higher than that of the equations of equilibrium. The general solutions for  $Z$  and  $\Phi$  are discussed next.

## 2.4 General Solutions for the Displacement Functions

Motivated by the stress analysis for isotropic spheres, the following solution form in terms of spherical harmonics is sought for the displacement function  $Z$

$$Z = \sum_{n=0}^{\infty} D_n e^{\lambda_n \eta} S_n(\theta, \varphi) \quad (2.30)$$

where  $D_n$  and  $\lambda_n$  are unknown constants to be determined and  $S_n(\theta, \varphi)$  is the spherical harmonics of order  $n$ , which satisfies

$$\nabla_1^2 S_n(\theta, \varphi) + n(n+1)S_n(\theta, \varphi) = 0 \quad (2.31)$$

Substitution of (2.30) into (2.21) leads to the following characteristic equation for  $\lambda_n$

$$\lambda_n^2 + \lambda_n - M_n = 0 \quad (2.32)$$

where

$$M_n = 2 + (n-1)(n+2)A_{66} / A_{44} \quad (2.33)$$

The two characteristic roots of (2.32) are

$$\lambda_{n1} = \frac{-1 + \sqrt{1 + 4M_n}}{2}, \quad \lambda_{n2} = \frac{-1 - \sqrt{1 + 4M_n}}{2} \quad (2.34)$$

Consequently, if  $\lambda_{n1} \neq \lambda_{n2}$ , the displacement function  $Z$  defined in (2.29) becomes

$$Z = \sum_{n=0}^{\infty} (D_{n1}e^{\lambda_{n1}\eta} + D_{n2}e^{\lambda_{n2}\eta})S_n(\theta, \varphi) \quad (2.35)$$

where  $D_{n1}$  and  $D_{n2}$  are unknown constants to be determined. Similarly, the following form is sought for the displacement function  $\Phi$

$$\Phi = \sum_{n=0}^{\infty} C_n e^{\mu_n \eta} S_n(\theta, \varphi) \quad (2.36)$$

Substitution of (2.36) into (2.26) yields the following characteristic equation for  $\mu_n$

$$(\mu_n^2 + \mu_n)^2 + 2P_n(\mu_n^2 + \mu_n) + Q_n = 0 \quad (2.37)$$

where

$$P_n = D - n(n+1)\frac{M}{2}, \quad Q_n = (n+2)(n-1)[2L + n(n+1)N] \quad (2.38)$$

The four characteristic roots for (2.37) can be solved analytically as

$$\mu_{n1} = \frac{-1 + \sqrt{\varsigma_n}}{2}, \quad \mu_{n2} = \frac{-1 + \sqrt{\xi_n}}{2}, \quad \mu_{n3} = \frac{-1 - \sqrt{\varsigma_n}}{2}, \quad \mu_{n4} = \frac{-1 - \sqrt{\xi_n}}{2} \quad (2.39)$$

where

$$\varsigma_n = 1 - 4[P_n + \sqrt{(P_n^2 - Q_n)}], \quad \xi_n = 1 - 4[P_n - \sqrt{(P_n^2 - Q_n)}] \quad (2.40)$$

The second subscript  $i$  ( $i = 1, 2, 3, 4$ ) of  $\mu_{ni}$  in (2.39) indicates the root number. When the roots for  $\mu_{ni}$  are distinct, the general solution form for  $\Phi$  becomes

$$\Phi = \sum_{n=0}^{\infty} (C_{n1}e^{\mu_{n1}\eta} + C_{n2}e^{\mu_{n2}\eta} + C_{n3}e^{\mu_{n3}\eta} + C_{n4}e^{\mu_{n4}\eta}) S_n(\theta, \varphi) \quad (2.41)$$

where  $C_{n1}, C_{n2}, C_{n3}$  and  $C_{n4}$  are constants to be determined by the boundary conditions of the sphere. Since the exact forms for  $Z$  and  $\Phi$  depend on the types of the characteristic roots for  $\mu_n$  and  $\lambda_n$ , it is necessary to discuss the possible root types for them.

## 2.5 Characteristic Roots for Solid Spheres

Physically, all components of displacement, strain and stress must be real, therefore the displacement functions  $Z$  and  $\Phi$  must be real functions of the coordinate  $r, \theta$  and  $\varphi$ . For problems involving solid spheres, it is necessary to ensure that all stress components remain bounded as the origin is approached. Substitution of (2.35) and (2.41) into (2.29), (2.4) and (2.2) leads to the stress fields inside the sphere, which are found to be proportional to the power  $\text{Re}[\mu_{ni}] - 1$  ( $i = 1, 2, 3, 4$ ) and  $\text{Re}[\lambda_{ni}] - 1$  ( $i = 1, 2$ ) of  $r$ , where  $\text{Re}[\ ]$  means the real part of  $[ \ ]$ . Since all

stress components have to be finite at  $r = 0$ , all  $r$  terms with power  $\text{Re}[\mu_{ni}] < 1$  and power  $\text{Re}[\lambda_{ni}] < 1$  should be discarded in view of this condition of boundedness at the center of the sphere.

It can be shown that the three characteristic roots:  $\mu_{ni}$ ,  $i = 3, 4$  and  $\lambda_{n2}$  will lead to unbounded condition at the origin of the sphere, regardless of the value of  $n$  and the elastic properties. That is,

$$\text{Re}[\lambda_{n2}] < 1, \quad \text{Re}[\mu_{n3}] < 1, \quad \text{Re}[\mu_{n4}] < 1 \quad (2.42)$$

To see the validity of the first of (2.42), it can be noted that if  $1+4M_n > 0$ ,  $\lambda_{n2}$  is real and the real part of  $\lambda_{n2}$  is always less than  $-1/2$  (i.e.  $\text{Re}[\lambda_{n2}] < 1$ ); if  $1+4M_n \leq 0$ , the real part equal exactly  $-1/2$  (i.e.  $\text{Re}[\lambda_{n2}] < 1$ ). Consequently, we have  $\text{Re}[\lambda_{n2}] < 1$  independent of the value of  $n$ . For the validity of the second and third of (2.42), the following argument can be applied. If  $P_n^2 - Q_n \geq 0$ , we have three possible scenarios: for  $\varsigma_n$  and  $\xi_n \geq 0$ , both  $\mu_{n3}$  and  $\mu_{n4}$  are real and the real parts of them are always less than or equal to  $-1/2$ ; for  $\varsigma_n$  and  $\xi_n < 0$ , both  $\mu_{n3}$  and  $\mu_{n4}$  are complex and the real parts of them equal  $-1/2$ ; and, finally, for  $\varsigma_n < 0$  and  $\xi_n > 0$ ,  $\mu_{n3}$  is complex with the real part equal to  $-1/2$  and  $\mu_{n4}$  is real and less than  $-1/2$ . If  $P_n^2 - Q_n < 0$ , we can let  $\xi_n = Ae^{i\theta}$  with the imaginary part of  $\xi_n$  being  $4\sqrt{|P_n^2 - Q_n|}$ , which is always positive. This implies that  $0 < \theta < \pi$ . Thus,  $\xi_n^{1/2}$  becomes  $A^{1/2}e^{i\theta/2}$  with  $0 < \theta/2 < \pi/2$ ; hence, we must have  $\text{Re}[\xi_n^{1/2}] > 0$ . Consequently, if  $P_n^2 - Q_n < 0$ , we have  $\text{Re}[\mu_{n3}] < 1$  as shown in (2.39). Since for  $P_n^2 - Q_n < 0$ ,  $\varsigma_n$  and  $\xi_n$  are complex



conjugates, so  $\text{Re}[\varsigma_n^{1/2}] = \text{Re}[\xi_n^{1/2}] > 0$ , hence  $\text{Re}[\mu_{n4}] < -1/2$ . Therefore, the proof for the validity of (2.42) is demonstrated. Thus, to ensure the stress field to be finite at  $r = 0$ , we have to set the constants for all terms corresponding to  $\lambda_{n2}$ ,  $\mu_{n3}$  and  $\mu_{n4}$  zero.

The solution forms for  $\Phi$  and  $Z$  now depend on the types of the possible roots for the remaining characteristic values  $\lambda_{n1}$ ,  $\mu_{n1}$  and  $\mu_{n2}$ . We further note here that our problem is axisymmetric with respect to the angle  $\varphi$ . Thus, the spherical harmonics reduces to

$$S_n(\theta, \varphi) = P_n(\cos\theta) \quad (2.43)$$

where  $P_n(\cos\theta)$  is the Legendre Polynomials (e.g. Abramowitz and Stegun, 1965). Therefore, all derivatives with respect to  $\varphi$  must be zero; consequently, it can be shown that the displacement  $Z$  is identically zero. To see this, we, by using (2.1), (2.4) and (2.29), first express the shear stress  $\sigma_{r\varphi}$  as

$$\sigma_{r\varphi} = G' \left\{ \frac{\partial^2 Z}{\partial r \partial \theta} - \frac{1}{r} \frac{\partial Z}{\partial \theta} \right\} \quad (2.44)$$

Since only one characteristic root remains for  $Z$  (i.e.  $\lambda_{n1}$ ), the boundary conditions (2.10) require that  $Z \equiv 0$ .

For the possible solution forms for  $\Phi$ , there are six possible scenarios for the types of roots for  $\mu_{n1}$  and  $\mu_{n2}$ : (I) when  $P_n^2 - Q_n > 0$ ,  $\varsigma_n > 0$ ,  $\xi_n > 0$ ,  $\mu_{n1}$  and  $\mu_{n2}$  are real unequal roots; (II) when  $P_n^2 - Q_n < 0$ ,  $\mu_{n1}$  and  $\mu_{n2}$  are complex conjugates; (III) when  $P_n^2 - Q_n > 0$ ,  $\varsigma_n < 0$ ,  $\xi_n > 0$ ,  $\mu_{n1}$  is complex and  $\mu_{n2}$  is real; (IV) when  $P_n^2 - Q_n > 0$ ,  $\varsigma_n < 0$ ,  $\xi_n < 0$ ,  $\mu_{n1}$  and  $\mu_{n2}$  are complex but not

conjugates; (V) when  $P_n^2 - Q_n = 0$ ,  $\varsigma_n = \xi_n > 0$ ,  $\mu_{n1} = \mu_{n2}$  are real (double real roots); and (VI) when  $P_n^2 - Q_n = 0$ ,  $\varsigma_n = \xi_n < 0$ ,  $\mu_{n1} = \mu_{n2}$  are complex (double complex roots). However, for Case (III) it is straightforward to see that  $\text{Re}[\mu_{n1}] = -1/2 < 1$ , thus the corresponding stress does not converge at  $r = 0$ . Consequently, this possible scenario is ruled out. Similarly, the solution form for Case (IV) can also be ruled out as it can be shown that  $\text{Re}[\mu_{n1}] = \text{Re}[\mu_{n2}] = -1/2 < 1$ . For Case (VI), it can be shown that  $\text{Re}[\mu_{n1}] = \text{Re}[\mu_{n2}] = -1/2 < 1$ , thus this possibility is again ruled out. For Cases (V), it is required that  $P_n^2 - Q_n = 0$ , which is unlikely to be satisfied by most real materials for any particular  $n$ . Therefore, these possibilities will not be considered in this study. The solutions for the remaining two possible scenarios are:

#### 2.5.1 Case I: Two real roots

For any spherically isotropic material with a fixed value of  $n$ , if we find that  $P_n^2 - Q_n > 0$ ,  $\varsigma_n > 0$ ,  $\xi_n > 0$ , then  $\mu_{n1}$  and  $\mu_{n2}$  are real unequal roots. If  $\mu_{n1}$  and  $\mu_{n2} \geq 1$ , the corresponding solution is:

$$\Phi_n = (C_{n1}e^{\mu_{n1}\eta} + C_{n2}e^{\mu_{n2}\eta})P_n(\cos\theta) \quad (2.45)$$

where  $C_{n1}$  and  $C_{n2}$  are real constants. If  $\mu_{n1}$  and  $\mu_{n2} < 1$ , no converging solution can be found for solid spheres.

#### 2.5.2 Case II: Two complex conjugate roots

For a particular spherically isotropic material with a specific  $n$ , if  $P_n^2 - Q_n < 0$ ,  $\mu_{n1}$  and  $\mu_{n2}$  are complex conjugates. If  $\text{Re}[\mu_{n1}]$  and  $\text{Re}[\mu_{n2}] \geq 1$ , the corresponding solution is:

$$\Phi_n = (D_n e^{\mu_n \eta} + \overline{D_n} e^{\overline{\mu_n} \eta}) P_n(\cos \theta) \quad (2.46)$$

where  $D_n = R_n + i I_n$  is a complex constant and the superimposed bar denotes the complex conjugate and  $\mu_n$  becomes

$$\mu_n = \frac{-1 + \sqrt{1 - 4P_n - i4\sqrt{|P_n^2 - Q_n|}}}{2} = x_n + iy_n. \quad (2.47)$$

Therefore, the general solution for  $\Phi$  can now be expressed as:

$$\Phi = \sum_{n=0}^{\infty} \Phi_n \quad (2.48)$$

where  $\Phi_n$  is defined in either (2.45) or (2.46), depending on the type of roots for  $\mu_n$ .

## 2.6 The Method of Solutions

### 2.6.1 The general solutions of stresses

Substitution of the displacement potential into (2.29), (2.4) and (2.2) yields the following expressions for the stress components:

$$\begin{aligned} \sigma_{\theta\theta} = & -\frac{1}{R} \sum_m \sum_{i=1}^2 C_{mi} \rho^{\mu_{mi}-1} \{ [A_{12} m(m+1) \Gamma_{mi} + (A_{13} \mu_{mi} + 2A_{12} + 2A_{66}) \Lambda_{mi}] \\ & \times P_m(\cos \theta) - 2A_{66} \Gamma_{mi} \frac{\partial^2 P_m(\cos \theta)}{\partial \theta^2} \} \\ & + \frac{1}{R} \sum_n \rho^{x_n-1} \{ P_n(\cos \theta) [\Omega_1(R_n, I_n) \cos(y_n \ln \rho) + \Omega_1(-I_n, R_n) \sin(y_n \ln \rho)] \\ & - \frac{\partial^2 P_n(\cos \theta)}{\partial \theta^2} [\Omega_2(R_n, I_n) \cos(y_n \ln \rho) + \Omega_2(-I_n, R_n) \sin(y_n \ln \rho)] \} \end{aligned} \quad (2.49)$$

$$\begin{aligned} \sigma_{r\theta} = & -\frac{1}{R} \sum_m \sum_{i=1}^2 \{ A_{44} C_{mi} \rho^{\mu_{mi}-1} [(1 - \mu_{mi}) \Gamma_{mi} + \Lambda_{mi}] \frac{\partial \mathcal{P}_n(\cos \theta)}{\partial \theta} \} \\ & + \frac{1}{R} \sum_n \rho^{x_n-1} [\Pi(R_n, I_n) \cos(y_n \ln \rho) + \Pi(-I_n, R_n) \sin(y_n \ln \rho)] \frac{\partial \mathcal{P}_n(\cos \theta)}{\partial \theta} \end{aligned} \quad (2.50)$$

where  $\rho = r/R$  is the normalized radial coordinate. Note that the first summation for  $m$  is done over all Case I (i.e. two real roots for  $\mu_n$ ) while the second summation for  $n$  is done over all Case II (i.e. two complex conjugates for  $\mu_n$ ). The following functions have been used in these expressions:

$$\Gamma_{mi} = \Gamma_{mi}(\mu_{mi}) = d\mu_{mi} + 2(a + b) \quad (2.51)$$

$$\Lambda_{mi} = \Lambda_{mi}(\mu_{mi}) = h\mu_{mi}(\mu_{mi} + 1) - 2b - am(m + 1) \quad (2.52)$$

$$\begin{aligned} \Omega_1(R_n, I_n) = & 4A_{44}(A_{12} + A_{66})[I_n(2x_n + 1)y_n - R_n(x_n^2 - y_n^2 + x_n)] \\ & + A_{12}n(n + 1)[2d(I_n y_n - x_n R_n) - 4(a + b)R_n] \\ & + 2A_{44}A_{13}[(x_n I_n + y_n R_n)(2x_n + 1)y_n - (x_n R_n - y_n I_n)(x_n^2 - y_n^2 + x_n)] \\ & + 2[2b + an(n + 1)][2(A_{12} + A_{66})R_n + A_{13}(x_n R_n - I_n y_n)] \end{aligned} \quad (2.53)$$

$$\Omega_2(R_n, I_n) = 2A_{66}[2d(I_n y_n - x_n R_n) - 4(a + b)R_n] \quad (2.54)$$

$$\begin{aligned} \Pi(R_n, I_n) = & A_{44}\{I_n y_n[2d(1 - 2x_n) - 4(a + b)] \\ & + R_n[2d(x_n^2 - y_n^2 - x_n) + 4(a + b)(x_n - 1)]\} \\ & - 2A_{44}^2[R_n(x_n^2 - y_n^2 + x_n) - I_n(2x_n + 1)y_n] + 2A_{44}[2b + an(n + 1)]R_n \end{aligned} \quad (2.55)$$

The expression for  $\sigma_{rr}$  can be obtained from (2.49) by replacing  $A_{12}$ ,  $(2A_{66})$ , and  $A_{13}$  by  $A_{13}$ , 0, and  $A_{33}$  respectively; while the expression for  $\sigma_{\varphi\varphi}$  can be obtained from (2.49) by replacing  $A_{12}$  and  $(2A_{66})$  by  $(2A_{66} + A_{12})$  and  $(-2A_{66})$  respectively.

### 2.6.2 Determination of unknown coefficients

In order to determine the unknown coefficients in these expressions, the Fourier-Legendre expansion (e.g. see Brown and Churchill, 1993) adopted by Hiramatsu and Oka (1966) is employed here to rewrite (2.9) as

$$\sigma_{rr} = (\cos \theta_0 - 1)p + \sum_{n=1}^{\infty} E_{2n} P_{2n}(\cos \theta) \quad (2.56)$$

where

$$E_{2n} = \frac{4n+1}{2n+1} [\cos \theta_0 P_{2n}(\cos \theta_0) - P_{2n-1}(\cos \theta_0)]p \quad (2.57)$$

The coefficients for this Fourier-Legendre expansion of the applied normal stress can be used to match with those from the internal stress field when the boundary values are considered.

By combining the shear traction free condition given in the second of (2.10) and (2.50), the following relations between  $C_{m1}$  and  $C_{m2}$  and between  $I_n$  and  $R_n$  are established:

$$C_{m1} = L_m C_{m2}, \quad I_n = K_n R_n \quad (2.58)$$

where

$$L_m = -\frac{(1 - \mu_{m2})\Gamma_{m2} + \Lambda_{m2}}{(1 - \mu_{m1})\Gamma_{m1} + \Lambda_{m1}}, \quad K_n = \frac{\Pi(1,0)}{\Pi(0,-1)} \quad (2.59)$$

Since  $\sigma_{rr}$ ,  $\sigma_{\theta\theta}$  and  $\sigma_{\varphi\varphi}$  are even functions of  $\theta$  while  $\sigma_{r\theta}$  is odd function of  $\theta$ , we can replace “ $n$ ” by “ $2n$ ” and “ $m$ ” by “ $2m$ ” in all of the above expressions. The expression of  $\sigma_{rr}$  on  $r = R$  must match with (2.56) and leads to the following solutions for  $C_{2m,2}$  and  $R_{2n}$  (note that to avoid confusion the subscript  $2m$  and 2 are separated by a “comma”):

$$C_{2m,2} = -\frac{E_{2m} R}{J_{2m}}, \quad R_{2n} = \frac{E_{2n} R}{H_{2n}} \quad (2.60)$$

where  $R$  is again the radius of the sphere

$$J_{2m} = L_{2m} [2A_{13} m(2m+1) \Gamma_{2m,1} + (2A_{13} + A_{33} \mu_{2m,1}) \Lambda_{2m,1}] \\ + 2A_{13} m(2m+1) \Gamma_{2m,2} + (2A_{13} + A_{33} \mu_{2m,2}) \Lambda_{2m,2} \quad (2.61)$$

$$H_{2n} = 4A_{44} A_{13} [K_{2n} (2x_{2n} + 1) y_{2n} - (x_{2n}^2 - y_{2n}^2 + x_{2n})] \\ + 2A_{13} n(2n+1) [2d(K_{2n} y_{2n} - x_{2n}) - 4(a+b)] \\ + 2A_{44} A_{33} [(x_{2n} K_{2n} + y_{2n})(2x_{2n} + 1) y_{2n} - (x_{2n} - y_{2n} K_{2n})(x_{2n}^2 - y_{2n}^2 + x_{2n})] \\ + 4[b + an(2n+1)] [2A_{13} + A_{33} (x_{2n} - K_{2n} y_{2n})] \quad (2.62)$$

### 2.6.3 Final solutions for stresses

By now, all unknown constants have been obtained, and substitution of (2.58) and (2.60) into (2.49) and (2.50) yields the final expressions of the stress components as

$$\sigma_{\theta\theta} = \sum_n \{ [L_{2n} \rho^{\mu_{2n,1}-1} [2A_{12} m(2m+1) \Gamma_{2m,1} + (A_{13} \mu_{2m,1} + 2A_{12} + 2A_{66}) \Lambda_{2m,1}] \\ + [2A_{12} m(2m+1) \Gamma_{2m,2} + (A_{13} \mu_{2m,2} + 2A_{12} + 2A_{66}) \Lambda_{2m,2}] \rho^{\mu_{2m,2}-1} ] P_{2m}(\cos\theta) \\ - 2A_{66} [\rho^{\mu_{2m,1}-1} \Gamma_{2m,1} L_{2m} + \rho^{\mu_{2m,2}-1} \Gamma_{2m,2}] \frac{\partial^2 P_{2m}(\cos\theta)}{\partial \theta^2} \} \times \frac{E_{2m}}{J_{2m}} \\ + \sum_n \rho^{2n-1} \{ P_{2n}(\cos\theta) [\Omega_1(1, K_{2n}) \cos(y_{2n} \ln \rho) + \Omega_1(-K_{2n}, 1) \sin(y_{2n} \ln \rho)] \\ - \frac{\partial^2 P_{2n}(\cos\theta)}{\partial \theta^2} [\Omega_2(1, K_{2n}) \cos(y_{2n} \ln \rho) + \Omega_2(-K_{2n}, 1) \sin(y_{2n} \ln \rho)] \} \times \frac{E_{2n}}{H_{2n}} \quad (2.63)$$

$$\begin{aligned}
\sigma_{r\theta} = & \sum_m \{ A_{44} L_{2m} \rho^{\mu_{2m,1}-1} [(1 - \mu_{2m,1}) \Gamma_{2m,1} + \Lambda_{2m,1}] \\
& + A_{44} \rho^{\mu_{2m,2}-1} [(1 - \mu_{2m,2}) \Gamma_{2m,2} + \Lambda_{2m,2}] \} \frac{\partial P_{2m}(\cos \theta)}{\partial \theta} \times \frac{E_{2m}}{J_{2m}} \\
& + \sum_n \rho^{x_{2n}-1} [\Pi(1, K_{2n}) \cos(y_{2n} \ln \rho) + \Pi(-K_{2n}, 1) \sin(y_{2n} \ln \rho)] \frac{\partial P_{2n}(\cos \theta)}{\partial \theta} \times \frac{E_{2n}}{H_{2n}} \quad (2.64)
\end{aligned}$$

And other shear stresses are zero (i.e.  $\sigma_{r\phi} = \sigma_{\phi\theta} = 0$ ). As mentioned previously, the expression for  $\sigma_{rr}$  can be obtained from (2.63) by replacing “ $A_{12}, (2A_{66}), A_{13}$ ” by “ $A_{13}, 0, A_{33}$ ” respectively; while those for  $\sigma_{\phi\phi}$  can be obtained from (2.63) by replacing “ $A_{12}, (2A_{66})$ ” by “ $(2A_{66} + A_{12}), (-2A_{66})$ ” respectively.

In the isotropic case, the coefficients in the generalized Hooke’s law take the values

$$E' = E, \quad \bar{\nu} = \nu' = \nu, \quad G' = \frac{E}{2(1 + \nu)} \quad (2.65)$$

Substitution of (2.65) into (2.63) and (2.64), the present solution reduces to the analytic solution by Hiramatsu and Oka (1966) for isotropic spheres subject to a pair of diametrical pointed loads, which has been found providing the theoretical basis in studying PLST

## 2.7 Numerical Results and Discussion

### 2.7.1 Stresses in isotropic spheres and comparisons with experiments

Hiramatsu and Oka (1966) concluded, by summing a finite number of terms in their analytic solution of infinite series, that the tensile stress induced along the axis through which the point loads are applied is *fairly uniform* (e.g. see Fig. 5 of their paper). However, a more careful study of Hiramatsu and Oka’s (1966) solution by

Wijk (1978) revealed that the maximum tensile stress may rise to double that of the ‘plateau’ value in the central part of the specimen for  $\nu = 1/3$  and the tensile stress distribution is *not uniform* (see Fig. 3 of Wijk 1978). This observation provides a means to check the accuracy of the present numerical results. In particular, the stresses for the case of isotropic spheres with  $\nu = 1/3$  and  $\theta_0 = 3^\circ$  were calculated, and our results coincide with those given in Fig. 2 of Wijk (1978), as expected. To further investigate the finding by Wijk (1978), Fig. 2-4 plots the variations of the normalized radial and tangential stresses,  $2\pi R^2 \sigma_{rr}/F$  and  $2\pi R^2 \sigma_{\theta\theta}/F$ , versus the radial distance  $r/R$  along the z-axis for various values of Poisson’s ratio  $\nu$  ( $= \nu' = \bar{\nu}$ ) for  $\theta_0 = 3^\circ$ . By following the usual sign convention of continuum mechanics, tension is plotted as positive. For small Poisson’s ratio (say  $\nu = 0.1$ ), a “local peak” near  $r/R = 0.9$  appears in the tensile stress concentration which is about ten times larger than those observed at the central part of the specimen. If the tensile strength or point load strength index (PLSI) is proportional to the maximum tensile stress within the specimen at the instant of failure, Fig. 2-4 indicates that the PLSI is extremely sensitive to the actual value of the Poisson’s ratio of the rock. However, the tensile stress at the central ‘plateau’ and the radial compression is relatively insensitive to the change in Poisson’s ratio.

Figure 2-5 illustrates the effect of the size of the contact zone,  $\theta_0$ , on the magnitude of the local peak of tensile stress for  $\nu = \nu' = \bar{\nu} = 0.1$ . Except for the varying  $\theta_0$ , the plot is the same as those given in Fig. 4. It is clear that the deviation of the maximum tensile stress from the ‘plateau’ value at the central portion of the



sphere increases drastically with the decrease of  $\theta_0$ , especially for  $\theta_0 < 5^\circ$ . For example, the increment of the maximum tensile stress rises about 180% as  $\theta_0$  decreases from  $5^\circ$  to  $3^\circ$ . For a large contact zone (say  $\theta_0 > 7^\circ$ ), the effect on local tensile zone is not significant.

Since for the case of anisotropic spheres, there is, to the best of our knowledge, no experimental measurement on the stress concentration within a sphere under diametral point loads. Figures 2-6 and 2-7 compare the predictions by our solution for isotropic spheres with the experimental observations by Frocht and Guernsey (1953), as well as the theoretical prediction by Sternberg and Rosenthal (1952). More specifically, Fig. 2-6 plots the compressive hoop stress versus the radius  $r/R$  along  $\theta = \pi / 2$  for an isotropic sphere with  $\nu = 0.48$  and  $\theta_0 = 5^\circ$ . Our prediction seems to agree better with the experiments than those by Sternberg and Rosenthal (1952), although both solutions agree well with experiments. Figure 2-7 plots both the radial and tangential stresses along the line between the point loads (i.e. along  $\theta = 0^\circ$ ) for  $\nu = 0.48$ . Since a large deformation of the sphere is observed in the loaded regions in the experiment (e.g. see Fig. 2-8 of Frocht and Guernsey, 1953), it is difficult to determine precisely the value of  $\theta_0$  in the experiments. Therefore, predictions have been obtained for both  $\theta_0 = 5^\circ$  and  $\theta_0 = 15^\circ$ . The predictions for  $\theta_0 = 15^\circ$  seems to agree better with experiments when  $r/R > 0.5$ , but both predictions and observations agree well for  $r/R < 0.5$ , independent of the values of  $\theta_0$ . Thus, this plot also provides a verification of our conclusion from Fig. 2-5 that the tensile stresses within the central portion of the specimen (say  $r/R < 0.5$ ) are independent of

the choice of  $\theta_0$ . Although there is discrepancy near the surface of the sphere, the agreement between the theoretical and experimental values is remarkably good in the neighborhood of the center of the sphere.

### 2.7.2 Stresses in anisotropic spheres

The main contribution of the present paper is in obtaining an analytic solution for spherically isotropic spheres under diametral point loads, and provides an anisotropic counterpart of the classic solution by Hiramatsu and Oka (1966) for isotropic spheres. Therefore, it is essential to investigate how the ‘local tensile zone’ near  $r/R = 0.9$  depends on the change in the degree of anisotropy, as most rocks found in nature are anisotropic. Three parameters indicating the degree of anisotropy are defined here and will be used as the control parameters in our calculations:

$$\beta = \frac{E}{E'}, \quad \alpha = \frac{\nu'}{\nu}, \quad \xi = \frac{A_{44}}{A_{66}} \quad (2-66)$$

Figure 2-8 plots both normalized radial and tangential stresses along the line between the center and the point load for various values of modulus ratio  $\beta$  (from 1.0 to 1.8) with  $\alpha=\xi=1.0$ ,  $\bar{\nu}=0.2$  and  $\theta_0 = 3^\circ$ . The maximum tensile stress at about  $r/R = 0.9$  increases with  $\beta$ . That is, if a sphere is stiffer against axial deformation along the tangential direction than along the radial direction, it is weaker in PLST (since a higher tensile stress concentration is resulted and the rock with a larger  $\beta$  is easier to break under the same applied loads). In addition, both the radial stress and tensile stress at the center of the sphere decreases with  $\beta$ . Therefore, in contrast to the

isotropic case, the stress concentration in anisotropic rocks is found to be sensitive to the value of the modulus (or the modulus ratio).

Figure 2-9 plots the variations of  $2\pi R^2 \sigma_{rr}/F$  and  $2\pi R^2 \sigma_{\theta\theta}/F$  versus the radial distance  $r/R$  along the  $z$ -axis for various values of  $\alpha$  ( $=\nu'/\bar{\nu}$ ) with  $\beta = 1.5$ ,  $\xi = 1.0$ ,  $\bar{\nu} = 0.2$  and  $\theta_0 = 3^\circ$ . In contrast to the effect of modulus ratio, the increase of anisotropy in terms of the changes in Poisson's ratio along different directions (i.e. increasing  $\alpha$ ) actually reduces the difference between the local tensile peak and the stress within the central part of the sphere. But, the effect of  $\alpha$  on the radial stress is not very significant.

Figure 2-10 plots the normalized stresses versus  $r/R$  along the  $z$ -axis for various values of  $\xi$  ( $= A_{44}/A_{66}$ ) with  $\beta = 1.0$ ,  $\bar{\nu} = 0.2$  and  $\theta_0 = 3^\circ$ . As shown in (2.3),  $A_{44}$  can be interpreted as the modulus governing shear deformation in the planes with normals perpendicular to the radial directions (i.e. transverse planes), and  $A_{66}$  can be interpreted as the modulus governing shear deformation in the planes of isotropy. The effect of this shear modulus ratio  $\xi$  is very similar to the observation in Fig. 2-8 for Young's modulus ratio  $\beta$ . That is, if a sphere is stiffer against shear deformation in the transverse planes than in the planes of isotropy, the local tensile stress concentration (near  $r/R = 0.9$ ) becomes larger and, thus, it is weaker under PLST. Compared with Fig. 2-8, the effect of the shear modulus ratio  $\xi$  is much larger than that of the Young's modulus ratio  $\beta$ . Therefore, anisotropy in shear modulus have greater effect on stress concentration than that in Young's modulus.

## 2.8 Point Loads Modeled by the Hertz Contact Stress

As mentioned in the Introduction, the double point loads are applied to spheres through a pair of steel cones with spherical heads. Thus, the stress acting on spheres is actually non-uniform, but should be the contact stress between the steel cones and the spherical specimen. Since the contact is only expected to develop between the spherical heads and the spherical specimen, this contact stress could be obtained by considering the contact problem between two spheres.

In particular, according to the general theory for the contact problem between two spheres by Hertz in 1881 (see Timoshenko and Goodier, 1982), the contact normal stress is obtained as

$$\sigma_r = \begin{cases} -p(\theta) & \text{for } 0 \leq \theta \leq \theta_0 \text{ and } \pi - \theta_0 \leq \theta \leq \pi \\ 0 & \text{for } \theta_0 < \theta < \pi - \theta_0 \end{cases} \quad (2.67)$$

where

$$p(\theta) = \frac{P_0}{R_0} \sqrt{R^2 \cos^2 \theta - (R^2 - R_0^2)} \quad (2.68)$$

$$P_0 = \frac{3F}{2\pi R_0^2} \quad (2.69)$$

$$R_0 = \left[ \frac{3\pi F(\delta_1 + \delta_2)R_1 R_2}{4(R_1 + R_2)} \right]^{1/3} \quad (2.70)$$

$$\delta_1 = \frac{1 - \nu_1^2}{\pi E_1}; \quad \delta_2 = \frac{1 - \nu_2^2}{\pi E_2} \quad (2.71)$$

where  $F$  is the magnitude of the applied point force,  $R_0$  is the radius of the circular contact area, and  $R_1$ ,  $E_1$  and  $\nu_1$  are the radius of the spherical heads, Young's modulus and Poisson's ratio of the steel cones respectively. As suggested by ISRM (1985), the spherical head is of radius  $R_1 = 5\text{mm}$  and is made of tungsten carbide.

Thus, Young's modulus  $E_s$  can be assumed to be large enough such that  $\delta_s = 0$  can be used in (2.71).

In order to match the stress field inside the sphere, (2.67) is also expanded into Fourier-Legendre series as (Farrell and Ross, 1971)

$$\sigma_r = \sum_{n=0}^{\infty} E_{2n} P_{2n}(\cos\theta) \quad (2.72)$$

where

$$E_{2n} = -\frac{(4n+1)\sqrt{R^2 - R_0^2} P_0}{R_0} \int_{\cos\theta_0}^1 \left(\frac{x^2}{\cos^2\theta_0} - 1\right)^{n/2} P_{2n}(x) dx \quad (2.73)$$

and

$$\cos\theta_0 = \frac{\sqrt{R^2 - R_0^2}}{R} \quad (2.74)$$

Numerical integration has been used in obtaining the values of  $E_{2n}$  in (2.73). Substitution of (2.73) and (2-65) into (2-63) and (2-64) yields the analytic solution for an isotropic sphere under the diametral PLST.

Figure 2-11 compares both normalized radial and tangential stresses along the line between the center of the sphere and one of the point loads under the action of uniform stress (solution in previous section) and contact stress (solution in this section) for  $E=18\text{GPa}$ ,  $\nu=0.1$ ,  $D=50\text{mm}$  and  $P=15\text{kN}$ . The angle  $\theta_0$  corresponding to the contact stress is  $3.14^\circ$ . Fig. 2-11 shows that the compressive stresses and the tensile stresses at the central part are almost the same for spheres under the action of the uniform stress and the contact stress, but the stress concentrations developed near the point loads are significantly different. Assuming a

larger or smaller  $\theta_0$  will lead to under or over estimation for the maximum tensile stress respectively. For example, assuming a smaller  $\theta_0$ , say  $\theta_0 = 2^\circ$ , will lead to about 100% over estimation of the actual maximum tensile stress, while assuming a larger  $\theta_0$ , say  $\theta_0 = 5^\circ$ , will lead to about 70% under estimation of it. It is also interesting to note that if we assume  $\theta_0$  equal to  $2.8^\circ$ , the stress distribution will be the same as that considering the Hertz contact problem.

Figure 2-12 plots both the normalized radial and tangential stresses along the line between the center of the sphere and one of the point loads under the action of uniform stress and contact stress for Poisson's ratio  $\nu = 0.3$ . Except for varying Poisson's ratio, the plot is the same as those given in Fig. 2-11. The angle  $\theta_0$  corresponding to the contact stress is  $3.10^\circ$ . Fig. 2-12 shows that the difference of tensile stress concentrations developed is relatively less significant for a large Poisson's ratio than those for smaller ones.

Figure 2-13 plots both the normalized radial and tangential stresses along the line between the center of the sphere and one of the point loads under the action of uniform stress and contact stress for Young's modulus  $E=70\text{GPa}$ . Except for assuming a larger Young's modulus  $E$ , the plot is the same as those given in Fig. 2-12. The angle  $\theta_0$  corresponding to the contact stress is  $1.94^\circ$ . Fig. 2-13 shows that the difference of concentrations developed near the point loads is relatively more significant for a larger Young's modulus than those for smaller ones. Note that the "uniform stress solution" is independent of Young's modulus of the specimen.

Above numerical results show that assuming a uniform stress acting on the contact area of spheres will leads to either over estimation or under estimation of the

maximum tensile stress. Therefore, in the analyses of Chapters 3 and 4 for the axial and diametral PLST on cylinders, the contact problem between the steel cones and surfaces of the cylinder will be considered.

## 2.9 Conclusion

An analytic solution for the stress concentration inside a spherically isotropic sphere under a pair of diametral point loads is obtained by employing the “displacement potential method” together with a Fourier-Legendre expansion for the boundary applied loads. When the isotropic limit is considered, the solution by Hiramatsu and Oka (1966) is recovered analytically. It was found that a local tensile zone near  $r/R = 0.9$  is developed, and such non-uniform distribution was first pointed out by Wijk (1978) for isotropic spheres. The difference between the local maximum tensile stress and the ‘plateau’ value in the central portion of the sphere increases with the decrease of both the Poisson’s ratio and the area of loading surfaces. To verify the present solution, the experimental observations by Frocht and Guernsey (1953) for isotropic spheres with  $\nu = 0.48$  are compared with our predictions, and the theory and experiment agree well. In addition, the contact problem between the steel cones and the surface of the sphere is also considered. We found that the assumption of uniform stress acting on the contact area would lead considerable over or under estimation of the maximum tensile stress.

For anisotropic spheres, it is found that the local maximum tensile stress increase with the degree of anisotropy in both the Young’s and shear moduli, but decrease with the anisotropy in Poisson’s ratio. In particular, if a sphere is stiffer against axial

deformation along the tangential direction than along the radial direction, higher tensile stress concentration is observed near  $r/R = 0.9$  and, thus, it is weaker under the PLST. Similarly, if a sphere is stiffer against shear deformation in the transverse planes than in the planes of isotropy, the local tensile stress concentration (near  $r/R = 0.9$ ) becomes larger and this leads to a smaller PLSI (i.e. a weaker rock). In contrast to the effect of modulus ratio, the increase of anisotropy in terms of the changes in Poisson's ratio along different directions (i.e. increasing  $\alpha$ ) actually reduces the difference between the local tensile peak and the stress in the central part of the sphere.

The present solution indicates that the tensile stress along the line of the applied point loads within the spheres is not uniform, in contrast to the conclusion by Hiramatsu and Oka (1966). The non-uniformity depends on the Poisson's ratio, size of contact zones, the degree of anisotropy of the tested rocks. In terms of further experimental verification, the local peak of the tensile zone near  $r/R = 0.9$  may provide a special feature for us to assess our prediction. If experimental technique, such as the acoustic emission test, can be used to identify the origin of fracture during the point load strength test, it is possible to see whether fracture originates at about  $r/R = 0.9$ . Nevertheless, further experimental and theoretical studies are recommended, especially for anisotropic rocks.

In addition to assuming a uniform distributed load in modeling the point loads, the Hertz contact stress is also considered. It is concluded that large error may be resulted if a realistic size of contact zone cannot be estimated.



## **Chapter 3**

# **AN EXACT ANALYTIC SOLUTION FOR THE AXIAL POINT LOAD STRENGTH TEST ON SOLID CIRCULAR CYLINDERS**

### **3.1 Introduction**

The direct tensile strength test on rock is seldom used due to the fact that tensile force is difficult to apply to rock samples without inducing eccentric moments, and the fact that the tensile stress is normally induced indirectly by compressions in rock masses in real situations. The Point Load Strength Test (PLST), which is a popular index test for strength estimation of rock, has been extensively used both in the field and in the laboratory because of its simple testing procedures, of its cheap operating cost, and of its short testing time (e.g. Chau and Wong, 1996). In estimating the strength of rocks, cylindrical cores obtained from drilling are the commonly used samples in the PLST. Specimens are normally split apart along the line joining the two applied point loads.

Extensive experimental studies have been done on the PLST (see the review by Chau and Wong, 1996), but there are relatively few theoretical studies for the PLST. The analytic studies for the PLST include the stress analyses of the diametral PLST on isotropic spheres (Hiramatsu and Oka, 1966), spherically isotropic spheres (Wei and Chau, 1998; Chau and Wei, 1999a), and the finite cylinders (Wijk, 1980; Chau, 1998a); and the stress analysis of the axial PLST on finite cylinders (Wijk, 1978). But, it should be emphasized that the solution for the axial PLST obtained by Wijk (1978) is only an approximation of the tensile stress at the center of the cylinder. Nevertheless, the

solution by Wijk (1978) was found useful in estimating analytically the index-strength conversion factor for the axial PLST (Chau and Wong, 1996; Chau and Wong, 1998).

The tensile stress field within a cylinder under the axial PLST has not been solved analytically, the only available approximation, as mentioned previously, is the stress at the center of the cylinder (Wijk, 1978). In addition, all previous analyses (except Chau, 1988a) neglected the contact problem between the indentors and the surfaces of the specimens and idealized the applied tractions as either point forces (e.g. Wijk, 1978) or uniform traction (Hiramatsu and Oka, 1966), whilst, in reality, the so-called point loads are actually applied through a pair of steel cones with spherical heads (ISRM, 1985). The finite element method has been applied to the axial PLST (e.g. Peng, 1976), but the contact problem between the steel cones and the end surfaces was not considered either.

Stress analysis for finite cylinders under various boundary conditions has been one of the most fundamental problems in the theory of elasticity. The most notable early development was the analysis by Filon (1902) for finite solid cylinders under uniaxial compression with end friction. Dougall (1914) proposed a general analysis for solid circular cylinders under various types of loading conditions. The application of Dougall's (1914) approach to the axial PLST is, however, not straightforward, as the physical meanings of the so-called *permanent free modes* and *transitory free modes* are not readily understandable.

Using Love's stress function for axisymmetric problems (e.g. Section 188 of Love, 1944), Saito (1952, 1954) proposed a Fourier-Bessel expansion of the stress function for satisfying any axisymmetric boundary loading conditions. By adopting a two stress function approach, Ogaki and Nakajima (1983) also proposed a general procedure and

derived an analytic solution for finite cylinders with parabolic distributed loads acting on the central part of the two end surfaces. Applying Saito (1952, 1954) approach, Watanabe (1996) obtained the analytic solution for cylinders under compression with perfectly or imperfectly constrained radial displacement on two loading end surfaces. This approach can also be used to find the Young's modulus from compression tests with end friction (Watanabe, 1998) and provides a check for other approximate methods (Chau, 1997, 1998b).

One important feature of the PLST is that all specimens are split apart into two or three pieces in the tensile mode, which is believed to be caused by the tensile stress between the two point loads. Thus, the stress distribution along the line joining the two point loads is of great importance to the PLST. As remarked earlier, there is no solution for the tensile stress distribution along the two applied point loads within cylindrical specimens under the axial PLST.

Therefore, this chapter considers the stress distribution in a finite circular cylinder subjected to the axial PLST. The method of solution, in contrast to the stress approach by Saito (1952, 1954) and Ogaki and Nakajima (1982), uses the displacement potential approach, while the boundary contact forces, similar to the approach by Saito (1952, 1954) and Ogaki and Nakajima (1982), are expanded into the Fourier-Bessel series. In contrast to all previous studies (except, Chau, 1998a), the two point forces are modeled more realistically as the contact stress between the flat end surfaces and the spherical heads of the indentors. In verifying the applicability of the present solution to real PLST, a series of the axial PLST have been carried out on rock-like plaster specimens.

Plaster is used in our PLST because man-made plaster is generally more homogeneous than natural rock, in which inherent defects inevitably exist.

Except in the vicinity of the contact zone between the indentors and the end surfaces, where crushing is the dominant mode of deformation, the present linear elastic solution should provide meaningful results for interpreting the failure mechanism and strength of the rock specimens under the axial PLST.

### 3.2 Governing Equations

Consider a cylindrical specimen of diameter  $D$  (or  $2R$ ) and length  $H$  (or  $2h$ ). For mathematical simplicity, we take the center of the cylinder as the origin of our cylindrical coordinates  $(r, \theta, z)$  with the  $z$ -axis coinciding with the axis of symmetry of the specimen, as shown in Fig. 3-1. Since the axial point forces are applied through by pressing two collinear indentors along the axis of the symmetry of the cylinder, all variables of the problem are independent of  $\theta$ . In the absence of body force, the equations of equilibrium are (Love, 1944)

$$\frac{\partial \sigma_r}{\partial r} + \frac{\partial \sigma_z}{\partial z} + \frac{\sigma_r - \sigma_\theta}{r} = 0 \quad (3.1)$$

$$\frac{\partial \sigma_z}{\partial z} + \frac{\partial \sigma_r}{\partial r} + \frac{\sigma_r}{r} = 0 \quad (3.2)$$

where the usual notation for Cauchy stress tensor is adopted.

For axisymmetric problems, strains and displacements are related by:

$$\varepsilon_r = \frac{\partial u}{\partial r}, \varepsilon_\theta = \frac{u}{r}, \varepsilon_z = \frac{\partial w}{\partial z}, \varepsilon_r = \frac{1}{2} \left( \frac{\partial u}{\partial z} + \frac{\partial w}{\partial r} \right) \quad (3.3)$$

where  $\sigma_z, \sigma_r, \sigma_{\theta\theta}$  are the normal stresses in the axial, radial and circumferential directions respectively,  $\sigma_r$  is the shearing stress on the  $rz$  plane,  $\varepsilon_z, \varepsilon_r, \varepsilon_{\theta\theta}$  and  $\varepsilon_r$  are the strains corresponding to those stresses, and  $u$  and  $w$  are the displacements in the  $r$ - and  $z$ -directions respectively.

The specimen is assumed to be linear elastic homogeneous and isotropic, thus the following Hook's law applies

$$\varepsilon_r = \frac{1}{E} [\sigma_r - \nu(\sigma_{\theta\theta} + \sigma_z)] \quad (3.4)$$

$$\varepsilon_{\theta\theta} = \frac{1}{E} [\sigma_{\theta\theta} - \nu(\sigma_z + \sigma_r)] \quad (3.5)$$

$$\varepsilon_z = \frac{1}{E} [\sigma_z - \nu(\sigma_{\theta\theta} + \sigma_r)] \quad (3.6)$$

$$\varepsilon_r = \frac{1}{2G} \sigma_r \quad (3.7)$$

where  $E$ ,  $\nu$  and  $G$  are the Young's modulus, Poisson's ratio and the shear modulus respectively.

As shown in Fig. 3-1, all the surfaces of the specimen are traction free, except for the two small circular contact areas where the spherical heads of the steel cones act on (one on the top and the other at the bottom). The standard size for the radius of the spherical heads is 5mm, as suggested by ISRM (1985); while our experimental results show that the size of the contact area is in the range of 1 to 5mm. Therefore, the contact is expected to develop only between the spherical heads of the steel cones and the end surfaces of the specimen (probably except for very soft rocks). In addition, the size of the contact area is much smaller than the standard diameter of the specimen (i.e.  $D=50\text{mm}$ ), as suggested by Broch and Franklin (1972) and ISRM (1985). Hence, the

contact stress acting between the steel cones and the end surfaces of the specimen can be approximated by considering the Hertz contact problem between a spherical surface of radius  $R_1$  and a semi-infinite flat surface. In particular, the formulae for contact stress in Section 140 of Timoshenko and Goodier (1982) can be specialized to the present case as

$$\sigma_z = \begin{cases} -p(r) & r \leq R_0 \\ 0 & r > R_0 \end{cases} \quad (3.8)$$

where

$$p(r) = \frac{P_0}{R_0} \sqrt{R_0^2 - r^2} \quad (3.9)$$

$$P_0 = \frac{3P}{2\pi R_0^2} \quad (3.10)$$

$$R_0 = \left[ \frac{3\pi P(\delta_1 + \delta_2)R_2}{4} \right]^{1/3} \quad (3.11)$$

$$\delta_1 = \frac{1 - \nu^2}{\pi E}; \quad \delta_2 = \frac{1 - \nu_2^2}{\pi E_2} \quad (3.12)$$

where  $P$  is the magnitude of the applied point force,  $R_0$  is the radius of the circular contact area, and  $R_2$ ,  $E_2$  and  $\nu_2$  are respectively the radius of the spherical heads, the Young's modulus and Poisson's ratio of the steel cones. As suggested by ISRM (1985), the spherical head is of radius  $R_2 = 5\text{mm}$  and is made of tungsten carbide. Thus, the Young's modulus  $E_2$  can be assumed large enough such that  $\delta_2 = 0$  will be used in (3.11) and (3.12).

Therefore, the boundary conditions for a solid cylinder subject to the axial PLST are:

$$\sigma_r = 0, \sigma_\theta = 0 \quad \text{on } r = R \quad (3.13)$$

$$\sigma_r = 0, \sigma_z = \begin{cases} -p(r) & r \leq R_0 \\ 0 & r > R_0 \end{cases} \quad \text{on } z = \pm h \quad (3.14)$$

where  $p(r)$  is the contact pressure given by (3.9).

The next task is to find the solution for the stresses governed by the equations of equilibrium (3.1) and (3.2) together the boundary conditions (3.13) and (3.14).

### 3.3 Method of Solution

In contrast to the stress potential approach used by Saito (1952, 1954) and by Ogaki and Nakajima (1983), the displacement potential approach is adopted. In particular, the following displacement potential  $\Phi$  is introduced

$$u = \frac{\partial^2 \Phi}{\partial r \partial z}, \quad w = -[2(1-\nu)\nabla_r \Phi + (1-2\nu)\frac{\partial^2 \Phi}{\partial z^2}] \quad (3.15)$$

where

$$\nabla_r = \frac{\partial^2}{\partial r^2} + \frac{1}{r} \frac{\partial}{\partial r} \quad (3.16)$$

Substitution of (3.15) into (3.1) and (3.2) and by the virtue of (3.3) to (3.7), the two equations of equilibrium are reduced to the following governing equation for the displacement function  $\Phi$

$$\nabla^4 \Phi = \nabla^2 \nabla^2 \Phi = 0 \quad (3.17)$$

where  $\nabla^2$  is the Laplacian operator, or  $\nabla^2 = \nabla_r + \partial^2 / \partial z^2$ . That is,  $\Phi$  satisfies the biharmonic equation.

Substitution of (3.15) into (3.3) then the results into (3.4) to (3.7) leads to the following stresses in terms of the displacement function  $\Phi$

$$\sigma_r = -2\nu G \nabla^2 \frac{\partial \Phi}{\partial z} + 2G \frac{\partial^3 \Phi}{\partial z \partial r^2} \quad (3.18)$$

$$\sigma_{\theta\theta} = -2\nu G \nabla^2 \frac{\partial \Phi}{\partial z} + 2G \frac{1}{r} \frac{\partial^2 \Phi}{\partial z \partial r} \quad (3.19)$$

$$\sigma_{zz} = -2G[(2-\nu) \frac{\partial}{\partial z} \nabla^2 - \frac{\partial^3}{\partial z^3}] \Phi \quad (3.20)$$

$$\sigma_{rz} = 2G[-(1-\nu) \frac{\partial}{\partial r} \nabla^2 + \nu \frac{\partial^3}{\partial r \partial z^2}] \Phi \quad (3.21)$$

Except differing by a constant, these expressions are, in essence, the same as those obtained by Love (see Section 188 of Love, 1944), although a different approach is adopted here.

### 3.4 Appropriate Form of the Displacement Potential

The most difficult task for solving our problem is to find the appropriate form for the displacement potential such that both the biharmonic equation (3.17) and the boundary conditions (3.13) and (3.14) can be satisfied. As shown in Fig. 3-1, the axial PLST is axisymmetric with respect to the axis of the cylinder. Due to this symmetry,  $\sigma_{rr}, \sigma_{\theta\theta}$  and  $\sigma_{zz}$  are expected to be even functions with respect to  $z$ , while  $\sigma_{rz}$  is odd function with respect to  $z$ . Thus, the following series representation for the displacement function  $\Phi$  is adopted

$$\begin{aligned} \Phi = & -\frac{R^3}{2G} \left\{ A_0 \frac{\kappa^3 \eta^3}{6} + C_0 \frac{\kappa \eta \rho^2}{2} + \sum_{n=1}^{\infty} \frac{\sin(n\pi\eta)}{\beta_n^3} [A_n I_0(\beta_n \rho) + B_n \beta_n \rho I_1(\beta_n \rho)] \right. \\ & \left. + \sum_{s=1}^{\infty} \frac{J_0(\lambda_s \rho)}{\lambda_s^3} [C_s \sinh(\gamma_s \eta) + D_s \gamma_s \eta \cosh(\gamma_s \eta)] \right\} \end{aligned} \quad (3.22)$$

where the two normalized coordinates  $\rho$  and  $\eta$  are defined as  $\rho = r/R$  and  $\eta = z/h$ ;  $\kappa$  is a geometrical shape ratio defined as  $\kappa = h/R$ ;  $\lambda_s$  is the  $s$ -th root of  $J_1(x) = 0$ ;  $\gamma_s = \lambda_s \kappa$  and  $\beta_n = n\pi/\kappa$ ;  $J_0(x), J_1(x), I_0(x)$  and  $I_1(x)$  are Bessel functions and



modified Bessel function of the first kind of zero and first order respectively;  $A_0, C_0, A_n, B_n, C,$  and  $D,$  are unknown coefficients to be determined. This solution form is similar to those proposed by Saito (1952), if the minor typos on the functions  $\sinh$  and  $\cosh$  are corrected.

It is straightforward to see that (3.22) satisfies the biharmonic equation (3.17), thus (3.22) is a probable solution for the problem. The next step is to see whether the boundary conditions can be satisfied exactly by the series expansion (3.22) by assigning appropriate value to the unknown coefficients.

### 3.5 Determination of Unknown Coefficients

To see whether the series representation given in (3.22) is appropriate for our problem of the axial PLST, the shear stress is first expressed in terms of the unknown coefficients by substituting (3.22) into (3.21)

$$\begin{aligned} \sigma_r = & \sum_{n=1}^{\infty} \sin(n\pi\eta) \{A_n I_1(\beta_n \rho) + B_n [2(1-\nu) I_1(\beta_n \rho) + \beta_n \rho I_0(\beta_n \rho)]\} \\ & + \sum_{n=1}^{\infty} J_1(\lambda_n \rho) [(C_n + 2\nu D_n) \sinh(\gamma_n \eta) + D_n \gamma_n \cosh(\gamma_n \eta)] \end{aligned} \quad (3.23)$$

By noting the fact that the shear stress  $\sigma_r$  is identically zero on the curved surface  $r = R$  (or  $\rho = 1$ ), we obtain the following expression between  $A_n$  and  $B_n$

$$\frac{A_n}{2(1-\nu) I_1(\beta_n) + \beta_n I_0(\beta_n)} = \frac{B_n}{-I_1(\beta_n)} = \frac{E_n}{\Delta_n} \quad (3.24)$$

where  $E_n$  and  $\Delta_n$  are constants introduced to simplify the subsequent analysis.

Similarly, the shear stress is also identically zero on the two end surfaces  $z = \pm h$  (or  $\eta = \pm 1$ ), and this condition yields the following relation between  $C_r$  and  $D_r$ ,

$$\frac{C_r}{2\nu \sinh \gamma_r + \gamma_r \cosh \gamma_r} = \frac{D_r}{-\sinh \gamma_r} = \frac{-F_r}{\Omega_r} \quad (3.25)$$

where  $F_r$  and  $\Omega_r$  are, again, constants introduced to simplify the expression involved in the subsequent analysis.

On the curved surface  $r=R$ , the radial stress can be found by substituting (3.22) into (3.18) and setting  $\rho = 1$  in the resulting equation:

$$\begin{aligned} \sigma_r = & A_0 \nu + (2\nu - 1)C_0 - \sum_{n=1}^{\infty} \cos(n\pi\eta) \{A_n [I_0(\beta_n) - I_1(\beta_n)/\beta_n] + B_n [(1-2\nu)I_0(\beta_n) + \beta_n I_1(\beta_n)]\} \\ & + \sum_{n=1}^{\infty} J_0(\lambda_n) \{[C_r + (2\nu + 1)D_r] \cosh(\gamma_r \eta) + D_r \gamma_r \eta \sinh(\gamma_r \eta)\} \end{aligned} \quad (3.26)$$

In terms of the constants newly-introduced in (3.24), (3.25) and (3.26) can be rewritten as

$$\begin{aligned} \sigma_r = & A_0 \nu + (2\nu - 1)C_0 + \sum_{n=1}^{\infty} E_n \cos(n\pi\eta) \\ & + \sum_{n=1}^{\infty} \frac{F_r J_0(\lambda_n)}{\Omega_r} [(\sinh \gamma_r - \gamma_r \cosh \gamma_r) \cosh(\gamma_r \eta) + \gamma_r \eta \sinh \gamma_r \sinh(\gamma_r \eta)] \end{aligned} \quad (3.27)$$

In obtaining (3.27), we have set

$$\Delta_n = \{[2(1 - \nu) + \beta_n^2] I_1^2(\beta_n) - \beta_n^2 I_0^2(\beta_n)\} / \beta_n \quad (3.28)$$

In order to apply the boundary condition for  $\sigma_r$  on  $r=R$  (or  $\rho = 1$ ), we first consider the following Fourier series expansion for the bracket term in the second summation of (3.27)

$$\begin{aligned}
& (\sinh \gamma_r, -\gamma_r, \cosh \gamma_r) \cosh(\gamma_r, \eta) + \gamma_r \eta \sinh \gamma_r, \sinh(\gamma_r, \eta) \\
& = 4\gamma_r \sinh^2 \gamma_r \sum_{n=1}^{\infty} \frac{(-1)^n (n\pi)^2}{\{\gamma_r^2 + (n\pi)^2\}^2} \cos(n\pi\eta)
\end{aligned} \tag{3.29}$$

Consequently, (3.27) can be expressed as a function of  $\cos(n\pi\eta)$  only

$$\sigma_{rr} = A_0 v + (2v - 1)C_0 + \sum_{n=1}^{\infty} [E_n + \sum_{r=1}^{\infty} F_r Q_{rn}] \cos(n\pi\eta) \tag{3.30}$$

where

$$Q_{rn} = \frac{4(-1)^n \gamma_r (n\pi)^2 J_0(\lambda_r) \sinh^2 \gamma_r}{\Omega_r \{\gamma_r^2 + (n\pi)^2\}^2} \tag{3.31}$$

Thus, substitution of (3.30) into the boundary condition (3.13) on the curved surface  $\rho = 1$  leads to the following relations between  $A_0$  and  $C_0$  and between  $E_n$  and  $F_r$ ,

$$A_0 v + (2v - 1)C_0 = 0 \tag{3.32}$$

$$E_n + \sum_{r=n}^{\infty} F_r Q_{rn} = 0 \tag{3.33}$$

Finally, by combining (3.20), (3.22), (3.24) and (3.25), we obtain the following expression for  $\sigma_{zz}$

$$\begin{aligned}
\sigma_{zz} = & A_0(1-v) + 2(2-v)C_0 + \sum_{n=1}^{\infty} \frac{E_n \cos(n\pi\eta)}{\Delta_n} \{[\beta_n I_0(\beta_n) - 2I_1(\beta_n)]I_0(\beta_n \rho) - \beta_n \rho I_1(\beta_n)I_1(\beta_n \rho)\} \\
& + \sum_{r=1}^{\infty} \frac{F_r J_0(\lambda_r \rho)}{\Omega_r} [(\sinh \gamma_r + \gamma_r \cosh \gamma_r) \cosh(\gamma_r, \eta) - \gamma_r \eta \sinh \gamma_r, \sinh(\gamma_r, \eta)]
\end{aligned} \tag{3.34}$$

On the end surface  $z = \pm h$ , we can set  $\eta = \pm 1$  in (3.34) and it is reduced to

$$\begin{aligned}
\sigma_{zz} = & A_0(1-v) + 2(2-v)C_0 \\
& + \sum_{n=1}^{\infty} \frac{E_n (-1)^n}{\Delta_n} \{[\beta_n I_0(\beta_n) - 2I_1(\beta_n)]I_0(\beta_n \rho) - \beta_n \rho I_1(\beta_n)I_1(\beta_n \rho)\} + \sum_{r=1}^{\infty} F_r J_0(\lambda_r \rho)
\end{aligned} \tag{3.35}$$

Note that in obtaining (3.35), we have set

$$\Omega_s = \sinh \gamma_s \cosh \gamma_s + \gamma_s, \quad (3.36)$$

In order to apply the end boundary condition for  $\sigma_z$ , we first expand the modified Bessel functions in the first summation of (3.35) to a Fourier-Bessel expansion (Watson, 1944):

$$[\beta_n I_0(\beta_n) - 2I_1(\beta_n)]I_0(\beta_n \rho) - \beta_n \rho I_1(\beta_n)I_1(\beta_n \rho) = -4\beta_n I_1^2(\beta_n) \sum_{s=1}^{\infty} \frac{\lambda_s^2}{[\lambda_s^2 + (\beta_n)^2]^2} J_0(\lambda_s \rho) \quad (3.37)$$

Thus,  $\sigma_z$  can be expressed in terms of a series of  $J_0(\lambda_s \rho)$  only.

In particular, substitution of (3.37) into (3.35) leads to

$$\sigma_z = A_0(1 - \nu) + 2(2 - \nu)C_0 + \sum_{s=1}^{\infty} [F_s + \sum_{n=1}^{\infty} E_n R_n] J_0(\lambda_s \rho) \quad (3.38)$$

where

$$R_n = \frac{4(-1)^{(n+1)} \lambda_s^2 \beta_n I_1^2(\beta_n)}{\Delta_n [\lambda_s^2 + (\beta_n)^2]^2 J_0(\lambda_s)} \quad (3.39)$$

In order to match the load-induced contact stress (3.8) on the end surfaces with the stress field given in (3.38), (3.8) is again expanded into Fourier-Bessel expansions:

$$\sigma_z = \sum_{s=1}^{\infty} \frac{2p_0 R}{\lambda_s^3 R_0 J_0^2(\lambda_s)} \left( \frac{\lambda_s R_0}{R} \cos \frac{\lambda_s R_0}{R} - \sin \frac{\lambda_s R_0}{R} \right) J_0(\lambda_s \rho) \quad (3.40)$$

The details of this expansion are described in Appendix II for the sake of completeness.

Finally, by comparing the coefficients of (3.38) and (3.40), we have

$$A_0(1 - \nu) + 2(2 - \nu)C_0 = 0 \quad (3.41)$$

$$F_s + \sum_{n=1}^{\infty} E_n R_n = \frac{2p_0 R}{\lambda_s^3 R_0 J_0^2(\lambda_s)} \left( \frac{\lambda_s R_0}{R} \cos \frac{\lambda_s R_0}{R} - \sin \frac{\lambda_s R_0}{R} \right) \quad (3.42)$$

It is straightforward that from (3.32) and (3.41) the only solution for  $A_0$  and  $C_0$  is

$$A_0 = C_0 = 0 \quad (3.43)$$

For the unknown coefficients  $E_n$  and  $F_s$ , the two coupled system of equations, (3.33) and (3.42), have to be solved simultaneously. For numerical implementation, we can truncate the infinite series in (3.33) and (3.42) and only retain the first  $n$  and  $s$  terms. Then, there will be  $(s+n)$  equations for the  $(s+n)$  unknown coefficients of  $F_s$  and  $E_n$ . Once these coefficients are solved, the following expressions can be used to evaluate the stress field inside the cylinder:

$$\begin{aligned} \sigma_z = & \sum_{n=1}^{\infty} \frac{E_n \cos(n\pi\eta)}{\Delta_n} \{[\beta_n I_0(\beta_n) - 2I_1(\beta_n)]I_0(\beta_n \rho) - \beta_n \rho I_1(\beta_n)I_1(\beta_n \rho)\} \\ & + \sum_{s=1}^{\infty} \frac{F_s J_0(\lambda_s \rho)}{\Omega_s} [(\gamma_s \cosh \gamma_s + \sinh \gamma_s) \cosh(\gamma_s \eta) - \gamma_s \eta \sinh \gamma_s \sinh(\gamma_s \eta)] \end{aligned} \quad (3.44)$$

$$\begin{aligned} \sigma_r = & \sum_{n=1}^{\infty} \frac{E_n \cos(n\pi\eta)}{\Delta_n} \{-[I_1(\beta_n) + \beta_n I_0(\beta_n)]I_0(\beta_n \rho) + \beta_n \rho I_1(\beta_n)I_1(\beta_n \rho) + [2(1-\nu)I_1(\beta_n) \\ & + \beta_n I_0(\beta_n)] \frac{I_1(\beta_n \rho)}{\beta_n \rho}\} + \sum_{s=1}^{\infty} \frac{F_s}{\Omega_s} \{J_0(\lambda_s \rho) [(\sinh \gamma_s - \gamma_s \cosh \gamma_s) \cosh(\gamma_s \eta) + \gamma_s \eta \sinh \gamma_s \sinh(\gamma_s \eta)] \\ & - \frac{J_1(\lambda_s \rho)}{\lambda_s \rho} [\gamma_s \eta \sinh \gamma_s \sinh(\gamma_s \eta) + [(1-2\nu) \sinh \gamma_s - \gamma_s \cosh \gamma_s] \cosh(\gamma_s \eta)]\} \end{aligned} \quad (3.45)$$

$$\begin{aligned} \sigma_{\theta} = & \sum_{n=1}^{\infty} \frac{E_n \cos(n\pi\eta)}{\Delta_n} \{(1-2\nu)I_1(\beta_n)I_0(\beta_n \rho) + [2(\nu-1)I_1(\beta_n) - \beta_n I_0(\beta_n)]I_1(\beta_n \rho) / (\beta_n \rho)\} \\ & + \sum_{s=1}^{\infty} \frac{F_s}{\Omega_s} \{2\nu \sinh \gamma_s \cosh(\gamma_s \eta) J_0(\lambda_s \rho) \\ & + \frac{J_1(\lambda_s \rho)}{\lambda_s \rho} [[(1-2\nu) \sinh \gamma_s - \gamma_s \cosh \gamma_s] \cosh(\gamma_s \eta) + \gamma_s \eta \sinh \gamma_s \sinh(\gamma_s \eta)]\} \end{aligned} \quad (3.46)$$

$$\begin{aligned}\sigma_z = & \sum_{n=1}^{\infty} \frac{E_n \sin(n\pi\eta)}{\Delta_n} \{\beta_n I_0(\beta_n) I_1(\beta_n \rho) - \beta_n \rho I_1(\beta_n) I_0(\beta_n \rho)\} \\ & - \sum_{s=1}^{\infty} \frac{F_s J_1(\lambda_s \rho)}{\Omega_s} [\gamma_s \cosh \gamma_s \sinh(\gamma_s \eta) - \gamma_s \sinh \gamma_s \cosh(\gamma_s \eta)]\end{aligned}\quad (3.47)$$

Therefore, the problem has been solved analytically, and thus the assumed form for the displacement potential (3.22) has been shown to be appropriate and complete.

### 3.6 Numerical Results and Discussions

The fracture surface of a failed rock specimen under the axial PLST must pass through both loading points, if the result is to be accepted as a valid data (ISRM, 1985). Indeed, our experiments show that almost all specimens are split into two or three prismatic fragments along the line joining the two loading points. Thus, the tensile stress along the line of two point loads (i.e. the axis of symmetry as shown in Fig. 3-1) is of crucial importance to interpret the data from the axial PLST. Therefore, subsequent discussions will focus on the stress distribution along the z-axis. It should be noted that the radial stress equals the tangential stress along the z-axis, and thus only the radial and vertical stresses are plotted in the following numerical examples.

Numerical results show that if  $h=R$  (i.e. a roughly equi-dimensional specimen), about 25 terms in both  $n$  and  $s$  are needed to achieve an accuracy of less than 3% error in the tensile stress field. Note that  $n$  and  $s$  are the summation indices of the first and second sum of (3.44) to (3.47). In general, more terms in  $n$  and less terms in  $s$  are needed for  $h>R$ , while more terms in  $s$  and less terms in  $n$  are needed for  $h<R$ , but a total of 50 terms for  $n$  and  $s$  are normally needed to limit the error to within 3%.

Figure 3-2 plots the variations of the normalized stresses  $\sigma_r / \sigma_0$  and  $\sigma_z / \sigma_0$  (where  $\sigma_0 = P / HD$ ) versus the normalized distance  $z/h$  along the  $z$ -axis for various values of Poisson's ratio  $\nu$ . The results are obtained for  $H/D = 1.1$ ,  $D = 2R = 50\text{mm}$ , and  $R_0 = 0.05R$ . Note that  $H/D=1.1$  is the recommended shape ratio for the axial PLST and that  $D=50\text{mm}$  is the standard size of rock core for determining the Point Load Strength Index (PLSI) suggested by ISRM (1985). In order to reflect only the effect of Poisson's ratio on the stress concentrations, we have fixed the size of the contact area in Fig. 3-2. Following the usual sign convention of continuum mechanics, tension is plotted as positive. In contrast to the elastic stress field in the Brazilian test, Fig. 3-2 shows that the tensile stress distribution along the  $z$ -axis is not uniform, a local tensile stress concentration is developed near  $z/h=0.9$ . As shown in Fig. 3-2, this maximum tensile stress increases with the decrease of Poisson's ratio  $\nu$ . Since the failure of the specimen under the axial PLST is believed to be dominant by brittle fracture, we speculate that the point where the crack initiates should be the same as the point where the maximum tensile stress is induced. Indeed, we will show in later discussion that our experimental observation basically agrees with this speculation. If the tensile strength or PLSI is proportional to the maximum tensile stress at the instant of failure, Fig. 3-2 shows that PLSI is extremely sensitive to the values of Poisson's ratio  $\nu$  of the rock. However, the tensile stress at the central part of the axis of symmetry and the axial compressive stress are insensitive to the change in Poisson's ratio. This conclusion is similar to that for an isotropic sphere or a spherically isotropic sphere subjected to the diametral PLST (Wei and Chau, 1998; Chau and Wei, 1999).

Figure 3-3 illustrates the effect of the radius  $R_0$  of the contact zone on the magnitude of the local peak of tensile stress for  $H/D = 1.1$ ,  $D = 2R = 50\text{mm}$  and  $\nu = 0.25$ . Except for the varying  $R_0$ , the other parameters used in the plot are the same as those used in Fig. 3-2. It is clear that the maximum tensile stress increases drastically with the decrease of  $R_0$ , especially for  $R_0 < 0.05R$ . For example, the maximum tensile stress rises to about 250% as  $R_0$  decreases from  $0.05R$  to  $0.01R$ , while the tensile stress at the central part of the z-axis and the axial compressive stress are relatively insensitive to the change of  $R_0$ . Note also that the Young's modulus  $E$  only has influence on the size of the contact area as given by (3.11) and (3.12). Therefore, the stiffer the specimen the smaller is the radius  $R_0$ , and thus a larger maximum tensile stress will be induced. Thus, it appears that the stiffer the rock, the smaller is the PLSI. This conclusion appears to be contrary to most experimental observations. In obtaining this result, we have actually assumed that the local tensile strength for fracture is independent of the stiffness of the material. However, in reality most natural rock strength and stiffness increase simultaneously. Nevertheless, if there were a number of solids having the same local tensile strength, the softer the rock the higher is the PLSI.

To verify the applicability of our analytic solution to actual axial PLST, the next section will compare our analytic solution with our experimental data for the axial PLST on cylinders made of a type of rock-like plaster.

### 3.7 Experiments and Comparison with the Theoretical Predictions

Experiments have also been done on rock-like plaster to verify the applicability of our theoretical solution to the axial PLST. Plaster, instead of natural rocks, was used



because the specimens will be more homogeneous and the results are more reproducible. Our plaster specimens were made by using the following procedures. Mixture of cool distilled water and gypsum with mass ratio of 3:10 was poured into a cylindrical mould made of a plastic hollow tube. The mould was filled with plaster paste in three consecutive phases and each phase covers one third of the length of the mould. When each one third of the mould is filled, a tiny wooden hammer was used to tap 50-70 times into the mixture in order to yield a homogeneous sample and to minimize the air content of the specimen. The procedure has to be completed swiftly as the mixture starts to coagulate within 8-10 minutes. If warmer water were used, the setting time of the plaster paste would be even shorter. The mould was removed after 10-15 minutes. The curing of specimens was done at room temperature and humidity (under air-conditioning). The weight of each specimen was recorded daily until a steady weight was maintained. Normally, the daily change in mass will be less 0.1% after about 45 days. To ensure a steady strength had been developed when the specimens were tested, all tests were conducted 60 days after the mixing. The density of the specimens is about  $1.75 - 1.78 \text{ g/cm}^3$ . For investigating the shape and size effects, a total of eighteen specimens were initially made for the axial PLST. Two samples were made for each of the following combinations of size and shape: (a) specimens of the same shape ( $H/D=1.1$ ) and various diameters of 41, 51, 56, and 67mm; and (b) specimens of the same diameter (56mm) and various lengths of 34, 44, 58, 63, and 69mm. All end surfaces of the specimens were polished to a tolerance of 0.02mm of flatness, and the maximum departure of the perpendicularity of the end surfaces from the axis of the specimens was controlled to within 0.001 radian or 0.05mm in 50mm. By following the

testing procedure suggested by ASTM for the uniaxial compression test, the average Young's modulus, Poisson's ratio and compressive strength of the specimens were obtained as 17.5GPa, 0.25 and 57.54MPa respectively. In addition, the uniaxial stress-strain curve of our samples show clearly the sign of dilatancy. For more discussion on the requirements of rock-like solids, we refer to Wong and Chau (1998).

To calibrate the maximum allowable local tensile field of the plaster under the axial PLST, two more specimens with  $H/D=1.1$  and  $D=56\text{mm}$  were cast. The point load  $P$  under which the specimen was broken was recorded for each specimen. Then, these data were input into our solutions, the calculated stresses  $\sigma_r$  and  $\sigma_z$  were plotted versus the normalized distance  $z/h$  from the center in Fig. 3-4. The calculated maximum tensile stresses for these four specimens are 23.06, 23.35, 21.50 and 23.21MPa with a mean of 22.78MPa. In order to predict the failure load for each sample, we make a major assumption that if the maximum tensile stress reaches 22.78MPa (which will be called local tensile strength hereafter) along the  $z$ -axis in the specimen, the specimen fails. From microscopic point of view, this assumption implies that a critical local tensile stress field of 22.78MPa is needed to initiate the unstable crack growth from a defect of typical size in the plaster material.

Since many previous experiments showed that the PLSI (i.e.  $I_c = P\pi/4HD$ ) depends on both the length and diameter of the specimens (Broch and Franklin, 1972; ISRM, 1985). By applying the concept of the local tensile strength (as described above) to our analytic solution, prediction on both shape and size effects on the PLSI can be made. In particular, the predicted PLSI (or  $I_c$ ) is plotted against the diameter in Fig. 3-5 for a fixed length/diameter ratio  $H/D=1.1$  together with our experimental results.

Because of the limited vertical clearance (10mm-89mm) of the loading frame of the PLST apparatus, only specimens of diameter from 41mm to 67mm were tested. Figure 3-6 plots the PLSI versus the length/diameter ratio for a fixed diameter  $D=56\text{mm}$ . As shown in Figs. 3-5 and 3-6, the predictions on both shape and size effects on the PLSI agree very well with our experimental results. Since the shape effect was examined experimentally only for specimens of  $D=56\text{mm}$  (see Fig. 3-6), Fig. 3-7 shows our theoretical predications for the PLSI versus length/diameter ratio for different diameters ( $D=40, 56$  and  $67\text{mm}$ ). These results illustrate the well-known observations that for a fixed  $H/D$ , the larger the specimen, the lower is the PLSI; for a fixed diameter  $D$ , the more slender the specimen, the weaker is the rock (Broch and Franklin, 1972; Brook, 1977, 1980; Forster, 1983).

To further justify our solution, the failure patterns are examined in more detail here. It was observed that all specimens are broken into either two or three prismatic fragments with two additional small pieces of fall-off cones under the point loads, as shown in Figs. 3-8 and 3-9. This failure pattern is very similar to that observed in the double-punch test used in concrete testing (see Figs. 2 and 3 of Chen and Yuan, 1980). These fall-off cones are in the shape of a single ridge (only one line of sharp ridge) if the specimen breaks into two pieces along a roughly flat fracture surface, but are in the shape of a triangular pyramid with a circular base if the specimen breaks into three pieces (of roughly the same size). There is also evidence of crushing at the inclined surfaces of the fall-off cones, as the plaster turns to pale yellow compared to the yellow color in the intact regions. The height of these fall-off cones (i.e.  $L_c$  in Figs. 3-8 and 3-9) is about 3-5, 5-6, and 6-7mm for specimens of diameter of 40, 56 and 67mm, while

the diameter of the circular base of the fall-off cones (i.e.  $L_c$  in Figs. 3-8 and 3-9) is about 3-4mm for specimens of diameters 40 and 56mm and 4-5mm for specimens of diameter 67mm. The size of the circular base of the fall-off cones indicates the size of the contact zone.

For the height of the fall-off cones, we speculate that it indicates the depth of the crushing zone under the contact points. To illustrate this idea, we propose a very simple model to estimate the size of the crushing zone. In particular, we estimate the crushing pressure for our plaster using the grain crushing model proposed by Zhang et al. (1990). Zhang et al. (1990) concluded that the porosity and the grain radius are the two major parameters strongly correlated with the critical pressure for the onset of grain crushing, which is illustrated in Fig. 10 of Zhang et al. (1990). For our plaster, the porosity is obtained as 37.4%, which is obtained from the weight difference between the dried and saturated samples, as suggested by Zhang et al. (1990). The average radius of the grain of the plaster is about  $5\mu m$ , which is measured by using the polarizing optical microscope with the maximum magnification power of 400x. From Fig. 10 of Zhang et al. (1990), we found that the crushing pressure is about 19MPa. Theoretically, the average hydrostatic pressure at any point within the specimen can be estimated by taking the average of the normal stresses (the axial, radial and tangential stresses) of our elastic solution. Figure 3-10 plots this predicted hydrostatic pressure (negative for pressure) versus the normalized distance  $z/h$  along the  $z$ -axis for various diameters ( $D = 40, 56$  and  $67mm$ ). Other parameters used in the calculation are  $H/D=1.1$ ,  $\nu=0.25$  and  $E=17.5GPa$ . If the hydrostatic pressure is larger than 19MPa, grain crushing is expected to occur. From Fig. 3-10, we can interpret that the predicted height of the fall-off cones

for specimens of diameter 40, 56 and 67mm are 5.5, 5.9 and 7.0mm respectively (corresponding to the size of the region with hydrostatic pressure larger than the crushing pressure). These values agree well with our experimental observations, and the present analysis indicates that the solution is capable of yielding the depth of the crushing zone which is comparable to the observations. In addition, the location of the maximum tensile stress field also coincides with the tip of the fall-off cones. This lends further credence that the point of maximum tensile stress beneath the contact zone is indeed the site of crack initiation.

### 3.8 Conclusion

In this chapter, we have presented a new analytical solution for the stress concentrations in an elastic, isotropic solid circular cylinder of finite length subjected to the axial point load strength test (PLST). Our analytic solution predicts that a local tensile zone will develop near  $z/h=0.9$  along the line joining the two point loads (or the axis of symmetry). Our numerical results show that the maximum tensile stress increases with the decrease of Poisson's ratio  $\nu$  and the size of the loading area, but increases with the Young's modulus. The non-uniform distributions of the stresses along the line joining the two point loads bear a close resemblance with those predictions for an isotropic sphere under the diametral PLST. Numerical results show that, for a fixed length/diameter ratio, the larger the specimen, the weaker is the Point Load Strength Index (PLSI); for a fixed diameter, the more slender the specimen, the weaker is the PLSI. A series of the axial PLST were also carried out on cylinders of a

rock-like plaster material, and our predictions on both size and shape effects agree very well with our experimental observations.

## **Chapter 4**

# **AN EXACT ANALYTIC SOLUTION FOR THE DIAMETRAL POINT LOAD STRENGTH TEST ON FINITE SOLID CIRCULAR CYLINDERS**

### **4.1 Introduction**

The Point Load Strength Test (PLST) has been a popular indirect tensile strength test used in rock engineering, partly because tensile stress field in rock mass is usually induced indirectly by compressive deviatoric stresses and partly because direct tension is difficult to apply to rock specimens without inducing any eccentric moments. The strength index measured in this test is called the Point Load Strength Index (PLSI), which is a measure of the indirect tensile strength and has been correlated empirically to both the tensile strength and compressive strength of rock. Although irregular lumps can also be used as specimens for the PLST (ISRM, 1985), solid circular cylinders which are cut from rock cores remain to be the most commonly used specimens. For cylindrical specimens, the PLST can be applied either axially or diametrically. Sample preparation is normally needed for the axial PLST (to achieve a pair of flat and parallel surfaces), while the diametral PLST can be applied directly to cylinders, requiring no time consuming sample preparation. Therefore, the diametral PLST is usually preferred (Bieniawski, 1975; Hassini et al., 1980), and thus the focus of the present paper is on the stress analysis for cylinders under the diametral PLST (see Fig. 4-1).

Although the PLST has been proposed and used since the sixties (D'Andrea et al., 1965; McWilliams, 1966; Hiramatsu and Oka, 1966; Reichmuth, 1963, 1968), it is the

work by Broch and Franklin (1972) that brings popularity to this inexpensive, quick and convenient test to the rock mechanics community. In addition, the PLST has also been employed for testing the tensile and compressive strengths of concrete (Robins, 1980; Richardson, 1989) and reinforced concrete (Robins and Austin, 1985).

The diametral PLST has been investigated by many experimental studies (e.g. Guidicini et al. 1973; Bieniawski 1974, 1975; Pells 1975; Carter and Sneddon 1977; Wijk et al. 1978; Hassani et al, 1980; Lajtai 1980; Read et al. 1980; Greminger 1982; Lumb 1983; Irfan and Powell 1985), but there are relatively few theoretical works on the PLST. Theoretical analyses have been carried out for the PLST on isotropic spheres (Sternberg and Rosenthal, 1952; Hiramatsu and Oka, 1966) and anisotropic spheres (Wei and Chau, 1998; Chau and Wei, 1999a), for the axial PLST on solid cylinders (e.g. Peng, 1976; Wijk, 1978; Chau and Wong, 1996; Wei et al., 1999), and for the diametral PLST on solid cylinders (Wijk, 1980; Chau 1998a).

In particular, regarding the tensile stress concentration in cylinders under the diametral PLST, Wijk (1980) provided an approximation for the tensile stress at the center of a solid circular cylinder. The tensile stress distribution along the line joining the two applied point loads is then interpolated between those tensile stresses obtained from the solution for the PLST on spheres by Hiramatsu and Oka (1996) and from the solution for the axial PLST on finite circular plates by Wijk (1978). Recently, Chau (1998a) obtained an analytic solution for a finite cylinder under the diametral PLST with shear displacements constrained on the two end surfaces, whereas in actual PLST the end boundaries are shear traction free. The main reason why Chau (1998a) considered this kind of modified end boundary is to simplify the problem and to make it



mathematically tractable. To date, there is no exact analysis available for evaluating the stresses within a finite solid cylinder under the diametral PLST.

In addition, the stress analysis for elastic isotropic cylinders under various boundary conditions is one of the most fundamental problems in theoretical elasticity and has a rich history in the field of solid mechanics. As remarked by Filon (1902), the general stress analysis (including non-axisymmetric) for an infinite circular cylinder subjected to an arbitrary surface load was considered independently by Pochhammer (1876) and Chree (1889). One of the commonly investigated problems for finite cylinders under axisymmetric deformation is the compression of cylinders between two blocks at the end surface. This problem was first considered by Filon (1902), and subsequently by many others (see the review by Chau, 1997). More general stress analyses for axisymmetric problems for circular cylinders were considered by Saito (1952, 1954) and Ogaki and Nakajima (1983). The only analysis for non-axisymmetric deformation of finite cylinders is the approximate solution by Dougall (1914), who introduced three displacement functions. There is, however, no exact analysis that has been proposed to solve non-axisymmetric problems for finite cylinders involving loads on the curved surface and with traction free end surfaces. The stress analysis for cylinders under the diametral PLST (our present problem) is one of these unsolved non-axisymmetric problems for finite circular cylinders. As mentioned earlier, the only approximation for a finite cylinder under the diametral PLST is the solution by Chau (1998a), which is one of the few solutions considering the non-axisymmetric deformations of finite solid cylinders.

Therefore, the objective of this chapter is to present a new analytic solution for finite cylinders under the diametral PLST. The method of solution basically follows the displacement function approach by Chau (1998a), but new solution forms are proposed for these displacement functions such that all the boundary conditions can be satisfied exactly. In addition, the point loads are modeled by indentors acting upon the solid cylinders (see Fig. 4-1), and the contact stress between the curved surface of the cylinder and the spherical heads of the indentors is expanded into a double Fourier series so as to match the boundary values of the internal stress field.

The results of the study should provide the fundamental understanding of the tensile stress field within a finite cylinder under the diametral PLST. In addition to the practical application to the diametral PLST, the present study also provides a general solution technique for the stress analysis for cylinders subjected to arbitrary normal stress on the curved surface and zero traction on the two end surfaces..

## 4.2 Governing Equations

The finite cylindrical specimen considered is of radius  $R$  (or diameter  $D$ ) and length  $2L$ , and is assumed to be homogeneous, linear elastic and isotropic. The origin and  $z$ -axis of the cylindrical polar coordinate  $(r, \theta, z)$  system coincide with the center and the axis of revolution of the specimen as shown in Fig. 4-1. For isotropic elastic cylinders, the stress and strain tensors are related by the following Hook's law

$$\sigma_{\alpha\beta} = 2G\varepsilon_{\alpha\beta} + \lambda\varepsilon_{\gamma\gamma}\delta_{\alpha\beta} \quad (4.1)$$

where  $\alpha, \beta, \gamma = r, \theta, z$ ;  $G$  and  $\lambda$  are the Lamé constants ( $G$  is normally referred as the shear modulus); and, as usual tensor equations, the repeated indices in (1) mean

summation. The Cauchy stress tensor and strain tensor are denoted by  $\sigma$  and  $\varepsilon$  respectively. For small deformation and small strain, the strain tensor relates to the displacement by

$$\varepsilon = \frac{1}{2}[(\nabla \mathbf{u})^T + \nabla \mathbf{u}] \quad (4.2)$$

where the displacement vector can be expressed in physical components as  $\mathbf{u} = u_r \mathbf{e}_r + u_\theta \mathbf{e}_\theta + u_z \mathbf{e}_z$ . In addition, the displacement gradient tensor is defined as

$$\nabla \mathbf{u} = \mathbf{e}_r \frac{\partial \mathbf{u}}{\partial r} + \mathbf{e}_\theta \frac{1}{r} \frac{\partial \mathbf{u}}{\partial \theta} + \mathbf{e}_z \frac{\partial \mathbf{u}}{\partial z} \quad (4.3)$$

It is straightforward to show that the physical components of the strain tensor in cylindrical coordinate are

$$\begin{aligned} \varepsilon_{rr} &= \frac{\partial u_r}{\partial r}, \varepsilon_{\theta\theta} = \frac{1}{r} \frac{\partial u_r}{\partial \theta} + \frac{\partial u_\theta}{\partial r} - \frac{u_\theta}{r}, \\ \varepsilon_{zz} &= \frac{\partial u_z}{\partial z}, \varepsilon_{r\theta} = \frac{1}{2} \left( \frac{\partial u_\theta}{\partial r} + \frac{1}{r} \frac{\partial u_r}{\partial \theta} - \frac{u_\theta}{r} \right), \\ \varepsilon_{\theta z} &= \frac{1}{2} \left( \frac{1}{r} \frac{\partial u_z}{\partial \theta} + \frac{\partial u_\theta}{\partial z} \right), \quad \varepsilon_{rz} = \frac{1}{2} \left( \frac{\partial u_r}{\partial z} + \frac{\partial u_z}{\partial r} \right). \end{aligned} \quad (4.4)$$

For the problem under consideration, the body force can be neglected. Thus, the equations of equilibrium,  $\nabla \cdot \sigma = \mathbf{0}$ , in terms of the displacements are (Malvern, 1969):

$$(\lambda + 2G) \frac{\partial e}{\partial r} + \frac{2G}{r} \frac{\partial \Omega_{\theta\theta}}{\partial \theta} + 2G \frac{\partial \Omega_{rz}}{\partial z} = 0 \quad (4.5)$$

$$(\lambda + 2G) \frac{1}{r} \frac{\partial e}{\partial \theta} + 2G \frac{\partial \Omega_{\theta z}}{\partial z} + 2G \frac{\partial \Omega_{r\theta}}{\partial r} = 0 \quad (4.6)$$

$$(\lambda + 2G) \frac{\partial e}{\partial z} + \frac{2G}{r} \frac{\partial}{\partial r} (r \Omega_{rz}) + \frac{2G}{r} \frac{\partial \Omega_{\theta\theta}}{\partial \theta} = 0 \quad (4.7)$$

where  $\Omega = [(\nabla \mathbf{u})^T - \nabla \mathbf{u}]/2$  and  $e = \nabla \cdot \mathbf{u}$  are the spin tensor and the volumetric strain respectively.

When the specimen is subjected to the diametral PLST, all the surfaces of the specimen are traction free except the contact stress within the elliptical contact zones between the spherical heads of the indentors and the curved surface of the cylinder (see Fig. 4-1), which was obtained by Chau (1998a) as

$$\sigma_r(R, \theta, z) = -\frac{3P}{2\pi ab} \left(1 - \frac{R^2 \theta^2}{a^2} - \frac{z^2}{b^2}\right)^{1/2} \quad (4.8)$$

for

$$|z| \leq b, \text{ and } |\theta| \leq \frac{a}{R} \left(1 - \frac{z^2}{b^2}\right)^{1/2} \text{ or } |\pi - \theta| \leq \frac{a}{R} \left(1 - \frac{z^2}{b^2}\right)^{1/2}, \quad (4.9)$$

where  $P$  is the magnitude of the applied force. The size of the contact zone is characterized by  $a$  and  $b$ , the half length of major and minor axes of the elliptical contact area, and they can be evaluated by using (Chau, 1998a)

$$b = \left[ \frac{3PE(e)(1-\nu)R_2R}{2\pi G(1-e^2)(R_2 + 2R)} \right]^{1/3}, \quad a = b(1-e^2)^{1/2} \quad (4.10)$$

where  $G$ ,  $\nu$ ,  $R$  and  $R_2$  are the shear modulus, the Poisson's ratio [note  $2\nu = \lambda / (\lambda + G)$ ], the radius of the cylinder, and the radius of the spherical heads of the indentors, respectively. The eccentricity of the elliptical region  $e$  [which should not be confused with the volumetric strain used in (4.5)-(4.7)] can be obtained by solving the following nonlinear equation

$$\frac{R_2}{R_2 + 2R} = \frac{2(1-e^2)}{e^2} \left[ \frac{K(e) - E(e)}{E(e)} \right] - 1 \quad (4.11)$$

where

$$K(e) = \int_0^{\pi/2} (1 - e^2 \sin^2 \phi)^{-1/2} d\phi, \quad E(e) = \int_0^{\pi/2} (1 - e^2 \sin^2 \phi)^{1/2} d\phi, \quad (4.12)$$

are the complete elliptic integrals of the first and second kinds. Note that  $E(e)$  should not be confused with the Young's modulus  $E$ .

In summary, the boundary conditions for the finite cylinder under the diametral PLST are

$$\sigma_z = 0, \quad \sigma_r = 0, \quad \sigma_{\theta} = 0 \quad (4.13)$$

on  $z = \pm L$ ; and

$$\sigma_r = 0, \quad \sigma_{\theta} = 0, \quad (4.14)$$

$$\begin{aligned} & \sigma_r(R, \theta, z) \\ &= \begin{cases} -\frac{3P}{2\pi ab} \left(1 - \frac{R^2 \theta^2}{a^2} - \frac{z^2}{b^2}\right)^{1/2} \text{ for } |z| \leq b, \text{ and } |\theta| \leq \frac{a}{R} \left(1 - \frac{z^2}{b^2}\right)^{1/2} \text{ or } |\pi - \theta| \leq \frac{a}{R} \left(1 - \frac{z^2}{b^2}\right)^{1/2} \\ 0 \quad \text{for } |z| > b, \text{ and } |\theta| > \frac{a}{R} \left(1 - \frac{z^2}{b^2}\right)^{1/2} \text{ or } |\pi - \theta| > \frac{a}{R} \left(1 - \frac{z^2}{b^2}\right)^{1/2} \end{cases} \end{aligned} \quad (4.15)$$

on  $r=R$ .

As proposed by Chau (1998), a double Fourier expansion with respect to  $z$  and  $\theta$  is applied to the contact stress (which will be used to match the boundary limit of the internal stress field)

$$\sigma_r(R, z, \theta) = \sum_{n=0}^{\infty} \sum_{m=0}^{\infty} \chi D_{mn} \cos(\eta_m z) \cos(2n\theta) \quad (4.16)$$

where

$$\chi = \begin{cases} 1/4 & \text{for } m = n = 0 \\ 1/2 & \text{for } m = 0, n \neq 0 \text{ or } m \neq 0, n = 0 \\ 1 & \text{for } n > 0 \text{ and } m > 0 \end{cases} \quad (4.17)$$

$$D_{mn} = -\frac{3P}{\pi R_0 L} \left[ \int_0^{\pi/2} \sin^2 \beta \cos(\eta_m b \cos \beta) J_0(\zeta \sin \beta) d\beta + \int_0^{\pi/2} \sin^2 \beta \cos(\eta_m b \cos \beta) J_2(\zeta \sin \beta) d\beta \right] \quad (4.18)$$

where

$$\zeta = 2na / R \quad (4.19)$$

Note that these expressions are the same as those given by Chau (1998a) after some minor mistakes are corrected.

### 4.3 Method of Solution

The following two displacement functions  $\Phi$  and  $\Psi$  are adopted from Chau (1998a) (except minor typo):

$$u_r = \frac{\partial^2 \Phi}{\partial r \partial z} + \frac{1}{r} \frac{\partial \Psi}{\partial \theta}, \quad u_\theta = \frac{1}{r} \frac{\partial^2 \Phi}{\partial \theta \partial z} - \frac{\partial \Psi}{\partial r}, \quad u_z = -[2(1-\nu) \nabla_1 \Phi + (1-2\nu) \frac{\partial^2 \Phi}{\partial z^2}] \quad (4.20)$$

where

$$\nabla_1 = \frac{1}{r} \frac{\partial}{\partial r} \left( r \frac{\partial}{\partial r} \right) + \frac{1}{r^2} \frac{\partial^2}{\partial \theta^2} \quad (4.21)$$

By substituting (4.20) into (4.5)-(4.7), the three equilibrium equations are converted to the following two uncoupled partial differential equations for  $\Phi$  and  $\Psi$

$$\nabla^4 \Phi = \nabla^2 \nabla^2 \Phi = 0, \quad \nabla^2 \Psi = 0 \quad (4.22)$$

where  $\nabla^2$  is the Laplacian operator, or  $\nabla^2 = \nabla_1 + \partial^2 / \partial z^2$ . That is,  $\Phi$  and  $\Psi$  satisfy the biharmonic and harmonic equations respectively.

Substitution of (4.20) into (4.4) and then the results into (4.1) gives the stress components in terms of two displacement functions  $\Phi$  and  $\Psi$  as

$$\sigma_r = -2\nu G \nabla^2 \frac{\partial \Phi}{\partial z} + 2G \left[ \frac{\partial^3 \Phi}{\partial z \partial r^2} + \frac{\partial}{\partial r} \left( \frac{1}{r} \frac{\partial \Psi}{\partial \theta} \right) \right] \quad (4.23)$$

$$\sigma_\theta = -2\nu G \nabla^2 \frac{\partial \Phi}{\partial z} + 2G \left[ \frac{1}{r} \frac{\partial^3 \Phi}{\partial z \partial r} + \frac{1}{r^2} \frac{\partial^3 \Phi}{\partial \theta^2 \partial z} - \frac{\partial}{\partial r} \left( \frac{1}{r} \frac{\partial \Psi}{\partial \theta} \right) \right] \quad (4.24)$$

$$\sigma_z = -2G[(2-\nu)\frac{\partial}{\partial z}\nabla^2 - \frac{\partial^3}{\partial z^3}]\Phi \quad (4.25)$$

$$\sigma_r = 2G[-(1-\nu)\frac{\partial}{\partial r}\nabla_1 + \nu\frac{\partial^3}{\partial r\partial z^2}]\Phi + \frac{G}{r}\frac{\partial^2\Psi}{\partial\theta\partial z} \quad (4.26)$$

$$\sigma_\theta = 2G[-(1-\nu)\frac{1}{r}\frac{\partial}{\partial\theta}\nabla_1 + \nu\frac{1}{r}\frac{\partial^3}{\partial\theta\partial z^2}]\Phi - G\frac{\partial^2\Psi}{\partial r\partial z} \quad (4.27)$$

$$\sigma_\phi = 2G[\frac{\partial}{\partial r}(\frac{1}{r}\frac{\partial^2\Phi}{\partial\theta\partial z}) + \frac{1}{2}(\frac{1}{r}\frac{\partial\Psi}{\partial r} + \frac{1}{r^2}\frac{\partial^2\Psi}{\partial\theta^2} - \frac{\partial^2\Psi}{\partial r^2})] \quad (4.28)$$

The next and in fact the most important step of the analysis is to assume appropriate forms for the two displacement functions such that both the governing equations (4.22) and the boundary conditions (4.13)-(4.15) can be satisfied.

#### 4.4 Series Expressions for the Displacement Functions

After a tedious step of trial and error, the following two series expressions for  $\Phi$  and  $\Psi$  are proposed:

$$\begin{aligned} \Phi = & -\frac{1}{2G}\{A_0\frac{Z^3}{6} + C_0\frac{Z}{2}r^2 + \sum_{n=0}^{\infty}\{H_{0n}r^{2n}z + \sum_{m=1}^{\infty}\frac{1}{\eta_m^3}[A_{mn}r\frac{\partial I_{2n}(\eta_m r)}{\partial r} + B_{mn}I_{2n}(\eta_m r)]\sin(\eta_m z) \\ & + \sum_{s=1}^{\infty}\frac{1}{\gamma_s^3}[C_{sn}\sinh(\gamma_s z) + D_{sn}\gamma_s z \cosh(\gamma_s z)]J_{2n}(\gamma_s r)\}\cos(2n\theta)\} \end{aligned} \quad (4.29)$$

$$\Psi = -\frac{1}{2G}\{\sum_{n=0}^{\infty}[E_{0n}r^{2n} + \sum_{m=1}^{\infty}\frac{E_{mn}}{\eta_m^2}I_{2n}(\eta_m r)\cos(\eta_m z)]\sin(2n\theta)\} \quad (4.30)$$

where  $\eta_m = m\pi / L$ ,  $\gamma_s = \lambda_s / R$ , and  $\lambda_s$  is the  $s$ -th root of  $J'_{2n}(\lambda_s) = 0$ ;

$J_{2n}(x)$  and  $I_{2n}(x)$  are the Bessel and modified Bessel functions of the first kind of order  $2n$  respectively; and  $A_0, C_0, H_{0n}, E_{0n}, A_{mn}, B_{mn}, C_{sn}, D_{sn}$  and  $E_{mn}$  are unknown coefficients

to be determined by the boundary conditions (4.13)-(4.15). Since the periodicity of the pair of point loads on the circumference is  $\pi$  (see Fig. 4-1), the periodicity of displacement functions  $\Phi$  and  $\Psi$  in  $\theta$  must also be  $\pi$  [i.e.  $\sin(2n\theta)$  and  $\cos(2n\theta)$ ]. The first two terms in (4.29) lead to constant normal stresses (it is evident from the expressions of stresses to be given later), and the first term within the summation for index  $n$  is resulted from considering the term  $m=0$  in the next summation. A major difference between (4.29) and the corresponding form given in (4.32) of Chau (1998a) is the inclusion of the additional summation for index  $s$  involving hyperbolic functions  $\sinh(\gamma, z)$  and  $\cosh(\gamma, z)$ . The use of these hyperbolic sine and cosine in the solution form appears to be first proposed by Schiff in 1883 (cited by Filon, 1902), and this form has subsequently been adopted by Saito (1952, 1954) and Ogaki and Nakajima (1983) as well. Similarly, the first term in the summation for index  $n$  in (4.30) is again resulted from considering the term  $m=0$  in the next summation. It is straightforward to show that the forms of  $\Phi$  and  $\Psi$  given in (4.29)-(4.30) satisfy the governing equations (4.22) identically.

If  $C_m = D_m = C_0 = A_0 = H_{0n} = E_{0n} = 0$ , the two displacement functions  $\Phi$  and  $\Psi$  given in (4.29)-(4.30) reduce to the corresponding expressions by Chau(1998a).

#### 4.5 General Expressions for Stresses

Substitution of (4.29) and (4.30) into (4.23)-(4.28) yields the following expressions for the stress components,



$$\begin{aligned}
\sigma_r = & (2\nu-1)C_0 + A_0 + \sum_{n=0}^{\infty} \{-2n(2n-1)(H_n + E_n)r^{2n-2} + \sum_{m=1}^{\infty} \{A_m[2M_n(\eta_m r) - \frac{1}{\eta_m^2} \frac{\partial}{\partial r} (r \frac{\partial I_n(\eta_m r)}{\partial r})]\} \\
& \frac{B_m}{\eta_m^2} \frac{\partial I_n(\eta_m r)}{\partial r} - \frac{2nE_m}{\eta_m^2} \frac{\partial}{\partial r} (\frac{I_n(\eta_m r)}{r})\} \cos(\eta_m z) + \sum_{n=1}^{\infty} \{[(C_n + (2\nu+1)D_n) \cosh(\gamma_n z) + D_n \gamma_n z \sinh(\gamma_n z)] J_n(\gamma_n r) \\
& + [(C_n + D_n) \cosh(\gamma_n z) + D_n \gamma_n z \sinh(\gamma_n z)] [\frac{1}{\gamma_n^2 r} \frac{\partial J_n(\gamma_n r)}{\partial r} - \frac{4n}{\gamma_n^2 r^2} J_n(\gamma_n r)]\} \cos(2n\theta)
\end{aligned} \tag{4.31}$$

$$\begin{aligned}
\sigma_{\theta} = & (2\nu-1)C_0 + A_0 + \sum_{n=0}^{\infty} \{2n(2n-1)(H_n + E_n)r^{2n-2} + \sum_{m=1}^{\infty} \{A_m[2M_n(\eta_m r) - \frac{1}{\eta_m^2} \frac{1}{r} \frac{\partial}{\partial r} (r \frac{\partial I_n(\eta_m r)}{\partial r}) + \frac{4n}{\eta_m^2 r} \frac{\partial I_n(\eta_m r)}{\partial r}] \\
& \frac{B_m}{\eta_m^2} [\frac{1}{r} \frac{\partial I_n(\eta_m r)}{\partial r} - \frac{4n}{r^2} I_n(\eta_m r)] + \frac{2nE_m}{\eta_m^2} \frac{\partial}{\partial r} (\frac{I_n(\eta_m r)}{r})\} \cos(\eta_m z) + \sum_{n=1}^{\infty} \{2\nu D_n \cosh(\gamma_n z) J_n(\gamma_n r) \\
& - [(C_n + D_n) \cosh(\gamma_n z) + D_n \gamma_n z \sinh(\gamma_n z)] [\frac{1}{\gamma_n^2 r} \frac{\partial J_n(\gamma_n r)}{\partial r} - \frac{4n}{\gamma_n^2 r^2} J_n(\gamma_n r)]\} \cos(2n\theta)
\end{aligned} \tag{4.32}$$

$$\begin{aligned}
\sigma_z = & 2(2-\nu)C_0 + (1-\nu)A_0 + \sum_{n=0}^{\infty} \{ \sum_{m=1}^{\infty} \{A_m[2(2-\nu)I_n(\eta_m r) + r \frac{\partial I_n(\eta_m r)}{\partial r}] + B_m I_n(\eta_m r)\} \cos(\eta_m z) \\
& - \sum_{n=1}^{\infty} [(C_n + (2\nu-1)D_n) \cosh(\gamma_n z) + D_n \gamma_n z \sinh(\gamma_n z)] J_n(\gamma_n r) \} \cos(2n\theta)
\end{aligned} \tag{4.33}$$

$$\begin{aligned}
\sigma_r = & \sum_{n=0}^{\infty} \{ \sum_{m=1}^{\infty} \{ -\frac{A_m}{\eta_m} [2(\nu-1) \frac{\partial I_n(\eta_m r)}{\partial r} - \frac{\partial}{\partial r} (r \frac{\partial I_n(\eta_m r)}{\partial r})] + \frac{B_m}{\eta_m} \frac{\partial I_n(\eta_m r)}{\partial r} + \frac{nE_m}{\eta_m} \frac{I_n(\eta_m r)}{r} \} \sin(\eta_m z) \\
& - \sum_{n=1}^{\infty} \{ \frac{1}{\gamma_n} [(C_n + 2\nu D_n) \sinh(\gamma_n z) + D_n \gamma_n z \cosh(\gamma_n z)] \frac{\partial J_n(\gamma_n r)}{\partial r} \} \cos(2n\theta)
\end{aligned} \tag{4.34}$$

$$\begin{aligned}\sigma_{z\theta} = & \sum_{n=0}^{\infty} \left\{ \sum_{m=1}^{\infty} \left\{ \frac{2nA_m}{\eta_m} [2(\nu-1) \frac{I_{2n}(\eta_m r)}{r} - \frac{\partial_{2n}(\eta_m r)}{\partial r}] - \frac{2nB_m}{\eta_m} \frac{I_{2n}(\eta_m r)}{r} - \frac{E_m}{2\eta_m} \frac{\partial_{2n}(\eta_m r)}{\partial r} \right\} \sin(\eta_m z) \right. \\ & \left. + \sum_{s=1}^{\infty} \left\{ \frac{2n}{\gamma_s} [(C_m + 2\nu D_m) \sinh(\gamma_s z) + D_m \gamma_s z \cosh(\gamma_s z)] \frac{J_{2n}(\gamma_s r)}{r} \right\} \sin(2n\theta) \right\}\end{aligned}\quad (4.35)$$

$$\begin{aligned}\sigma_{rs} = & \sum_{n=0}^{\infty} \left\{ 2n(2n-1)(H_{0n} - E_{0n})r^{2n-2} + \sum_{m=1}^{\infty} \left\{ \frac{2nA_m}{\eta_m^2} \frac{\partial^2 I_{2n}(\eta_m r)}{\partial r^2} + \frac{2nB_m}{\eta_m^2} \left[ \frac{1}{r} \frac{\partial I_{2n}(\eta_m r)}{\partial r} - \frac{1}{r^2} I_{2n}(\eta_m r) \right] \right. \right. \\ & \left. \left. + \frac{E_m}{2\eta_m^2} \left[ -\frac{1}{r} \frac{\partial I_{2n}(\eta_m r)}{\partial r} + \frac{4n^2}{r^2} I_{2n}(\eta_m r) + \frac{\partial^2 I_{2n}(\eta_m r)}{\partial r^2} \right] \right\} \cos(\eta_m z) \right. \\ & \left. + \sum_{s=1}^{\infty} \frac{2n}{\gamma_s^2} [(C_m + D_m) \cosh(\gamma_s z) + D_m \gamma_s z \sinh(\gamma_s z)] \left[ \frac{1}{r} \frac{\partial J_{2n}(\gamma_s r)}{\partial r} - \frac{1}{r^2} J_{2n}(\gamma_s r) \right] \right\} \sin(2n\theta)\end{aligned}\quad (4.36)$$

#### 4.6 Determination of the Unknown Coefficients

Specializing the shear stresses (4.34)-(4.35) to the end boundary conditions given in (4.13) (i.e.  $\sigma_{rz}$  and  $\sigma_{z\theta} = 0$  on  $z = \pm L$ ), we have

$$(C_m + 2\nu D_m) \sinh(\gamma, L) + D_m \gamma, L \cosh(\gamma, L) = 0 \quad (4.37)$$

This equation can be rewritten as

$$\frac{C_m}{2\nu \sinh(\gamma, L) + \gamma, L \cosh(\gamma, L)} = -\frac{D_m}{\sinh(\gamma, L)} = -\frac{G_m}{\Lambda_s} \quad (4.38)$$

where  $G_m$  and  $\Lambda_s$  are constants introduced to simplify the equations involved in the subsequent analysis. Then, the constants  $C_m$  and  $D_m$  can be expressed in terms of the newly introduced constants as:

$$C_m = -\frac{G_m}{\Lambda_s} [2\nu \sinh(\gamma, L) + \gamma, L \cosh(\gamma, L)] \quad (4.39)$$

$$D_{\pm} = \frac{G_{\pm}}{\Lambda_{\pm}} \sinh(\gamma, L) \quad (4.40)$$

Substituting (4.39) and (4.40) into (4.33) then specializing the resulting stress to the end boundary  $z = \pm L$ , we have

$$\begin{aligned} \sigma_{\pm} = & 2(2-\nu)C_0 + (1-\nu)A_0 + \sum_{n=0}^{\infty} \left\{ \sum_{m=1}^{\infty} \{A_{mn}[2(2-\nu-n)I_{2n}(\eta_m r) + \eta_m r I_{2n-1}(\eta_m r)] + B_{mn}I_{2n}(\eta_m r)\}(-1)^m \right. \\ & \left. + \sum_{s=1}^{\infty} \frac{G_{\pm}}{\Lambda_{\pm}} [\gamma, L + \sinh(\gamma, L) \cosh(\gamma, L)] J_{2n}(\gamma_s r) \right\} \cos(2n\theta) \end{aligned} \quad (4.41)$$

The first of the boundary conditions (4.13) requires that the normal stress is identically zero on two end surfaces, independent of both  $r$  and  $\theta$  (i.e.  $\sigma_{\pm} = 0$  on  $z = \pm L$ ). In view of this, we expand all terms with the  $r$ -dependency (i.e. the modified Bessel functions) in (4.41) into series expansion of Bessel function (Watson, 1944) and then assign the following value for  $\Lambda_{\pm}$ :

$$\Lambda_{\pm} = \gamma, L + \sinh(\gamma, L) \cosh(\gamma, L) \quad (4.42)$$

Subsequently, (4.41) is simplified to the following compact form,

$$\sigma_{\pm} = 2(2-\nu)C_0 + (1-\nu)A_0 \quad (4.43)$$

$$+ \sum_{n=0}^{\infty} \sum_{s=1}^{\infty} \{G_{\pm n} + \sum_{m=1}^{\infty} \{A_{mn}[2(2-\nu-n)T_{ms} + U_{ms}] + B_{mn}T_{ms}\}(-1)^m\} J_{2n}(\gamma_s r) \cos(2n\theta)$$

where

$$T_{ms} = \frac{2\lambda_s^2}{(\lambda_s^2 - 4n^2)[(\eta_m R)^2 + \lambda_s^2]J_{2n}^2(\lambda_s)} [\eta_m R I_{2n-1}(\eta_m R) J_{2n}(\lambda_s) + \lambda_s I_{2n}(\eta_m R) J_{2n+1}(\lambda_s)] \quad (4.44)$$

$$\begin{aligned}
U_{ns} = & \frac{2\lambda_z^2 \eta_n R}{(\lambda_z^2 - 4n^2)[(\eta_n R)^2 + \lambda_z^2]} J_{2n}^2(\lambda_z) \left\{ \frac{(4n-2)\eta_n R}{(\eta_n R)^2 + \lambda_z^2} [\eta_n R I_{2n+1}(\eta_n R) J_{2n}(\lambda_z) \right. \\
& + \lambda_z I_{2n}(\eta_n R) J_{2n+1}(\lambda_z)] + \frac{4n\lambda_z}{(\eta_n R)^2 + \lambda_z^2} [\eta_n R I_{2n}(\eta_n R) J_{2n-1}(\lambda_z) + \lambda_z I_{2n-1}(\eta_n R) J_{2n}(\lambda_z)] \\
& \left. + \eta_n R I_{2n}(\eta_n R) J_{2n}(\lambda_z) - \lambda_z I_{2n-1}(\eta_n R) J_{2n-1}(\lambda_z) \right\}
\end{aligned} \quad (4.45)$$

The procedure in obtaining (4.44) and (4.45) is reported briefly in the Appendix III for the sake of completeness. Finally, the end boundary condition ( $\sigma_z = 0$  on  $z = \pm L$ ) yields the follow equations for the unknown coefficients

$$2(2-\nu)C_0 + (1-\nu)A_0 = 0 \quad (4.46)$$

$$G_{ns} + \sum_{n=1}^{\infty} \{A_{ns} [2(2-\nu-n)T_{ns} + U_{ns}] + B_{ns} T_{ns}\} (-1)^n = 0 \quad (4.47)$$

So far, all end boundary conditions given in (4.13) have been considered. The next step is to ensure that the curved boundary conditions (4.14)-(4.15) will be satisfied. Substitution of (4.34) into the shear traction free condition (4.14) (i.e.,  $\sigma_{rz} = 0$  on  $r=R$ ) leads to

$$-\frac{A_{ns}}{\eta_n} [(2\nu-3) \frac{\partial I_{2n}(\eta_n R)}{\partial r} - R \frac{\partial^2 I_{2n}(\eta_n R)}{\partial r^2}] + \frac{B_{ns}}{\eta_n} \frac{\partial I_{2n}(\eta_n R)}{\partial r} + \frac{nE_{ns}}{\eta_n} \frac{I_{2n}(\eta_n R)}{R} = 0 \quad (4.48)$$

To consider the boundary condition for the shear stress  $\sigma_{\theta z}$ , we, by applying similar technique leading to the results given in (4.46)-(4.47), substitute (4.39)-(4.40) into (4.36) and specialize the result on  $r=R$ . Then, all  $\cosh(\gamma, z)$  and  $\gamma, z \sinh(\gamma, z)$  terms involved are expanded into series of  $\cos(\eta_n z)$  and the final form is

$$\begin{aligned}
\sigma_{r,\theta} = & \sum_{n=0}^{\infty} \{2n(2n-1)(H_{0n} - E_{0n})R^{2n-2} + \sum_{s=1}^{\infty} \frac{4n\nu G_s \sinh^2(\gamma_s L)}{\Lambda_s \gamma_s L} \frac{J_{2n}(\gamma_s R)}{\gamma_s^2 R^2} + \sum_{m=1}^{\infty} \left\{ \frac{2nA_m}{\eta_m^2} \frac{\partial^2 I_{2n}(\eta_m R)}{\partial r^2} \right. \\
& + \frac{2nB_m}{\eta_m^2} \left[ \frac{1}{R} \frac{\partial I_{2n}(\eta_m R)}{\partial r} - \frac{1}{R^2} I_{2n}(\eta_m R) \right] + \frac{E_m}{2\eta_m^2} \left[ -\frac{1}{R} \frac{\partial I_{2n}(\eta_m R)}{\partial r} + \frac{4n^2}{R^2} I_{2n}(\eta_m R) + \frac{\partial^2 I_{2n}(\eta_m R)}{\partial r^2} \right] \\
& \left. - \sum_{s=1}^{\infty} \frac{G_s}{\Lambda_s} \frac{8}{\gamma_s L(\gamma_s^2 + \eta_m^2)} \frac{n(-1)^m \sinh^2(\gamma_s L)}{\gamma_s L(\gamma_s^2 + \eta_m^2)} \frac{J_{2n}(\gamma_s R)}{R^2} \left[ \frac{\eta_m^2}{\gamma_s^2 + \eta_m^2} - \nu \right] \right\} \cos(\eta_m z) \sin(2n\theta)
\end{aligned} \tag{4.49}$$

Subsequently, we can apply the second of the boundary conditions (4.14) to (4.49). That is, the shear stress  $\sigma_{r,\theta}$  on the curved boundary is identically zero for any value of  $z$  and  $\theta$ , and this leads to

$$\begin{aligned}
2n(2n-1)(H_{0n} - E_{0n})R^{2n-2} = & - \sum_{s=1}^{\infty} \frac{4n\nu G_s \sinh^2(\gamma_s L)}{\Lambda_s \gamma_s L} \frac{J_{2n}(\gamma_s R)}{\gamma_s^2 R^2} \\
& \frac{2nA_m}{\eta_m^2} \frac{\partial^2 I_{2n}(\eta_m R)}{\partial r^2} + \frac{2nB_m}{\eta_m^2} \left[ \frac{1}{R} \frac{\partial I_{2n}(\eta_m R)}{\partial r} - \frac{1}{R^2} I_{2n}(\eta_m R) \right] + \frac{E_m}{2\eta_m^2} \left[ -\frac{1}{R} \frac{\partial I_{2n}(\eta_m R)}{\partial r} \right. \\
& \left. + \frac{4n^2}{R^2} I_{2n}(\eta_m R) + \frac{\partial^2 I_{2n}(\eta_m R)}{\partial r^2} \right] - \sum_{s=1}^{\infty} \frac{G_s}{\Lambda_s} \frac{8n(-1)^m \sinh^2(\gamma_s L)}{\gamma_s L(\gamma_s^2 + \eta_m^2)} \frac{J_{2n}(\gamma_s R)}{R^2} \left[ \frac{\eta_m^2}{\gamma_s^2 + \eta_m^2} - \nu \right] = 0
\end{aligned} \tag{4.51}$$

In order to satisfy the last boundary condition (4.15), we set  $r=R$  in (4.31) to yield

$$\begin{aligned}
\sigma_r = & (2\nu-1)C_0 + \nu A_0 + \sum_{n=0}^{\infty} \{-2n(2n-1)(H_{0n} + E_{0n})R^{2n-2} + \sum_{m=1}^{\infty} \{A_m[2\nu I_{2n}(\eta_m R) \\
& - \frac{1}{\eta_m^2} [2 \frac{\partial^2 I_{2n}(\eta_m R)}{\partial r^2} + R \frac{\partial^3 I_{2n}(\eta_m R)}{\partial r^3}] - \frac{B_m}{\eta_m^2} \frac{\partial^2 I_{2n}(\eta_m R)}{\partial r^2} + \frac{2nE_m}{\eta_m^2} [\frac{I_{2n}(\eta_m R)}{R^2} - \frac{1}{R} \frac{\partial I_{2n}(\eta_m R)}{\partial r}] \} \cos(\eta_m z) \\
& - \sum_{m=1}^{\infty} \{[(C_m + D_m) \cosh(\gamma, z) + D_m \gamma, z \sinh(\gamma, z)] \frac{4n^2}{\gamma^2 R^2} J_{2n}(\gamma, R) \\
& + [(C_m + (2\nu+1)D_m) \cosh(\gamma, z) + D_m \gamma, z \sinh(\gamma, z)] J_{2n}(\gamma, R) \} \} \cos(2n\theta)
\end{aligned} \tag{4.52}$$

Before we apply the boundary condition, we again substitute (4.39)-(4.40) into (4.52) and expand all functions of  $z$ -dependency in terms of  $\cos(\eta_m z)$

$$\begin{aligned}
\sigma_r = & (2\nu-1)C_0 + \nu A_0 + \sum_{n=0}^{\infty} \{-2n(2n-1)(H_{0n} + E_{0n})R^{2n-2} + \sum_{m=1}^{\infty} \frac{G_m}{\Lambda_s} \frac{8n^2 \gamma, \sinh^2(\gamma, L)}{\gamma, L} \frac{J_{2n}(\gamma, R)}{\gamma^2 R^2} \\
& + \sum_{m=1}^{\infty} \{A_m[2\nu I_{2n}(\eta_m R) - \frac{1}{\eta_m^2} [2 \frac{\partial^2 I_{2n}(\eta_m R)}{\partial r^2} + R \frac{\partial^3 I_{2n}(\eta_m R)}{\partial r^3}] - \frac{B_m}{\eta_m^2} \frac{\partial^2 I_{2n}(\eta_m R)}{\partial r^2} + \frac{2nE_m}{\eta_m^2} [\frac{I_{2n}(\eta_m R)}{R^2} - \frac{1}{R} \frac{\partial I_{2n}(\eta_m R)}{\partial r}] \\
& - \sum_{m=1}^{\infty} \frac{G_m}{\Lambda_s} \frac{4\gamma, (-1)^n \sinh^2(\gamma, L)}{L(\gamma^2 + \eta_m^2)} [\frac{\eta_m^2}{\gamma^2 + \eta_m^2} (1 + \frac{4n^2}{\gamma^2 R^2}) - \frac{4n^2 \nu}{\gamma^2 R^2}] J_{2n}(\gamma, R) \} \cos(\eta_m z) \} \cos(2n\theta)
\end{aligned} \tag{4.53}$$

Finally, equating all the coefficients of (4.53) to those of (4.16) for all terms of  $z$  and  $\theta$ , we have

$$(2\nu-1)C_0 + \nu A_0 = D_{00} / 4 \tag{4.54}$$

$$-2n(2n-1)(H_{0n} + E_{0n})R^{2n-2} + \sum_{m=1}^{\infty} \frac{G_m}{\Lambda_s} \frac{8n^2 \nu \gamma, \sinh^2(\gamma, L)}{\gamma, L} \frac{J_{2n}(\gamma, R)}{\gamma^2 R^2} = D_{0n} / 2 \tag{4.55}$$

$$\begin{aligned}
& A_m [2\nu I_{2m}(\eta_m R) - \frac{1}{\eta_m^2} [2 \frac{\partial^2 I_{2m}(\eta_m R)}{\partial r^2} + R \frac{\partial^3 I_{2m}(\eta_m R)}{\partial r^3}]] - \frac{B_m}{\eta_m^2} \frac{\partial^2 I_{2m}(\eta_m R)}{\partial r^2} + \frac{2nE_m}{\eta_m^2} [\frac{I_{2m}(\eta_m R)}{R^2} \\
& - \frac{1}{R} \frac{\partial I_{2m}(\eta_m R)}{\partial r}] - \sum_{n=1}^{\infty} \frac{G_n}{\Lambda_n} \frac{4\gamma_n (-1)^n \sinh^2(\gamma_n L)}{L(\gamma_n^2 + \eta_m^2)} [\frac{\eta_m^2}{\gamma_n^2 + \eta_m^2} (1 + \frac{4n^2}{\gamma_n^2 R^2}) - \frac{4n^2 \nu}{\gamma_n^2 R^2}] J_{2n}(\gamma_n R) \\
& = \begin{cases} D_{m0}/2 & \text{for } n=0, m>0 \\ D_m & \text{for } n>0, m>0 \end{cases}
\end{aligned} \tag{4.56}$$

By now, all boundary conditions have been satisfied, and all unknown coefficients should be uniquely determined. More specifically, the unknown constants  $A_0$  and  $C_0$  can be solved from (4.46) and (4.54) and  $A_m, B_m, E_m$  and  $G_m$  can be solved from the coupled system of equations (4.47), (4.48), (4.51) and (4.56). Finally,  $H_{0m}$  and  $E_{0m}$  can be solved from (4.50) and (4.55), and  $C_m$  and  $D_m$  can then be back calculated from (4.39) and (4.40). Therefore, the form of the displacement functions given in (4.29)-(4.30) is indeed appropriate and complete. Numerical results for our analytical solutions are given and discussed in the next section.

#### 4.7 Numerical Results and Discussion

The analytic results given in the previous section involve the solution of systems of coupled equations for the coefficients of the infinite series. In actual computation, we have to truncate the infinite series and retain only finite number of terms.

In addition, the roots of  $J'_{2n}(x) = 0$  play a very important role in series solution, it is necessary to calculate these roots accurately and efficiently. Thus, we will discuss briefly our strategy to obtain these roots. As discussed by Watson (1944), the smallest root  $\lambda_n$  of  $J'_{2n}(x) = 0$  can be bounded by

$$\frac{\sqrt{\{2n(2n+2)\}}}{\sqrt{\{2n(2n+3)\}}} \text{ (for } 1 \leq n \leq 2) < \lambda_1 < \sqrt{\{4n(2n+1)\}} \text{ (for } n > 2) \quad (4.57)$$

So the first root  $\lambda_1$  could be searched within this range by using standard procedure (e.g., Press et al., 1992). Once this first root is obtained, we can generate the subsequent roots efficiently if the following properties are noted: (i) The difference between any two nonzero consecutive roots equals approximately  $\pi$  if  $x$  is large; (ii) There must exist a root of  $J'_{2n-1}(x) = 0$  between any two consecutive roots of  $J'_{2n}(x) = 0$ ; (iii) Consequently, there must exist a root of  $J'_{2n}(x) = 0$  between any two consecutive roots of  $J'_{2n-1}(x) = 0$ . Because tables for the roots of  $J'_{2n-1}(x) = 0$  is not readily available in the literature, Table 4-1 tabulates the first ten roots for  $n$  from 0 to 7.

Numerical calculations show that the system of equations for solving  $A_m, B_m, E_m$  and  $G_m$  becomes ill-conditioned for large  $m$  and  $s$ . More specifically, the coefficients for  $A_m, B_m$  and  $E_m$  become very large while the coefficients corresponding to  $G_m$  become relatively small. We found that the ill-condition can be alleviated by a proper scaling of the coefficient. In particular, we divide all coefficients for  $A_m, B_m$  and  $E_m$  with  $I_{2n}(\eta_m R)$  and multiply all coefficients for  $G_m$  with  $\lambda_1$ ; and after solving  $A_m, B_m, E_m$  and  $G_m$ , all solutions of  $A_m, B_m$  and  $E_m$  are divided by  $I_{2n}(\eta_m R)$  while the solution for  $G_m$  is multiplied by  $\lambda_1$ . We found that more terms in  $m$  than in  $n$  are needed for acquiring the same degree of convergence for  $\sigma_z$ , while less terms in  $m$  than in  $n$  are needed for acquiring the same degree of convergence for  $\sigma_{\theta}$ . In general, 50 terms in  $n$  and 25 terms in each of  $m$  and  $s$  are needed to control the error of tensile stresses  $\sigma_z$  and  $\sigma_{\theta}$  to within 1%.



Before we discuss the distribution of the tensile stress within the cylinder, it is instructive to compare the present solution with the approximation by Wijk (1980) for the tensile stress at the center of the cylinder. Table 4-2 compares the tensile stresses at the center of the cylinder predicted by Wijk (1980) and by the present solution, for cylinders with geometric ratio  $L/D=1$  and  $\infty$ , and for Poisson's ratio  $\nu = 0, 0.1, 0.2, 0.3, 0.4$ , and  $0.5$ . Since our solution for the contact stress depends upon the values of the Young's moduli and the actual magnitude of point forces at failure, we present in Table 4-2 the results based on different Young's modulus and point force for the case of  $L/D=1$ . It is clear from Table 4-2 that Wijk's (1980) solution overestimates the value of the tensile stress (about 4% for  $L/D=1$ , and about 0.3% for  $L/D \rightarrow \infty$ ). Wijk's (1980) approximation is much better for a longer cylinder than for the case of  $L/D=1$ . This is expected because the end surface boundary conditions were satisfied only approximately by Wijk's (1980) solution. Although the approximation by Wijk (1980) is considered to be very accurate, we will show next that the maximum tensile stress is not necessarily at the center of the specimen.

Figures 4-2 and 4-3 plot the normalized stresses  $\sigma_{\theta\theta}/\sigma_0$ ,  $\sigma_{zz}/\sigma_0$ , and  $\sigma_{rr}/\sigma_0$  (where  $\sigma_0 = P/D^2$ ) versus the normalized distance  $r/R$  for various sizes of contact zone  $r_0/R$  (where  $r_0$  is a nominal radius for the elliptical contact area between the spherical heads of the indentors and the curved surface of the cylinder and is defined as  $r_0 = \sqrt{ab}$ ). The plots are calculated for the standardized size and shape suggested by Broch and Franklin (1972) and by ISRM (1985). More specifically, we have assumed the following parameters:  $D=50\text{mm}$ ,  $2L=70\text{mm}$ ,  $R_s = 5\text{mm}$  and  $\nu = 0.25$ . By following the usual sign convention of continuum mechanics, tension is plotted as positive. As shown in

Figs. 4-2 and 4-3, both  $\sigma_{\theta\theta}/\sigma_0$  and  $\sigma_{zz}/\sigma_0$  are tensile along the line joining the two point loads, and a zone of tensile stress concentration is developed at about  $r/R \approx 0.9$ , comparing to the roughly constant value at central portion of the line (say for  $r/R < 0.6$ ). Both figures show that the smaller the loading area, the larger the maximum tensile stress is induced. It is interesting to note that both the tensile stress distributions ( $\sigma_{\theta\theta}/\sigma_0$  and  $\sigma_{zz}/\sigma_0$ ) and the compressive stress distribution ( $\sigma_{rr}/\sigma_0$ ) along the line of loading are remarkably similar to those of a sphere under the diametral PLST (Wei and Chau, 1998; Chau and Wei, 1999) and of a cylinder under the axial PLST (Wei et al., 1999).

Since both of the hoop stress  $\sigma_{\theta\theta}$  and the axial stress  $\sigma_{zz}$  are in tension, it is necessary to check which one is the maximum tensile stress and thus should be responsible for the tensile breakage of the specimens. Therefore, Fig. 4-4 compares the normal stresses ( $\sigma_{\theta\theta}/\sigma_0$ ,  $\sigma_{zz}/\sigma_0$ , and  $\sigma_{rr}/\sigma_0$ ) in a typical specimen along the normalized distance  $r/R$ . The plot is for  $r_0/R = 0.039$  and other parameters are the same as those used in Fig. 4-2. For this case,  $\sigma_{zz}/\sigma_0$  is larger than  $\sigma_{\theta\theta}/\sigma_0$  in the central part, but  $\sigma_{\theta\theta}/\sigma_0$  increases faster than  $\sigma_{zz}/\sigma_0$  when the point loads are approached. Consequently the maximum tensile stress of the specimen is controlled by  $\sigma_{\theta\theta}/\sigma_0$ , and this maximum tensile stress is usually induced at about  $r/R = 0.9$ . Therefore, for the following numerical results, only  $\sigma_{\theta\theta}/\sigma_0$  is plotted if the standard geometric ratio  $2L/D=1.4$  is used. However, it should be noted that the hoop stress is not always the dominant tensile stress, there is some fewer cases that the maximum tensile stress in a

specimen may be determined by  $\sigma_z / \sigma_0$ , such as when Poisson's ratio and the diameter of the specimen are relatively large (see Fig. 4-9).

The effect of Poisson's ratio on stress distribution is illustrated in Fig. 4-5, which plots the normalized stresses  $\sigma_{\theta\theta} / \sigma_0$  and  $\sigma_{rr} / \sigma_0$  versus the normalized distance  $r/R$  for various Poisson's ratio  $\nu$ . The loading area is fixed at  $r_0 / R = 0.039$ , and parameters used are the same as those given in Fig. 4-2. The smaller the Poisson's ratio is, the larger the maximum tensile stress is induced. But the tensile stress at the central part along the line of loading and the compressive stress distribution along the same line are insensitive to the change of Poisson's ratio. It is interesting to note that the maximum tensile stress concentrations near the point loads disappear and thus the maximum tensile stress is induced at the center when the solid becomes incompressible ( $\nu=0.5$ ).

The size effect of the spherical head of the indenter ( $R_i$ ) is demonstrated in Fig. 4-6, which plots the normalized stresses  $\sigma_{\theta\theta} / \sigma_0$  and  $\sigma_{rr} / \sigma_0$  versus the normalized distance  $r/R$  for various values of  $R_i$  and  $r_0/R=0.039$ . Except for varying  $R_i$ , the plots are the same as those given in Fig. 4-2. As expected, a smaller radius of the spherical head  $R_i$  leads to a higher tensile stress concentration. For example, the maximum tensile stress may increase by 35% if  $R_i = 3\text{mm}$  is used instead of the standard size of  $R_i = 5\text{mm}$  (ISRM, 1985).

Figure 4-7 plots the normalized stresses  $\sigma_{\theta\theta} / \sigma_0$  and  $\sigma_{rr} / \sigma_0$  versus the normalized distance  $r/R$  for various values of diameter  $D$  (all other parameters used are the same as those used in Fig. 4-2). If we keep the size of the contact zone constant ( $r_0 / R = 0.039$ ), it

is observed that a larger specimen size leads to a larger tensile stress concentration, and hence a smaller point load strength index (PLSI) defined as  $P/D^2$ . This conclusion agrees with the size effect that has observed repeatedly in many experiments (Broch and Franklin, 1972; Brook, 1980; Greminger, 1982). The reason why we set the contact area constant in the calculations shown in Fig. 4-7 is because our experimental observations (to be discussed) show that the amount of indentation (hence the contact area) does not change significantly for different sizes of specimens. In particular, we observe that the indentation is on average 0.90, 1.07, and 1.55mm for cylinders of diameters of 35, 40, and 56mm respectively. Fig. 2-13 to be followed will further compare the predicted and the observed size and shape effects of specimens on the PLSI.

Figure 4-8 shows the maximum normalized stresses  $\sigma_{\theta\theta}/\sigma_0$  and  $\sigma_{zz}/\sigma_0$  (which appear at about  $r/R=0.9$ ) versus half length to diameter ratio  $L/D$  for different Poisson's ratio  $\nu$  and for  $D=50\text{mm}$ . The solid lines are for the maximum value of  $\sigma_{\theta\theta}/\sigma_0$  and the dotted lines are for those of  $\sigma_{zz}/\sigma_0$ . The maximum value of  $\sigma_{zz}/\sigma_0$  decreases drastically with the increase of  $L/D$  while the drop of  $\sigma_{\theta\theta}/\sigma_0$  with  $L/D$  is relatively gentle. Consequently, for  $\nu=0.25$  the axial stress is the dominant tensile stress for  $L/D < 0.4$  and the hoop stress becomes dominant for larger  $L/D$ ; and for  $\nu=0.35$  the geometric ratio  $L/D$  that separates the dominance between the axial and hoop stresses equals 0.7. Since a larger tensile stress concentration implies a smaller PLSI ( $I_t=P/D^2$ ), a clear shape effect is observed in Fig.4-8. This shape dependency has been observed repeatedly on natural rocks (Broch and Franklin, 1972; Greminger, 1982). To further illustrate the shape effect on the maximum tensile stress (i.e. the maximum among the axial and hoop stresses), Fig. 4-9 plots the maximum stress envelope versus

$L/D$  for various values of Poisson's ratio. For  $\nu > 0.25$ , the maximum tensile stress is insensitive to the shape as long as  $L/D > 0.4$ , but for  $\nu = 0.08$ , the maximum tensile stress continues to decrease even for  $L/D > 0.7$ . That is, shape effect is more severe for more compressible solids or very soft rocks (i.e. rocks with small Poisson's ratio).

Figure 4-10 shows these tensile stress envelope versus  $L/D$  for different diameters of specimens. For specimen size smaller than 50mm, the shape effect can be neglected if the  $L/D$  is larger than 0.4; but, for larger specimen (say  $D=80\text{mm}$ ) the maximum stress continues to decrease even for  $L/D > 0.7$ , which is a value recommended by Broch and Franklin (1972) to remove the shape effect. To avoid this shape effect, ISRM (1985) recommended a value of  $L/D > 0.5$  while Broch and Franklin (1972) suggested a value of  $L/D > 0.7$ . Our analytic solutions show, however, that if Poisson's ratio is small (say  $\nu < 0.1$ ) and the size of the cylinder is large (say  $D = 80\text{mm}$ ), the shape effect cannot be ignored even for  $L/D > 0.7$ .

#### 4.8 Experimental Validation

A series of the diametral PLST were carried out on cylinders of a rock-like plaster material. A total of over 40 cylinders were cast using a plastic hollow mould of various size ( $D= 35, 40, 50$ , and  $56\text{mm}$ ) and of shape factors ( $L/D=0.4, 0.5, 0.63, 0.76, 0.86$  and  $1.0$ ). These specimens were made of a water-plaster-mixture with water/plaster mass ratio of 3/10, and other mechanical properties for the material are:  $\nu=0.25$ ,  $E=17.5\text{GPa}$ , the uniaxial compressive strength (UCS) =  $57.54\text{MPa}$ , and density= $1.75\text{-}1.78\text{g/cm}^3$ . When the plaster mixture was poured into the mould layer by layer, it was tapped using a small wooden hammer to minimize the content of air and to achieve a homogenous

solid with reproducible properties. All tests were carried out after all the samples were cured for 60 days and maintain a constant weight. For more discussion on the requirements of judging a rock-like material using Buckingham pi-theorem, we refer to Wong and Chau (1998).

To calibrate the maximum allowable local tensile stress of the plaster material under the diametral PLST, the theoretical stress profiles of three specimens with  $D=56\text{mm}$  and  $L/D=1.4$  were calculated using our analytic solution. The magnitude of the point force at the failure of each specimen together with other elastic properties of the material have been substituted into our solution. Figure 4-11 shows the predicted stress profiles for  $\sigma_{\theta\theta}$ ,  $\sigma_z$  and  $\sigma_{rr}$  versus the normalized distance  $r/R$ . Stress profiles for these three specimens basically overlap and cannot be distinguished easily on the figure. The calculated maximum tensile stresses for these specimens are 26.133, 25.888, 26.315MPa with an average of 26.112MPa. In order to predict the failure load for samples of other size and shape, we assume that if the maximum tensile stress in the solid reaches 26.112MPa (which will be called the local tensile strength hereafter), the specimen fails. From microscopic point of view, this assumption implies that a critical local tensile stress of 26.112MPa is needed to initiate unstable crack growth within the sample.

By using this local tensile strength, the maximum point force, and hence the PLSI, can be predicted for specimens of any shape and size. Figure 4-12 plots the predicted PLSI (or  $I_c$ ) versus  $L/D$  together with our experimental results for specimens of  $D=56\text{mm}$ . Basically, theoretical prediction agrees well with experiments. Our theoretical calculations show a very strong shape effect for  $L/D < 0.3$  for  $D=56\text{mm}$ . As

remarked earlier, this shape effect has been observed in other experimental studies (e.g. Broch and Franklin, 1972; Greminger, 1982).

The predicted size effect on the PLSI is showed in Fig. 4-13 together with our experimental data. Specimens of diameter of 35, 40, 50, and 56mm were tested. The trends of the predicted and observed size effects agree very well. It should be noted that we do not assume a constant contact area, as we did for the calculations show in Fig. 4-7 (since the point force at failure is input in our analysis).

Figure 4(a) of ISRM (1985) shows the typical modes of failure of specimens under the diametral PLST observed in experiments; in particular, specimens are normally broken into two or three pieces. The relation between these modes of failure in the PLST and the shape of the specimens has not studied before; and the main reason is probably due to the lack of information on the tensile stress field inside the specimens.

Figure 4-14 sketches two typical modes of failure observed in our experiments (we call them T-mode and S-mode for indicating Tri-fracture and Single-fracture in the failure mechanism), while Table 4-3 tabulates the failure mode and pattern for 9 particular samples that we have tested. It is observed that for cylinders with  $L/D = 0.4$ , T-mode is more likely to occur, while for cylinders with  $L/D \geq 0.5$ , S-mode appears to be dominant. Note that out of the 36 samples with  $L/D \geq 0.5$  that we have tested, only three samples failed in T-mode. This observation can be explained by checking the numerical results showed in Fig. 4-8. In particular, for  $L/D = 0.4$  and  $\nu = 0.25$  Fig. 4-8 shows that the magnitudes of  $\sigma_{\theta\theta}$  and  $\sigma_{zz}$  are comparable. That is, tensile failure is likely to occur along both axial and transverse directions; thus, multi-fracture showed in the T-mode of Fig. 4-14 is more likely to occur than the S-mode. However, for longer

cylinders (say  $L/D \geq 0.5$ ) the upper curve in Fig. 4-8 suggests that the maximum tensile stress is always dominated by  $\sigma_{\theta\theta}$ , thus, we speculate that a single fracture may be more likely to occur. However, more elaborated analysis and experiments are still required to make our conclusion more convincing.

#### 4.9 Conclusion

This chapter presents a new analytic solution for the stresses inside an isotropic solid circular cylinder of finite length subjected to the diametral point load strength test (PLST). The method of solution uses the displacement function approach together with double Fourier expansion for the contact stress, which is obtained by considering the Hertz contact between the indentors and the curved surface of the cylinder. Appropriate forms for the displacement functions are proposed so that all boundary conditions and all governing equations can be satisfied. Numerical results show that, similar to the results for a sphere under the diametral PLST or a cylinder under the axial PLST, tensile stress concentrations are developed near the point loads. The maximum tensile stress decreases with the increase of Poisson's ratio, the contact area, the radius of spherical heads of the indentors, but increases with the increase of diameter  $D$ . The hoop stress is the dominant tensile stress for long cylinders (say  $L/D$  larger than 0.7), but the axial stress may become dominant if  $L/D$  is small (say smaller than 0.4). The proximity of the values of normal stresses ( $\sigma_{\theta\theta}$  and  $\sigma_{zz}$ ) also provide a plausible explanation why specimens break into three pieces for  $D/L = 0.4$ , but into two pieces when  $D/L > 0.7$ . Both size and shape effects of specimens on the point load strength index (PLSI), which is defined as  $P/D^2$ , are predicted by our solution, and these predictions agree well with



our experiments. In addition to the practical application to the diametral PLST, the present study also provides a general solution technique for the stress analysis of cylinders under arbitrary normal stress on the curved surface and with zero end tractions.

## **Chapter 5**

# **THEORETICAL BASIS FOR TESTING IRREGULAR LUMPS UNDER THE POINT LOAD STRENGTH TEST**

### **5.1 Introduction**

The possibility of using relatively unprepared specimens for rock classification and strength estimation has always been attractive. The Point Load Strength Test (PLST) seems potentially to be the most likely choice. Because the so-called point loads are applied to specimens within very small surface areas, we speculate that the PLST is more tolerant of the possible irregularity of specimens than other tests. In fact, samples with various shapes, such as spheres, rock cores and irregular lumps, have been used as specimens for the PLST (Hiramatsu and Oka, 1966).

The use of irregular lumps for rock testing, as described by Protodyakonov and Voblikov (1957), was developed in Russia. The testing procedure was first formalized by the International Bureau for Rock mechanics in 1961 (IBRM, 1961). Thereafter, irregular lumps have been used for classifying sedimentary rocks (Hobbs, 1963), and for testing mechanical performance of rockfill material (Pigeon 1969). For interpreting the strength from the PLST on irregular lumps, the shape, size and orientation effects of granite and other rocks on PLST have been experimentally investigated (Diernat and Duffaut, 1966; Duffaut, 1968; Duffaut and Maury, 1970; Brook, 1985). In addition, irregular lumps have also been employed for studying rock weathering (e. g. Fookes et al., 1971). For those samples of more highly weathered or jointed rocks, which can be crumbled easily, are very difficult to prepare into rock cores or other regular-shaped

samples. In such cases, irregular lumps must be directly used for the PLST.

However, results from irregular lumps suffer more scattering than those from rock cores. Though the scattering can be compensated to certain extent by testing a large number of lumps (the test is very quick) together with using some empirical formulas to correct the size and shape effects (Brook, 1985), the stress state and the failure mechanism of irregular lumps under the PLST is not well understood. The only experimental investigation of stress field within irregular lumps is photoelastic experiments by Hiramatsu and Oka (1966) which showed that the stress states in the vicinity of the line joining the two applied point loads on a sphere, a cube, a rectangular prism are roughly the same. This experimental stress analysis is considered to have provided a very important experimental basis for testing irregular lumps under the PLST, but so far there exists no exact theoretical analysis for it. The only theoretical approximation is considered by Hiramatsu and Oka (1966) by assuming that irregular lumps can be modeled by spheres under the PLST.

Therefore, this chapter investigates the stress distribution within irregular lumps under the PLST. Since all of the failure surfaces of irregular lumps under the PLST pass through or nearly pass through the line joining the two applied point loads, our investigation will focus on the stress distribution along this line. To avoid the insurmountable difficulty in mathematics in analyzing stress distribution within irregular lumps with arbitrary shapes, we analyze and compare the stress distributions in isotropic spheres and cylinders under the axial and diametral PLST (see Fig. 2-1). Considering the difference in the shapes of spheres and cylinders under the axial and diametral PLST, the comparison should provide insight into the stress distribution along the line joining the two point loads in irregular lumps under the PLST. The isotropic

limit of our analytic solution obtained in Chapter 2 for spherically isotropic spheres under the diametral PLST can be used to analyze the stress field in isotropic spheres, while the analytic solutions obtained in Chapters 3 and 4 can be used to analyze the stress distribution in cylinders under the axial and diametral PLST respectively. Note that all of these solutions have considered the Hertz contact problem between the surfaces of specimens and the steel cones through which the point loads are applied.

## 5.2 Isotropic Spheres Under the Diametral PLST

The boundary conditions for a sphere of radius  $R$  under the diametral PLST are

$$\sigma_{rr} = \begin{cases} -p(\theta) & \text{for } 0 \leq \theta \leq \theta_0 \quad \text{and} \quad \pi - \theta_0 \leq \theta \leq \pi \\ 0 & \text{for } \theta_0 < \theta < \pi - \theta_0 \end{cases} \quad (5.1)$$

where

$$p(\theta) = \frac{3F}{2\pi R_0^3} \sqrt{R^2 \cos^2 \theta - (R^2 - R_0^2)} \quad (5.2)$$

$$\sigma_{r\phi} = \sigma_{r\theta} = 0 \quad (5.3)$$

on  $r = R$ , where  $R_0$  is the radius of the contact circular area and has been obtained in (2.70) of Chapter 2, and  $F$  is the magnitude of the applied point force.

The exact analytic solution for a spherically isotropic sphere under the diametral PLST has been obtained in Chapter 2. In particular, the tangential stress  $\sigma_{\theta\theta}(r, \theta)$  and the radial stress  $\sigma_{rr}(r, \theta)$  are

$$\begin{aligned}
\sigma_{\theta\theta} = & \sum_m \{ [L_{2m} \rho^{\mu_{2m,1}-1} [2A_{12} m(2m+1) \Gamma_{2m,1} + (A_{13} \mu_{2m,1} + 2A_{12} + 2A_{66}) \Lambda_{2m,1}] \\
& + [2A_{12} m(2m+1) \Gamma_{2m,2} + (A_{13} \mu_{2m,2} + 2A_{12} + 2A_{66}) \Lambda_{2m,2}] \rho^{\mu_{2m,2}-1} ] P_{2m}(\cos\theta) \\
& - 2A_{66} [\rho^{\mu_{2m,1}-1} \Gamma_{2m,1} L_{2m} + \rho^{\mu_{2m,2}-1} \Gamma_{2m,2}] \frac{\partial^2 P_{2m}(\cos\theta)}{\partial \theta^2} \} \times \frac{E_{2m}}{J_{2m}} \\
& + \sum_n \rho^{2n-1} \{ P_{2n}(\cos\theta) [\Omega_1(1, K_{2n}) \cos(y_{2n} \ln \rho) + \Omega_1(-K_{2n}, 1) \sin(y_{2n} \ln \rho)] \\
& - \frac{\partial^2 P_{2n}(\cos\theta)}{\partial \theta^2} [\Omega_2(1, K_{2n}) \cos(y_{2n} \ln \rho) + \Omega_2(-K_{2n}, 1) \sin(y_{2n} \ln \rho)] \} \times \frac{E_{2n}}{H_{2n}}
\end{aligned} \tag{5.4}$$

where the functions  $\Gamma_{mi}$ ,  $\Lambda_{mi}$ ,  $\Omega_1(R_n, I_n)$  and  $\Omega_2(R_n, I_n)$  and constants  $L_{2m}, J_{2m}, H_{2n}$  and  $K_{2n}$  are defined in Chapter 2, and  $E_{2n}$  can be obtained from (2.73) of Chapter 2. The expression for  $\sigma_r(r, \theta)$  can be obtained from (5.4) by replacing “ $A_{12}, (2A_{66}), A_{13}$ ” by “ $A_{13}, 0, A_{33}$ ” respectively.

As mentioned in Chapter 2, for isotropic case the coefficients for spherically isotropic material take the values

$$E' = E, \quad \bar{\nu} = \nu' = \nu, \quad G' = \frac{E}{2(1 + \nu)} \tag{5.5}$$

Substitution of (5.5) and (2.73) into (2.63) to (2.64), we derive the analytic solution for isotropic spheres under the diametral PLST.

### 5.3 Solid Circular Cylinders Under the Axial PLST

The boundary conditions for a circular cylinder of diameter  $2R$  and height  $2h$  under the axial PLST can be formulated as:

$$\sigma_z = \begin{cases} -p & \text{for } 0 \leq r \leq r_0 \\ 0 & \text{for } r_0 < r < R \end{cases} \tag{5.6}$$

$$\sigma_{rz} = 0 \quad (5.7)$$

on two end surfaces  $z = \pm h$ ; and

$$\sigma_{rr} = \sigma_{\theta\theta} = 0 \quad (5.8)$$

on the curved surface  $r = R$ , where

$$p = \frac{F}{\pi r_0^2} \quad (5.9)$$

where  $r_0$  is the radius of the circular contact area obtained in (3.11) of Chapter 3, and  $F$  is the magnitude of the applied point force.

The exact analytic solution for a finite isotropic cylinder under a pair of axial point loads has been obtained in Chapter 3. The details of the method of solution will not be repeated here, instead for the sake of completeness, we quote the following formulas for the axial stress  $\sigma_z(r, \theta, z)$  and hoop stress  $\sigma_{\theta\theta}(r, \theta, z)$  within the cylinder:

$$\begin{aligned} \sigma_z = & \sum_{n=1}^{\infty} \frac{E_n \cos(n\pi\eta)}{\Delta_n} \{ [\beta_n I_0(\beta_n) - 2I_1(\beta_n)] I_0(\beta_n \rho) - \beta_n \rho I_1(\beta_n) I_1(\beta_n \rho) \} \\ & + \sum_{s=1}^{\infty} \frac{F_s J_0(\lambda_s \rho)}{\Omega_s} [(\gamma_s \cosh \gamma_s + \sinh \gamma_s) \cosh(\gamma_s \eta) - \gamma_s \eta \sinh \gamma_s \sinh(\gamma_s \eta)] \end{aligned} \quad (5.10)$$

$$\begin{aligned} \sigma_{\theta\theta} = & \sum_{n=1}^{\infty} \frac{E_n \cos(n\pi\eta)}{\Delta_n} \{ (1-2\nu) I_1(\beta_n) I_0(\beta_n \rho) + [2(\nu-1) I_1(\beta_n) - \beta_n I_0(\beta_n)] I_1(\beta_n \rho) / (\beta_n \rho) \} \\ & + \sum_{s=1}^{\infty} \frac{F_s}{\Omega_s} \{ 2\nu \sinh \gamma_s \cosh(\gamma_s \eta) J_0(\lambda_s \rho) \\ & + \frac{J_1(\lambda_s \rho)}{\lambda_s \rho} [ [(1-2\nu) \sinh \gamma_s - \gamma_s \cosh \gamma_s] \cosh(\gamma_s \eta) + \gamma_s \eta \sinh \gamma_s \sinh(\gamma_s \eta) ] \} \end{aligned} \quad (5.11)$$

where  $E_n, F_s, \Delta_n$  and  $\Omega_s$  have been obtained in Chapter 3; and  $\beta_n$  and  $\gamma_s$  are defined in Section 3.4 of Chapter 3.

#### 5.4 Solid Circular Cylinders Under the Diametral PLST

The boundary conditions for a cylinder of diameter  $2R$  and length  $2L$  under the diametral PLST are

$$\sigma_z = 0, \quad \sigma_r = 0, \quad \sigma_{\theta} = 0 \quad (5.12)$$

on two end surfaces  $z = \pm h$ ; and

$$\sigma_z = 0, \quad \sigma_{\theta} = 0, \quad (5.13)$$

$$\sigma_r(R, \theta, z) = \begin{cases} -\frac{3F}{2\pi ab} \left(1 - \frac{R^2 \theta^2}{a^2} - \frac{z^2}{b^2}\right)^{1/2} & \text{for } |z| \leq b, \text{ and } |\theta| \leq \frac{a}{R} \left(1 - \frac{z^2}{b^2}\right)^{1/2} \text{ or } |\pi - \theta| \leq \frac{a}{R} \left(1 - \frac{z^2}{b^2}\right)^{1/2} \\ 0 & \text{for } |z| > b, \text{ and } |\theta| > \frac{a}{R} \left(1 - \frac{z^2}{b^2}\right)^{1/2} \text{ or } |\pi - \theta| > \frac{a}{R} \left(1 - \frac{z^2}{b^2}\right)^{1/2} \end{cases} \quad (5.14)$$

on the curved surface  $r=R$ . In (5.14),  $a$  and  $b$ , the half length of major and minor axes of the elliptical contact area, are derived in (4.10) of Chapter 4, and  $F$  is the magnitude of the applied point force.

We have derived the analytic solution for finite solid circular cylinders under the diametral PLST in Chapter 4. Again, without going into the details, we just quote the following formulae for the normal stresses  $\sigma_r(r, \theta, z)$ ,  $\sigma_{\theta}(r, \theta, z)$ , and  $\sigma_z(r, \theta, z)$  as

$$\begin{aligned} \sigma_r = & (2\nu - 1)C_0 + \sum_{n=0}^{\infty} \left\{ -2n(2n-1)(H_n + E_n)r^{2n-2} + \sum_{m=1}^{\infty} \left[ A_m [2M_m(\eta_m r) - \frac{1}{\eta_m^2} \frac{\partial}{\partial z} \left( r \frac{\partial A_m(\eta_m r)}{\partial r} \right)] \right. \right. \\ & \left. \left. - \frac{B_m}{\eta_m^2} \frac{\partial I_n(\eta_m r)}{\partial z} - \frac{2nE_m}{\eta_m^2} \frac{\partial}{\partial z} \left( \frac{I_n(\eta_m r)}{r} \right) \right] \cos(\eta_m z) + \sum_{m=1}^{\infty} \left\{ [C_m + (2\nu + 1)D_m] \cosh(\zeta_m z) + D_m \gamma_m z \sinh(\zeta_m z) \right\} V_n(\gamma_m r) \right. \\ & \left. + [(C_m + D_m) \cosh(\zeta_m z) + D_m \gamma_m z \sinh(\zeta_m z)] \left[ \frac{1}{\gamma_m^2 r} \frac{\partial J_n(\gamma_m r)}{\partial z} - \frac{4n}{\gamma_m^2 r^2} J_n(\gamma_m r) \right] \right\} \cos(2n\theta) \end{aligned} \quad (5.15)$$

$$\begin{aligned}
\sigma_{\theta} = & (2\nu-1)C_0 + \nu A_0 + \sum_{n=0}^{\infty} \{2n(2n-1)(H_{0n} + E_{0n})r^{2n-2} + \sum_{m=1}^{\infty} \{A_m[2\nu I_{2n}(\eta_m r) - \frac{1}{\eta_m^2} \frac{1}{r} \frac{\partial}{\partial r} (r \frac{\partial I_{2n}(\eta_m r)}{\partial r}) + \frac{4n^2}{\eta_m^2 r} \frac{\partial I_{2n}(\eta_m r)}{\partial r}] \\
& \frac{B_m}{\eta_m^2} [\frac{1}{r} \frac{\partial I_{2n}(\eta_m r)}{\partial r} - \frac{4n^2}{r^2} I_{2n}(\eta_m r)] + \frac{2nE_m}{\eta_m^2} \frac{\partial}{\partial r} (\frac{I_{2n}(\eta_m r)}{r})\} \cos(\eta_m z) + \sum_{s=1}^{\infty} \{2\nu D_s \cosh(\gamma_s z) J_{2n}(\gamma_s r) \\
& - [(C_s + D_s) \cosh(\gamma_s z) + D_s \gamma_s z \sinh(\gamma_s z)] [\frac{1}{\gamma_s^2 r} \frac{\partial J_{2n}(\gamma_s r)}{\partial r} - \frac{4n^2}{\gamma_s^2 r^2} J_{2n}(\gamma_s r)]\} \cos(2n\theta)
\end{aligned} \tag{5.16}$$

$$\begin{aligned}
\sigma_z = & 2(2-\nu)C_0 + (1-\nu)A_0 + \sum_{n=0}^{\infty} \{ \sum_{m=1}^{\infty} \{A_m[2(2-\nu)I_{2n}(\eta_m r) + r \frac{\partial I_{2n}(\eta_m r)}{\partial r}] + B_m I_{2n}(\eta_m r)\} \cos(\eta_m z) \\
& - \sum_{s=1}^{\infty} [(C_s + (2\nu-1)D_s) \cosh(\gamma_s z) + D_s \gamma_s z \sinh(\gamma_s z)] J_{2n}(\gamma_s r) \} \cos(2n\theta)
\end{aligned} \tag{5.17}$$

where  $\eta_m$  and  $\gamma_s$  are defined in Section 4.4 of Chapter 4, the governing equations for  $A_0, C_0, E_{0n}, H_{0n}, A_{mn}, B_{mn}, C_{sn}, D_{sn}$  and  $E_{mn}$  are given in Section 4.6 of Chapter 4.

## 5.5 Numerical Comparison of Stress Distribution Within Spheres and Cylinders

As mentioned before, the stress distribution along the line joining the two point loads within a specimen is very important to the PLST, our discussion will focus only on analyzing and comparing the stress distribution along the lines joining the two point loads within isotropic spheres and cylinders under the PLST. It should be noted that there is no shear stress along the lines within specimens under the axial and diametral PLST. Thus, we only present the numerical results for the normal stresses along these lines. Since lots of experiments (ISRM, 1985) indicate that the Point Load Strength Index (PLSI) should be comparable same for a standard test, regardless of whether the specimen is in shape of sphere, cylinder or irregular lump and whether the two point



loads are applied axially or diametrically. Our objective of this chapter is to compare and analyze the stress distribution along these lines within spheres and cylinders of standard size under the axial and diametral PLST, so as to provide a theoretical basis for testing irregular lumps under the PLST.

In addition, a series of PLST experiments have also been done on a kind of rock-like plaster material, with the specimens made in standard shape and size of sphere and cylinder. More specifically, 18 spherical and cylindrical specimens with the diameter of 50, 60 and 75mm are made for the axial and diametral PLST, at least two tests are done for specimens with the same size (note that no test for the diametral PLST on cylinders with diameter 75mm). All dimensions of specimens are set according to the standard test suggested by ISRM (1985) and by Broch and Franklin(1972). For the axial PLST, the length/diameter ratio of a cylindrical specimen is 1.1, while for the standard diametral PLST, the length/diameter ratio of a cylindrical specimen is 1.4 (Broch and Franklin, 1972). The mean magnitude of the point force at failure for each set of specimens together with the elastic properties of the material (such as Poisson's ratio  $\nu = 0.25$  and the Young's modulus  $E=17.5\text{GPa}$ ) are substituted into the corresponding analytic solutions. All stresses are normalized with the point load strength index, which is defined as

$$I_p = \frac{F}{D^2} \quad (5-18)$$

where  $F$  is the applied load at failure and  $D$  is the distance between the two point loads.

The numerical results for the tensile and compressive stress within the specimens shown in Fig. 5-1 to Fig. 5-4 are the predictions by our solutions. Since the maximum tensile stresses are dominated by the hoop stresses in cylinders under the diametral

PLST, we only plot the hoop stresses in Fig. 5-1 to Fig. 5-3.

Figure 5-1 plots both the normalized tensile stress  $\sigma_t D^2 / F$  and compressive stress  $\sigma_c D^2 / F$  along the line joining the center of the specimen (either spherical or cylindrical) and one of the point loads acting on the surface of the specimen under the axial and diametral PLST with  $D=50\text{mm}$ . It is obviously that both of the tensile and compressive stress distributions along these lines are indeed roughly the same, both in terms of pattern and magnitude, if the stresses are normalized with respect to the PLSI.

Figures 5-2 and 5-3 plot both the normalized tensile stresses  $\sigma_t D^2 / F$  and compressive stresses  $\sigma_c D^2 / F$  along the line joining the center of specimen and one of the point loads acting on the surface of the specimen under the axial and diametral PLST for spheres and cylinders with different diameters 60 and 75mm. Both of the tensile and compressive stress distributions along these lines are roughly the same for different sizes, but the magnitudes of the normalized stresses, especially the maximum tensile stresses, are different. For spheres and cylinders with  $D=50\text{mm}$ , the maximum tensile stresses are 14.35, 12.80 and 12.29MPa; with  $D=60\text{mm}$  the corresponding maximum tensile stresses are 15.52, 15.17 and 15.30MPa; and with  $D=75\text{mm}$  the corresponding maximum tensile stresses are 18.03 and 17.50MPa. It seems that the normalized maximum tensile stress is a constant for a specimen with fixed size, no matter whatever the shape of the specimen is. Figure 5-4 plots the mean values  $\sigma_m D^2 / F$  of the maximum tensile stresses versus different diameter  $D$ . The coefficient of correlation is up to 0.996. Consequently, once the PLSI is calculated, the line shown in Fig. 5-4 can be used to predict the maximum tensile stress in irregular lumps and thus to further interpret the strength of rocks.

However, our experimental data are limited, thus more experiments and theoretical analysis are needed to make our conclusion more convincing.

## **5.6 Conclusion**

In this chapter, we have compared the stress distributions along the line joining the two point loads within isotropic spheres and cylinders under the diametral PLST and isotropic cylinders under the axial PLST. It seems that the ratio of the maximum tensile stress and the Point Load Strength Index (PLSI) is roughly a constant for a specimen no matter whatever shape of the specimen is. Thus, a theoretical basis for the PLST on irregular lumps has been formulated.

## Chapter 6

# EXACT STRESS ANALYSIS OF FINITE SOLID CIRCULAR CYLINDERS SUBJECTED TO ARBITRARY SURFACE LOAD

### 6.1 Introduction

Solid circular cylinders are the most commonly used specimens in various standard tests in engineering, such as the uniaxial compressive strength test, the triaxial compressive strength test, the Brazilian test, the double punch test, and the point load strength test. In fact, the elastic stress analysis of solid circular cylinders is one of the most fundamental problems in theoretical elasticity and has a rich history in solid mechanics.

Pochhammer (1876) appears to be the first to propose a general analytic solution for an infinite circular cylinder subjected to arbitrary surface loads, the same solution was also derived independently by Chree (1889). A typical example of axisymmetric problem for infinite cylinders is the problem of applying band pressure on the curved surface (Timoshenko and Goodier, 1982; Williams, 1996). If the cylinder is semi-infinite in length, the problem has been considered by Horvay and Mirabal (1958).

For finite solid cylinders subjected to arbitrary loads, Dougall (1914) employed three displacement functions and proposed an approximate approach for the stress analysis. For axisymmetric deformations of finite cylinders, Filon (1902) presented an analytic approach for the stress analysis, and particularly provided the first analytic solution considering the effect of friction between the loading platen and the end surfaces of a solid cylinder on the nonuniform stress distribution within the cylinder

undercompression. Employing Love's (1944) stress function, Saito (1952, 1954) also proposed a general solution form for axisymmetric stress analysis, in terms of the Bessel and modified Bessel functions of the first kind of zero and first orders for  $r$ -dependency, and in terms of trigonometric and hyperbolic functions in  $z$ -dependency. Using a similar technique of series expansion, Ogaki and Nakajima (1983) proposed appropriate forms for two stress functions and analyzed the stress field in a solid circular cylinder subjected to parabolically distributed loads on part of the end surfaces. By using Saito's (1952) approach, Watanabe (1996) derived an analytic solution for axisymmetric finite cylinders under the uniaxial and confined compression tests, in which the radial displacement at the ends is partially constrained. Actually, the problem of compression test on solid finite cylinders with end friction has been the subject of a number of theoretical studies (e.g. Kimura, 1931; Pickett, 1944; Edelman, 1948; Balla, 1960a, 1960b; Brady, 1971; Peng, 1971; Al-chalabi and Huang, 1974; Al-chalabi *et al.*, 1974; Chau, 1997, 1998b). This analysis has been found useful in the interpretation of the strength of rock in the uniaxial and triaxial tests (Kotte *et al.*, 1969). For problems with displacements applied on the end surfaces and with zero traction on the curved surface, Robert and Keer (1987a-b) considered the stress singularities at the flat ends of the cylinder. Wei *et al.* (1999) used the displacement function approach and presented an analytic solution for the axial point load strength test (PLST), which provides an improvement over the approximation by Wijk (1978). One particular type of axisymmetric problems of finite solid cylinder that has been solved analytically is the torsion problem. For example, the twisting of a finite cylinder by a pair of identical annular stamps attached to its ends was considered by Hasegawa (1984), and the

twisting of a finite solid cylinder with the free curved surface and fixed base by a rigid die attached to the top surface was considered by Gladwell and Lamczyk (1990). Except for the study by Dougall (1914), all of these analyses are only restricted to axisymmetric problems of finite elastic cylinders; while Dougall's (1914) solution is only an approximation. In fact, only the axisymmetric problems of solid cylinders are considered in classical textbooks in elasticity (e.g. Timoshenko and Goodier, 1982; Love, 1944), no general treatment on non-axisymmetric problems of solid cylinders is available.

For non-axisymmetric deformations of finite solid cylinders, Wijk (1980) derived a simple approximation for the tensile stress at the center of the cylinder subjected to the diametral PLST, in which two point forces are diametrically applied on the curved surface of the cylinder. Chau (1998a) introduced two displacement functions and derived a solution for a finite circular cylinder under the action of two diametral indentors and with constrained shear displacements on the two end surfaces. This solution is an approximation for cylinders under the diametral PLST. To model the actual traction free end boundaries (which is the realistic boundary for the PLST), Chau and Wei (1999b) proposed more general solution forms for the two displacement functions such that all boundary conditions are satisfied exactly. However, there is no closed-form solution for finite elastic circular cylinders under arbitrary surface load.

Therefore, this paper presents a general analytic solution for finite elastic isotropic cylinders under arbitrary surface loads. The method of solution is generalized from those used by Wei et al. (1999) and Chau and Wei (1999b). Complete solution forms for the displacement functions are introduced here such that any traction problems of

finite solid isotropic cylinders can be solved exactly. The tractions on the curved surface are expanded into double Fourier series expansion while the tractions on the end surfaces are expanded into Fourier-Bessel series expansion, in order to match the internal stress field resulting from the general solution forms of the displacement functions. The solutions by Filon (1902), Saito (1952,1954), Watanabe (1996), Chau (1998a), Chau and Wei (1999) and Wei et al. (1999) can be considered as a special case of the present solution; that is, they can be re-derived independently using the present unified approach.

Although the present paper considers only traction boundary value problems for cylinders, it is straightforward to generalize the present approach to problems with mixed boundary conditions (including both traction and displacement boundary conditions).

## 6.2 Governing Equations

Consider a homogeneous isotropic and elastic cylinder of radius  $R$  (or diameter  $D$ ) and length  $2L$  in a cylindrical co-ordinate system as shown in Fig. 6-1. The stress and strain tensors are related by the following Hook's law

$$\sigma_{\alpha\beta} = 2G\varepsilon_{\alpha\beta} + \lambda\varepsilon_{\gamma\gamma}\delta_{\alpha\beta} \quad (6.1)$$

where  $\alpha, \beta, \gamma = r, \theta, z$ ;  $G$  and  $\lambda$  are the Lamé constants ( $G$  is normally referred as the shear modulus); and the repeated indices in (6.1) imply summation. The Cauchy stress tensor and strain tensor are denoted by  $\sigma$  and  $\varepsilon$  respectively. The strain tensor is related to the displacements ( $\mathbf{u} = u_r\mathbf{e}_r + u_\theta\mathbf{e}_\theta + u_z\mathbf{e}_z$ ) by

$$\varepsilon = \frac{1}{2}[(\nabla\mathbf{u})^T + \nabla\mathbf{u}] \quad (6.2)$$

where

$$\nabla\mathbf{u} = \mathbf{e}_r \frac{\partial\mathbf{u}}{\partial r} + \mathbf{e}_\theta \frac{1}{r} \frac{\partial\mathbf{u}}{\partial\theta} + \mathbf{e}_z \frac{\partial\mathbf{u}}{\partial z} \quad (6.3)$$

In terms of cylindrical coordinates, the physical components of the strain tensor given in (6.2) are

$$\begin{aligned} \varepsilon_z &= \frac{\partial u_z}{\partial z}, \quad \varepsilon_r = \frac{\partial u_r}{\partial r}, \quad \varepsilon_{\theta\theta} = \frac{u_r}{r} + \frac{1}{r} \frac{\partial u_\theta}{\partial\theta}, \quad \varepsilon_{\theta r} = \frac{1}{2} \left( \frac{\partial u_\theta}{\partial r} + \frac{1}{r} \frac{\partial u_r}{\partial\theta} - \frac{u_\theta}{r} \right), \\ \varepsilon_{\theta z} &= \frac{1}{2} \left( \frac{1}{r} \frac{\partial u_z}{\partial\theta} + \frac{\partial u_\theta}{\partial z} \right), \quad \varepsilon_{rz} = \frac{1}{2} \left( \frac{\partial u_r}{\partial z} + \frac{\partial u_z}{\partial r} \right). \end{aligned} \quad (6.4)$$

In the absence of body force, the equations of equilibrium,  $\nabla \cdot \sigma = \mathbf{0}$ , in terms of displacements are (e.g., Malvern, 1969):

$$(\lambda + 2G) \frac{\partial e}{\partial r} + \frac{2G}{r} \frac{\partial \Omega_{\theta\theta}}{\partial\theta} + 2G \frac{\partial \Omega_{rz}}{\partial z} = 0 \quad (6.5)$$



$$(\lambda + 2G) \frac{1}{r} \frac{\partial e}{\partial \theta} + 2G \frac{\partial \Omega_{\theta}}{\partial z} + 2G \frac{\partial \Omega_r}{\partial r} = 0 \quad (6.6)$$

$$(\lambda + 2G) \frac{\partial e}{\partial z} + \frac{2G}{r} \frac{\partial}{\partial r} (r \Omega_r) + \frac{2G}{r} \frac{\partial \Omega_{\theta}}{\partial \theta} = 0 \quad (6.7)$$

where  $\Omega = [(\nabla \mathbf{u})^T - \nabla \mathbf{u}] / 2$  and  $e = \nabla \cdot \mathbf{u}$  are the spin tensor and the volumetric strain respectively.

When the cylinder is subjected to arbitrary stresses on the surfaces, the general boundary conditions are

$$\sigma_r = f_r(z, \theta), \quad \sigma_z = f_z(z, \theta), \quad \sigma_{\theta} = f_{\theta}(z, \theta) \text{ for } r=R. \quad (6.8)$$

$$\sigma_r = f_r(r, \theta), \quad \sigma_z = f_z(r, \theta), \quad \sigma_{\theta} = f_{\theta}(r, \theta) \text{ for } z=+L. \quad (6.9)$$

$$\sigma_r = f_r(r, \theta), \quad \sigma_z = f_z(r, \theta), \quad \sigma_{\theta} = f_{\theta}(r, \theta) \text{ for } z=-L. \quad (6.10)$$

where  $f_i$  ( $i = 1, 2, 3; j = r, z, \theta$ ) are the prescribed tractions on the curved surface and on the end surfaces of the cylinder. The first subscript  $i=1, 2, 3$  indicates the curved, top and bottom end surfaces respectively; the second subscript  $j$  ( $=r, \theta, z$ ) indicates the direction along which the traction acts. To simplify the later discussion, these boundary conditions are called BC $ij$  ( $i, j=1, 2, 3$ ) as defined in Table 6-1. For example, the first of (6.8) is denoted by BC11.

### 6.3 Method of Solution

The main objective of the present paper is to obtain the exact solution satisfying both the equations of equilibrium (6.5)-(6.7) and the boundary conditions (6.8)-(6.10). Similar to the analyses by Chau (1998a) and by Chau and Wei (1999), two displacement

functions  $\Phi$  and  $\Psi$  are introduced in such a way to uncouple the governing equations (6.5)-(6.7),

$$u_r = \frac{\partial^2 \Phi}{\partial r \partial z} + \frac{1}{r} \frac{\partial \Psi}{\partial \theta}, \quad u_\theta = \frac{1}{r} \frac{\partial^2 \Phi}{\partial \theta \partial z} - \frac{\partial \Psi}{\partial r}, \quad u_z = -[2(1-\nu) \nabla_1 \Phi + (1-2\nu) \frac{\partial^2 \Phi}{\partial z^2}] \quad (6.11)$$

where

$$\nabla_1 = \frac{1}{r} \frac{\partial}{\partial r} \left( r \frac{\partial}{\partial r} \right) + \frac{1}{r^2} \frac{\partial^2}{\partial \theta^2} \quad (6.12)$$

Substitution of (6.11) into (6.5)-(6.7) yields two uncoupled governing equations of the displacement functions  $\Phi$  and  $\Psi$ :

$$\nabla^4 \Phi = \nabla^2 \nabla^2 \Phi = 0, \quad \nabla^2 \Psi = 0 \quad (6.13)$$

where  $\nabla^2$  is the Laplacian operator, or  $\nabla^2 = \nabla_1 + \partial^2 / \partial z^2$ . That is,  $\Phi$  and  $\Psi$  satisfy the biharmonic and harmonic equations respectively.

In terms of these two displacement functions, the physical components of the stress tensor can be obtained by substituting (6.11) into (6.4) and (6.1) as,

$$\sigma_r = -2\nu G \nabla^2 \frac{\partial \Phi}{\partial z} + 2G \left[ \frac{\partial^3 \Phi}{\partial z \partial r^2} + \frac{\partial}{\partial r} \left( \frac{1}{r} \frac{\partial \Psi}{\partial \theta} \right) \right] \quad (6.14)$$

$$\sigma_\theta = -2\nu G \nabla^2 \frac{\partial \Phi}{\partial z} + 2G \left[ \frac{1}{r} \frac{\partial^2 \Phi}{\partial z \partial r} + \frac{1}{r^2} \frac{\partial^3 \Phi}{\partial \theta^2 \partial z} - \frac{\partial}{\partial r} \left( \frac{1}{r} \frac{\partial \Psi}{\partial \theta} \right) \right] \quad (6.15)$$

$$\sigma_z = -2G \left[ (2-\nu) \frac{\partial}{\partial z} \nabla^2 - \frac{\partial^3}{\partial z^3} \right] \Phi \quad (6.16)$$

$$\sigma_{rz} = 2G \left[ -(1-\nu) \frac{\partial}{\partial r} \nabla_1 + \nu \frac{\partial^3}{\partial r \partial z^2} \right] \Phi + \frac{G}{r} \frac{\partial^2 \Psi}{\partial \theta \partial z} \quad (6.17)$$

$$\sigma_{\theta z} = 2G \left[ -(1-\nu) \frac{1}{r} \frac{\partial}{\partial \theta} \nabla_1 + \nu \frac{1}{r} \frac{\partial^3}{\partial \theta \partial z^2} \right] \Phi - G \frac{\partial^2 \Psi}{\partial r \partial z} \quad (6.18)$$

$$\sigma_{\theta\theta} = 2G \left[ \frac{\partial}{\partial r} \left( \frac{1}{r} \frac{\partial^2 \Phi}{\partial \theta \partial z} \right) + \frac{1}{2} \left( \frac{1}{r} \frac{\partial \Psi}{\partial r} + \frac{1}{r^2} \frac{\partial^2 \Psi}{\partial \theta^2} - \frac{\partial^2 \Psi}{\partial r^2} \right) \right] \quad (6.19)$$

#### 6.4 Series Expressions for the Two Displacement Functions

The most difficult step to solve the problem is to find the appropriate and complete solution forms for the two displacement potentials  $\Phi$  and  $\Psi$ , which should satisfy both of the governing equation (6.13), and the boundary conditions (6.8)-(6.10) for any arbitrary applied traction  $f_i$ .

The method of separation of variables is employed here to solve (6.13). In particular, we assume the series solution for  $\Psi$  as

$$\Psi(r, z, \theta) = \sum_{n=0}^{\infty} [\psi_1(r, z) \cos(\omega_n \theta) + \psi_2(r, z) \sin(\omega_n \theta)] \quad (6.20)$$

where  $\omega_n$  is defined as  $\omega_n = 2n\pi / T$ , and  $T$  is the periodicity of  $\Psi$  in  $\theta$ , which should match the periodicity of the external applied traction in  $\theta$ . Substitution of (6.20) into (6.13) leads to the governing equation for function  $\psi_i(r, z)$ ,  $i=1, 2$ ,

$$\frac{\partial^2 \psi_i}{\partial r^2} + \frac{1}{r} \frac{\partial \psi_i}{\partial r} + \frac{\partial^2 \psi_i}{\partial z^2} - \frac{\omega_n^2}{r^2} \psi_i = 0 \quad (6.21)$$

The general solution of (6.21) is

$$\psi_i(r, z) = [AI_{\omega_n}(\eta r) + BK_{\omega_n}(\eta r)] \frac{\sin(\eta z)}{\cos(\eta z)} + [CJ_{\omega_n}(\gamma r) + DY_{\omega_n}(\gamma r)] \frac{\sinh(\gamma z)}{\cosh(\gamma z)} \quad (6.22)$$

where  $J_{\omega_n}(\gamma r)$ ,  $Y_{\omega_n}(\gamma r)$ ,  $I_{\omega_n}(\eta r)$  and  $K_{\omega_n}(\eta r)$  are the Bessel functions and modified Bessel functions of the first kind and second kind with fractional order  $\omega_n$ ; and  $A$ ,  $B$ ,  $C$ ,  $D$ ,  $\eta$  and  $\gamma$  are constants to be determined. Because the stress field at the center of the finite cylinder must be finite, all terms that relate to  $Y_{\omega_n}(\gamma r)$  and  $K_{\omega_n}(\eta r)$  must be discarded. Therefore, the general expression for  $\Psi$  is assumed as:

$$\Psi = -\frac{1}{2G} \left\{ E_{\infty} r^3 + \sum_{n=0}^{\infty} [E_{0n}^{(l)} r^{\alpha_n} + \sum_{m=1}^{\infty} \frac{E_{mn}^{(k)}}{\eta_m^2} I_{\alpha_n}(\eta_m r) \frac{\cos(\eta_m z)}{\sin(\eta_m z)} + \sum_{s=1}^{\infty} \frac{F_{sn}^{(k)}}{\gamma_s^2} J_{\alpha_n}(\gamma_s r) \frac{\cosh(\gamma_s z)}{\sinh(\gamma_s z)}] \frac{\sin(\omega_n \theta)}{\cos(\omega_n \theta)} \right\} \quad (6.23)$$

where  $G$  is the shear modulus,  $\eta_m = m\pi / L$ ,  $\gamma_s = \lambda_s / R$ , and  $\lambda_s$  is the  $s$ -th root of  $J_{\alpha_n}'(x) = 0$ . The characteristics of  $\lambda_s$  will be discussed later.  $E_{0n}^{(l)}, E_{mn}^{(k)}$  and  $F_{sn}^{(k)}$  ( $l=1,2$ ;  $k=1,2,3,4$ ) are unknown constants to be determined by the boundary conditions. The superscript  $(l)$  is from 1 to 2 since the  $\theta$ -dependency can be either sin or cos; and for general case, we should include both  $l=1$  and 2. For the superscript  $(k)$ , we can have 4 combinations for the  $z$ - and  $\theta$ -dependencies; and in general all four combinations are needed for the most general case of applied traction. The corresponding  $z$ - and  $\theta$ -dependencies for each  $k$  and  $l$  are tabulated in Table 6-2. The summation for  $m$  can be used to fit any  $z$ -dependency of applied traction on the curved surface while the summation for  $s$  can take care of any  $r$ -dependency of applied traction on the end surfaces. Note that the term  $\psi_1(r, z) = Er^{\alpha_0}$  is resulted by considering the case of  $\eta = 0$ ; and that the term for  $E_{\infty}$  will lead to constant shear stress field for  $\sigma_{rz}$  only.

To find the general solution for  $\Phi$ , we let  $\nabla^2 \Phi = \bar{\Psi}$  and note that the general solution for  $\bar{\Psi}$  is the same as those for  $\Psi$  given in (6.23). By back substitution of this solution into  $\nabla^2 \Phi = \bar{\Psi}$  and by careful inspection, we propose the following general solution for  $\Phi$ :

$$\begin{aligned}
\Phi = & -\frac{1}{2G} \left\{ A_{\infty} \frac{z^3}{6} + C_{\infty} \frac{z}{2} r^2 \right. \\
& + \sum_{n=0}^{\infty} \left\{ A_{0n}^{(l)} r^{2n} z + \sum_{m=1}^{\infty} \frac{1}{\eta_n^3} \left[ A_{mn}^{(k)} r \frac{\partial I_{*n}(\eta_n r)}{\partial r} + B_{mn}^{(k)} I_{*n}(\eta_n r) \right] \frac{\sin(\eta_n z)}{\cos(\eta_n z)} \right. \\
& \left. + \sum_{s=1}^{\infty} \frac{1}{\gamma_s^3} \left[ C_{sn}^{(k)} \frac{\sinh(\gamma_s z)}{\cosh(\gamma_s z)} + D_{sn}^{(k)} \gamma_s z \frac{\cosh(\gamma_s z)}{\sinh(\gamma_s z)} \right] J_{*n}(\gamma_s r) \right\} \frac{\cos(\omega_n \theta)}{\sin(\omega_n \theta)} \left. \right\}
\end{aligned} \tag{6.24}$$

where  $A_{\infty}, C_{\infty}, A_{0n}^{(l)}, A_{mn}^{(k)}, B_{mn}^{(k)}, C_{sn}^{(k)}$  and  $D_{sn}^{(k)}$  ( $l=1,2; k=1,2,3,4$ ) are unknown coefficients to be determined by the boundary conditions. Each combination of  $l$  and  $k$  corresponds to a particular combination of the upper and lower functions of  $z$  and  $\theta$  given in (6.24). More specifically, the corresponding  $z$ - and  $\theta$ -dependencies for each  $k$  and  $l$  are given in Table 6-2; and in general all combinations of  $k$  and  $l$  are needed for general loading cases. Note that the choices for  $k$  and  $l$  given in Table 2 will lead to  $\sigma_r(r, z, \theta)$  being an even function in  $\theta$  [i.e.  $\cos(\omega_n \theta)$ ] if  $l=1$  and being an odd function [i.e.  $\sin(\omega_n \theta)$ ] if  $l=2$ . In addition, the  $z$ -dependency/ $\theta$ -dependency for  $\sigma_r(r, z, \theta)$  will be even/even, even/odd, odd/even and odd/odd for  $k=1,2,3,4$  respectively. Note that the constants  $A_{\infty}$  and  $C_{\infty}$  will only lead to constant normal stresses. In addition, it is straightforward to show that (6.23) and (6.24) satisfy the governing equations (6.13) identically.

## 6.5 General Expressions for Stresses

Substitution of (6.23) and (6.24) into (6.14)-(6.19) leads to the following general expressions for the stress components:

$$\begin{aligned}
\sigma_{\pi} = & (2\nu-1)C_{\omega} + \nu A_{\omega} + \sum_{m=0}^{\infty} \left\{ -\omega_{\pi}(\omega_{\pi}-1) \left( A_{\omega}^{(m)} \frac{\cos(\omega_{\pi}\theta)}{\sin(\omega_{\pi}\theta)} + E_{\omega}^{(m)} \frac{\cos(\omega_{\pi}\theta)}{-\sin(\omega_{\pi}\theta)} \right) r^{-m-2} \right. \\
& + \left\{ \sum_{n=1}^{\infty} \left\{ A_{\pi}^{(n)} [2\nu I_{\omega_{\pi}}(\eta_n r) - \frac{1}{\eta_n^2} \frac{\partial}{\partial r} (r \frac{\partial I_{\omega_{\pi}}(\eta_n r)}{\partial r})] - \frac{B_{\pi}^{(n)}}{\eta_n^2} \frac{\partial^2 I_{\omega_{\pi}}(\eta_n r)}{\partial r^2} \right\} \cos(\eta_n z) \right. \\
& + \sum_{n=1}^{\infty} \left\{ [(C_{\pi}^{(n)} + D_{\pi}^{(n)}) \frac{\cosh(\gamma, z)}{\sinh(\gamma, z)} + D_{\pi}^{(n)} \gamma, z \frac{\sinh(\gamma, z)}{\cosh(\gamma, z)}] \left[ \frac{1}{\gamma^2 r} \frac{\partial J_{\omega_{\pi}}(\gamma, r)}{\partial r} - \frac{\omega_{\pi}^2}{\gamma^2 r^2} J_{\omega_{\pi}}(\gamma, r) \right] \right. \\
& + [(C_{\pi}^{(n)} + (2\nu+1)D_{\pi}^{(n)}) \frac{\cosh(\gamma, z)}{\sinh(\gamma, z)} + D_{\pi}^{(n)} \gamma, z \frac{\sinh(\gamma, z)}{\cosh(\gamma, z)}] J_{\omega_{\pi}}(\gamma, r) \left. \right\} \frac{\cos(\omega_{\pi}\theta)}{\sin(\omega_{\pi}\theta)} \\
& - \left. \left\{ \sum_{n=1}^{\infty} \frac{E_{\pi}^{(n)} \omega_{\pi}}{\eta_n^2} \frac{\partial}{\partial r} \left( \frac{I_{\omega_{\pi}}(\eta_n r)}{r} \right) \frac{\cos(\eta_n z)}{\sin(\eta_n z)} + \sum_{n=1}^{\infty} \frac{F_{\pi}^{(n)} \omega_{\pi}}{\gamma_n^2} \frac{\partial}{\partial r} \left( \frac{J_{\omega_{\pi}}(\gamma, r)}{r} \right) \frac{\cosh(\gamma, z)}{\sinh(\gamma, z)} \right\} \frac{\cos(\omega_{\pi}\theta)}{-\sin(\omega_{\pi}\theta)} \right\}
\end{aligned} \tag{6.25}$$

$$\begin{aligned}
\sigma_{\omega} = & (2\nu-1)C_{\omega} + \nu A_{\omega} + \sum_{m=0}^{\infty} \left\{ \omega_{\pi}(\omega_{\pi}-1) \left( A_{\omega}^{(m)} \frac{\cos(\omega_{\pi}\theta)}{\sin(\omega_{\pi}\theta)} + E_{\omega}^{(m)} \frac{\cos(\omega_{\pi}\theta)}{-\sin(\omega_{\pi}\theta)} \right) r^{-m-2} \right. \\
& + \left\{ \sum_{n=1}^{\infty} \left\{ A_{\pi}^{(n)} [2\nu I_{\omega_{\pi}}(\eta_n r) - \frac{1}{\eta_n^2 r} \frac{\partial}{\partial r} (r \frac{\partial I_{\omega_{\pi}}(\eta_n r)}{\partial r}) + \frac{\omega_{\pi}^2}{\eta_n^2 r} \frac{\partial I_{\omega_{\pi}}(\eta_n r)}{\partial r}] - \frac{B_{\pi}^{(n)}}{\eta_n^2} \left[ \frac{1}{r} \frac{\partial I_{\omega_{\pi}}(\eta_n r)}{\partial r} - \frac{\omega_{\pi}^2}{r^2} J_{\omega_{\pi}}(\eta_n r) \right] \right\} \frac{\cos(\eta_n z)}{-\sin(\eta_n z)} \right. \\
& + \sum_{n=1}^{\infty} \left\{ 2\nu D_{\pi}^{(n)} J_{\omega_{\pi}}(\gamma, r) \frac{\cosh(\gamma, z)}{\sinh(\gamma, z)} - [(C_{\pi}^{(n)} + D_{\pi}^{(n)}) \frac{\cosh(\gamma, z)}{\sinh(\gamma, z)} + D_{\pi}^{(n)} \gamma, z \frac{\sinh(\gamma, z)}{\cosh(\gamma, z)}] \left[ \frac{1}{\gamma^2 r} \frac{\partial J_{\omega_{\pi}}(\gamma, r)}{\partial r} - \frac{\omega_{\pi}^2}{\gamma^2 r^2} J_{\omega_{\pi}}(\gamma, r) \right] \right\} \frac{\cos(\omega_{\pi}\theta)}{\sin(\omega_{\pi}\theta)} \\
& + \left. \left\{ \sum_{n=1}^{\infty} \frac{E_{\pi}^{(n)} \omega_{\pi}}{\eta_n^2} \frac{\partial}{\partial r} \left( \frac{I_{\omega_{\pi}}(\eta_n r)}{r} \right) \frac{\cos(\eta_n z)}{\sin(\eta_n z)} + \sum_{n=1}^{\infty} \frac{F_{\pi}^{(n)} \omega_{\pi}}{\gamma_n^2} \frac{\partial}{\partial r} \left( \frac{J_{\omega_{\pi}}(\gamma, r)}{r} \right) \frac{\cosh(\gamma, z)}{\sinh(\gamma, z)} \right\} \frac{\cos(\omega_{\pi}\theta)}{-\sin(\omega_{\pi}\theta)} \right\}
\end{aligned} \tag{6.26}$$

$$\begin{aligned}
\sigma_{\pi} = & 2(2-\nu)C_{\omega} + (1-\nu)A_{\omega} + \sum_{m=0}^{\infty} \left\{ \left\{ \sum_{n=1}^{\infty} \left\{ A_{\pi}^{(n)} [2(2-\nu)I_{\omega_{\pi}}(\eta_n r) + r \frac{\partial I_{\omega_{\pi}}(\eta_n r)}{\partial r}] + B_{\pi}^{(n)} I_{\omega_{\pi}}(\eta_n r) \right\} \frac{\cos(\eta_n z)}{-\sin(\eta_n z)} \right. \right. \\
& - \sum_{n=1}^{\infty} \left\{ [(C_{\pi}^{(n)} + (2\nu-1)D_{\pi}^{(n)}) \frac{\cosh(\gamma, z)}{\sinh(\gamma, z)} + D_{\pi}^{(n)} \gamma, z \frac{\sinh(\gamma, z)}{\cosh(\gamma, z)}] J_{\omega_{\pi}}(\gamma, r) \right\} \frac{\cos(\omega_{\pi}\theta)}{\sin(\omega_{\pi}\theta)} \left. \right\}
\end{aligned} \tag{6.27}$$

$$\begin{aligned}
\sigma_z = & 9(1-\nu)E_\infty + \sum_{n=0}^{\infty} \left\{ \left\{ \sum_{m=1}^{\infty} \left\{ \frac{A_m^{(k)}}{\eta_m} \left[ 2(1-\nu) \frac{\partial I_{*n}(\eta_m r)}{\partial r} + \frac{\partial}{\partial r} \left( r \frac{\partial I_{*n}(\eta_m r)}{\partial r} \right) \right] + \frac{B_m^{(k)}}{\eta_m} \frac{\partial I_{*n}(\eta_m r)}{\partial r} \right\} \frac{\sin(\eta_m z)}{\cos(\eta_m z)} \right. \right. \\
& - \sum_{s=1}^{\infty} \frac{1}{\gamma_s} \left[ (C_s^{(k)} + 2\nu D_s^{(k)}) \frac{\sinh(\gamma_s z)}{\cosh(\gamma_s z)} + D_s^{(k)} \gamma_s z \frac{\cosh(\gamma_s z)}{\sinh(\gamma_s z)} \right] \frac{\partial J_{*n}(\gamma_s r)}{\partial r} \left. \frac{\cos(\omega_n \theta)}{\sin(\omega_n \theta)} \right\} \\
& - \left\{ \sum_{m=1}^{\infty} \frac{E_m^{(k)} \omega_n}{2\eta_m r} I_{*n}(\eta_m r) \frac{-\sin(\eta_m z)}{\cos(\eta_m z)} + \sum_{s=1}^{\infty} \frac{F_s^{(k)} \omega_n}{2\gamma_s r} J_{*n}(\gamma_s r) \frac{\sinh(\gamma_s z)}{\cosh(\gamma_s z)} \right\} \frac{\cos(\omega_n \theta)}{-\sin(\omega_n \theta)} \Big\}
\end{aligned} \tag{6.28}$$

$$\begin{aligned}
\sigma_\theta = & \sum_{n=0}^{\infty} \left\{ \left\{ \sum_{m=1}^{\infty} \left\{ \frac{\omega_n A_m^{(k)}}{\eta_m} \left[ 2(1-\nu) \frac{I_{*n}(\eta_m r)}{r} + \frac{\partial I_{*n}(\eta_m r)}{\partial r} \right] + \frac{\omega_n B_m^{(k)}}{\eta_m} \frac{I_{*n}(\eta_m r)}{r} \right\} \frac{\sin(\eta_m z)}{\cos(\eta_m z)} \right. \right. \\
& - \sum_{s=1}^{\infty} \left\{ \frac{\omega_n}{\gamma_s} \left[ (C_s^{(k)} + 2\nu D_s^{(k)}) \frac{\sinh(\gamma_s z)}{\cosh(\gamma_s z)} + D_s^{(k)} \gamma_s z \frac{\cosh(\gamma_s z)}{\sinh(\gamma_s z)} \right] \frac{J_{*n}(\gamma_s r)}{r} \right\} \left. \frac{-\sin(\omega_n \theta)}{\cos(\omega_n \theta)} \right\}
\end{aligned} \tag{6.29}$$

$$\begin{aligned}
& + \left\{ \sum_{m=1}^{\infty} \frac{E_m^{(k)}}{2\eta_m} \frac{\partial I_{*n}(\eta_m r)}{\partial r} \frac{-\sin(\eta_m z)}{\cos(\eta_m z)} + \sum_{s=1}^{\infty} \frac{F_s^{(k)}}{2\gamma_s} \frac{\partial J_{*n}(\gamma_s r)}{\partial r} \frac{\sinh(\gamma_s z)}{\cosh(\gamma_s z)} \right\} \frac{\sin(\omega_n \theta)}{\cos(\omega_n \theta)} \Big\} \\
\sigma_r = & \sum_{n=0}^{\infty} \left\{ -\omega_n (\omega_n - 1) \left( A_{*n}^{(n)} \frac{-\sin(\omega_n \theta)}{\cos(\omega_n \theta)} - E_{*n}^{(n)} \frac{-\sin(\omega_n \theta)}{\cos(\omega_n \theta)} \right) r^{\omega_n - 2} \right. \\
& - \left\{ \sum_{m=1}^{\infty} \left\{ \frac{\omega_n A_m^{(k)}}{\eta_m^2} \frac{\partial^2 I_{*n}(\eta_m r)}{\partial r^2} + \frac{\omega_n B_m^{(k)}}{\eta_m^2} \left[ \frac{1}{r} \frac{\partial I_{*n}(\eta_m r)}{\partial r} - \frac{1}{r^2} I_{*n}(\eta_m r) \right] \right\} \frac{\cos(\eta_m z)}{-\sin(\eta_m z)} \right. \\
& + \sum_{s=1}^{\infty} \left\{ \frac{\omega_n}{\gamma_s^2} \left[ (C_s^{(k)} + D_s^{(k)}) \frac{\cosh(\gamma_s z)}{\sinh(\gamma_s z)} + D_s^{(k)} \gamma_s z \frac{\sinh(\gamma_s z)}{\cosh(\gamma_s z)} \right] \left[ \frac{1}{r} \frac{\partial J_{*n}(\gamma_s r)}{\partial r} - \frac{1}{r^2} J_{*n}(\gamma_s r) \right] \right\} \left. \frac{-\sin(\omega_n \theta)}{\cos(\omega_n \theta)} \right\} \Big\} \\
& - \left\{ \sum_{m=1}^{\infty} \frac{E_m^{(k)}}{2\eta_m^2} \left[ \frac{1}{r} \frac{\partial I_{*n}(\eta_m r)}{\partial r} - \frac{\omega_n^2}{r^2} I_{*n}(\eta_m r) - \frac{\partial^2 I_{*n}(\eta_m r)}{\partial r^2} \right] \frac{\cos(\eta_m z)}{\sin(\eta_m z)} \right. \\
& + \sum_{s=1}^{\infty} \frac{F_s^{(k)}}{2\gamma_s^2} \left[ \frac{1}{r} \frac{\partial J_{*n}(\gamma_s r)}{\partial r} - \frac{\omega_n^2}{r^2} J_{*n}(\gamma_s r) - \frac{\partial^2 J_{*n}(\gamma_s r)}{\partial r^2} \right] \frac{\cosh(\gamma_s z)}{\sinh(\gamma_s z)} \left. \frac{\sin(\omega_n \theta)}{\cos(\omega_n \theta)} \right\} \Big\}
\end{aligned} \tag{6.30}$$

For the sake of completeness, the proper choice of the upper and lower functions in  $z$  and  $\theta$  corresponding to each value of  $k$  and  $l$  are tabulated in Table 6-3. It should be emphasized again that all terms of  $k$  and  $l$  are needed in general.

## 6.6 Determination of the Unknown Coefficients

By using double Fourier expansion technique, all boundary tractions acting on the curved surface of the cylinder given in (6.8) can be expressed as (Brown and Churchill, 1993):

$$\sigma_{\alpha} = \sum_{m=0}^{\infty} \sum_{n=0}^{\infty} \{ \lambda_{mn} [a_{mn}^{(\alpha)} \cos(\eta_m z) \cos(\omega_n \theta) + b_{mn}^{(\alpha)} \sin(\eta_m z) \cos(\omega_n \theta) + c_{mn}^{(\alpha)} \cos(\eta_m z) \sin(\omega_n \theta) + d_{mn}^{(\alpha)} \sin(\eta_m z) \sin(\omega_n \theta)] \} \quad (6.31)$$

where  $\alpha = r, z, \theta$ , and

$$\lambda_{mn} = \begin{cases} 1/4 & \text{for } m = n = 0 \\ 1/2 & \text{for } n = 0, m > 0 \text{ or } m = 0, n > 0 \\ 1 & \text{for } m > 0, n > 0 \end{cases} \quad (6.32)$$

$$a_{mn}^{(\alpha)} = \frac{2}{LT} \int_{-r/2}^{r/2} \int_L^L f_{\alpha}(z, \theta) \cos(\eta_m z) \cos(\omega_n \theta) dz d\theta, \quad b_{mn}^{(\alpha)} = \frac{2}{LT} \int_{-r/2}^{r/2} \int_L^L f_{\alpha}(z, \theta) \sin(\eta_m z) \cos(\omega_n \theta) dz d\theta, \quad (6.33)$$

$$c_{mn}^{(\alpha)} = \frac{2}{LT} \int_{-r/2}^{r/2} \int_L^L f_{\alpha}(z, \theta) \cos(\eta_m z) \sin(\omega_n \theta) dz d\theta, \quad d_{mn}^{(\alpha)} = \frac{2}{LT} \int_{-r/2}^{r/2} \int_L^L f_{\alpha}(z, \theta) \sin(\eta_m z) \sin(\omega_n \theta) dz d\theta. \quad (6.34)$$

In order to match our general expressions of the stress field with the applied stress given in (6.31) on the curved boundary (corresponding to BC11, BC12, and BC13). We first substitute  $r=R$  into (6.25), (6.28) and (6.30) then expand all functions of  $z$  in terms of Fourier sine and cosine series. Finally the shear and normal stresses on the curved boundary can be expressed as:



$$\begin{aligned}
\sigma_r = & (2\nu-1)C_\infty + \nu A_\infty + \sum_{n=0}^{\infty} \left\{ -\omega_n(\omega_n-1)(A_{\omega_n}^{(n)} \frac{\cos(\omega_n \theta)}{\sin(\omega_n \theta)} + E_{\omega_n}^{(n)} \frac{\cos(\omega_n \theta)}{-\sin(\omega_n \theta)}) R^{\omega_n-2} - \mathfrak{H}_{\omega_n}^{(n)}(R) \frac{\cos(\omega_n \theta)}{\sin(\omega_n \theta)} \right. \\
& + \mathfrak{J}_{\omega_n}^{(n)}(R) \frac{\cos(\omega_n \theta)}{-\sin(\omega_n \theta)} + \sum_{m=1}^{\infty} \left\{ \{A_{\omega_n}^{(m)} [2\nu I_{\omega_n}(\eta_m R) - \frac{2}{\eta_m^2} \frac{\partial^2 I_{\omega_n}(\eta_m R)}{\partial r^2} - \frac{R}{\eta_m^2} \frac{\partial I_{\omega_n}(\eta_m R)}{\partial r}] - \frac{B_{\omega_n}^{(m)}}{\eta_m^2} \frac{\partial^2 I_{\omega_n}(\eta_m R)}{\partial r^2} \} \frac{\cos(\eta_m z)}{-\sin(\eta_m z)} \right. \\
& - \sum_{s=1}^{\infty} \left\{ \frac{\omega_n^2}{\gamma_s^2 R^2} [(C_{\omega_n}^{(s)} + D_{\omega_n}^{(s)}) \Gamma_{\omega_n}^{(s)} + D_{\omega_n}^{(s)} \Lambda_{\omega_n}^{(s)}] - [(C_{\omega_n}^{(s)} + (2\nu+1)D_{\omega_n}^{(s)}) \Gamma_{\omega_n}^{(s)} + D_{\omega_n}^{(s)} \Lambda_{\omega_n}^{(s)}] \} J_{\omega_n}(\gamma_s R) \frac{\cos(\eta_m z)}{\sin(\eta_m z)} \right\} \frac{\cos(\omega_n \theta)}{\sin(\omega_n \theta)} \\
& \left. - \left\{ \frac{E_{\omega_n}^{(k)} \omega_n}{\eta_m^2} \left( \frac{1}{R} \frac{\partial I_{\omega_n}(\eta_m R)}{\partial r} - \frac{I_{\omega_n}(\eta_m R)}{R^2} \right) \frac{\cos(\eta_m z)}{\sin(\eta_m z)} - \sum_{s=1}^{\infty} \frac{F_{\omega_n}^{(k)} \omega_n}{\gamma_s^2} \Gamma_{\omega_n}^{(s)} \frac{J_{\omega_n}(\gamma_s R)}{R^2} \frac{\cos(\eta_m z)}{\sin(\eta_m z)} \right\} \frac{\cos(\omega_n \theta)}{-\sin(\omega_n \theta)} \right\}
\end{aligned} \tag{6.35}$$

$$\begin{aligned}
\sigma_r = & 9(1-\nu)E_\infty + \sum_{n=0}^{\infty} \left\{ -\mathfrak{K}_{\omega_n}^{(n)}(R) \frac{\cos(\omega_n \theta)}{\sin(\omega_n \theta)} \right. \\
& + \sum_{m=1}^{\infty} \left\{ \left\{ \frac{A_{\omega_n}^{(k)}}{\eta_m} [(3-2\nu) \frac{\partial I_{\omega_n}(\eta_m R)}{\partial r} + R \frac{\partial^2 I_{\omega_n}(\eta_m R)}{\partial r^2}] + \frac{B_{\omega_n}^{(k)}}{\eta_m} \frac{\partial I_{\omega_n}(\eta_m R)}{\partial r} \right\} \frac{\sin(\eta_m z)}{\cos(\eta_m z)} \frac{\cos(\omega_n \theta)}{\sin(\omega_n \theta)} \right. \\
& \left. - \left\{ \frac{E_{\omega_n}^{(k)} \omega_n}{2\eta_m R} I_{\omega_n}(\eta_m R) \frac{-\sin(\eta_m z)}{\cos(\eta_m z)} + \sum_{s=1}^{\infty} \frac{F_{\omega_n}^{(k)} \omega_n}{2\gamma_s R} J_{\omega_n}(\gamma_s R) \Gamma_{\omega_n}^{(s)} \frac{\sin(\eta_m z)}{\cos(\eta_m z)} \right\} \frac{\cos(\omega_n \theta)}{-\sin(\omega_n \theta)} \right\}
\end{aligned} \tag{6.36}$$

$$\begin{aligned}
\sigma_\theta = & \sum_{n=0}^{\infty} \left\{ -\omega_n(\omega_n-1)(A_{\omega_n}^{(n)} \frac{-\sin(\omega_n \theta)}{\cos(\omega_n \theta)} - E_{\omega_n}^{(n)} \frac{-\sin(\omega_n \theta)}{-\cos(\omega_n \theta)}) R^{\omega_n-2} + \mathfrak{J}_{\omega_n}^{(n)}(R) \frac{-\sin(\omega_n \theta)}{\cos(\omega_n \theta)} \right. \\
& + \mathfrak{K}_{\omega_n}^{(n)}(R) \frac{\sin(\omega_n \theta)}{\cos(\omega_n \theta)} - \sum_{m=1}^{\infty} \left\{ \left\{ \left[ \frac{\omega_n A_{\omega_n}^{(k)}}{\eta_m^2} \frac{\partial^2 I_{\omega_n}(\eta_m R)}{\partial r^2} + \frac{\omega_n B_{\omega_n}^{(k)}}{\eta_m^2} \left[ \frac{1}{R} \frac{\partial I_{\omega_n}(\eta_m R)}{\partial r} - \frac{1}{R^2} I_{\omega_n}(\eta_m R) \right] \right] \right\} \frac{\cos(\eta_m z)}{-\sin(\eta_m z)} \right. \\
& - \sum_{s=1}^{\infty} \left\{ \frac{\omega_n}{\gamma_s^2 R^2} [(C_{\omega_n}^{(s)} + D_{\omega_n}^{(s)}) \Gamma_{\omega_n}^{(s)} + D_{\omega_n}^{(s)} \Lambda_{\omega_n}^{(s)}] J_{\omega_n}(\gamma_s R) \frac{\cos(\eta_m z)}{\sin(\eta_m z)} \right\} \frac{-\sin(\omega_n \theta)}{\cos(\omega_n \theta)} \\
& + \left\{ \frac{E_{\omega_n}^{(k)}}{2\eta_m^2} \left[ \frac{1}{R} \frac{\partial I_{\omega_n}(\eta_m R)}{\partial r} - \frac{\omega_n^2}{R^2} I_{\omega_n}(\eta_m R) - \frac{\partial^2 I_{\omega_n}(\eta_m R)}{\partial r^2} \right] \right. \\
& \left. - \sum_{s=1}^{\infty} \frac{F_{\omega_n}^{(k)} \Gamma_{\omega_n}^{(s)}}{2\gamma_s^2} \left[ \frac{\omega_n^2}{R^2} J_{\omega_n}(\gamma_s R) + \frac{\partial^2 J_{\omega_n}(\gamma_s R)}{\partial r^2} \right] \right\} \frac{\cos(\eta_m z) \sin(\omega_n \theta)}{\sin(\eta_m z) \cos(\omega_n \theta)} \right\}
\end{aligned} \tag{6.37}$$

where

$$\mathfrak{R}_{0n}^{(i)}(R) = \sum_{s=1}^{\infty} \left\{ \left[ \left( \frac{\omega_s^2}{\gamma_s^2 R^2} - 1 \right) C_{sn}^{(i)} - 2\nu D_{sn}^{(i)} \right] \frac{\sinh(\gamma_s L)}{\gamma_s L} + D_{sn}^{(i)} \cosh(\gamma_s L) \left( \frac{\omega_s^2}{\gamma_s^2 R^2} - 1 \right) \right\} J_{sn}(\gamma_s R) \quad (6.38)$$

$$\mathfrak{S}_{0n}^{(i)}(R) = \sum_{s=1}^{\infty} \frac{F_{sn}^{(i)} \omega_s}{\gamma_s^2 R^2} \frac{\sinh(\gamma_s L)}{\gamma_s L} J_{sn}(\gamma_s R) \quad (6.39)$$

$$\mathfrak{N}_{0n}^{(i)}(R) = \sum_{s=1}^{\infty} \frac{F_{sn}^{(i)} \omega_s}{2\gamma_s R} \frac{\sinh(\gamma_s L)}{\gamma_s L} J_{sn}(\gamma_s R) \quad (6.40)$$

$$\mathfrak{P}_{0n}^{(i)}(R) = \sum_{s=1}^{\infty} \frac{\omega_s^2}{\gamma_s^2 R^2} \left[ C_{sn}^{(i)} \frac{\sinh(\gamma_s L)}{\gamma_s L} + D_{sn}^{(i)} \cosh(\gamma_s L) \right] J_{sn}(\gamma_s R) \quad (6.41)$$

$$\mathfrak{K}_{0n}^{(i)} = \sum_{s=1}^{\infty} \frac{F_{sn}^{(i)}}{2\gamma_s^2} \left[ \frac{\omega_s^2}{R^2} J_{sn}(\gamma_s R) + \frac{\partial^2 J_{sn}(\gamma_s R)}{\partial r^2} \right] \frac{\sinh(\gamma_s L)}{\gamma_s L} \quad (6.42)$$

In (6.35)-(6.37),  $\Gamma_{sn}^{(i)}$  ( $i=1,2$ ) are the factors for the Fourier expansion of  $\cosh(\gamma, z)$  and  $\sinh(\gamma, z)$  respectively:

$$\Gamma_{sn}^{(1)} = \frac{2\gamma_s (-1)^n \sinh(\gamma_s L)}{L(\gamma_s^2 + \eta_{sn}^2)} \quad (6.43)$$

$$\Gamma_{sn}^{(2)} = \frac{2\eta_{sn} (-1)^{n+1} \sinh(\gamma_s L)}{L(\gamma_s^2 + \eta_{sn}^2)} \quad (6.44)$$

While  $\Lambda_{sn}^{(i)}$  ( $i=1,2$ ) are the factors for the Fourier expansion of  $\gamma_s z \sinh(\gamma_s z)$  and  $\gamma_s z \cosh(\gamma_s z)$  respectively:

$$\Lambda_{sn}^{(1)} = \frac{2\gamma_s (-1)^n \sinh(\gamma_s L)}{L(\gamma_s^2 + \eta_{sn}^2)} \left[ \gamma_s L \cosh(\gamma_s L) + \frac{\eta_{sn}^2 - \gamma_s^2}{\gamma_s^2 + \eta_{sn}^2} \sinh(\gamma_s L) \right] \quad (6.45)$$

$$\Lambda_{sn}^{(2)} = \frac{2\eta_{sn} \gamma_s (-1)^{n+1} \sinh(\gamma_s L)}{\gamma_s^2 + \eta_{sn}^2} \quad (6.46)$$

Equating coefficients of the Fourier expansions in  $z$  and  $\theta$  in (6.35)-(6.37) to those corresponding to BC11, BC12 and BC13 given by (6.31), we obtain a system of equations for relating the unknown constants.

In particular, the following equations are obtained by BC11:

$$(2\nu - 1)C_{00} + \nu A_{00} = a_{00}^{(r)} / 4 \quad (6.47)$$

$$-\omega_n(\omega_n - 1)(A_{0n}^{(1)} + E_{0n}^{(1)})R^{n-2} - \mathfrak{H}_{0n}^{(1)}(R) + \mathfrak{I}_{0n}^{(1)}(R) = a_{0n}^{(r)} / 2 \quad (6.48)$$

$$-\omega_n(\omega_n - 1)(A_{0n}^{(2)} - E_{0n}^{(2)})R^{n-2} - \mathfrak{H}_{0n}^{(2)}(R) - \mathfrak{I}_{0n}^{(2)}(R) = c_{0n}^{(r)} / 2 \quad (6.49)$$

$$\begin{aligned} & \alpha_{1k} \left\{ A_{nn}^{(k)} \left[ 2\nu I_{nn}(\eta_n R) - \frac{2}{\eta_n^2} \frac{\partial^2 I_{nn}(\eta_n R)}{\partial r^2} - \frac{R}{\eta_n^2} \frac{\partial^3 I_{nn}(\eta_n R)}{\partial r^3} \right] - \frac{B_{nn}^{(k)}}{\eta_n^2} \frac{\partial^2 I_{nn}(\eta_n R)}{\partial r^2} \right\} \\ & + \alpha_{2k} \left\{ \frac{E_{nn}^{(k)} \omega_n}{\eta_n^2} \left[ \frac{1}{R} \frac{\partial I_{nn}(\eta_n R)}{\partial r} - \frac{I_{nn}(\eta_n R)}{R^2} \right] \right\} + \sum_{s=1}^{\infty} \left\{ \left\{ \frac{\omega_n^2}{\gamma_s^2 R^2} [(C_{sn}^{(k)} + D_{sn}^{(k)}) \Gamma_{sn}^{(i)} + D_{sn}^{(k)} \Lambda_{sn}^{(i)}] \right. \right. \\ & \left. \left. - [(C_{sn}^{(k)} + (2\nu + 1)D_{sn}^{(k)}) \Gamma_{sn}^{(i)} + D_{sn}^{(k)} \Lambda_{sn}^{(i)}] \right\} J_{\omega_n}(\gamma_s R) - \alpha_{2k} \frac{F_{sn}^{(k)} \omega_n}{\gamma_s^2} \Gamma_{sn}^{(i)} \frac{J_{\omega_n}(\gamma_s R)}{R^2} \right\} = \lambda_{nn} \Omega_{nn}^{(r)} \end{aligned} \quad (6.50)$$

where  $\alpha_k$  ( $i=1,2$ ) and  $\Omega_{nn}^{(r)}$  are defined in Table 6-4 for  $k=1,2,3$ , and 4.

The following equations are obtained by BC12:

$$9(1 - \nu)E_{00} - \mathfrak{H}_{00}^{(1)}(R) = a_{00}^{(z)} / 2 \quad (6.51)$$

$$\begin{aligned} & \frac{A_{nn}^{(k)}}{\eta_n} \left[ (3 - 2\nu) \frac{\partial I_{nn}(\eta_n R)}{\partial r} + R \frac{\partial^2 I_{nn}(\eta_n R)}{\partial r^2} \right] + \frac{B_{nn}^{(k)}}{\eta_n} \frac{\partial I_{nn}(\eta_n R)}{\partial r} \\ & + \beta_{1k} \frac{E_{nn}^{(k)} \omega_n}{2\eta_n R} I_{nn}(\eta_n R) + \beta_{2k} \sum_{s=1}^{\infty} \frac{F_{sn}^{(k)} \omega_n}{2\gamma_s R} J_{\omega_n}(\gamma_s R) \Gamma_{sn}^{(2)} = \lambda_{nn} \Omega_{nn}^{(z)} \end{aligned} \quad (6.52)$$

where  $\beta_k$  ( $i=1,2$ ) and  $\Omega_{nn}^{(z)}$  are defined in Table 6-5.

The following equations are obtained by BC13:

$$\omega_n(\omega_n - 1)(A_{0n}^{(1)} - E_{0n}^{(1)})R^{n-2} - \mathfrak{H}_{0n}^{(1)}(R) + \mathfrak{I}_{0n}^{(1)}(R) = c_{0n}^{(g)} / 2 \quad (6.53)$$

$$-\omega_n(\omega_n - 1)(A_{0n}^{(2)} + E_{0n}^{(2)})R^{\alpha_n - 2} + \wp_{0n}^{(2)}(R) + \tilde{\chi}_{0n}^{(2)}(R) = a_{0n}^{(\theta)} / 2 \quad (6.54)$$

$$\begin{aligned} & \kappa_{1k} \left\{ \frac{\omega_n A_{nn}^{(k)}}{\eta_n^2} \frac{\partial^2 I_{\omega_n}(\eta_n R)}{\partial r^2} + \frac{\omega_n B_{nn}^{(k)}}{\eta_n^2} \left[ \frac{1}{R} \frac{\partial I_{\omega_n}(\eta_n R)}{\partial r} - \frac{1}{R^2} I_{\omega_n}(\eta_n R) \right] \right\} \\ & + \frac{E_{nn}^{(k)}}{2\eta_n^2} \left[ \frac{1}{R} \frac{\partial I_{\omega_n}(\eta_n R)}{\partial r} - \frac{\omega_n^2}{R^2} I_{\omega_n}(\eta_n R) - \frac{\partial^2 I_{\omega_n}(\eta_n R)}{\partial r^2} \right] + \sum_{s=1}^n \left\{ \kappa_{2k} \frac{\omega_n}{\gamma_s^2 R^2} [(C_{nn}^{(k)} + D_{nn}^{(k)}) \Gamma_{nn}^{(1)} \right. \\ & \left. + D_{nn}^{(k)} \Lambda_{nn}^{(1)}] J_{\omega_n}(\gamma_s R) - \frac{F_{nn}^{(k)} \Gamma_{nn}^{(1)}}{2\gamma_s^2} \left[ \frac{\omega_n^2}{R^2} J_{\omega_n}(\gamma_s R) + \frac{\partial^2 J_{\omega_n}(\gamma_s R)}{\partial r^2} \right] \right\} = \lambda_{nn} \Omega_{nn}^{(\theta)} \end{aligned} \quad (6.55)$$

where  $\kappa_{ik}$  ( $i=1,2$ ) and  $\Omega_{nn}^{(\theta)}$  are defined in Table 6-6.

On the end surfaces,  $z=L$ , (6.9) can be rewritten as

$$\sigma_r = \sum_{n=0}^{\infty} \sum_{s=1}^{\infty} \zeta_{nn} [e_{nn}^+ \sin(\omega_n \theta) + f_{nn}^+ \cos(\omega_n \theta)] \frac{J_{\omega_n}(\gamma_s r)}{r} \quad (6.56)$$

$$\sigma_z = \sum_{n=0}^{\infty} \sum_{s=1}^{\infty} \zeta_{nn} [g_{nn}^+ \sin(\omega_n \theta) + h_{nn}^+ \cos(\omega_n \theta)] J_{\omega_n}(\gamma_s r) \quad (6.57)$$

$$\sigma_{\theta} = \sum_{n=0}^{\infty} \sum_{s=1}^{\infty} \zeta_{nn} [k_{nn}^+ \sin(\omega_n \theta) + l_{nn}^+ \cos(\omega_n \theta)] \frac{J_{\omega_n}(\gamma_s r)}{r} \quad (6.58)$$

On the other end surface  $z = -L$ , (6.10) is rewritten as

$$\sigma_r = \sum_{n=0}^{\infty} \sum_{s=1}^{\infty} \zeta_{nn} [e_{nn}^- \sin(\omega_n \theta) + f_{nn}^- \cos(\omega_n \theta)] \frac{J_{\omega_n}(\gamma_s r)}{r} \quad (6.59)$$

$$\sigma_z = \sum_{n=0}^{\infty} \sum_{s=1}^{\infty} \zeta_{nn} [g_{nn}^- \sin(\omega_n \theta) + h_{nn}^- \cos(\omega_n \theta)] J_{\omega_n}(\gamma_s r) \quad (6.60)$$

$$\sigma_{\theta} = \sum_{n=0}^{\infty} \sum_{s=1}^{\infty} \zeta_{nn} [k_{nn}^- \sin(\omega_n \theta) + l_{nn}^- \cos(\omega_n \theta)] \frac{J_{\omega_n}(\gamma_s r)}{r} \quad (6.61)$$

where

$$\zeta_{nn} = \begin{cases} 1/2 & \text{for } n=0 \\ 1 & \text{for } n \neq 0 \end{cases} \quad (6.62)$$

$$e_m^+ = \frac{4\lambda_s^2}{R^2 T(\lambda_s^2 - \omega_n^2) J_{\omega_n}^2(\lambda_s)} \int_0^R \int_{-T/2}^{T/2} r^2 f_{2r}(r, \theta) J_{\omega_n}(\gamma, r) \sin(\omega_n \theta) d\theta dr \quad (6.63)$$

$$f_m^+ = \frac{4\lambda_s^2}{R^2 T(\lambda_s^2 - \omega_n^2) J_{\omega_n}^2(\lambda_s)} \int_0^R \int_{-T/2}^{T/2} r^2 f_{2r}(r, \theta) J_{\omega_n}(\gamma, r) \cos(\omega_n \theta) d\theta dr \quad (6.64)$$

$$g_m^+ = \frac{4\lambda_s^2}{R^2 T(\lambda_s^2 - \omega_n^2) J_{\omega_n}^2(\lambda_s)} \int_0^R \int_{-T/2}^{T/2} r f_{2z}(r, \theta) J_{\omega_n}(\gamma, r) \sin(\omega_n \theta) d\theta dr \quad (6.65)$$

$$h_m^+ = \frac{4\lambda_s^2}{R^2 T(\lambda_s^2 - \omega_n^2) J_{\omega_n}^2(\lambda_s)} \int_0^R \int_{-T/2}^{T/2} r f_{2z}(r, \theta) J_{\omega_n}(\gamma, r) \cos(\omega_n \theta) d\theta dr \quad (6.66)$$

$$k_m^+ = \frac{4\lambda_s^2}{R^2 T(\lambda_s^2 - \omega_n^2) J_{\omega_n}^2(\lambda_s)} \int_0^R \int_{-T/2}^{T/2} r^2 f_{2\theta}(r, \theta) J_{\omega_n}(\gamma, r) \sin(\omega_n \theta) d\theta dr \quad (6.67)$$

$$l_m^+ = \frac{4\lambda_s^2}{R^2 T(\lambda_s^2 - \omega_n^2) J_{\omega_n}^2(\lambda_s)} \int_0^R \int_{-T/2}^{T/2} r^2 f_{2\theta}(r, \theta) J_{\omega_n}(\gamma, r) \cos(\omega_n \theta) d\theta dr \quad (6.68)$$

$e_m^-, f_m^-, g_m^-, h_m^-, k_m^-$  and  $l_m^-$  can be obtained by replacing superscript “+” by “-” and “ $f_{2\alpha}$ ” by “ $f_{1\alpha}$ ” ( $\alpha = r, z, \theta$ ) in (6.63)-(6.68).

It can be shown that once one end boundary (say  $z=L$ ) is satisfied, the other end boundary will be satisfied automatically. To see this, let us consider  $\sigma_z$  as an example and rewritten (6.57) and (6.60) as

$$\sigma_z = \sum_{n=0}^{\infty} \sum_{s=1}^{\infty} \frac{1}{2} \zeta_n \{ [(g_m^+ + g_m^-) \sin(\omega_n \theta) + (h_m^+ + h_m^-) \cos(\omega_n \theta)] + [(g_m^+ - g_m^-) \sin(\omega_n \theta) + (h_m^+ - h_m^-) \cos(\omega_n \theta)] \} J_{\omega_n}(\gamma, r) \quad (6.69)$$

$$\sigma_z = \sum_{n=0}^{\infty} \sum_{s=1}^{\infty} \frac{1}{2} \lambda_n \{ [(g_m^+ + g_m^-) \sin(\omega_n \theta) + (h_m^+ + h_m^-) \cos(\omega_n \theta)] - [(g_m^+ - g_m^-) \sin(\omega_n \theta) + (h_m^+ - h_m^-) \cos(\omega_n \theta)] \} J_{\omega_n}(\gamma, r) \quad (6.70)$$

on  $z=L$  and  $z=-L$  respectively.

Comparing (6.69) and (6.70), we found that the term inside the first [ ] in (6.69) and (6.70) is an even function with respect to  $z$ , while the terms inside the second [ ] is an odd function with respect to  $z$ . Similar consideration can also be made to  $\sigma_{z\theta}$  and  $\sigma_{rz}$ .

To consider BC21, BC22, and BC23, the internal stress field given in (6.27)-(6.29) is first expanded into Fourier-Bessel series (See Appendix IV for more details)

$$\sigma_z = 2(2-\nu)C_0 + (1-\nu)A_0 + \sum_{m=0}^{\infty} \left\{ \sum_{n=1}^{\infty} \sum_{p=1}^{\infty} \left\{ \{A_{mn}^{(k)}[(4-2\nu-\omega_n)T_m + U_m] + B_{mn}^{(k)}T_m\} \frac{\cos(\eta_m z)}{-\sin(\eta_m z)} \right. \right. \\ \left. \left. - [(C_m^{(k)} + (2\nu-1)D_m^{(k)}) \frac{\cosh(\gamma_p z)}{\sinh(\gamma_p z)} + D_m^{(k)}\gamma_p z \frac{\sinh(\gamma_p z)}{\cosh(\gamma_p z)}] J_{\omega_n}(\gamma_p r) \frac{\cos(\omega_n \theta)}{\sin(\omega_n \theta)} \right\} \right. \quad (6.71)$$

$$\sigma_r = \sum_{n=1}^{\infty} \sum_{m=0}^{\infty} \left\{ \sum_{p=1}^{\infty} \left\{ \left\{ \frac{A_{mn}^{(k)}}{\eta_m} [(\omega_n^2 - 2\omega_n(1-\nu))T_m + U_m + W_m] + \frac{B_{mn}^{(k)}}{\eta_m} [U_m - \omega_n T_m] \right\} \frac{\sin(\eta_m z) \cos(\omega_n \theta)}{\cos(\eta_m z) \sin(\omega_n \theta)} \right. \right. \\ \left. \left. - \frac{E_{mn}^{(k)} \omega_n}{2\eta_m} T_m \frac{-\sin(\eta_m z) \cos(\omega_n \theta)}{\cos(\eta_m z) - \sin(\omega_n \theta)} + \frac{F_{mn}^{(k)} \omega_n}{2\gamma_p} \frac{\sinh(\gamma_p z) \cos(\omega_n \theta)}{\cosh(\gamma_p z) - \sin(\omega_n \theta)} \right\} \right. \\ \left. - \sum_{p=1}^{\infty} \frac{V_{pn}}{\gamma_p} [(C_m^{(k)} + 2\nu D_m^{(k)}) \frac{\sinh(\gamma_p z)}{\cosh(\gamma_p z)} + D_m^{(k)}\gamma_p z \frac{\cosh(\gamma_p z)}{\sinh(\gamma_p z)}] \frac{\cos(\omega_n \theta)}{\sin(\omega_n \theta)} \right\} \frac{J_{\omega_n}(\gamma_p r)}{r} \quad (6.72)$$

$$\sigma_{z\theta} = \sum_{n=1}^{\infty} \sum_{m=0}^{\infty} \left\{ \sum_{p=1}^{\infty} \left\{ \left\{ \frac{\omega_n A_{mn}^{(k)}}{\eta_m} [(2-2\nu-\omega_n)T_m + U_m] + \frac{\omega_n B_{mn}^{(k)}}{\eta_m} T_m \right\} \frac{\sin(\eta_m z) - \sin(\omega_n \theta)}{\cos(\eta_m z) \cos(\omega_n \theta)} \right. \right. \\ \left. \left. - \frac{E_{mn}^{(k)}}{2\eta_m} [U_m - \omega_n T_m] \frac{-\sin(\eta_m z) \sin(\omega_n \theta)}{\cos(\eta_m z) \cos(\omega_n \theta)} - \frac{\omega_n}{\gamma_p} [(C_m^{(k)} + 2\nu D_m^{(k)}) \frac{\sinh(\gamma_p z)}{\cosh(\gamma_p z)} + D_m^{(k)}\gamma_p z \frac{\cosh(\gamma_p z)}{\sinh(\gamma_p z)}] \frac{-\sin(\omega_n \theta)}{\cos(\omega_n \theta)} \right\} \right. \\ \left. + \sum_{p=1}^{\infty} \frac{F_{pn}^{(k)} V_{pn}}{2\gamma_p} \frac{\sinh(\gamma_p z) \sin(\omega_n \theta)}{\cosh(\gamma_p z) \cos(\omega_n \theta)} \right\} \frac{J_{\omega_n}(\gamma_p r)}{r} \quad (6.73)$$

where

$$T_m = \frac{2\lambda_r^2}{(\lambda_r^2 - \omega_n^2)[(\eta_m R)^2 + \lambda_r^2]} J_{\omega_n}^2(\lambda_r) [\eta_m R I_{\omega_n+1}(\eta_m R) J_{\omega_n}(\lambda_r) + \lambda_r I_{\omega_n}(\eta_m R) J_{\omega_n+1}(\lambda_r)] \quad (6.74)$$

$$\begin{aligned}
U_m = & \frac{2\lambda_s^2 \eta_m R}{(\lambda_s^2 - \omega_s^2)[(\eta_m R)^2 + \lambda_s^2]} J_{\omega_s}^2(\lambda_s) \left\{ \frac{2(\omega_s - 1)\eta_m R}{(\eta_m R)^2 + \lambda_s^2} [\eta_m R I_{\omega_{s+1}}(\eta_m R) J_{\omega_s}(\lambda_s) \right. \\
& + \lambda_s I_{\omega_s}(\eta_m R) J_{\omega_{s+1}}(\lambda_s)] + \frac{2\omega_s \lambda_s}{(\eta_m R)^2 + \lambda_s^2} [\eta_m R I_{\omega_s}(\eta_m R) J_{\omega_{s+1}}(\lambda_s) + \lambda_s I_{\omega_{s+1}}(\eta_m R) J_{\omega_s}(\lambda_s)] \\
& \left. + \eta_m R I_{\omega_s}(\eta_m R) J_{\omega_s}(\lambda_s) - \lambda_s I_{\omega_{s+1}}(\eta_m R) J_{\omega_{s+1}}(\lambda_s) \right\}
\end{aligned} \quad (6.75)$$

$$\begin{aligned}
W_m = & \frac{2\lambda_s^2 \eta_m^2 R^2}{(\lambda_s^2 - \omega_s^2)[(\eta_m R)^2 + \lambda_s^2]} J_{\omega_s}^2(\lambda_s) \left\{ \eta_m R I_{\omega_{s+1}}(\eta_m R) J_{\omega_s}(\lambda_s) + \lambda_s I_{\omega_s}(\eta_m R) J_{\omega_{s+1}}(\lambda_s) \right. \\
& + \frac{2}{(\eta_m R)^2 + \lambda_s^2} \left\{ \frac{2(\nu+1)(\lambda_s^2 - \eta_m^2 R^2)}{(\eta_m R)^2 + \lambda_s^2} [\eta_m R I_{\omega_{s+1}}(\eta_m R) J_{\omega_s}(\lambda_s) + \lambda_s I_{\omega_s}(\eta_m R) J_{\omega_{s+1}}(\lambda_s)] \right. \\
& + \frac{4\nu \eta_m R \lambda_s}{(\eta_m R)^2 + \lambda_s^2} [\eta_m R I_{\omega_{s+2}}(\eta_m R) J_{\omega_{s+1}}(\lambda_s) + \lambda_s I_{\omega_{s+1}}(\eta_m R) J_{\omega_{s+2}}(\lambda_s)] \\
& \left. \left. + \lambda_s \eta_m R I_{\omega_{s+1}}(\eta_m R) J_{\omega_{s+1}}(\lambda_s) - (\lambda_s^2 - \eta_m^2 R^2) I_{\omega_s}(\eta_m R) J_{\omega_s}(\lambda_s) \right\} \right\}
\end{aligned} \quad (6.76)$$

If  $\lambda_p \neq \lambda_s$ , then

$$\begin{aligned}
V_m = & \frac{2\lambda_s^2}{(\lambda_s^2 - \omega_s^2)(\lambda_p^2 - \lambda_s^2)} J_{\omega_s}^2(\lambda_s) \left\{ \lambda_p^2 J_{\omega_s}(\lambda_p) J_{\omega_s}(\lambda_s) + \lambda_s \lambda_p J_{\omega_{s+1}}(\lambda_p) J_{\omega_{s+1}}(\lambda_s) \right. \\
& - \frac{2\lambda_p \lambda_s \omega_s}{\lambda_p^2 - \lambda_s^2} [\lambda_p J_{\omega_s}(\lambda_p) J_{\omega_{s+1}}(\lambda_s) - \lambda_s J_{\omega_{s+1}}(\lambda_p) J_{\omega_s}(\lambda_s)] \\
& \left. + \frac{\omega_s(\lambda_p^2 + \lambda_s^2) - 2\lambda_p^2}{\lambda_p^2 - \lambda_s^2} [\lambda_p J_{\omega_{s+1}}(\lambda_p) J_{\omega_s}(\lambda_s) - \lambda_s J_{\omega_s}(\lambda_p) J_{\omega_{s+1}}(\lambda_s)] \right\}
\end{aligned} \quad (6.77)$$

If  $\lambda_p = \lambda_s$ , then

$$V_m = \frac{\lambda_s^2 J_{\omega_{s+1}}(\lambda_s) J_{\omega_{s+1}}(\lambda_s)}{(\lambda_s^2 - \omega_s^2) J_{\omega_s}^2(\lambda_s)} \quad (6.78)$$

By substituting  $z=L$  into (6.71) and comparing the corresponding coefficients of (6.69), we have

$$2(2-\nu)C_{\infty} + (1-\nu)A_{\infty} = 0 \quad (6.79)$$

$$\sum_{n=1}^{\infty} \{A_{nn}^{(1)} [(4-2\nu-\omega_n)T_n + U_n] + B_{nn}^{(1)} T_n\} (-1)^n$$

$$-[(C_n^{(1)} + (2\nu-1)D_n^{(1)}) \cosh(\gamma, L) + D_n^{(1)} \gamma, L \sinh(\gamma, L)] = \frac{1}{2} \zeta_n (h_n^+ + h_n^-) \quad (6.80)$$

$$\sum_{n=1}^{\infty} \{A_{nn}^{(2)} [(4-2\nu-\omega_n)T_n + U_n] + B_{nn}^{(2)} T_n\} (-1)^n$$

$$-[(C_n^{(2)} + (2\nu-1)D_n^{(2)}) \cosh(\gamma, L) + D_n^{(2)} \gamma, L \sinh(\gamma, L)] = \frac{1}{2} \zeta_n (g_n^+ + g_n^-) \quad (6.81)$$

$$(C_n^{(3)} + (2\nu-1)D_n^{(3)}) \sinh(\gamma, L) + D_n^{(3)} \gamma, L \cosh(\gamma, L) = \frac{1}{2} \zeta_n (h_n^+ - h_n^-) \quad (6.82)$$

$$(C_n^{(4)} + (2\nu-1)D_n^{(4)}) \sinh(\gamma, L) + D_n^{(4)} \gamma, L \cosh(\gamma, L) = \frac{1}{2} \zeta_n (g_n^+ - g_n^-) \quad (6.83)$$

The same system of equation is obtained if we substitute  $z=-L$  into (6.71) and comparing the corresponding coefficients of (6.70). Thus, only one of the end boundaries (either BC22 or BC32) has to be satisfied by the stress  $\sigma_z$  given in (6.71). Similar consideration can also be made for  $\sigma_{z\theta}$  and  $\sigma_{zr}$  and leads to the same conclusion.

Applying BC21 or BC31 into (6.72), we have

$$\frac{F_n^{(1)} \omega_n}{2\gamma_z} \sinh(\gamma_r L) - \sum_{p=1}^{\infty} \frac{V_p}{\gamma_p} [(C_{pn}^{(1)} + 2\nu D_{pn}^{(1)}) \sinh(\gamma_p L) + D_{pn}^{(1)} \gamma_p L \cosh(\gamma_p L)] = \frac{1}{2} \zeta_n (f_n^+ + f_n^-) \quad (6.84)$$

$$-\frac{F_n^{(2)} \omega_n}{2\gamma_z} \sinh(\gamma_r L) - \sum_{p=1}^{\infty} \frac{V_p}{\gamma_p} [(C_{pn}^{(2)} + 2\nu D_{pn}^{(2)}) \sinh(\gamma_p L) + D_{pn}^{(2)} \gamma_p L \cosh(\gamma_p L)] = \frac{1}{2} \zeta_n (e_n^+ + e_n^-) \quad (6.85)$$



$$\sum_{n=1}^{\infty} \left\{ \left\{ \frac{A_n^{(3)}}{\eta_n} [(\omega_n^2 - 2\omega_n(1-\nu))T_n + U_n + W_n] + \frac{B_n^{(3)}}{\eta_n} [U_n - \omega_n T_n] \right\} - \frac{E_n^{(3)}\omega_n}{2\eta_n} T_n \right\} (-1)^n + \frac{F_n^{(3)}\omega_n}{2\gamma_s} \cosh(\gamma_s L) \\ - \sum_{p=1}^{\infty} \frac{V_p}{\gamma_p} [(C_p^{(3)} + 2\nu D_p^{(3)}) \cosh(\gamma_p L) + D_p^{(3)} \gamma_p L \sinh(\gamma_p L)] = \frac{1}{2} \zeta(f_n^* - f_n^-) \quad (6.86)$$

$$\sum_{n=1}^{\infty} \left\{ \left\{ \frac{A_n^{(4)}}{\eta_n} [(\omega_n^2 - 2\omega_n(1-\nu))T_n + U_n + W_n] + \frac{B_n^{(4)}}{\eta_n} [U_n - \omega_n T_n] \right\} + \frac{E_n^{(4)}\omega_n}{2\eta_n} T_n \right\} (-1)^n - \frac{F_n^{(4)}\omega_n}{2\gamma_s} \cosh(\gamma_s L) \\ - \sum_{p=1}^{\infty} \frac{V_p}{\gamma_p} [(C_p^{(4)} + 2\nu D_p^{(4)}) \cosh(\gamma_p L) + D_p^{(4)} \gamma_p L \sinh(\gamma_p L)] = \frac{1}{2} \zeta(e_n^* - e_n^-) \quad (6.87)$$

Finally, applying BC23 or BC33 into (6.73), we have

$$\frac{\omega_n}{\gamma_s} [(C_n^{(1)} + 2\nu D_n^{(1)}) \sinh(\gamma_s L) + D_n^{(1)} \gamma_s L \cosh(\gamma_s L)] + \sum_{p=1}^{\infty} \frac{F_p^{(1)} V_p}{2\gamma_p} \sinh(\gamma_p L) = \frac{1}{2} \zeta_n(k_n^* + k_n^-) \quad (6.88)$$

$$\frac{\omega_n}{\gamma_s} [(C_n^{(2)} + 2\nu D_n^{(2)}) \sinh(\gamma_s L) + D_n^{(2)} \gamma_s L \cosh(\gamma_s L)] + \sum_{p=1}^{\infty} \frac{F_p^{(2)} V_p}{2\gamma_p} \sinh(\gamma_p L) = \frac{1}{2} \zeta_n(l_n^* + l_n^-) \quad (6.89)$$

$$\sum_{n=1}^{\infty} \left\{ \left\{ \frac{\omega_n A_n^{(3)}}{\eta_n} [(2 - 2\nu - \omega_n)T_n + U_n] + \frac{\omega_n B_n^{(3)}}{\eta_n} T_n \right\} + \frac{E_n^{(3)}}{2\eta_n} [U_n - \omega_n T_n] \right\} (-1)^n \\ + \frac{\omega_n}{\gamma_s} [(C_n^{(3)} + 2\nu D_n^{(3)}) \cosh(\gamma_s L) + D_n^{(3)} \gamma_s L \sinh(\gamma_s L)] + \sum_{p=1}^{\infty} \frac{F_p^{(3)} V_p}{2\gamma_p} \cosh(\gamma_p L) = \frac{1}{2} \zeta(k_n^* - k_n^-) \quad (6.90)$$

$$\sum_{n=1}^{\infty} \left\{ \left\{ \frac{\omega_n A_n^{(4)}}{\eta_n} [(2 - 2\nu - \omega_n)T_n + U_n] + \frac{\omega_n B_n^{(4)}}{\eta_n} T_n \right\} + \frac{E_n^{(4)}}{2\eta_n} [U_n - \omega_n T_n] \right\} (-1)^n \\ - \frac{\omega_n}{\gamma_s} [(C_n^{(4)} + 2\nu D_n^{(4)}) \cosh(\gamma_s L) + D_n^{(4)} \gamma_s L \sinh(\gamma_s L)] + \sum_{p=1}^{\infty} \frac{F_p^{(4)} V_p}{2\gamma_p} \cosh(\gamma_p L) = \frac{1}{2} \zeta(l_n^* - l_n^-) \quad (6.91)$$

Therefore,  $A_{\infty}$  and  $C_{\infty}$  can be obtained from (6.47) and (6.79);  $E_{\infty}$  can be obtained from (6.51);  $A_0^{(l)}$  and  $E_0^{(l)}$  ( $l=1,2$ ) can be obtained from (6.48)-(6.49) and (6.53)-(6.54);

for each  $n$ ,  $12(M+S)$  unknown constants  $A_{mn}^{(k)}, B_{mn}^{(k)}, E_{mn}^{(k)}, C_{sn}^{(k)}, D_{sn}^{(k)}$ , and  $F_{sn}^{(k)}$ , ( $k = 1, 2, 3, 4$ ;  $m=1, 2, \dots, M$ ;  $s=1, 2, \dots, S$ ) can be solved from a system of equations (6.50), (6.52) and (6.55) with  $m$  from 1 to  $M$ , and (6.80)-(6.91) with  $s$  from 1 to  $S$ . Thus, we have exactly  $12(M+S)$  equations for  $12(M+S)$  unknowns for each  $n$ . If the summation  $n$  is from 1 to  $N$ , the total number of unknowns and equations are  $7+12N(M+S)$ . Finally, all stress components can be obtained by back substituting all these coefficients into (6.25)-(6.30). Therefore, the general elastic solution for stresses within the finite isotropic cylinders subjected to arbitrary surface loads is obtained, and some special cases of this general solution will be discussed next.

## 6.7 Special Cases

Let us consider some special loading cases of our general solution given in the previous section. When we set  $\omega_n = 2n$  ( $n=1, 2, \dots$ ) and  $k=l=1$ , the solution reduces to the solution for finite cylinders under the diametral point load strength test considered by Chau and Wei (1999); when we set  $\omega_n = 2n$  ( $n=1, 2, \dots$ ),  $k=l=1$ , and  $C_{sn}^{(1)} = D_{sn}^{(1)} = F_{sn}^{(1)} = 0$ , the solution reduces to the solution for finite cylinders with zero shear displacements on the end surface under the diametral point load strength test by Chau (1998a); when we set  $\omega_n = 0$ ,  $k=l=1$ , and  $E_{mn}^{(1)} = F_{sn}^{(1)} = 0$ , the solution reduces to the solution for finite cylinders under the axial point load strength test by Wei et al. (1999); when we set  $\omega_n = 0$  and  $E_{mn}^{(1)} = F_{sn}^{(1)} = 0$ , the solution reduces to the general solution for finite cylinders under axisymmetric load by Saito (1954, 1952). In addition, the solutions for finite cylinders constrained the radial displacement of the loading end

under confined of unconfined compression tests by Filon (1902) and Watanabe (1996) are also special cases of the present general solution.

## 6.8 Characteristics of Roots of the Derivative of the Bessel Function

When  $\omega_n = 0$  (or cylinders under axisymmetric loads), Saito (1952) has considered the roots of  $J'_0(\lambda_n) = 0$  in obtaining his numerical solution. These roots have also been used by various authors, including Ogaki *et al* (1983), Watanabe (1996), and Wei *et al.* (1999).

For obtaining the analytic solution for the diametral point load strength test, Chau and Wei (1999) has evaluated the roots of  $J'_{2n}(\lambda_n) = 0$  ( $n=0,1,2,\dots$ ). Since the accuracy of the present approach is also depend on the accuracy of the roots  $\lambda_n$ , in this section we will consider some general characteristics of the roots of  $J'_{2n}(\lambda_n) = 0$ , so that these roots can be found more accurately and efficiently.

In particular, the following four regularities are observed for the roots of  $J'_{2n}(\lambda_n) = 0$ :

### (i) *The upper and lower bounds for the first root*

As discussed by Watson (1944), the smallest root  $\lambda_n$  of  $J'_{2n}(x) = 0$  can be bounded by

$$\frac{\sqrt{2n(2n+2)}}{\sqrt{2n(2n+3)}} \text{ (for } 1 \leq n \leq 2) < \lambda_n < \sqrt{4n(2n+1)} \text{ (for } n > 2) \quad (6.92)$$

The first roots can be searched within these upper and lower bounds. Once we obtain the first root, we can generate the subsequent roots more efficiently if the following properties are noted.

(ii) For large  $\lambda_r$ , any two non-zero neighboring roots  $\lambda_{r+1}$  and  $\lambda_r$  of  $J'_{\alpha_r}(x) = 0$  differ by  $\pi$  (or  $\lambda_{r+1} - \lambda_r \approx \pi$ )

Since the Bessel function  $J_{\alpha_r}(x)$  can be expressed as (Watson, 1944)

$$J_{\alpha_r}(x) = \sqrt{\frac{2}{\pi x}} \cos\left(x - \frac{\omega_r \pi}{2} - \frac{\pi}{4}\right) + O(x^{-3/2}) \quad (6.93)$$

For large  $x$ , we can retain the first order term. Considering the differentiation of it, we have

$$J'_{\alpha_r}(x) \approx -\sqrt{\frac{2}{\pi x}} \sin\left(x - \frac{\omega_r \pi}{2} - \frac{\pi}{4}\right) \quad (6.94)$$

Consequently, the roots of  $J'_{\alpha_r}(\lambda_r) = 0$  should satisfy

$$\lambda_r - \frac{\omega_r \pi}{2} - \frac{\pi}{4} = k\pi, k=0, 1, 2, \dots \quad (6.95)$$

Therefore, the difference between any two neighboring roots is given by

$$\lambda_{r+1} - \lambda_r \approx \pi \quad (6.96)$$

if  $\lambda_r$  is large enough.

(iii) There must be a root of  $J'_{\alpha_{r+1}}(x) = 0$  between any two neighbor roots of  $J'_{\alpha_r}(x) = 0$

To prove this characteristic, the following argument is applied. By following the procedure given in Section 15.22 of Watson (1944), we define a function  $f(x) = x^{\alpha_r + 1} J'_{\alpha_r}(x)$ . Suppose that  $\lambda_r$  and  $\lambda_{r+1}$  are two neighboring roots of  $J'_{\alpha_r}(x) = 0$ , obviously,  $f(\lambda_r) = f(\lambda_{r+1}) = 0$ . It is well known that there must exist a value  $\xi$

between  $\lambda_i$  and  $\lambda_{i+1}$  that satisfies  $f'(\xi) = 0$ . In addition, it can be proved that  $f'(\xi) = \xi^{\alpha+1} J'_{\alpha+1}(\xi)$ , so we have  $J'_{\alpha+1}(\xi) = 0$ . That is, between any two neighboring roots  $\lambda_i$  and  $\lambda_{i+1}$  of  $J'_\alpha(x) = 0$ , we can find a root  $\xi$  for  $J'_{\alpha+1}(\xi) = 0$ .

(iv) *There must be a root of  $J'_{\alpha+1}(x) = 0$  between any two neighbor roots of  $J'_{\alpha+1}(x) = 0$*

The proof for this property is similar to those used in the previous characteristic (iii). In particular, we can define another function  $g(x) = x^{\alpha+1} J'_{\alpha+1}(x)$ , and follow the same procedure as employed for (iii). Because the proof follows trivially, the details will not be given here.

In numerical computation, the above four regularities can be used to evaluate the roots of  $J'_{\alpha+1}(x) = 0$  efficiently.

## 6.9 Conclusion

In this paper, we have presented a general solution for a finite isotropic solid cylinder subjected to arbitrary boundary loads. Equations of equilibrium are first converted to two uncoupled differential equations by using the displacement function approach. Appropriate solution forms of these displacement functions are proposed in terms of series expression involving the Bessel and modified Bessel functions in  $r$ -dependency, trigonometric and hyperbolic functions in  $z$ -dependency, and trigonometric functions in  $\theta$ -dependency. The boundary tractions on the curved surface are expanded into double Fourier series expansion, while those on the end surfaces are expanded into Fourier-

Bessel series expansion. System of simultaneous equations for the unknown constants of the displacement functions is given explicitly for any arbitrary boundary loads. It was demonstrated that only one of the end boundary conditions need to be satisfied, while the other end boundary will be satisfied automatically. Solution for axisymmetric problems given by Saito (1952, 1954) for finite solid cylinders, solution for the axial point load strength test given by Wei et al. (1999), and solution for the diametral point load strength test given by Chau and Wei (1999b) can all be recovered as special cases of the present general solution. The framework of analysis given here can also be extended to mixed boundary value problems (i.e. both displacement and traction are applied on the boundary of the finite cylinders).

## Chapter 7

### CONCLUSION

#### 7.1 Summary of Results

This dissertation presents a series of exact analytic solutions for spheres and cylinders. More specifically, the analytic solutions are for: spherically isotropic spheres under the diametral Point Load Strength Test (PLST), finite isotropic cylinders under the axial PLST, finite isotropic cylinders under the diametral PLST, and finite isotropic cylinders subjected to arbitrary surface load.

In particular, Chapter 2 presents an analytic solution for the stress concentrations within a spherically isotropic sphere under the diametral PLST. For the case of isotropic sphere, our solution reduces to the classical solution by Hiramatsu and Oka (1966) and agrees well with the published experimental observations by Frocht and Guernsey (1953). A zone of higher tensile stress concentration is developed near the point loads. The pattern of stress distribution along the axis of loading is relatively insensitive to anisotropy of rock, while the maximum tensile stress is very sensitive to it, and the difference between this maximum tensile stress and the uniform tensile stress in the central part of the sphere increases with  $E/E'$  (where  $E$  and  $E'$  are the Young's moduli governing the axial deformations along directions parallel and normal to the plane of isotropy respectively),  $G/G'$  (where  $G$  and  $G'$  are the moduli governing the shear deformations in the planes of isotropy and the planes parallel to the radial direction), and  $\bar{\nu}/\nu'$  (where  $\bar{\nu}$  and  $\nu'$  are the Poisson's ratios characterizing the transverse reduction in the plane of isotropy under tension in the same plane and under radial

tension respectively). This stress difference, in general, decreases with the size of loading area and the Poisson's ratio in isotropic planes.

Chapter 3 presents an analytic solution for the stress field within an finite cylinder under the axial PLST. Our solution shows that a zone of higher tensile stress is developed in the vicinity of the applied point loads, compared to the roughly uniform tensile stress in the central portion of the line between the two point loads. This peak tensile stress along the axis of loading decreases with the Poisson's ratio and the size of the loading area, but increases with the Young's modulus. The tensile stress distribution along the axis of loading in a cylinder under the axial PLST is remarkably similar to that observed in a sphere under the diametral PLST. Our solution also demonstrates both size and shape effects on the point load strength index (PLSI) that we observed in our experiments. In particular, for a fixed length/diameter ratio, the larger the specimen the smaller is the PLSI; while for a fixed diameter, the longer the specimen the smaller is the PLSI.

Chapter 4 presents an analytic solution for a finite isotropic cylinder under the diametral PLST. Numerical results show that, similar to an isotropic sphere under the diametral PLST or an isotropic cylinder under the axial PLST, the tensile stress distribution along the axis of loading is not uniform, a zone of high tensile stress concentrations are developed near the two point loads for both of the hoop stress and the radial stress along the axis of revolution. Both of these maximum tensile stresses decrease with Poisson's ratio, the contact area, the radius of spherical heads of the indentors, but increase with diameter of the specimen. The maximum tensile stress along the axis of revolution decreases drastically with the increase of length/diameter



ratio of the specimen, while the maximum hoop tensile stress is relatively insensitive to it. The size effect is also well predicted by the solution, that is, the larger the diameter, the weaker the specimen.

More importantly, Chapter 5, by using all of the analytic solutions obtained in Chapters 2, 3 and 4, analyzes and compares the tensile stress distributions in isotropic spheres under the diametral PLST and cylinders under the axial and diametral PLSTs. Numerical results show that, if the sizes of the specimens are comparable (say by following the suggested dimension by ISRM, 1985), the distribution of the normalized tensile stresses are very similar along the axis of loading in spheres under the diametral PLST and cylinders under the axial and diametral PLST, both in terms of magnitude and pattern of the distribution. This lends credence that the PLSI is relatively insensitive to the exact shape of the specimen under PLST, and thus the first theoretical basis for irregular lumps under PLST is provided.

Chapter 6 presents a new framework for stress analysis for finite isotropic cylinders subjected to arbitrary surface load. The special cases of the solution include the analytic solutions by Filon (1902), Saito (1952,1954), Watanabe (1996) and Wei et al. (1999) for axisymmetric problems and the solutions by Chau (1998a) and Chau and Wei (1999b) for non-axisymmetric problems for finite solid circular cylinders.

## **7.2 Further Studies**

The Brazilian test is another popular indirect tensile strength test for brittle materials. The theoretical basis for this test is the analytic solution by Hondros (1959), which considered an infinite circular cylinder subjected to a uniform radial pressure

acting over small angle of  $2\alpha$  at both ends of a diameter, as shown by Fig. 7.1. However, in fact, the thickness of the cylindrical specimens under the Brazilian test, according to the standard test suggested by the International Society for Rock Mechanics (ISRM), should be approximately equal to the specimen radius, which is finite. Thus, theoretically speaking, it is necessary to consider the stress analysis for a finite cylinder under the Brazilian test, not the infinite case considered by Hondros (1959). Since in Chapter 6 we have obtained a new framework for stress analyses of finite cylinders subjected to arbitrary surface load, the analytic solution for a finite cylinder under the Brazilian test can be obtained by setting parameters in Chapter 6 as  $\omega_n = 2n$ ,  $n = 1, 2, \dots$ , and  $k = l = 1$  in the solution given in Chapter 6. Furthermore, the interaction between the curved surface of the cylinder and two steel loading jaws, through which the two line loads are applied, can be more realistically modeled by considering the contact problem between them. One major advantage of considering the finite cylinder under the Brazilian test is that both of the size and shape effects of the specimen can be predicted by the analytic solution.

A modification to the traditional Brazilian test has been proposed by applying three line loads instead of two, as shown by Fig. 7.2. The two-dimensional analytic solution has been obtained by Jaeger (1979). However, the traction free boundary conditions on two end surfaces and the contact problem on the curved surface of the cylinder are not considered either. Therefore, further theoretical improvement can be made on these two aspects. The method of solution is similar to that proposed for the traditional Brazilian test, but the parameters should be set to  $\omega_n = 3n$ ,  $n = 1, 2, \dots$ , and  $k = l = 1$  instead in the

solution given in Chapter 6. Thus, an exact analytic solution for the modified Brazilian test which satisfies all the boundary conditions can be obtained.

In addition, the preliminary study on spherically isotropic spheres under the diametral PLST shows that the anisotropy of material does have certain effect on the tensile stress distribution within specimens, but, all analytic solutions obtained in this dissertation for cylinders are restricted to considering cylindrical specimens to be linear elastic and isotropic. This assumption, of course, can be restrictive for natural rock specimens, since some rocks are inevitably anisotropic by nature. Thus, further theoretical investigations on the effects of anisotropy on the stresses in cylinders under the PLST are recommended.

In particular, it is possible to consider a transversely isotropic cylinder under the axial and diametral PLST. The so-called transversely isotropy can be regarded as the limiting case of spherically isotropy if we let the radius of the sphere be infinite. The method of displacement potentials proposed by Hu (1953) for transversely isotropic solid can be used. But the main difficulty lies on the choice of appropriate displacement potentials that can satisfy all boundary conditions. Again, similar to the consideration by Chau (1998a), the contact problem between the surface of the cylinder and the spherical heads of the steel cones can be considered. The results of such a study should provide the theoretical basis for the point load strength anisotropy index  $I_a$  (Broch and Franklin, 1972; ISRM, 1985), which is defined as the ratio of the greatest to the least Point Load Strength Indices. As mentioned earlier, the point load strength anisotropy index  $I_a$  has long been extensively used in experiments to characterize the effect of anisotropy on the PLST.

**Table 4-1** The first ten roots of  $J'_n(\lambda_r) = 0$  for  $n$  from 0 to 7

$\lambda_r \backslash n$	0	1	2	3	4	5	6	7
1	3.8317	3.0542	5.3176	7.5013	9.6474	11.7709	13.8788	15.9754
2	7.0156	6.7061	9.2824	11.7349	14.1155	16.4479	18.7451	21.0154
3	10.1735	9.9695	12.6819	15.2682	17.7740	20.2230	22.6293	25.002
4	13.3237	13.1704	15.9641	18.6374	21.2291	23.7607	26.2460	28.6943
5	16.4706	16.3475	19.1960	21.9317	24.5872	27.1820	29.7290	32.2370
6	19.6159	19.5129	22.4010	25.1839	27.8893	30.5345	33.1314	35.6885
7	22.7601	22.6716	25.5898	28.4098	31.1553	33.8420	36.4805	39.0790
8	25.9037	25.8260	28.7678	31.6179	34.3966	37.1180	39.7919	42.4259
9	29.0468	28.9777	31.9385	34.8134	37.6201	40.3711	43.0755	45.7402
10	32.1897	32.1273	35.1039	37.9996	40.8302	43.6068	46.3378	49.0296

**Table 4-2** Comparison of the theoretical predictions of the normalized tensile stress,  $\sigma_{center}/(P/D^2)$ , at the center of a solid circular cylinder under the diametral PLST given by Wijk (1980) and by the present study. Note that the results by Wijk (1980) were re-calculated to 4 significant digits.

Poisson's ratio	$L/D=1.0$				$L/D \rightarrow \infty$	
	Wijk (1980)	$E=40\text{GPa}$ $P=10\text{KN}$	$E=70\text{GPa}$ $P=10\text{KN}$	$E=70\text{GPa}$ $P=20\text{KN}$	Wijk (1980)	Present ( $E=70\text{GPa}$ $P=20\text{KN}$ )
0.0	0.7678	0.7360	0.7365	0.7358	0.7372	0.7352
0.1	0.7144	0.6865	0.6870	0.6863	0.6877	0.6858
0.2	0.6685	0.6436	0.6441	0.6435	0.6448	0.6430
0.3	0.6284	0.6061	0.6066	0.6060	0.6072	0.6056
0.4	0.5931	0.5730	0.5734	0.5729	0.5740	0.5725
0.5	0.5618	0.5435	0.5439	0.5434	0.5444	0.5431

**Table 4-3** Summary of some of the observed failure patterns. The T-mode and S-mode are depicted in Fig. 4-14 and  $\theta_1$  and  $\theta_2$  are defined as the two minimum angles between the cracks and the transverse line joining the two applied point loads.

Sample No.	L/D	$I_s$ (MPa)	Failure Mode	$\theta_1(^{\circ})$	$\theta_2(^{\circ})$
1	0.40	1.69	T	8	50
2	0.40	1.64	T	25	50
3	0.40	1.68	T	50	30
4	0.40	1.54	S	18	18
5	0.50	1.73	S	45	45
6	0.63	1.74	S	60	80
7	0.70	1.88	S	60	60
8	0.86	1.85	S	35	45
9	1.00	1.86	S	35	60

**Table 6-1** The definitions for boundary conditions BC $ij$  ( $i,j=1,2,3$ ).

Surface	Direction		
	1 ( $r$ )	2 ( $z$ )	3 ( $\theta$ )
1 ( $r=R$ )	$\sigma_r = f_{1r}$	$\sigma_z = f_{1z}$	$\sigma_{r\theta} = f_{1\theta}$
2 ( $z=L$ )	$\sigma_z = f_{2r}$	$\sigma_z = f_{2z}$	$\sigma_{z\theta} = f_{2\theta}$
3 ( $z=-L$ )	$\sigma_z = f_{3r}$	$\sigma_z = f_{3z}$	$\sigma_{z\theta} = f_{3\theta}$

**Table 6-2** The  $\theta$ - and  $z$ -dependencies for superscripts  $l$  ( $=1,2$ ) and  $k$  ( $=1,2,3,4$ ) used for the displacement functions  $\Psi$  and  $\Phi$  given in Equations (6.23) and (6.24).

Constants for $\Psi$ and $\Phi$	Superscripts $l/k$	$\theta$ -dependency	$z$ -dependency
$E_{0n}^{(l)} / A_{0n}^{(l)}$	1	sin/cos	-
	2	cos/sin	-
$E_{mn}^{(k)} / F_{mn}^{(k)}$	1	sin	cos/cosh
	2	cos	cos/cosh
	3	sin	sin/sinh
	4	cos	sin/sinh
$A_{mn}^{(k)} / B_{mn}^{(k)}$	1	cos	sin
	2	sin	sin
	3	cos	cos
	4	sin	cos
$C_{mn}^{(k)} / D_{mn}^{(k)}$	1	cos	sinh/zcosh
	2	sin	sinh/zcosh
	3	cos	cosh/zsinh
	4	sin	cosh/zsinh



**Table 6-3** The  $\theta$ - and  $z$ -dependencies in (6.25)-(6.30) used for the stresses for superscripts  $l$  ( $=1,2$ ) and  $k$  ( $=1,2,3,4$ ). The symbols used are: E1=sin, E2=cos, cosh, zsinh; O1=sin, O2=sin, sinh, zcosh

$l/k$	Dependency	$\sigma_{rr}$	$\sigma_{\theta\theta}$	$\sigma_{\phi\phi}$	$\sigma_{zz}$	$\sigma_{z\theta}$
$l=1$	$\theta$	E1	E1	O1	E1	O1
$l=2$	$\theta$	O1	O1	E1	O1	E1
$k=1$	$\theta$	E1	E1	O1	E1	O1
	$z$	E2	O2	E2	E2	O2
$k=2$	$\theta$	O1	O1	E1	O1	E1
	$z$	E2	O2	E2	E2	O2
$k=3$	$\theta$	E1	E1	O1	E1	O1
	$z$	O2	E2	O2	O2	E2
$k=4$	$\theta$	O1	O1	E1	O1	E1
	$z$	O2	E2	O2	O2	E2

**Table 6-4** The definitions of  $\alpha_{ik}$  ( $i=1,2,3$ ) and  $\Omega_{mn}^{(r)}$  used in (6.50) for  $k=1,2,3$ , and 4.

$k$	$\alpha_{1k}$	$\alpha_{2k}$	$\Omega_{mn}^{(r)}$
1	+1	-1	$a_{mn}^{(r)}$
2	+1	+1	$c_{mn}^{(r)}$
3	-1	-1	$b_{mn}^{(r)}$
4	-1	+1	$d_{mn}^{(r)}$

**Table 6-5** The definitions of  $\beta_{ik}$  ( $i=1,2$ ) and  $\Omega_{\text{int}}^{(z)}$  used in (6.52) for  $k=1,2,3$ , and 4.

$k$	$\beta_{1k}$	$\beta_{2k}$	$\Omega_{\text{int}}^{(z)}$
1	+1	-1	$b_{\text{int}}^{(z)}$
2	-1	+1	$d_{\text{int}}^{(z)}$
3	-1	-1	$a_{\text{int}}^{(z)}$
4	+1	+1	$c_{\text{int}}^{(z)}$

**Table 6-6** The definitions of  $\kappa_{ik}$  ( $i=1,2$ ) and  $\Omega_{mn}^{(\theta)}$  used in (6.55) for  $k=1,2,3$ , and 4.

$k$	$\kappa_{1k}$	$\kappa_{2k}$	$\Omega_{mn}^{(\theta)}$
1	+1	+1	$c_{mn}^{(\theta)}$
2	-1	-1	$a_{mn}^{(\theta)}$
3	-1	+1	$d_{mn}^{(\theta)}$
4	+1	-1	$b_{mn}^{(\theta)}$

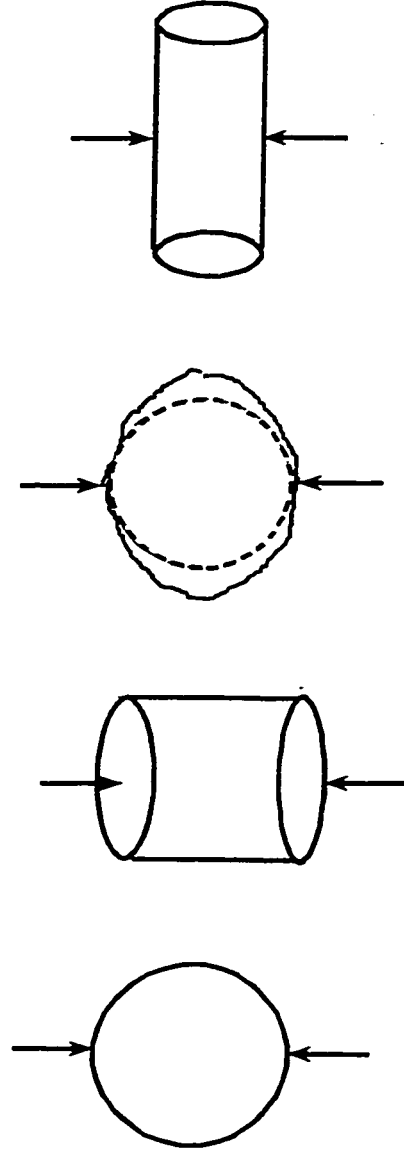


**Fig. 2-1** Test specimens used for the Point Load Strength Test (from the left): sphere, cylinder under the axial point loads, irregular lump, cylinder under the diametral point loads

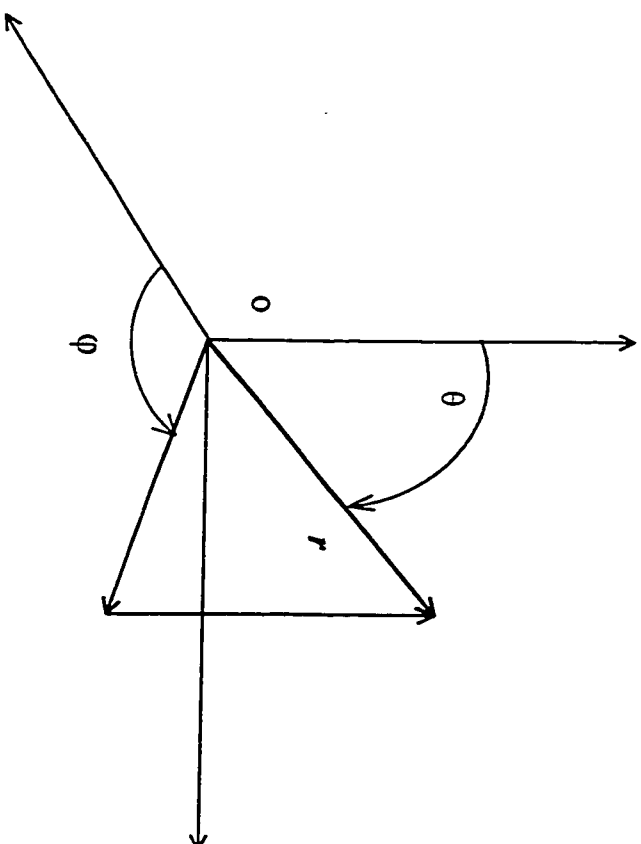


**Fig. 2-2** The spherical polar coordinate system used

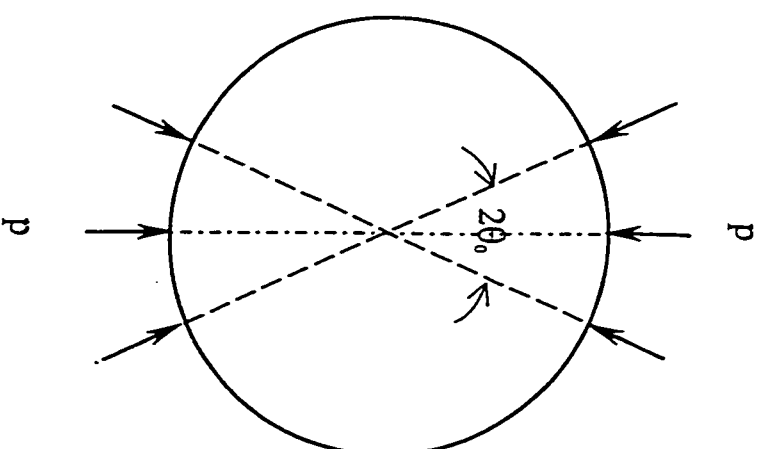


**Fig. 2-3** A sphere under the Point Load Strength Test is modeled by uniform radial stress applied over two small spherical areas subtending an angle of  $2\theta_0$

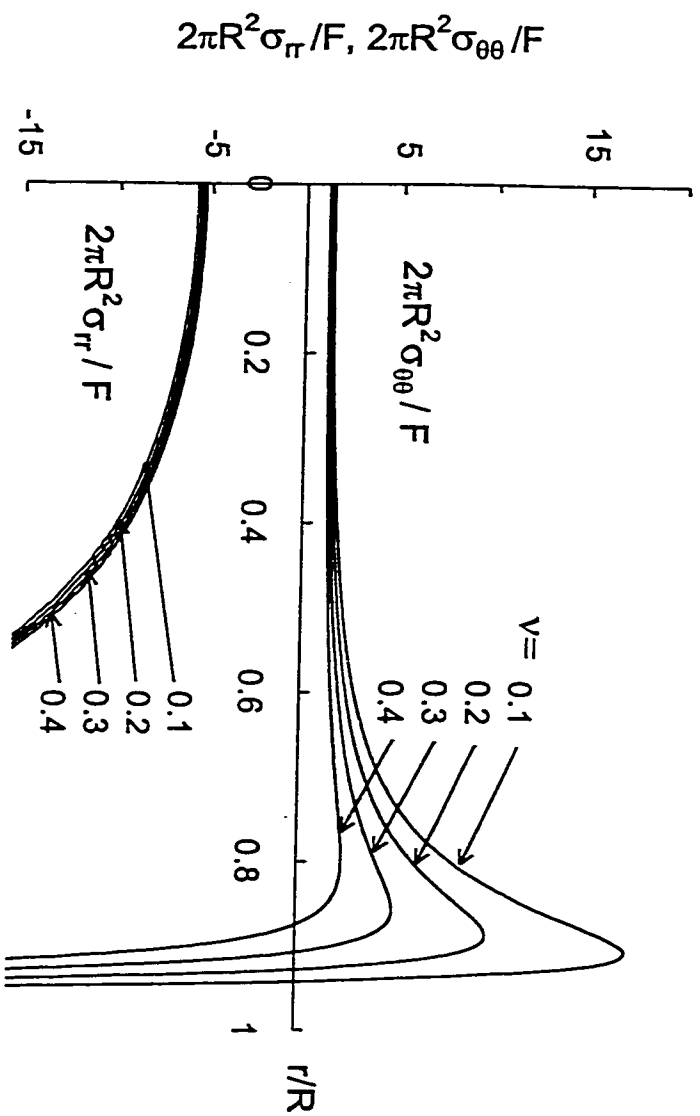


**Fig. 2-4** The normalized stresses  $2\pi R^2 \sigma_{rr}/F$  and  $2\pi R^2 \sigma_{\theta\theta}/F$  versus the normalized radial coordinate  $r/R$  (along  $z$ -axis or with  $\theta = 0^\circ$ ) for various values of Poisson's ratio of isotropic spheres (i.e.  $\bar{\nu} = \nu' = \nu$ ) for  $\theta_0 = 3^\circ$



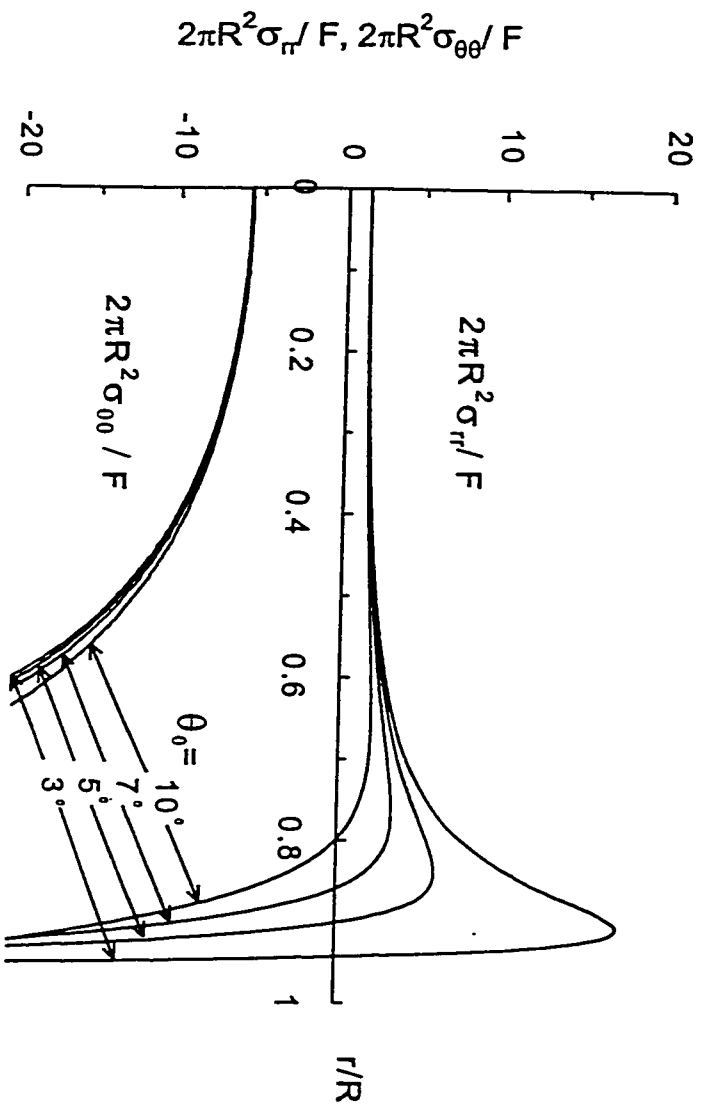


**Fig. 2-5** The normalized stresses  $2\pi R^2 \sigma_r / F$  and  $2\pi R^2 \sigma_{\theta\theta} / F$  versus the normalized radial coordinate  $r/R$  (along z-axis or with  $\theta = 0^\circ$ ) for various values of  $\theta_0$  for isotropic spheres with  $\bar{\nu} = 0.1$

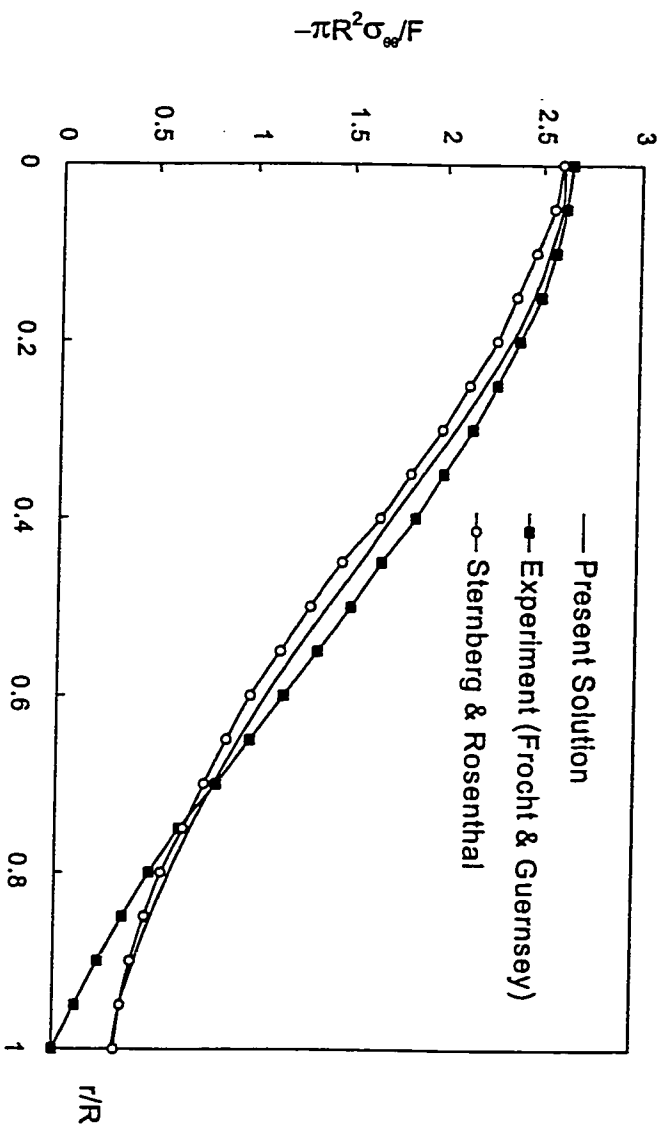


**Fig. 2-6** The normalized tangential Stress  $-\pi R^2 \sigma_{\theta\theta} / F$  versus the horizontal axis  $r/R$  (with  $\theta = \pi / 2$ ) for isotropic sphere with  $\bar{\nu} = 0.48$ . The line with squares is the experimental result by Frocht and Guernsey (1953), the line with open circles is the solution by Sternberg & Rosenthal (1952), and the solid line is our prediction for  $\theta_0 = 5^\circ$

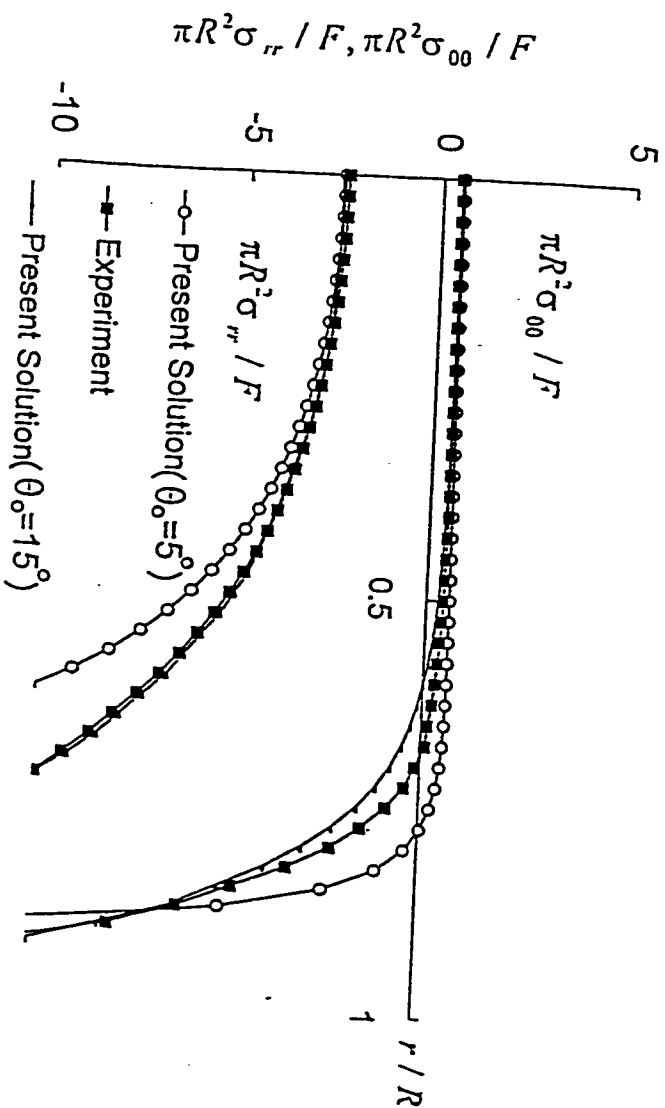
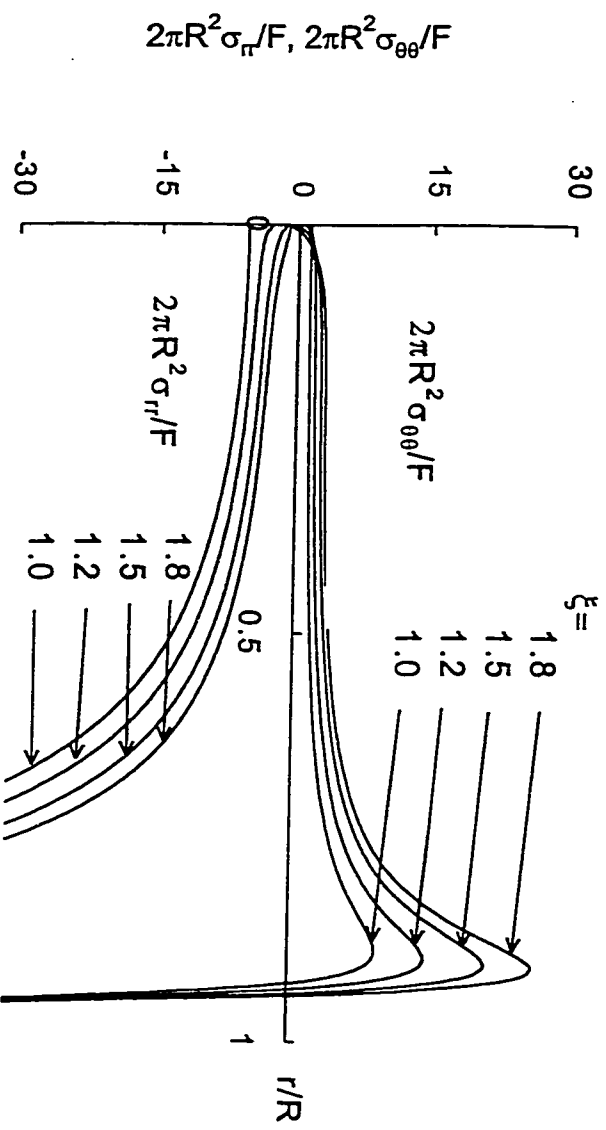


Fig. 2-7 Comparisons of the present solutions and the experimental results by Frocht and Guemsey (1953) for the normalized stresses  $\pi R^2 \sigma_{rr} / F$  and  $\pi R^2 \sigma_{\theta\theta} / F$  versus the normalized radial coordinate  $r/R$  (along z-axis or with  $\theta = 0^\circ$ ) for  $\bar{\nu} = \nu' = 0.48$ . Our predictions for  $\theta_0 = 5^\circ$  and  $\theta_0 = 15^\circ$  are given in lines with circles and solid lines respectively, while the experimental results are given in lines with squares.



**Fig. 2-8** The normalized stresses  $2\pi R^2 \sigma_{rr}/F$  and  $2\pi R^2 \sigma_{\theta\theta}/F$  versus the normalized radial coordinate  $r/R$  (along z-axis

or with  $\theta = 0^\circ$ ) for various values of modulus ratio  $\beta$  ( $=E/E'$ ) of anisotropic spheres with

$\alpha = 1.0, \bar{\nu} = 0.2, \xi = 1.0$  and  $\theta_0 = 3^\circ$

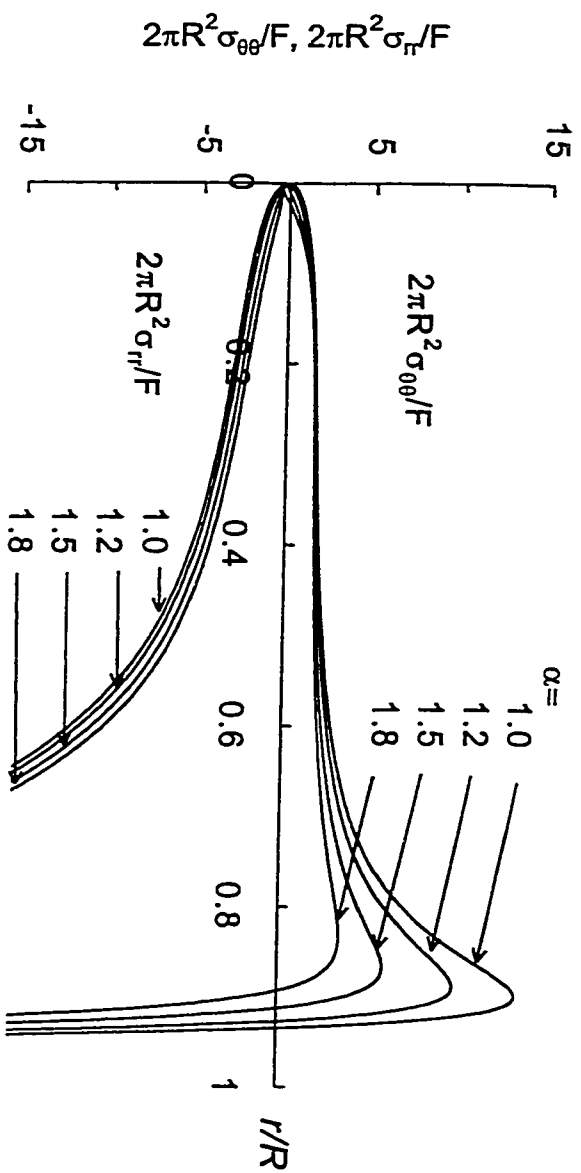


**Fig. 2-9** The normalized stresses  $2\pi R^2 \sigma_{rr}/F$  and  $2\pi R^2 \sigma_{\theta\theta}/F$  versus the normalized radial coordinate  $r/R$  (along z-axis

or with  $\theta = 0^\circ$ ) for various values of  $\alpha$  ( $=\bar{\nu}'/\bar{\nu}$ ) for anisotropic spheres with  $\beta = 1.5$ ,  $\bar{\nu} = 0.2$ ,  $\xi = 1.0$  and

$$\theta_0 = 3^\circ$$

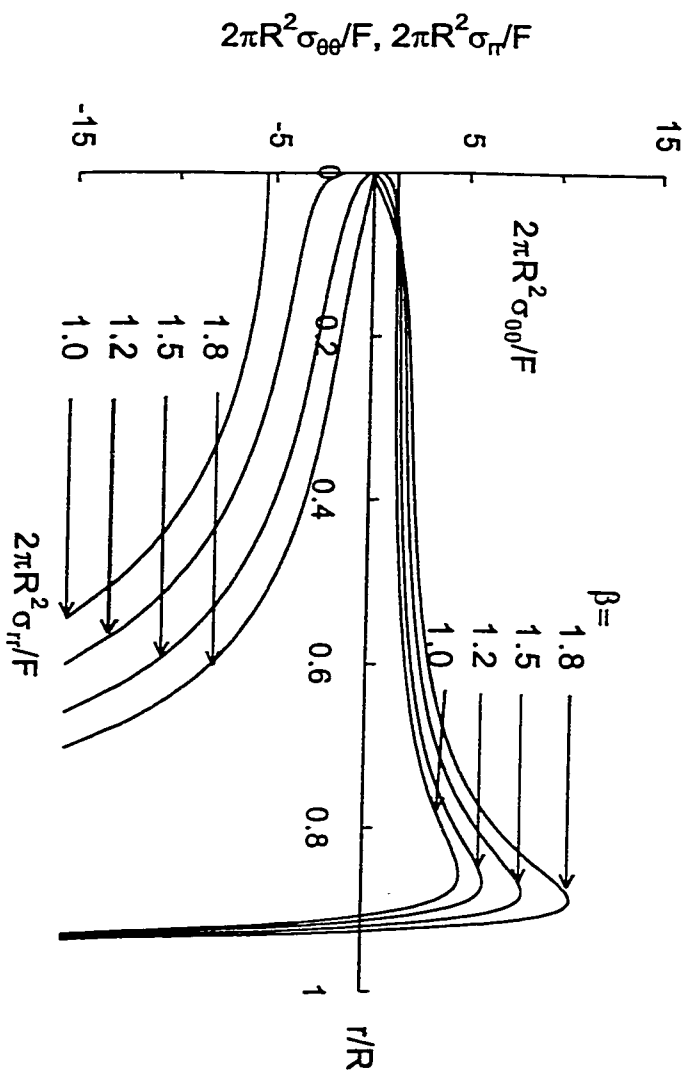


**Fig. 2-10** The normalized stresses  $2\pi R^2 \sigma_{rr}/F$  and  $2\pi R^2 \sigma_{\theta\theta}/F$  versus the normalized radial coordinate  $r/R$  (along  $z$ -axis or with  $\theta = 0^\circ$ ) for various values of  $\xi$  ( $=A_{44}/A_{66}$ ) for anisotropic spheres with  $\beta = 1.0, \bar{\nu} = 0.2, \alpha = 1.0$  and  $\theta_0 = 3^\circ$

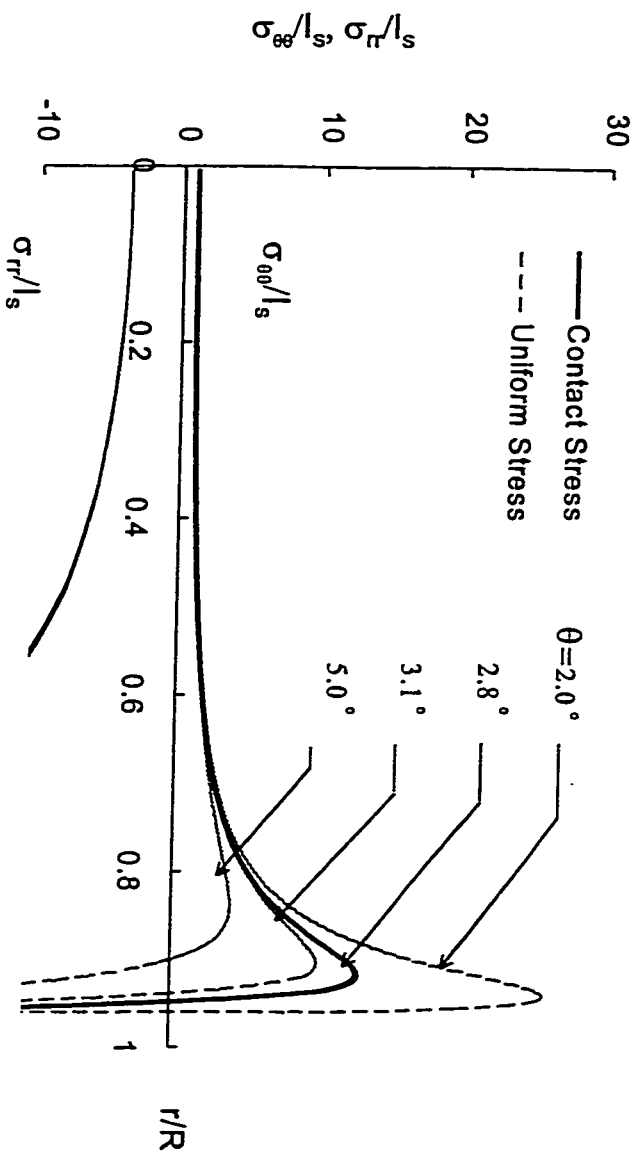


**Fig. 2-11** The normalized radial and tangential stresses along the line between the center of the sphere and one of the point loads under the action of uniform stress and contact stress for  $E=18\text{GPa}$ ,  $\nu=0.1$ ,  $D=50\text{mm}$  and  $P=15\text{kN}$

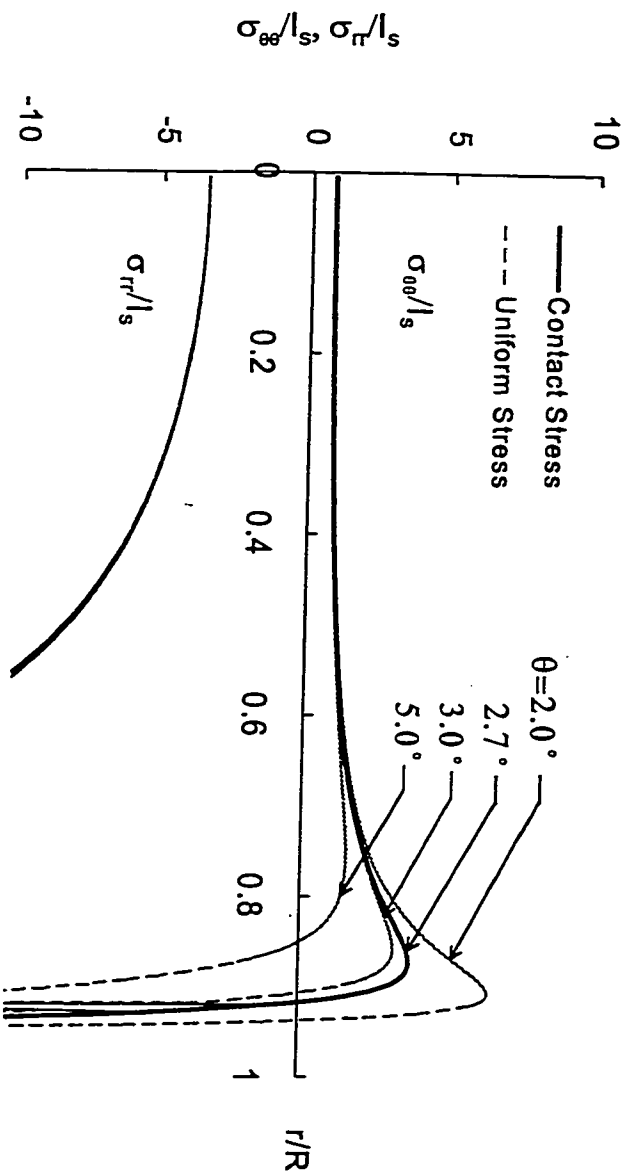


**Fig. 2-12** The normalized radial and tangential stresses along the line between the center of the sphere and one of the point loads under the action of uniform stress and contact stress for  $E=18\text{GPa}$ ,  $\nu = 0.3$ ,  $D=50\text{mm}$  and  $P = 15\text{kN}$



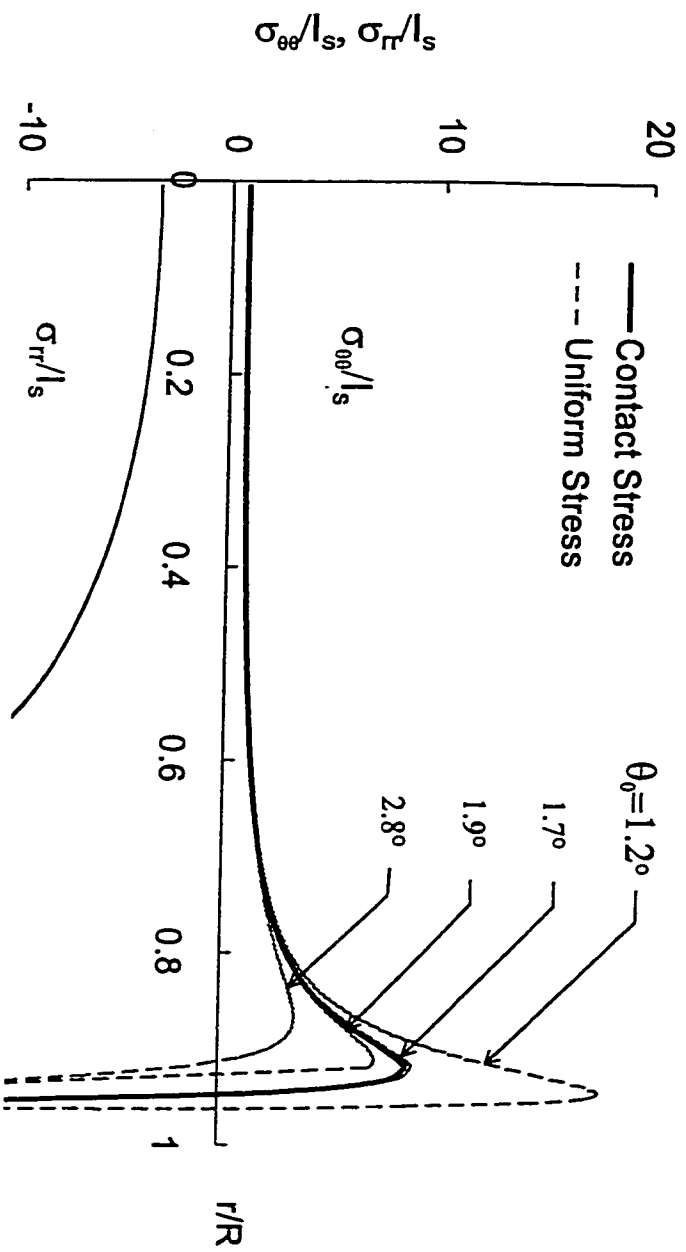


**Fig. 2-13** The normalized radial and tangential stresses along the line between the center of the sphere and one of the point loads under the action of uniform stress and contact stress for  $E=70\text{GPa}$ ,  $\nu=0.1$ ,  $D=50\text{mm}$  and  $P=15\text{kN}$

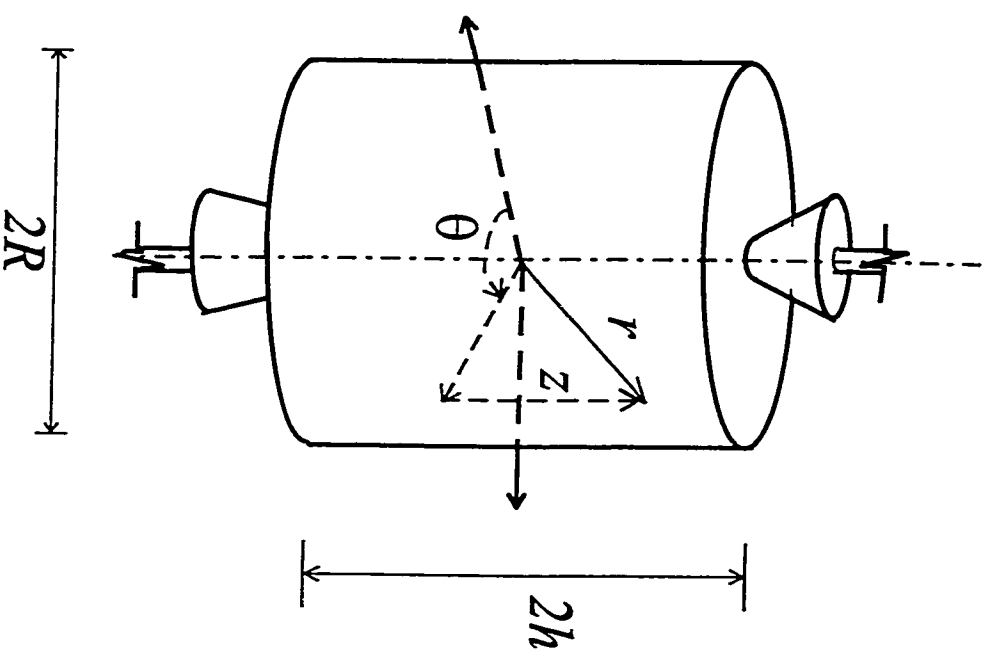


**Fig. 3-1** A sketch for the axial Point Load Strength Test for a cylindrical rock core of radius  $R$  and length  $2h$ . The origin and  $z$ -axis of the coordinates is set at the center of the cylinder and the axis of revolution

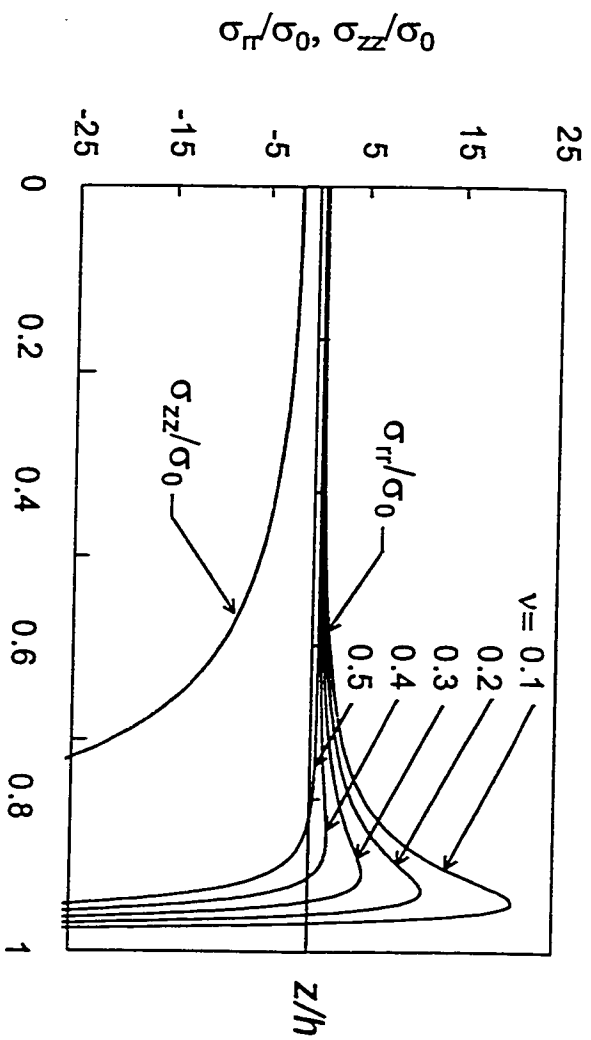
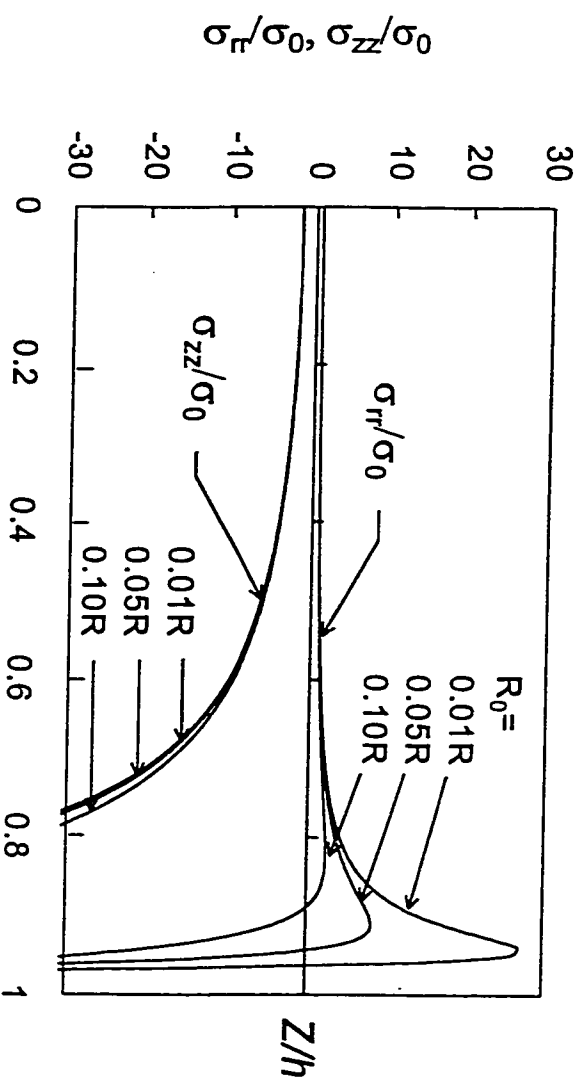
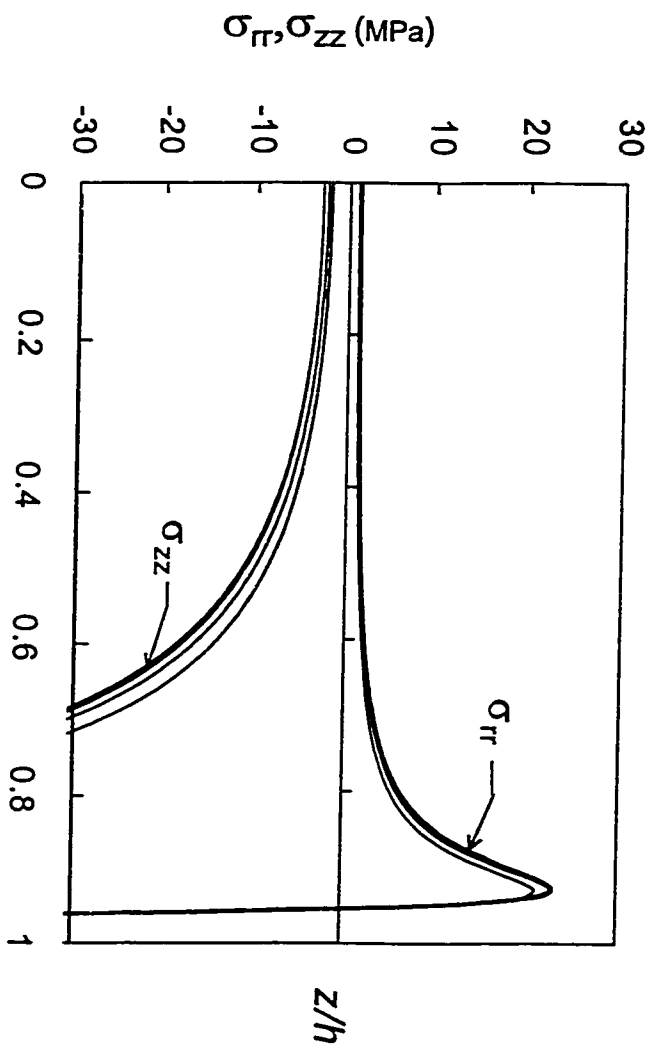


Fig. 3-2 The normalized stresses  $\sigma_r/\sigma_0$  and  $\sigma_{zz}/\sigma_0$  versus the normalized distance  $z/h$  along the  $z$ -axis for various values of Poisson's ratio  $\nu$  for  $H/D = 1.1$ ,  $D = 2R = 50mm$ , and  $R_0 = 0.05R$



**Fig.3-3** The normalized stresses  $\sigma_\pi/\sigma_0$  and  $\sigma_{zz}/\sigma_0$  versus the normalized distance  $z/h$  along the  $z$ -axis for various diameter  $R_0$  of the contact area for  $H/D=1.1$ ,  $D=2R=50mm$ , and  $\nu=0.25$



**Fig. 3-4** Stresses  $\sigma_{rr}$  and  $\sigma_{zz}$  versus the normalized distance  $z/h$  along the  $z$ -axis for four specimens of  $H/D=1.1$ ,  $D=56\text{mm}$ ,  $\nu = 0.25$  under the critical load  $P$

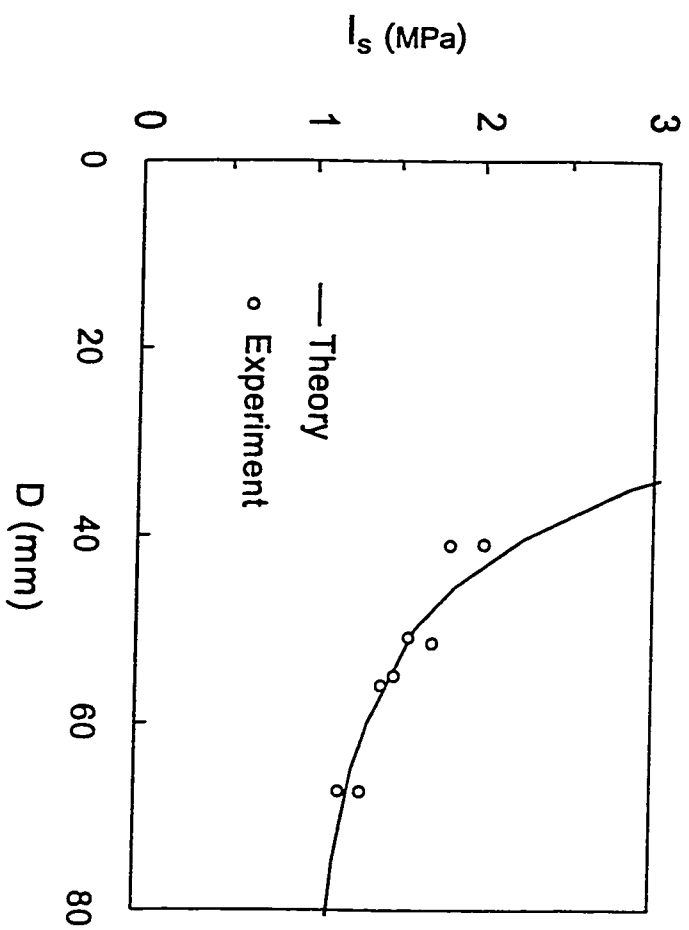


**Fig. 3-5** Comparisons of the theoretical predictions and the experimental results for the Point Load strength Index  $I_s$  versus diameter for a fixed length/diameter Ratio  $H/D=1.1$ , and  $\nu = 0.25$

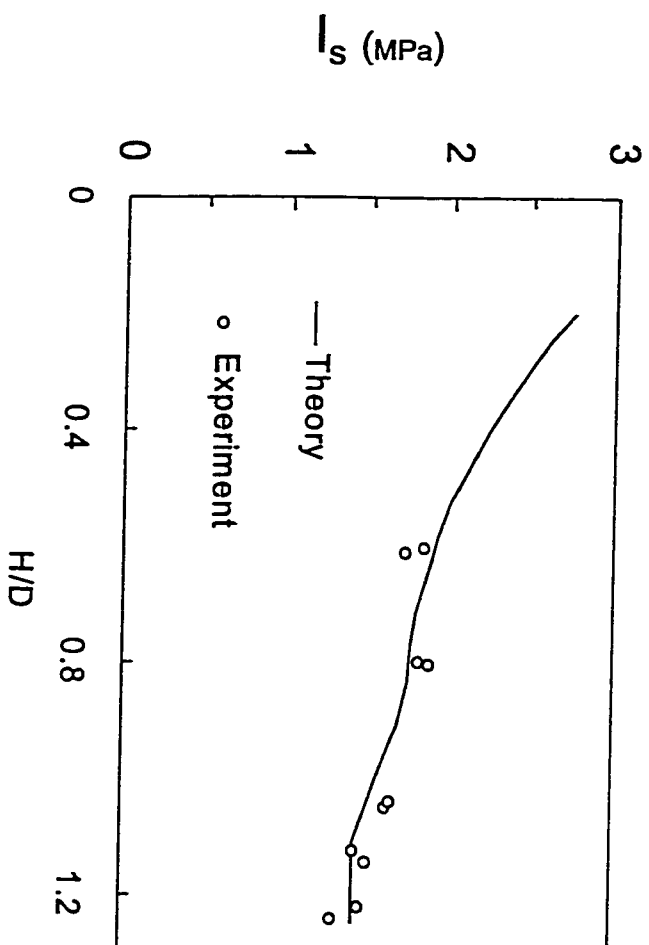


**Fig. 3-6** Comparisons of the theoretical predictions and the experimental results for the Point Load Strength Index  $I_s$  versus length/diameter Ratio for a fixed diameter  $D=56\text{mm}$ , and  $\nu = 0.25$

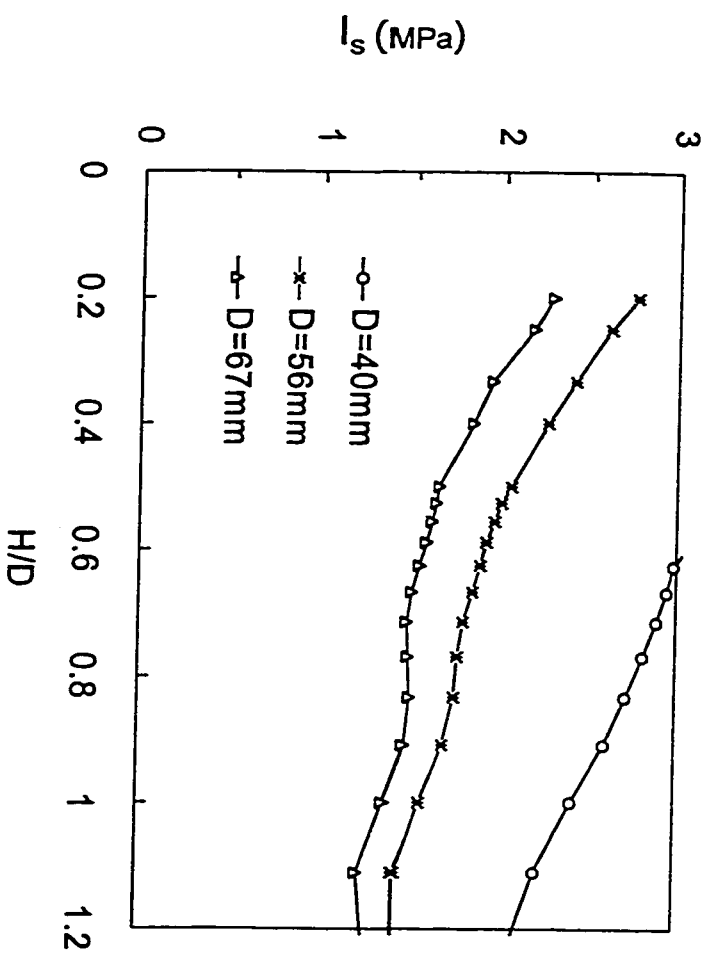


**Fig 3-7** Theoretical predictions for the Point Load Strength Index  $I_s$  versus length/diameter ratio for various diameters for Poisson's ratio  $\nu = 0.25$



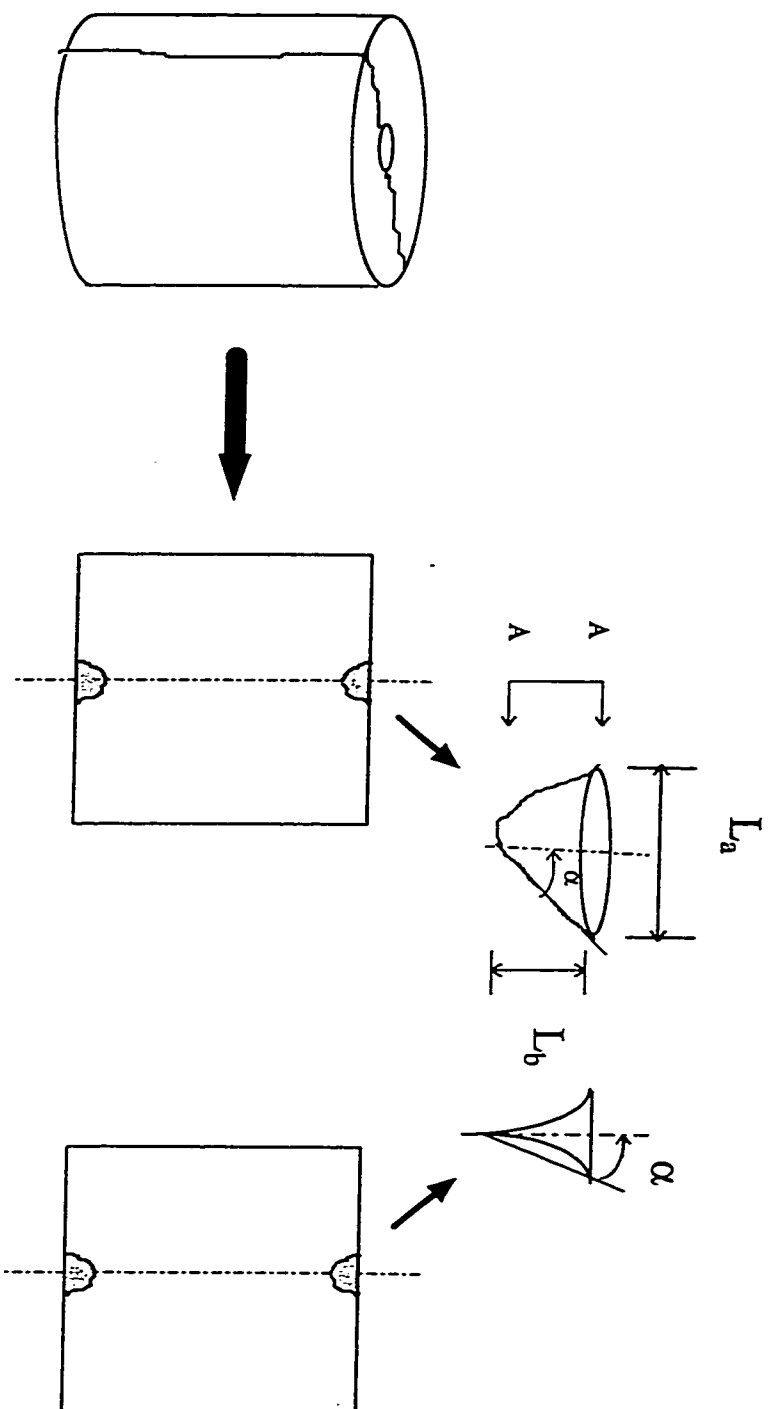


**Fig. 3-8** A sketch showing the failure pattern of a solid cylinder of plaster material under the axial PLST if the specimen breaks into two pieces along a flat surface

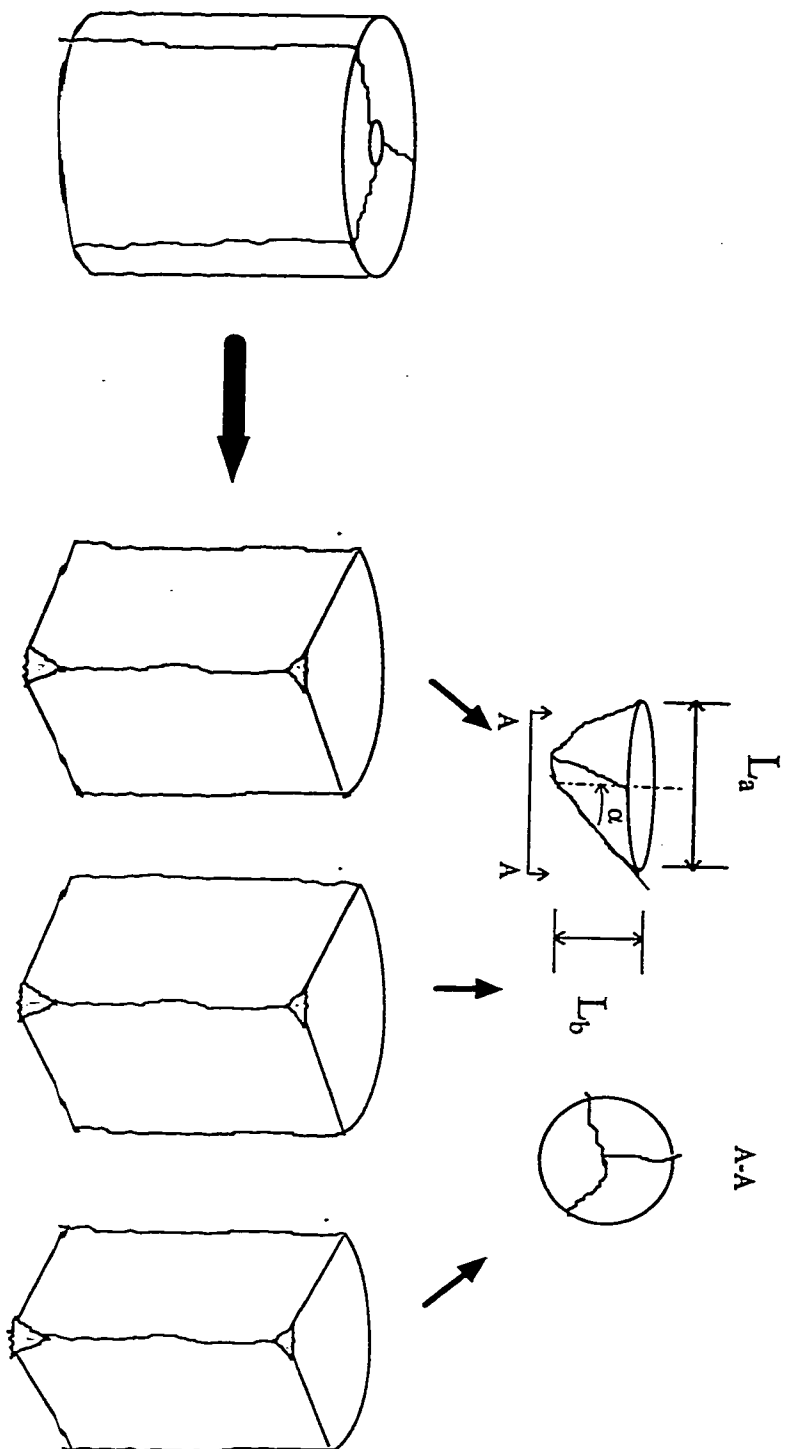


**Fig. 3-9** A sketch showing the failure pattern of a solid cylinder of plaster material under the axial PLST if the specimen breaks into three pieces

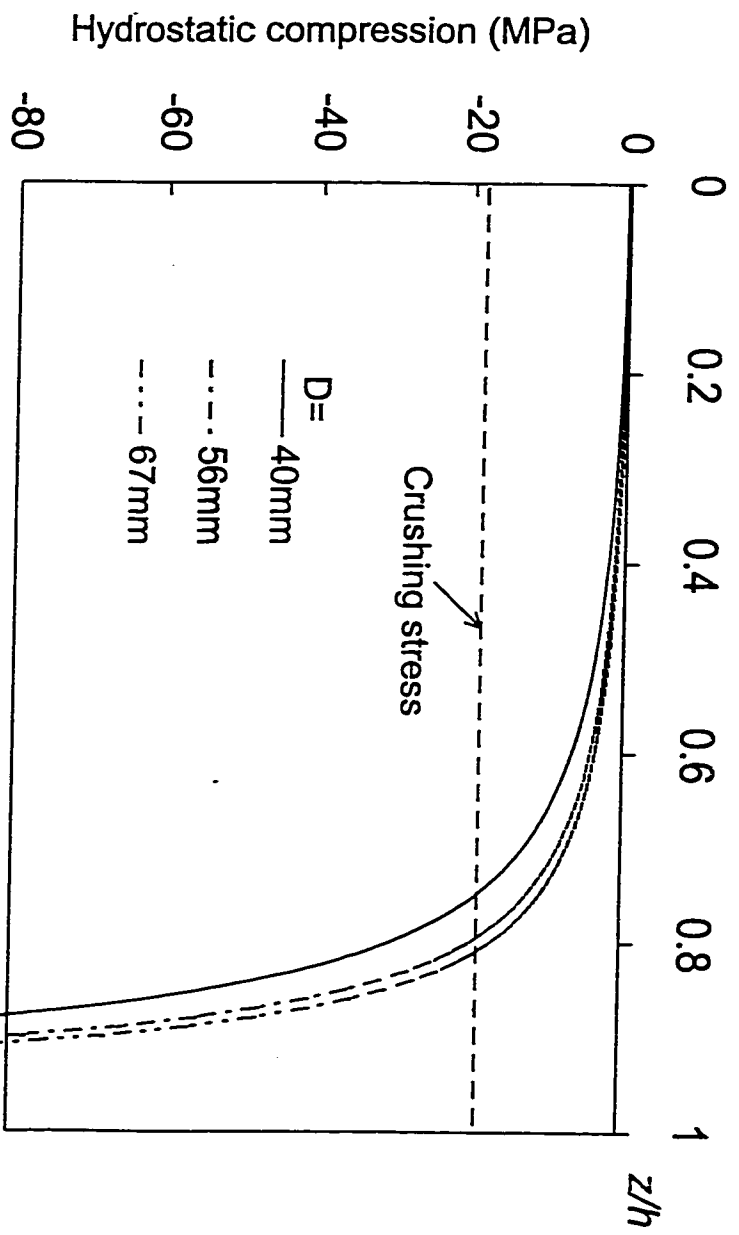


**Fig. 3-10** Theoretical predictions for the hydrostatic stress versus the normalized distance  $z/h$  along the  $z$ -axis for different diameters for Poisson's ratio  $\nu = 0.25$ , together with the crushing pressure interpreted from Zhang et al. (1990)

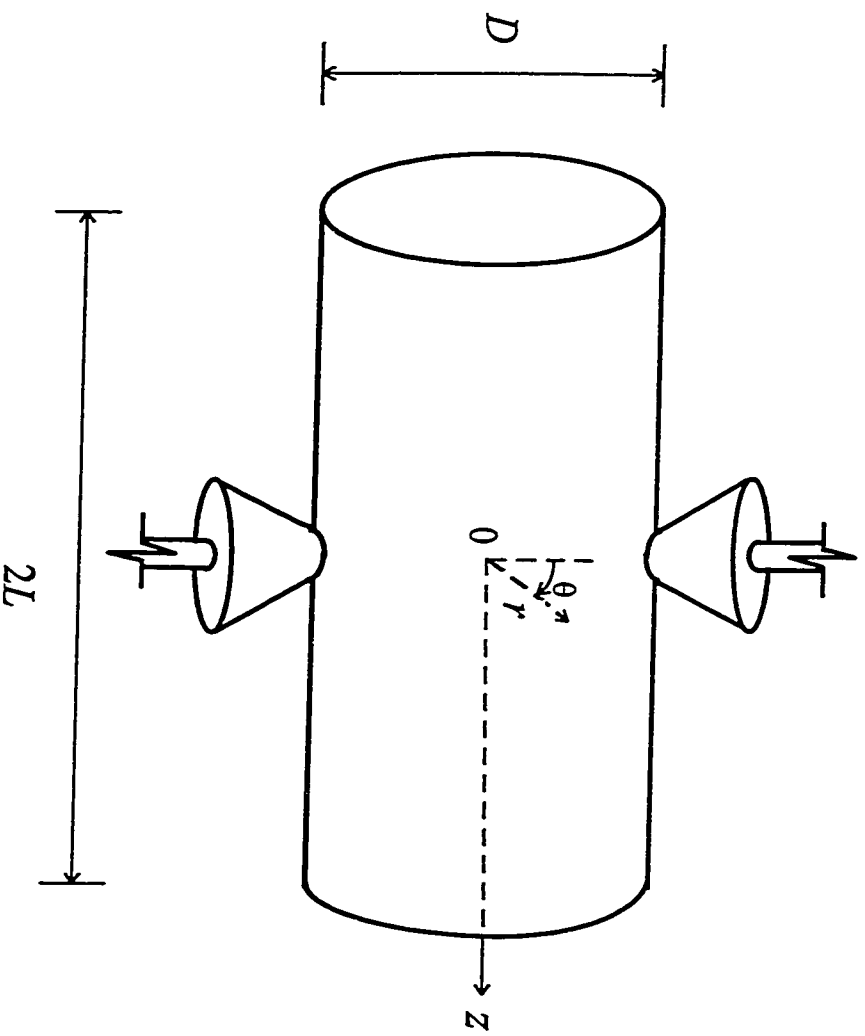


**Fig. 4-1** A cylindrical rock specimen subjected to the diametral Point Load Strength Test (PLST)

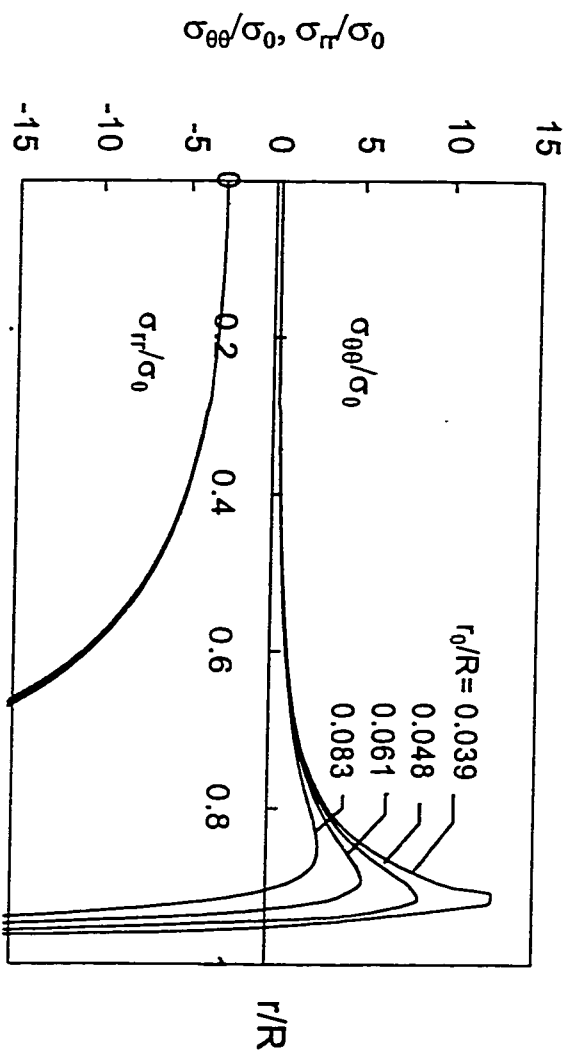


**Fig. 4-2** The normalized stresses  $\sigma_{\theta\theta}/\sigma_0$ , and  $\sigma_{rr}/\sigma_0$  versus  $r/R$  for various values of  $r_0/R$  and for  $\nu=0.25$ ,  $L/D=1.4$  and  $R_j=5\text{mm}$

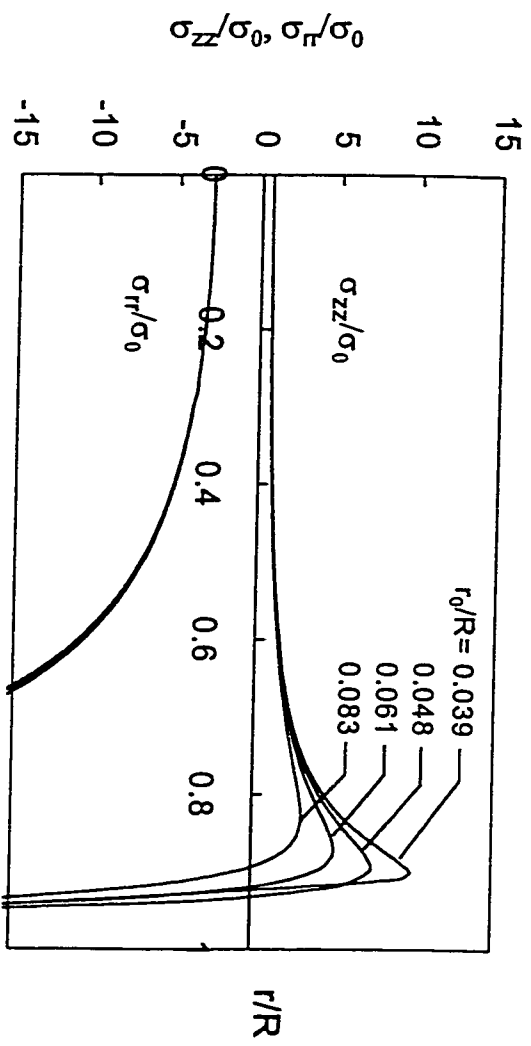
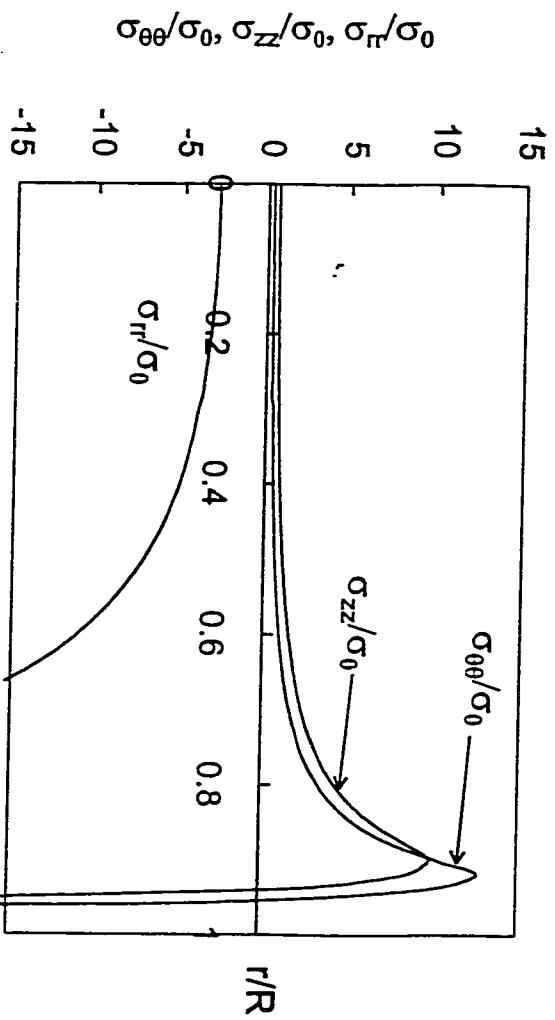
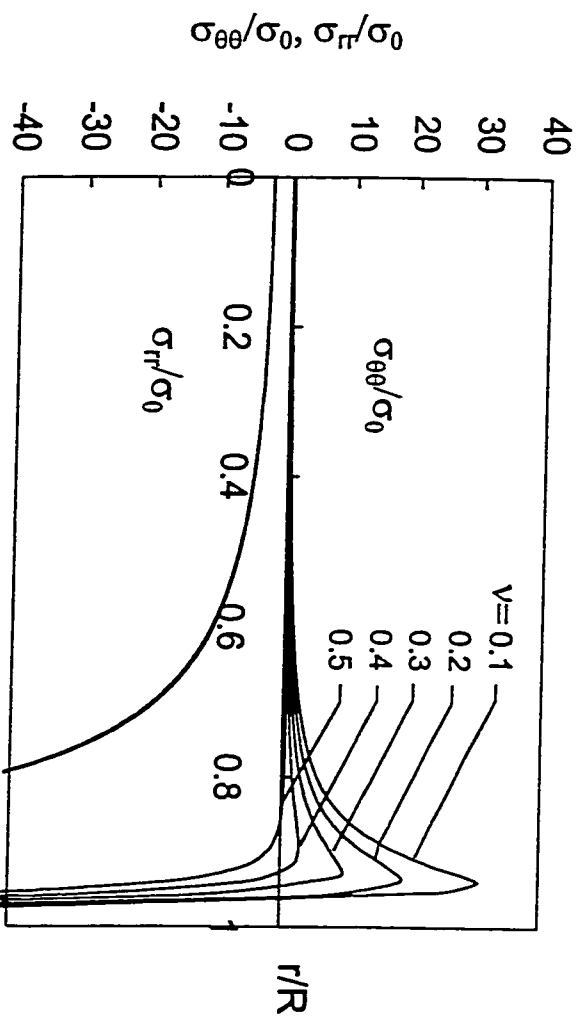


Fig. 4-3 The normalized stresses  $\sigma_{\infty}/\sigma_0$ , and  $\sigma_r/\sigma_0$  versus  $r/R$  for various values of  $r_0/R$  and for  $\nu=0.25$ ,  $L/D=1.4$  and  $R_2=5\text{mm}$



**Fig. 4-4** A typical stress distribution of the normalized stresses  $\sigma_{\theta\theta}/\sigma_0$ ,  $\sigma_{zz}/\sigma_0$  and  $\sigma_{rr}/\sigma_0$  versus  $r/R$  for  $\nu=0.25$  and  $r_0/R = 0.039$



**Fig. 4-5** The normalized stresses  $\sigma_{\theta\theta}/\sigma_0$ , and  $\sigma_{rr}/\sigma_0$  versus  $r/R$  for various values of  $\nu$  and  $r_0/R = 0.039$



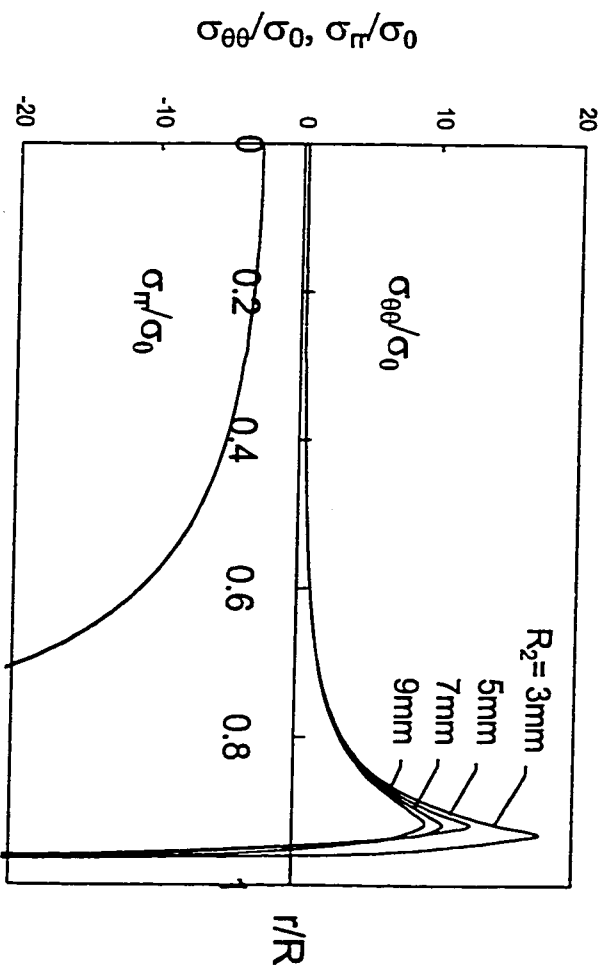


**Fig. 4-6** The normalized stresses  $\sigma_{\theta\theta}/\sigma_0$  and  $\sigma_{rr}/\sigma_0$  versus  $r/R$  for various values of  $R_2$  and  $r_0/R = 0.039$

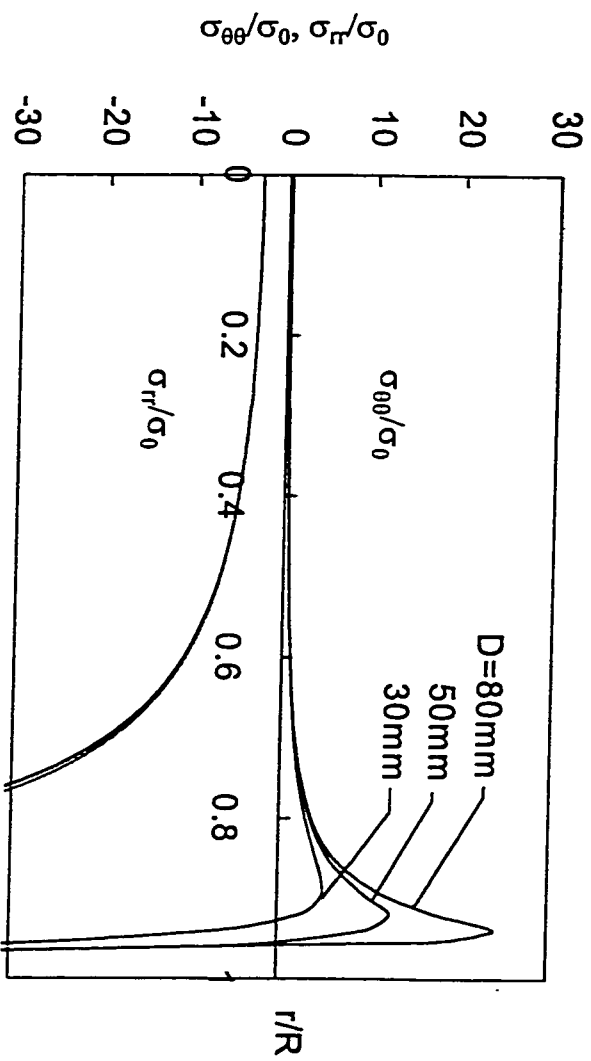


**Fig. 4-7** The normalized stresses  $\sigma_{\theta}/\sigma_0$ ,  $\sigma_r/\sigma_0$ , and  $\sigma_{\phi}/\sigma_0$  versus  $r/R$  for various values of  $D$  and  $r_0/R = 0.039$

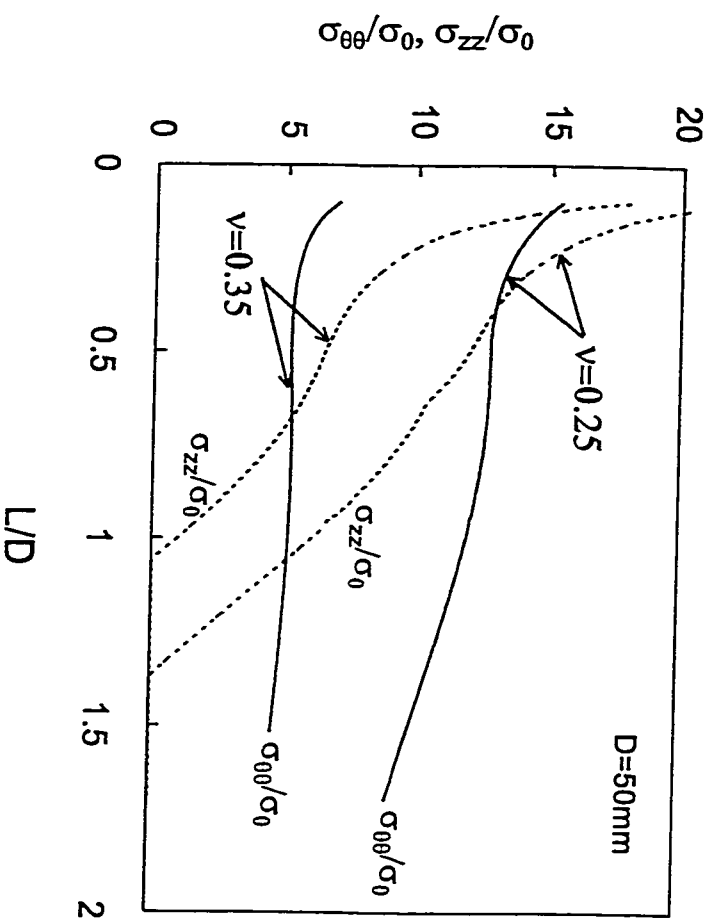


**Fig. 4-8** The normalized tensile stresses  $\sigma_{\theta\theta}/\sigma_0$  and  $\sigma_{zz}/\sigma_0$  versus  $L/D$  for various values of  $\nu$  and for  $D=50\text{mm}$  and  $r_0/R = 0.039$ . The dotted and solid lines are for the axial and hoop stresses respectively

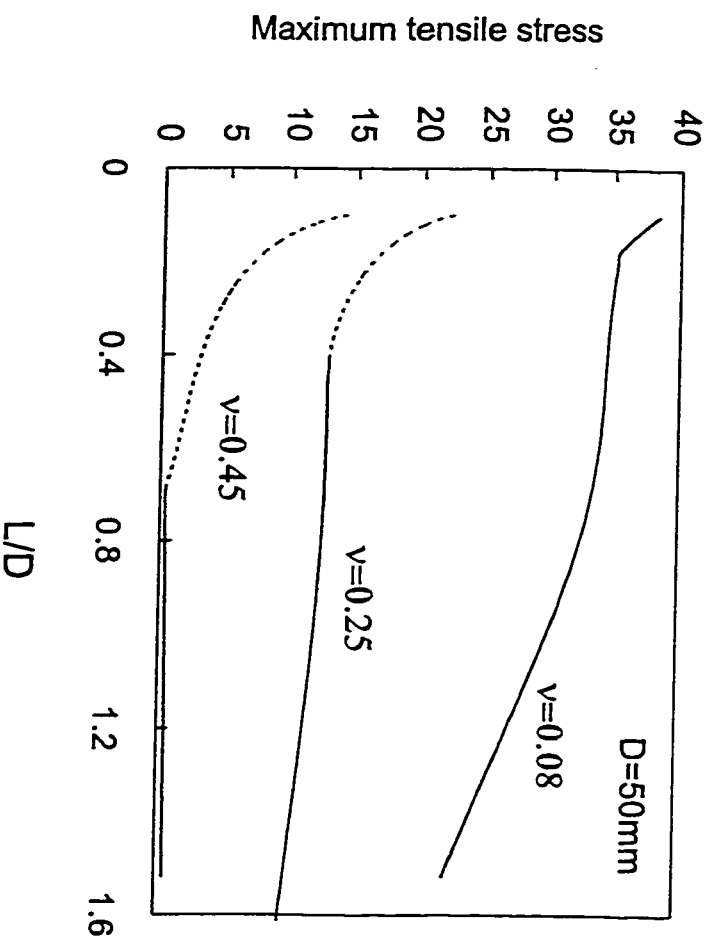


**Fig. 4-9** The maximum tensile stress envelopes versus  $L/D$  for various values of  $\nu$  and for  $D=50\text{mm}$ . The dotted and solid lines are for axial and hoop stresses respectively

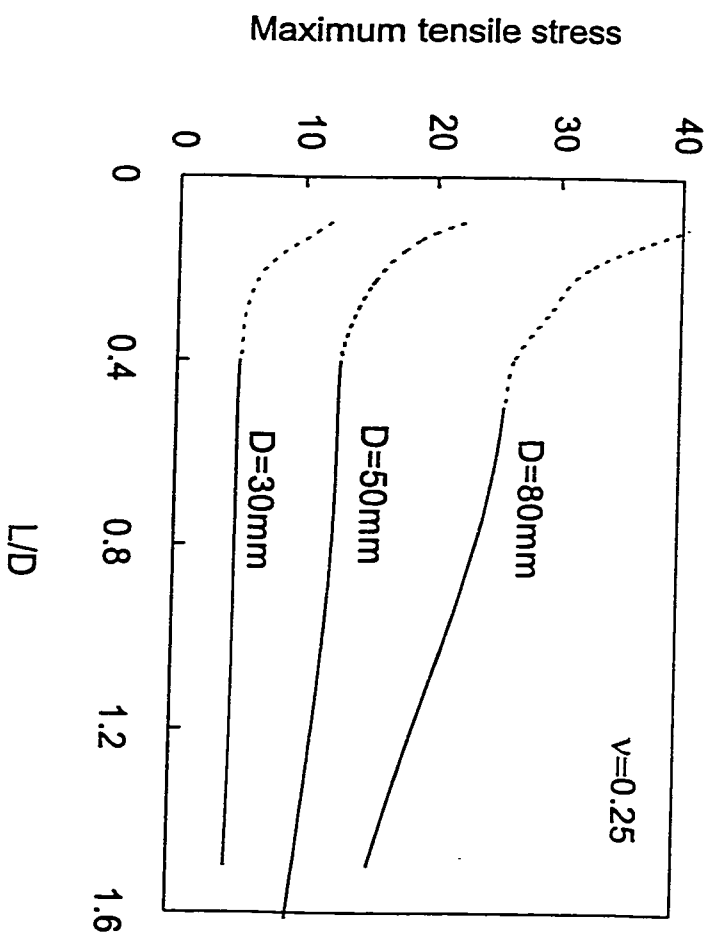


**Fig. 4-10** The maximum tensile stress envelopes versus  $L/D$  for various values of  $D$  and for  $\nu=0.25$ . The dotted and solid lines are for axial and hoop stresses respectively

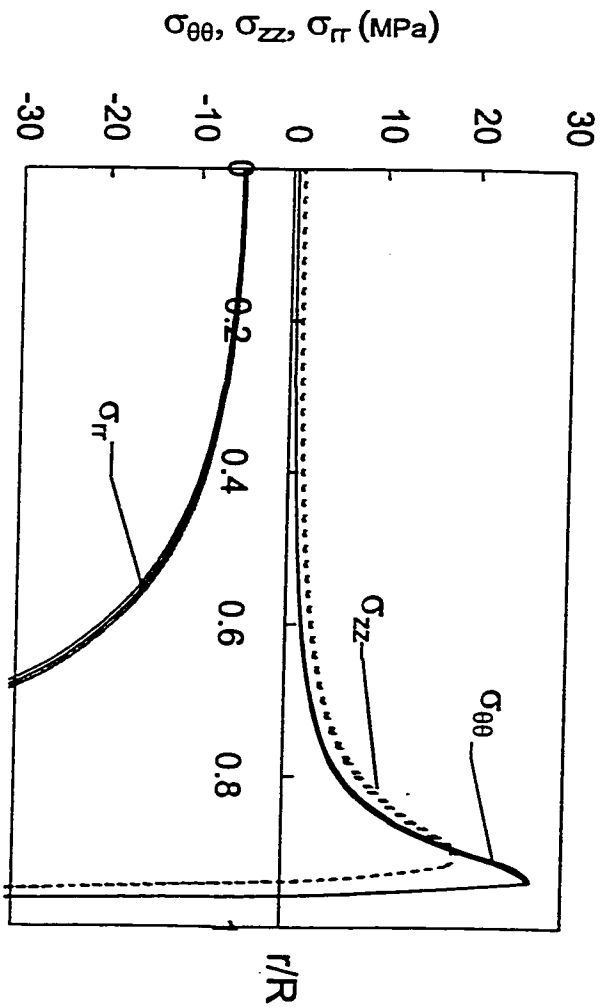


**Fig. 4-11** The theoretical stress distributions for  $\sigma_{\theta\theta}$ ,  $\sigma_{rr}$  and  $\sigma_{zz}$  versus  $r/R$  for three plaster specimens of size  $D=56\text{mm}$  ( $\nu=0.25$  and  $E=17.5\text{GPa}$ )

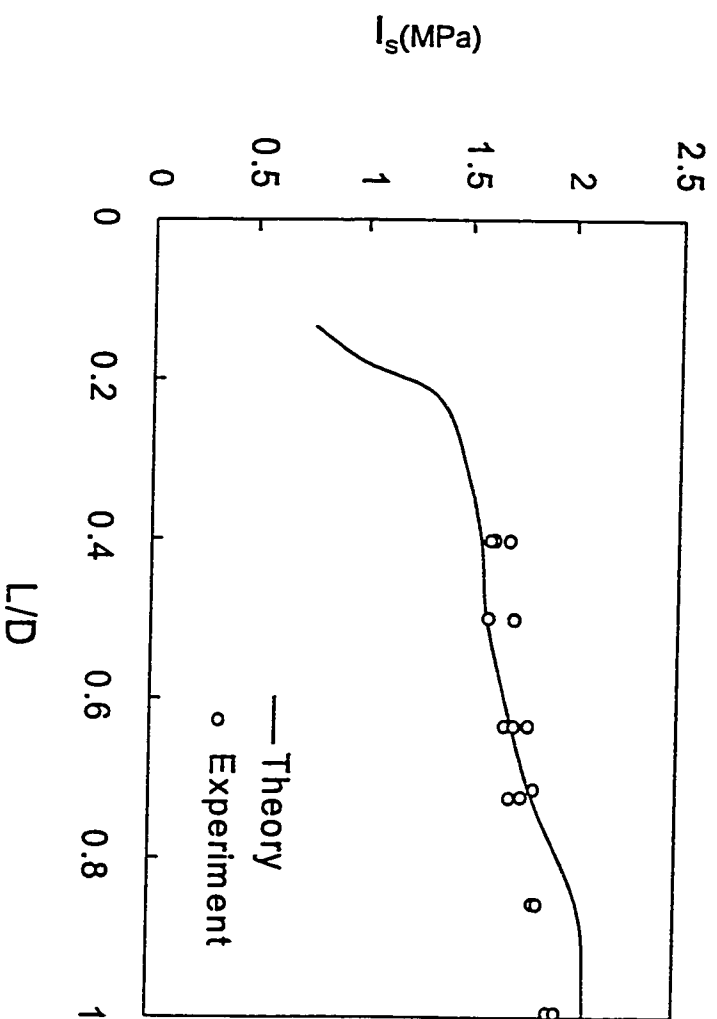


**Fig. 4-12** The theoretical and experimental point load strength index ( $I_s = P/D^2$ ) versus the geometric ratio  $D/L$  for the rock-like plaster material and for  $D=56\text{mm}$

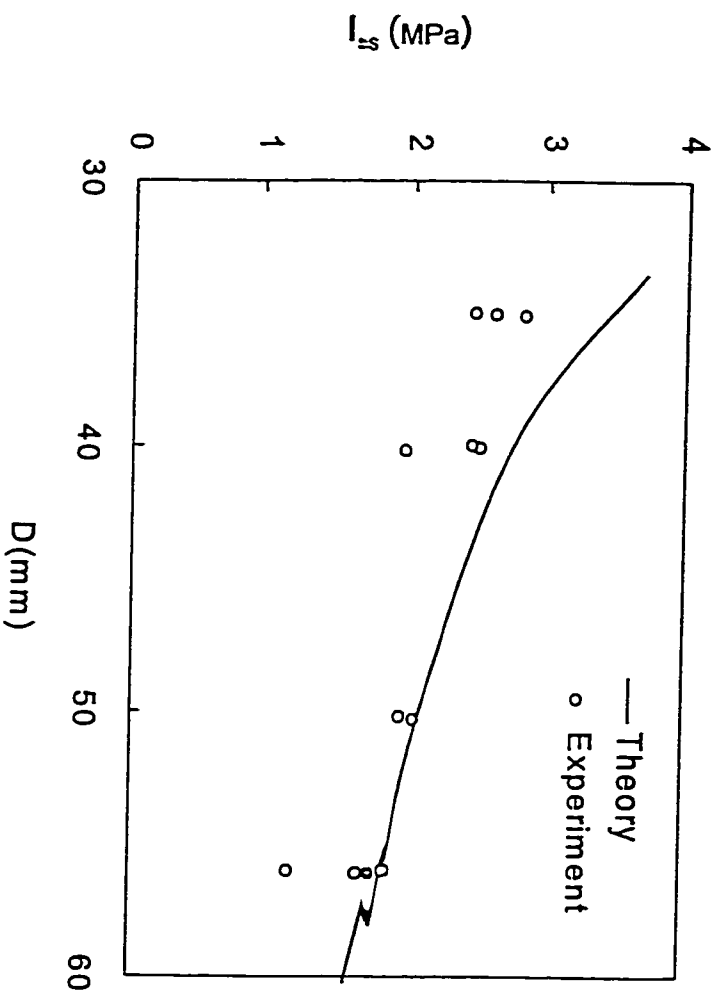


**Fig. 4-13** The theoretical and experimental point load strength index ( $I_p = P/D^2$ ) versus the diameter  $D$  for the rock-like plaster material for  $L/D=0.7$



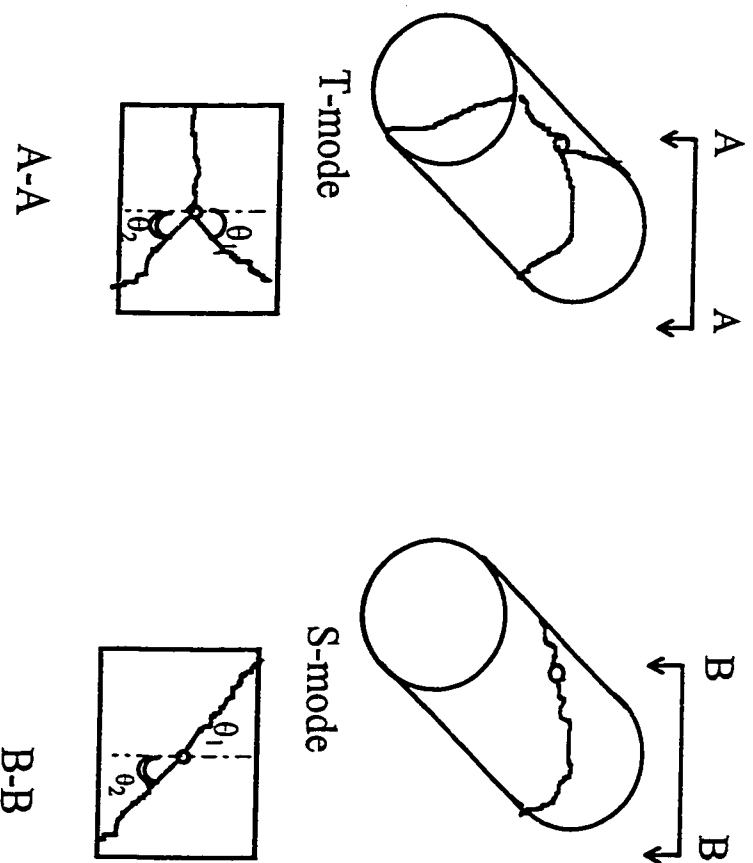


**Fig. 4-14** A sketch of the two failure modes (T-mode and S-mode) of cylinders under the diametral point load strength test ( $\theta_1$  and  $\theta_2$  are defined as the two minimum angles between the cracks and the transverse line joining the two applied point loads)

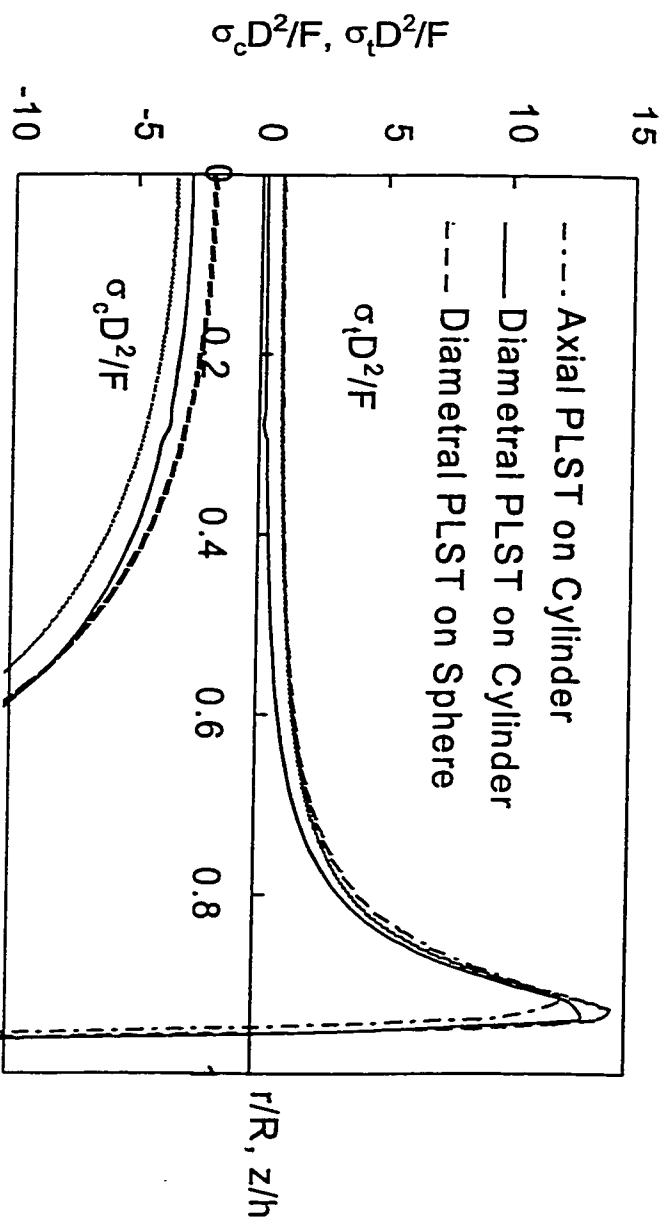


**Fig. 5-1** The normalized tensile stress  $\sigma_t D^2 / F$  and compressive stress  $\sigma_c D^2 / F$  versus the normalized distance  $r/R$  or  $z/h$  for cylinders and spheres under the axial and diametral PLST for  $D=50\text{mm}$

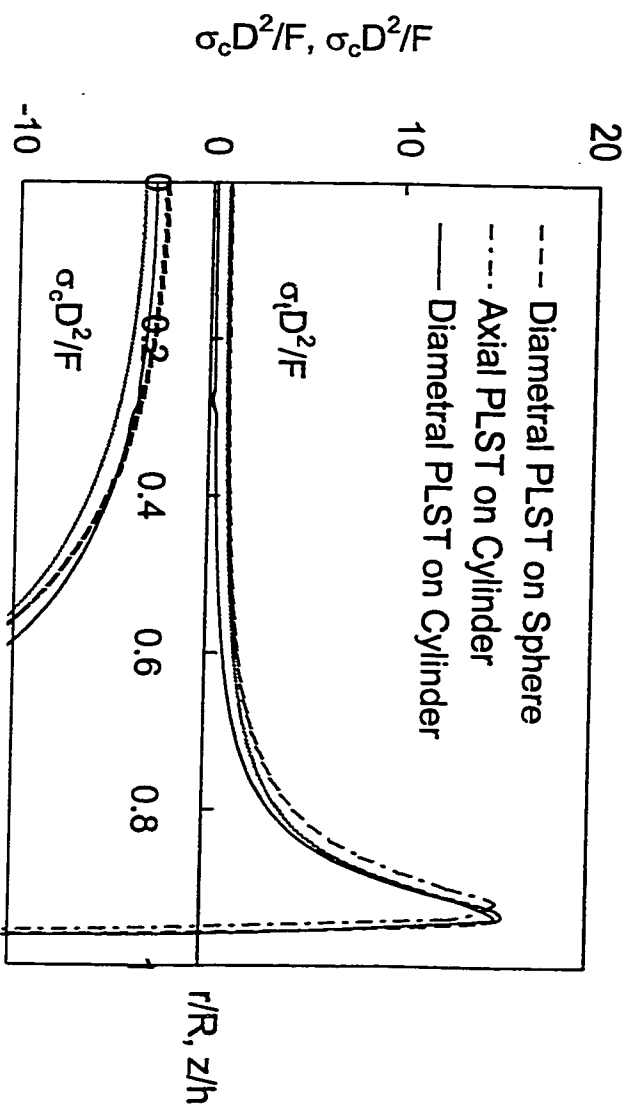


**Fig. 5-2** The normalized tensile stress  $\sigma_l D^2 / F$  and compressive stress  $\sigma_c D^2 / F$  versus the normalized distance  $r/R$  or  $z/h$  for cylinders and spheres under the axial and diametral PLST for  $D=60\text{mm}$

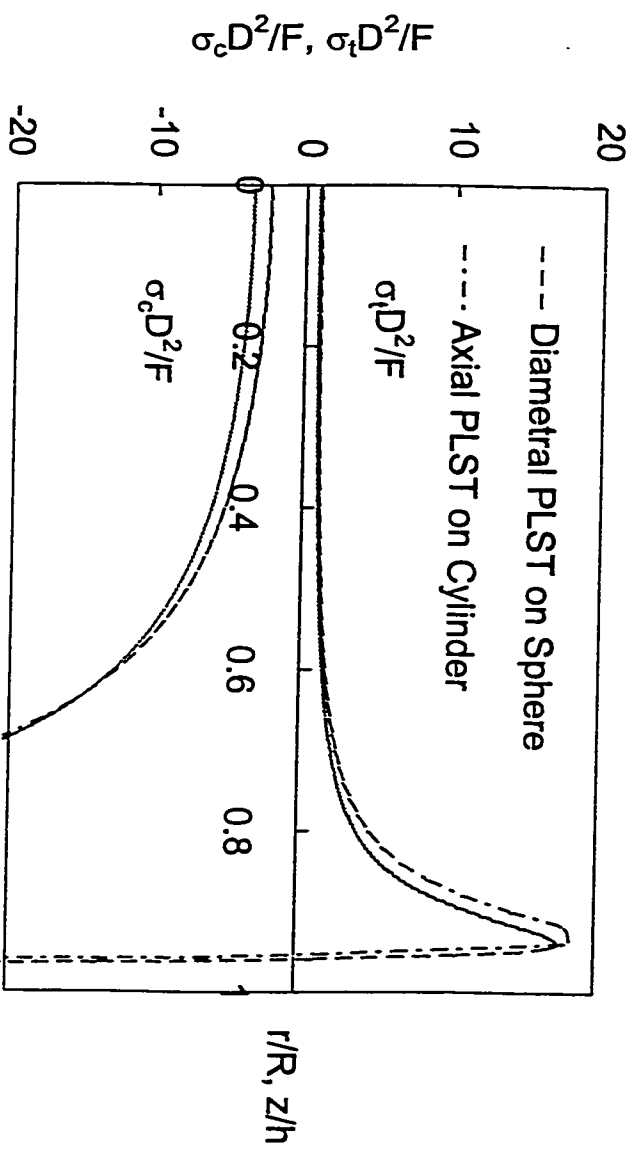


**Fig. 5-3** The normalized tensile stress  $\sigma_t D^2/F$  and compressive stress  $\sigma_c D^2/F$  versus the normalized distance  $r/R$  or  $z/h$  for cylinders and spheres under the axial and diametral PLST for  $D=75\text{mm}$

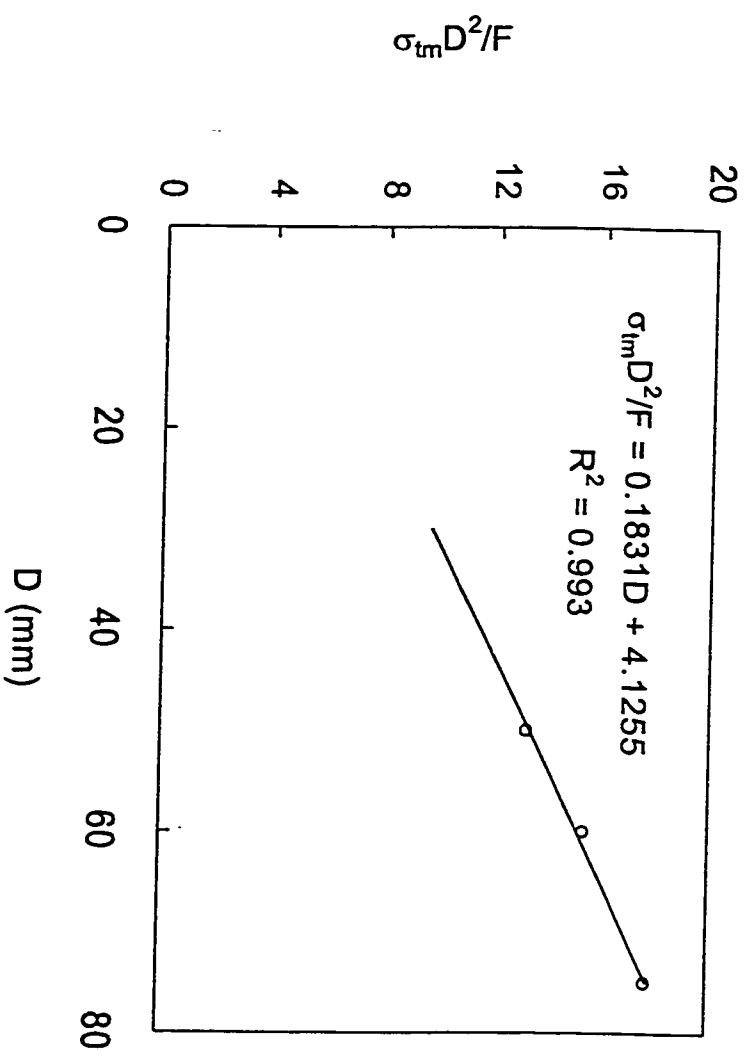


**Fig. 5-4** The normalized mean values of the maximum tensile stress  $\sigma_m D^2 / F$  versus different diameter  $D$

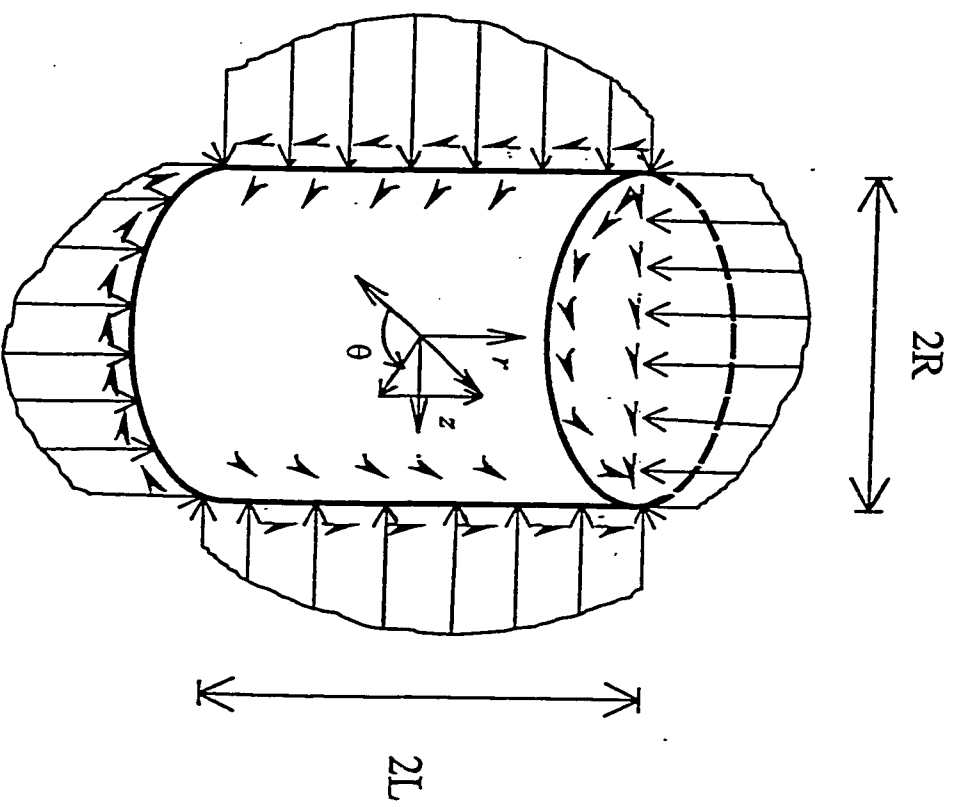


**Fig. 6-1** A sketch of a finite solid circular cylinder of length  $2L$  and radius  $R$  subjected to arbitrary tractions on the curved and end surfaces.

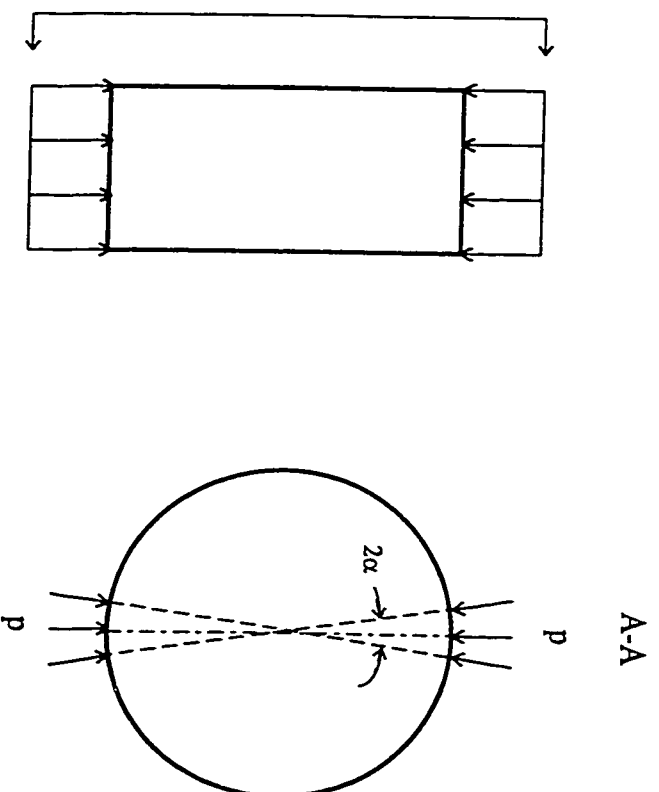


**Fig. 7-1** A cylinder under the Brazilian Test

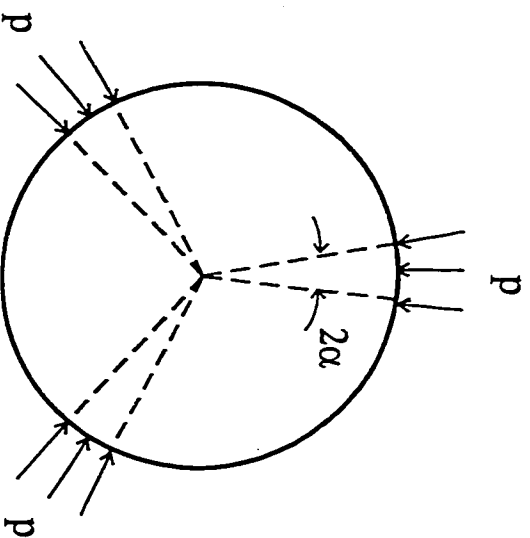


**Fig7-2** A cross-section of a cylinder under the modified Brazilian Test



## REFERENCES

- Abramian, B. L., Aruntunian, H. X. and Babloian, A. A. (1964). On two-contact problems for an elastic sphere. *Fizika Metall.*, **28**, 622-629 (in Russian).
- Abramowitz, M. and Stegun, I. A. (Eds.) (1965). *Handbook of Mathematical Functions*, Dover, New York.
- Al-chalabi, M. and Huang, C.L. (1974). Stress distribution within circular cylinders in compression. *Int. J. Rock Mech. Min. Sci. & Geomech. Abstr.*, **11**, 45-56.
- Al-chalabi, M., McCormick, F. J. and Huang C. L. (1974). Strain distribution within compressed circular cylinders. *Experimental Mech.*, **14**, 497-561.
- Balla, A. (1960). Stress conditions in triaxial compression. *J. soil Mech. & Foundations Div., Proc ASCE*, **86**, 57-84.
- Bieniawski, Z. T. (1974). Estimating the strength of rock materials. *J. South Afr. Inst. Mining and Metall* **74**, 312-320.
- Boisen, B. P. (1977). A hand-portable point load tester for field measurements. In *Energy Resources and Excavation Technology. 18th US Sym. Rock Mech.*, F. D. Wang and G. B. Clark, eds., Keystone, Colo. pp. 5C2-1-5C2-4.
- Brady, B. T. (1971). An exact solution to the radially end-constrained circular cylinder under triaxial loading. *Int. J. Rock Mech. Min. Sci.*, **8**, 165-178.
- Broch, E. (1983). Estimation of strength anisotropy using the point load test. *Int. J. Rock Mech. Min. Sci.*, **20**, 181-187.
- Broch E. and Franklin J. A. (1972). The point-load strength test. *Int. J. Rock Mech. Min. Sci.*, **9**, 669-697.

- Brook N. (1977). The use of irregular specimens for rock strength tests. *Int. J. Rock Mech. Min. Sci. & Geomech. Abstr.*, **14**, 193-202.
- Brook N. (1980). Size correction for point load testing. *Int. J. Rock Mech. Min. Sci. & Geomech. Abstr.*, **17**, 231-235.
- Brook N. (1985). The equivalent core diameter method of size and shape correction in point load testing. *Int. J. Rock Mech. Min. Sci. & Geomech. Abstr.*, **22**, 61-70.
- Brown, J. W. and Churchill, R. (1993). *Fourier Series and Boundary Value Problems*. 5th Ed., McGraw-Hill International Editions, New York.
- Chau, K. T. (1995). Bifurcation of a spherical cavity in a compressible solid with spherical isotropy. *Int. J. Numer. Anal. Meth. Geomech.* **29**, 381-398.
- Chau, K. T. (1997). Young's modulus interpreted from compression tests with end friction. *J. Engng. Mech. ASCE*, **123**, 1-7.
- Chau, K.T. (1998a). Analytic solutions for diametral point load strength tests. *J. Engng. Mech. ASCE*, **124**, 875-883.
- Chau, K. T. (1998b). Author's closure to discussion by S. Watanabe on 'Young's modulus interpreted from compression tests with end friction'. *J. Engng. Mech. ASCE*, **124**, 1171-1174.
- Chau, K. T. (1998c). Toroidal vibrations of anisotropic spheres with spherical isotropy. *J. Appl. Mech. ASME*, **65**, 59-65.
- Chau K.T. and Wei X.X. (1999a). Spherically isotropic, elastic spheres subject to diametral point load strength test, *Int. J. of Solids and Struct.*, **36**, 4473-4496.

- Chau, K. T. and Wei, X. X. (1999b). A new analytic solution for the diametral point load strength test on finite solid circular cylinders. Submitted to *Int. J. Solids and Struct.*.
- Chau K.T. and Wei X.X. (1999c), Finite solid circular cylinders subjected to arbitrary surface load: part I. Analytic solution, submitted to *Int. J. of Solids and Struct.*.
- Chau, K. T. and Wong, R. H. C. (1996). Uniaxial compressive strength and point load strength of rocks. *Int. J. Rock Mech. Min. Sci. & Geomech. Abstr.*, **33**, 183-188.
- Chau, K.T. and Wong, R.H.C. (1998). Author's Reply to Discussion by T.Y. IRFAN and L.S. CHEUNG on 'Uniaxial Compressive Strength and Point Load Strength of Rocks' by K.T. CHAU and R.H.C. WONG. *Int. J. Rock Mech. Min. Sci.*, **35**, 103-106.
- Chen, W.F. and Yuan, R.L. (1980). Tensile strength of concrete: Double-punch test. *J. Struct. Div. ASCE*, **106**, 1673-1693.
- Chen, W. T. (1966). On some problems in spherically isotropic elastic materials. *J. Appl. Mech. ASME*, **61**, 964-970.
- Chen, T. L. and Durelli, A. J. (1973). Stress field in a sphere subjected to large deformation. *Int. J. Solids and Struct.*, **9**, 1035-1052.
- Chree, C. (1889). The equations of an isotropic elastic solid in polar and cylindrical coordinates, their solution and application. *Camb. Phil. Trans.*, **14**, 250.
- Diernat F and Duffaut P. (1966). Essais sur Echantillons des forms irreguliere. *Proc. 1st Cong. Int. Soc. Rock Mech., Lisbon*, pp405-409.
- Ding, H.-J., and Ren, Y.-J. (1991). Equilibrium problems of spherically isotropic bodies. *Appl. Math. Mech. (English Edition)* **12**, 155-162.

- Dougall, J. (1914). An analytical theory of the equilibrium of an isotropic elastic rod of circular section. *Trans. Royal Soc. Edinburgh*, **59**, 895-978.
- Duffaut P. (1968). Size effect on crushing blocks of irregular shape. *Revue Ind. Miner. (Special No.)*, pp62-67.
- Deffaut P. and Maury V. (1970). Etudes photoelastiques pour l'Essai protodyakonov. *Proc. 2ed Cong. Int. Soc. Rock Mech., Belgrade*, **3**, 5-15.
- Durelli, A. J. and Chen, T. L. (1973). Displacement and finite-strain fields in a sphere subjected to large deformation. *Int. J. Non-linear Mech.*, **8**, 17-30.
- Durelli, A. J., and Daniel, I. M. (1961). A non-destructive three-dimensional strain-analysis method. *J. Appl. Mech. ASME Series E*, **83**, 83-86.
- Eason, G. (1962). Transient thermal stresses in anisotropic bodies with spherical symmetry. *Appl. Sci. Res.*, **13**, 1-15.
- Edelman F. (1948). On the compression of a short cylinder between rough end-blocks. *Quart. Appl. Meth.*, **7**, 334-337.
- Farrell O. J. and Ross B. (1971). *Solved problems in analysis*. Dover, New York.
- Filon, L. N. G. (1902). On the equilibrium of circular cylinders under certain practical systems of load. *Philosophical Trans. Royal Soc., London, England, Ser. A*, **198**, 147-233.
- Fookes P. G., Dearman W. and Franklin J. A. (1971). Some engineering aspects of rock weathening with field examples from Dartmoor and elsewhere. *Q. J. Engng. Geol.*, **4**, 139-185.
- Forster, I. R. (1983). The influence of core sample geometry on the axial point-load test. *Int. J. Rock Mech. Min. Sci.*, **20**, 291-295.

- Frocht, M. M., and Guernsey, J. R. (1953). A Special Investigation to Develop a General Method for Three-Dimensional Photoelastic Stress Analysis. *NACA Report 1148*, National Advisory Committee for Aeronautics.
- Gladwell, G.M.L., (1990). The static Reissner-Sagoci problem for a finite cylinder: another variation on a theme of I.N. Sneddon. In *Elasticity: Mathematical methods and applications*. (ed. G. Eason and R.W. Ogden), pp. 113-123, Ellis Horwood, New York.
- Gradshteyn, I. S. and Ryzhik, I. M. (1980). *Table of Integrals, Series, and Products*, Corrected and Enlarged Ed., Academic Press, Inc., New York, N. Y.
- Greminger, M. (1982). Experimental studies of the influence of rock anisotropy on size and shape effects in point-load testing. *Int. J. Rock Mech. Min. Sci.*, **19**, 241-246.
- Guidicini, G., Nieble, C. M. and Cornides, A. T. (1973). Analysis of point load test as a method for preliminary geotechnical classification of rocks. *Int. Assoc. Engng. Geol.* **7**, 37-52.
- Hasegawa, H. (1984). Elastic circular finite cylinder under torsion by a pair of annular rigid stamps. *Bull. JSME.* **27**, 630-638.
- Hassani, F. P., Scoble, M. J. and Whittaker, B. N. (1980). Application of the point load index test to strength determination of rock and proposals for a new size-correction chart. *The State of the Art in Rock Mechanics, Proc. 21st U.S. Symp. Rock Mech.*, pp. 543-553.
- Hata, T. (1993). Stress-focusing effect in a uniformly heated transversely isotropic sphere. *Int. J. Solids and Struct.* **30**, 1419-1428.

- Hiramatsu, Y. and Oka, Y., (1966). Determination of the tensile strength of rock by a compression test of an irregular test piece. *Int. J. Rock Mech. Min. Sci.*, **3**, 89-99.
- Hobbs D. W. (1963). A simple method for assessing the uniaxial compressive strength of rock. *Int. J. Rock Mech. Min. Sci.*, **1**, 5-15.
- Hondros G. (1959). The evaluation of Poisson's ratio and the modulus of materials of a low tensile resistance by the Brazilian (indirect tensile ) test with particular reference to concrete. *Aust. J. Appl. Sci.*, **10**, 243-268.
- Horvay G. and Mirabal J. A. (1958) The end problem of cylinders *J. Appl. Mech., ASME*, 561-570.
- Hu, H-C. (1953). On the three-Dimensional problems of the theory of elasticity of a transversely isotropic body. *Acta Scientia Sinica*, **2**, 145-151.
- Hu, H.-C. (1954). On the general theory of elasticity for a spherical isotropic medium. *Acta Scientia Sinica*, **3**, 247-260.
- IBRM Group III (1961). Strength research. *Appendix H, Prague*.
- Irfan, T. Y. and Powell, G. E. (1985). Engineering geological investigations for pile foundations on deeply weathered granite rock in Hong Kong. *Bull. Int. Assoc. Eng. Geology*, **32**, 67-80.
- ISRM (1985). Suggested method for determining point load strength. *Int. J. Rock Mech. Min. Sci. & Geomech. Abstr.*, **22**, 53-60.
- Jaeger J. C. (1979). *Fundamentals of Rock Mechanics*, 3rd Ed., Chapman and Hall London:
- Keer L. M. and Mowry, D. B. (1979). The stress field created by a circular sliding contact on transversely isotropic spheres. *Int. J. Solids and Struct.*, **15**, 33-39.

- Kimura, J., (1931). On the stress distribution in the cylinder under compression test. *J. of JSCE*, **17**, 713-731.
- Kotte J. J., Berczes, J. Gramberg J. and Seldenrath TH. R. (1969). Stress-strain relations and breakage of cylindrical granite rock specimens under uniaxial and triaxial loads. *Int. J. Rock Mech. Min. Sci.*, **6**, 581-595.
- Lajtai, E. Z. (1980). Tensile strength and its anisotropy measured by point and line-loading of sandstone. *Engng. Geol.*, **15**, 163-171.
- Love, A. E. H. (1944). *A Treatise on the Mathematical Theory of Elasticity*, Dover, New York.
- Lumb, P. (1983). Engineering properties of fresh and decomposed igneous rocks from Hong Kong. *Engng. Geol.*, **19**, 81-94.
- Malvern, L.E. (1969). *Introduction to the Mechanics of a Continuous Medium*, Prentice-Hall, New Jersey.
- McWilliams, J.R. (1966). The role of microstructure in the physical properties of rock. *Testing techniques for rock mechanics, ASTM STP 402, Am. Soc. Testing Mats.*, 175-189.
- Nowinski, J. (1959). Note on a thermoelastic problem for a transversely isotropic hollow sphere embedded in an elastic medium. *J. Appl. Mech. ASME*, **26**, 649-650.
- Ogaki, Y. and Nakajima, N. (1983). Stress analysis of a circular cylinder of finite length subjected to loads symmetrical to middle plane and to axis of revolution. *Sci. Eng. Review of Doshisha Univ.*, **23**, 195-205.
- Pells, P. J. N. (1975). The use of the point load test in predicting the compressive strength of rock materials. *Aust. Geomech. J.*, **G5**, 54-56.
- Peng S. D. (1971). Stresses within elastic circular cylinders loading uniaxially and triaxially. *Int. J. Rock Mech. Min. Sci.*, **8**, 399-432.

- Peng, S.S. (1976). Stress analysis of cylindrical rock discs subjected to axial double point load. *Int. J. Rock Mech. Min. Sci. & Geomech. Abstr.*, **13**: 97-101.
- Pickett G. (1944). Application of the Fourier Method to the solution of certain boundary problems in the theory of elasticity. *J. Appl. Mech.*, A176-A182.
- Pigeon Y. (1969). The compressibility of rock fill. Ph. D thesis, University of London.
- Pochhammer, L. (1876). Beitrag zur theorie der biegun des Kreiscylinders. *Crelle's Journal*, **81**, 33.
- Press W. H., Flannery, B. P., Teukolsky, S. A. and Vetterling, W. T. (1992). Numerical recipes: the art of scientific computing, 2ed Ed., Cambridge University Press, New York.
- Protodyakonov M. M. and Voblikov V. S. (1957). Determining rock strength with specimens of irregular shape. *Ugol'*, **32**(4).
- Read, J. R. L., Thornton, P. N. and Regan, W. M. (1980). A rational approach to the point load test. *Proc. Australia-New Zealand Geomech. Conf.*, **2**, pp. 35-39.
- Reichmuth, D.R. (1963). Correlation of force-displacement data with physical properties of rock for percussive drilling systems. *Proc. 5th Symp. Rock Mech.*, 33-59.
- Reichmuth, D.R. (1968). Point load testing of brittle materials to determine tensile strength and relative brittleness. *Proc. 9th Symp. on rock Mechanics, Am. Inst. Min. Metall. Petro. Engng., New York*, 134-159.
- Richardson, D. N. (1989). Point-load test for estimating concrete compressive strength. *ACI Mat. J.*, **86**, 409-416.
- Robert M. and Keer L. M. (1987a). An elastic circular cylinder with displacement prescribed at the ends-axially symmetric case. *Q. J. Mech. Appl. Math.*, **40**, 339-361.
- Robert M. and Keer L. M. (1987b). An elastic circular cylinder with prescribed displacements at the ends-asymmetric case. *Q. J. Mech. Appl. Math.*, **40**, 365-381.



- Robins, P. J. (1980). The point-load strength test for concrete cores. *Mag. of Concrete Res.*, **32**, 101-111.
- Robins, P. J. Austin, S. A. (1985). Core point-load test for steel-fibre-reinforced concrete. *Mag. of Concrete Res.*, **37**, 238-242.
- Saito, H. (1952). The axially symmetrical deformation of a short cylinder. *Trans. JSME*, **18**, 21-28 (in Japanese with English abstract).
- Saito, H. (1954). The axially symmetrical deformation of a short cylinder. *Trans. JSME*, **20**, 185-190 (in Japanese with English abstract).
- Shah, K. R. and Wong T. -F. (1996). Grain fracturing and comminution in porous materials. *Rock Mech., Tools and Techniques, Proc. 2nd North American Rock Mech. Symp. NARM'96, M. Aubertin, F. Hassani, and H. Mitri eds., Montreal, Canada*, pp. 859-866.
- Shah, K. R., and Wong T. -F. (1997). Fracturing at contact surfaces subjected to normal and tangential loads. *Int. J. Rock Mech. Min. Sci.*, **34**, 727-739.
- Sternberg, E. and Rosenthal, F. (1952). The elastic sphere under concentrated loads. *J. of Appl. Mech. ASME*, **19**, 413-421.
- Tatara, Y. (1991). On compression of rubber elastic sphere over a large range of displacements-Part 1: Theoretical study. *J. Engng. Mat. and Tech. ASME*, **113**, 285-291.
- Tatara, Y., Shima, S. and Lucero, J. C. (1991). On compression of rubber elastic sphere over a large range of displacements-Part 2: Comparison of theory and experiment. *J. Engng. Mat. and Tech. ASME*, **113**, 292-295.

- Timoshenko, S. P. and Goodier, J. N. (1982). *Theory of elasticity*, 3rd Ed., McGraw-Hill, New York.
- Watanabe, S. (1996). Elastic analysis of axi-symmetric finite cylinder constrained radial displacement on the loading end. *Structural Eng. /Earthquake Eng., JSCE*, **13**, 175s-185s.
- Watanabe, S. (1998). Discussion on 'Young's modulus interpreted from compression tests with end friction' by K.T. Chau. *J. Engng. Mech. ASCE*, **124**, 1170-1171.
- Watson, G. N. (1944). *A treatise on the theory of Bessel functions*, 2nd Ed., Cambridge University Press, Cambridge.
- Wei, X. X. and Chau, K. T. (1998). Spherically isotropic spheres subject to diametral point load test: analytic solutions. *Int. J. Rock Mech. Min. Sci.*, **35**: 4-5, paper No. 006.
- Wei, X.X., Chau, K.T. and Wong, R.H.C. (1999). A new analytic solution for the axial point load strength test for solid circular cylinders. Submitted *J. Engng. Mech., ASCE*.
- Wijk, G. (1978). Some new theoretical aspects of indirect measurements of the tensile strength of rocks. *Int. J. Rock Mech. Min. Sci. & Geomech. Abstr.*, **15**, 149-160.
- Wijk, G. (1980). Point load test for the tensile strength of rocks. *Geot. Testing J.*, **3**, 49-54.
- Wijk, G., Rehbinder, G. and Logdstrom, G. (1978). The relation between the uniaxial tensile strength and the sample size for Bohus granite. *Rock Mech.*, **10**, 201-219.
- Williams, D.K. (1996). Circular cylinders with bands of pressure: axisymmetric closed form solutions utilizing Bessel's functions & Fourier series. In *Pressure Vessels and*

*Piping Design, Analysis, and Severe Accidents*, PVP- 331, pp. 77-87, ASME, Washington.

Wong, R.H.C. and Chau, K.T. (1998). Patterns of coalescence in a rock-like material containing two parallel inclined frictional cracks under uniaxial compression. *Int. J. Rock Mech. Min. Sci.*, **35**, 147-164.

Zhang, J., Wong, T. F. and Davis, D. M. (1990). Micromechanics of pressure-induced grain crushing in porous rocks. *J. Geophys. Res.*, **95**, 341-352.

## Appendix I THE PROOF OF $A=B=0$

The proof for (2.19) given here follows that of Hu (1954). In particular, it can be shown, by eliminating either  $A$  or  $B$  from (2.14) and (2.15), that both  $A$  and  $B$  satisfy the plane Laplacian equation

$$\nabla_1^2 A = \nabla_1^2 B = 0. \quad (\text{A1})$$

where  $\nabla_1^2$  is defined in (2.8). Therefore, any harmonic functions can be the solutions for  $A$  and  $B$ . However, as shown in Section V of Hu (1954), without loss of generality, both  $A$  and  $B$  can be set to zeros (i.e.  $A = B = 0$ ). To see this, it should be first noted that the determination of  $u_\theta$  and  $u_\varphi$  from (2.12) is not unique as there is a homogeneous solution for:

$$\frac{1}{r \sin \theta} \frac{\partial \psi_0}{\partial \varphi} + \frac{1}{r} \frac{\partial G_0}{\partial \theta} = 0, \quad \frac{1}{r} \frac{\partial \psi_0}{\partial \theta} - \frac{1}{r \sin \theta} \frac{\partial G_0}{\partial \varphi} = 0, \quad (\text{A2})$$

Similar to the derivation of (A1), it is straightforward to show that both of these homogeneous solutions,  $\psi_0$  and  $G_0$ , satisfy the plane Laplacian equation

$$\nabla_1^2 \psi_0 = \nabla_1^2 G_0 = 0. \quad (\text{A3})$$

Thus, the complete solution for  $\psi_0$  and  $G_0$  are harmonic functions. Alternatively, if a change of variables  $\xi = \ln \tan(\theta/2)$  is introduced as suggested by Hu (1954), the solutions can be expressed in the form of complex function as  $\psi_0 + iG_0 = f(\xi + i\varphi, r)$ , where  $f$  is an arbitrary analytic function of the complex variable  $\xi + i\varphi$ . Thus, any arbitrary analytic functions  $\psi_0$  and  $G_0$  can be added to  $\psi$  and  $G$  without loss of generality.

Following the same procedure, one can show that the general solution for  $A$  and  $B$  given in (A1) can be written as  $A + iB = F(\xi + i\varphi, r)$ , where  $F$  is again any arbitrary analytic functions. Without loss of generality, functions  $\psi_0$  and  $G_0$  can be now added to  $\psi$  and  $G$ , then the resultant  $u_\theta$  and  $u_\varphi$  are substituted into (2.6). It can be shown that if the analytic function of  $\psi_0$  and  $G_0$  are chosen such that

$$\frac{2b}{r^2} f - h \frac{\partial^2 f}{\partial \tau^2} = -iF(\xi + i\varphi, r), \quad (\text{A4})$$

then the  $A_0$  and  $B_0$  corresponds to  $\psi_0$  and  $G_0$  satisfy  $A_0 + iB_0 = -F(\xi + i\varphi, r)$ . Therefore,  $F$ , or in turn both  $A$  and  $B$ , can always be adjusted to zero by imposing homogeneous analytic solution  $f$ . Consequently, we can always set  $A$  and  $B$  to zero without loss of generality.

## Appendix II

### FOURIER-BESSEL EXPANSION OF CONTACT STRESS

The expression (3.8) for  $\sigma_z$  can be expanded into series of  $J_0(\lambda, \rho)$  by using the following formula (e.g. Watson, 1944):

$$\sigma_z = \sum_{n=1}^{\infty} E_n J_0(\lambda_n, \rho) = \sum_{n=1}^{\infty} E_n J_0\left(\lambda_n, \frac{r}{R}\right) \quad (\text{B1})$$

where

$$E_n = \frac{2}{R^2 J_0^2(\lambda_n)} \int_0^R r \sigma_z J_0\left(\lambda_n, \frac{r}{R}\right) dr \quad (\text{B2})$$

Since  $\sigma_z$  is nonzero only within the circular contact area, (B2) can be evaluated by substituting (3.14) into (B2) as

$$E_n = -\frac{2}{R^2 J_0^2(\lambda_n)} \int_0^{R_0} p_0 \frac{r}{R_0} \sqrt{R_0^2 - r^2} J_0\left(\lambda_n, \frac{r}{R}\right) dr \quad (\text{B3})$$

Applying the change of variable  $r = R_0 \sin \theta$ , (B3) becomes

$$E_n = -\frac{2p_0 R_0^2}{R^2 J_0^2(\lambda_n)} \int_0^{\pi/2} \sin \theta \cos^2 \theta J_0\left(\frac{R_0}{R} \lambda_n, \sin \theta\right) d\theta \quad (\text{B4})$$

This integration can be done exactly by setting  $\mu = 0$  and  $\delta = 1/2$  into the following formula (formula 6.683 of Gradshteyn and Ryzhik, 1980):

$$\int_0^{\pi/2} J_{\mu}(a \sin \theta) (\sin \theta)^{\mu-1} (\cos \theta)^{2\delta-1} d\theta = 2^{\delta} \Gamma(\delta+1) a^{-\delta-1} J_{\delta-\mu+1}(a) \quad (\text{B5})$$

for  $\text{Re}(\delta) > -1$ ,  $\text{Re}(\mu) > -1$ .

The result of this integration gives

$$E_r = -\frac{p_0(2\pi R_0)^{1/2}}{\lambda_r^{1/2} R^{1/2} J_0^2(\lambda_r)} J_{1/2}\left(\frac{R_0}{R} \lambda_r\right) \quad (\text{B6})$$

Since  $J_{1/2}(\lambda_r R_0 / R)$  can be written in terms of  $\sin(\lambda_r R_0 / R)$  and  $\cos(\lambda_r R_0 / R)$  as (e.g. formula 8.464 of Gradshteyn and Ryzhik, 1980):

$$J_{1/2}\left(\frac{R_0}{R} \lambda_r\right) = \sqrt{\frac{2R}{\pi R_0 \lambda_r}} \left[ \frac{R}{R_0 \lambda_r} \sin\left(\frac{R_0}{R} \lambda_r\right) - \cos\left(\frac{R_0}{R} \lambda_r\right) \right] \quad (\text{B7})$$

(B6) can further be simplified to the following function of sine and cosine

$$E_r = \frac{2p_0 R}{\lambda_r R_0 J_0^2(\lambda_r)} \left( \frac{\lambda_r R_0}{R} \cos \frac{\lambda_r R_0}{R} - \sin \frac{\lambda_r R_0}{R} \right) \quad (\text{B8})$$

Thus, finally we arrive at

$$\sigma_z = \sum_{r=1}^{\infty} \frac{2p_0 R}{\lambda_r R_0 J_0^2(\lambda_r)} \left( \frac{\lambda_r R_0}{R} \cos \frac{\lambda_r R_0}{R} - \sin \frac{\lambda_r R_0}{R} \right) J_0(\lambda_r \rho) \quad (\text{B9})$$

which is the result given in (3.40) of the text.

### Appendix III

#### Fourier-Bessl Expansion for $I_{2n}(\eta_m r)$ and $\eta_m r I_{2n-1}(\eta_m r)$

By applying Fourier-Bessel expansion to any function (Watson, 1944),  $I_{2n}(\eta_m r)$  and  $\eta_m r I_{2n-1}(\eta_m r)$  involved in (4.41) can be expressed in terms of  $J_{2n}(\gamma, r)$  as

$$I_{2n}(\eta_m r) = \sum_{s=1}^{\infty} T_{ns} J_{2n}(\gamma_s r) \quad (C1)$$

$$\eta_m r I_{2n-1}(\eta_m r) = \sum_{s=1}^{\infty} U_{ns} J_{2n}(\gamma_s r) \quad (C2)$$

where

$$T_{ns} = \frac{2\lambda_s^2}{R^2(\lambda_s^2 - 4n^2)J_{2n}^2(\lambda_s)} \int_0^R r I_{2n}(\eta_m r) J_{2n}(\gamma_s r) dr \quad (C3)$$

$$U_{ns} = \frac{2\lambda_s^2}{R^2(\lambda_s^2 - 4n^2)J_{2n}^2(\lambda_s)} \int_0^R \eta_m r^2 I_{2n-1}(\eta_m r) J_{2n}(\gamma_s r) dr \quad (C4)$$

Note again that  $\gamma_s = \lambda_s / R$  and  $\lambda_s$  is the root of  $J'_{2n}(\lambda_s) = 0$ . To integrate (C3) exactly, we first note the following formula (5.54.1 of Gradshteyn and Ryzhik, 1980):

$$\int_0^R r J_{2n}(\eta_m r) J_{2n}(\gamma_s r) dr = \frac{\eta_m R J_{2n+1}(\eta_m R) J_{2n}(\lambda_s) - \lambda_s J_{2n}(\eta_m R) J_{2n+1}(\lambda_s)}{\eta_m^2 - \gamma_s^2} \quad (C5)$$

and the following identities

$$I_{2n}(\eta_m r) = (-1)^n J_{2n}(i\eta_m r) \quad (C6)$$

$$I_{2n+1}(\eta_m r) = -i(-1)^n J_{2n+1}(i\eta_m r) \quad (C7)$$

Substitution of (C6) and (C7) into (C5) and then into (C3) yields (4.44) given in the text. To see the validity of (4.45), we first consider the following derivatives:



$$\frac{d}{dr}[r^2 I_{2n}(\eta_n r) J_{2n}(\gamma, r)] = 2(1-2n)r I_{2n}(\eta_n r) J_{2n}(\gamma, r) + r^2 [\eta_n I_{2n-1}(\eta_n r) J_{2n}(\gamma, r) + \gamma, I_{2n}(\eta_n r) J_{2n-1}(\gamma, r)] \quad (C8)$$

and

$$\frac{d}{dr}[r^2 I_{2n-1}(\eta_n r) J_{2n-1}(\gamma, r)] = 4nr I_{2n-1}(\eta_n r) J_{2n-1}(\gamma, r) + r^2 [\eta_n I_{21}(\eta_n r) J_{2n-1}(\gamma, r) - \gamma, I_{2n-1}(\eta_n r) J_{2n}(\gamma, r)] \quad (C9)$$

We then consider the integration of an equation resulting from the subtraction of (C9) $\times \gamma,$  from (C8) $\times \eta_n,$  and by virtue of (4.44) the expression given in (4.45) can be derived.

## Appendix IV

### Fourier-Bessel Expansion for

$$I_{\omega_n}(\eta_n r), \eta_n r I_{\omega_n-1}(\eta_n r), \eta_n^2 r I_{\omega_n}(\eta_n r) \text{ and } r \frac{\partial J_{\omega_n}(\gamma_p r)}{\partial r}$$

In order to apply the end boundary condition, the following  $r$ -dependent functions

$I_{\omega_n}(\eta_n r)$ ,  $\eta_n r I_{\omega_n-1}(\eta_n r)$ ,  $\eta_n^2 r I_{\omega_n}(\eta_n r)$ , and  $r \frac{\partial J_{\omega_n}(\gamma_p r)}{\partial r}$  can be expressed in series of

Bessel function  $J_{\omega_n}(\gamma_s r)$  as (Watson, 1944):

$$I_{\omega_n}(\eta_n r) = \sum_{s=1}^{\infty} T_{ns} J_{\omega_n}(\gamma_s r) \quad (D1)$$

$$\eta_n r I_{\omega_n-1}(\eta_n r) = \sum_{s=1}^{\infty} U_{ns} J_{\omega_n}(\gamma_s r) \quad (D2)$$

$$\eta_n^2 r I_{\omega_n}(\eta_n r) = \sum_{s=1}^{\infty} W_{ns} J_{\omega_n}(\gamma_s r) \quad (D3)$$

$$r \frac{\partial J_{\omega_n}(\gamma_p r)}{\partial r} = \sum_{s=1}^{\infty} V_{sn} J_{\omega_n}(\gamma_s r) \quad (D4)$$

where

$$T_{ns} = \frac{2\lambda_s^2}{R^2(\lambda_s^2 - \omega_n^2)J_{\omega_n}^2(\lambda_s)} \int_0^R r I_{\omega_n}(\eta_n r) J_{\omega_n}(\gamma_s r) dr \quad (D5)$$

$$U_{ns} = \frac{2\lambda_s^2 \eta_n}{R^2(\lambda_s^2 - \omega_n^2)J_{\omega_n}^2(\lambda_s)} \int_0^R r^2 I_{\omega_n-1}(\eta_n r) J_{\omega_n}(\gamma_s r) dr \quad (D6)$$

$$W_{ns} = \frac{2\lambda_s^2 \eta_n^2}{R^2(\lambda_s^2 - \omega_n^2)J_{\omega_n}^2(\lambda_s)} \int_0^R r^3 I_{\omega_n}(\eta_n r) J_{\omega_n}(\gamma_s r) dr \quad (D7)$$

$$V_m = \frac{2\lambda_s^2}{R^2(\lambda_s^2 - \omega_n^2)J_{\omega_n}^2(\lambda_s)} \int_0^R r^2 \frac{\partial J_{\omega_n}(\gamma_s r)}{\partial r} J_{\omega_n}(\gamma_s r) dr \quad (D8)$$

To integrate (D5), we first note the following formula (Watson, 1944):

$$\int_0^R r J_{\omega_n}(\eta_n r) J_{\omega_n}(\gamma_s r) dr = \frac{\eta_n R J_{\omega_n+1}(\eta_n R) J_{\omega_n}(\lambda_s) - \lambda_s J_{\omega_n}(\eta_n R) J_{\omega_n+1}(\lambda_s)}{\eta_n^2 - \gamma_s^2} \quad (D9)$$

and

$$I_{\omega_n}(\eta_n r) = e^{\frac{\omega_n \pi}{2}} J_{\omega_n}(i \eta_n r) \quad (D10)$$

where  $\lambda_s = \gamma_s R$ .

Substitution of (D10) into (D9) leads to

$$\int_0^R r I_{\omega_n}(\eta_n r) J_{\omega_n}(\gamma_s r) dr = \frac{\eta_n R I_{\omega_n+1}(\eta_n R) J_{\omega_n}(\lambda_s) + \lambda_s I_{\omega_n}(\eta_n R) J_{\omega_n+1}(\lambda_s)}{\eta_n^2 + \gamma_s^2} \quad (D11)$$

Substitution of (D11) into (D5) leads to (6.74) given in the text.

We can integrate (D6) by integration by part, but this procedure is tedious. We propose a simpler approach here. In particular, we first consider the differentiation of the following functions:

$$\frac{d}{dr} [r^2 I_{\omega_n}(\eta_n r) J_{\omega_n}(\gamma_s r)] = 2(1 - \omega_n) r I_{\omega_n}(\eta_n r) J_{\omega_n}(\gamma_s r) + r^2 [\eta_n I_{\omega_n+1}(\eta_n r) J_{\omega_n}(\gamma_s r) + \gamma_s I_{\omega_n}(\eta_n r) J_{\omega_n+1}(\gamma_s r)] \quad (D12)$$

and

$$\frac{d}{dr} [r^2 I_{\omega_n+1}(\eta_n r) J_{\omega_n+1}(\gamma_s r)] = 2\omega_n r I_{\omega_n+1}(\eta_n r) J_{\omega_n+1}(\gamma_s r) + r^2 [\eta_n I_{\omega_n}(\eta_n r) J_{\omega_n+1}(\gamma_s r) - \gamma_s I_{\omega_n+1}(\eta_n r) J_{\omega_n}(\gamma_s r)] \quad (D13)$$

The result given in (6.75) can be obtained by virtue of (D11) together with the equation resulting from subtracting (D13)  $\times \gamma_s$  from (D12)  $\times \eta_n$ .

Similarly, for the integration of (D7) we can consider the differentiation of the following functions:

$$\frac{d}{dr}[r^3 I_{\omega_n}(\eta_n r) J_{\omega_n+1}(\gamma, r)] = 2r^2 I_{\omega_n}(\eta_n r) J_{\omega_n+1}(\gamma, r) + \eta_n r^3 I_{\omega_n+1}(\eta_n r) J_{\omega_n+1}(\gamma, r) + \gamma r^3 I_{\omega_n}(\eta_n r) J_{\omega_n}(\gamma, r) \quad (D14)$$

and

$$\frac{d}{dr}[r^3 I_{\omega_n+1}(\eta_n r) J_{\omega_n}(\gamma, r)] = 2r^2 I_{\omega_n+1}(\eta_n r) J_{\omega_n}(\gamma, r) - \gamma r^3 I_{\omega_n+1}(\eta_n r) J_{\omega_n+1}(\gamma, r) + \eta_n r^3 I_{\omega_n}(\eta_n r) J_{\omega_n}(\gamma, r) \quad (D15)$$

Integration of the equation resulting from the subtraction of (D14)  $\times \gamma$ , from (D15)  $\times \eta_n$  leads to

$$\begin{aligned} & \int_0^R r^3 I_{\omega_n}(\eta_n r) J_{\omega_n}(\gamma, r) \\ &= R^3 [\gamma I_{\omega_n}(\eta_n R) J_{\omega_n+1}(\lambda_r) + \eta_n I_{\omega_n+1}(\eta_n R) J_{\omega_n}(\lambda_r)] - 2 \int_0^R [\gamma r^2 I_{\omega_n}(\eta_n r) J_{\omega_n+1}(\gamma, r) + \eta_n r^2 I_{\omega_n+1}(\eta_n r) J_{\omega_n}(\gamma, r)] dr \end{aligned} \quad (D16)$$

The integration in the right side of (D16) can be obtained by replacing “ $\omega_n$ ” by “ $\omega_n + 1$ ” in (D12) and (D13) and substituting the related terms into (D16). Finally, (6.76) can be obtained by substituting (D16) into (D7).

The integration for (D8) can be obtained by using the following procedure. We first note that:

$$r \frac{\partial J_{\omega_n}(\gamma_p r)}{\partial r} = \gamma_p r J_{\omega_n+1}(\gamma_p r) - \omega_n J_{\omega_n}(\gamma_p r) \quad (D17)$$

then (D8) can be integrated exactly if we know the integration of  $r^2 J_{\omega_n+1}(\gamma_p r) J_{\omega_n}(\gamma_s r)$  and  $r J_{\omega_n}(\gamma_p r) J_{\omega_n}(\gamma_s r)$ .

When  $\gamma_p \neq \gamma_s$ , the first integration can be obtained by following the similar procedure as getting the integration in (D6) simply by replacing the modified Bessel function by the Bessel function. The second integration can be derived directly from (D9).

When  $\gamma_p = \gamma_s$ , the integration of  $rJ_{\omega_n}(\gamma_p r)J_{\omega_n}(\gamma_s r)$  is given by Watson (1944)

$$\int_0^r rJ_{\omega_n}(\gamma, r)J_{\omega_n}(\gamma, r)dr = \frac{1}{4}R^2[2J_{\omega_n}(\lambda_s)J_{\omega_n}(\lambda_s) - J_{\omega_n-1}(\lambda_s)J_{\omega_n+1}(\lambda_s) - J_{\omega_n+1}(\lambda_s)J_{\omega_n-1}(\lambda_s)] \quad (D18)$$

The integration of  $r^2J_{\omega_n-1}(\gamma_s r)J_{\omega_n}(\gamma_s r)$  can be obtained by integrating the following equation and using (D18):

$$\frac{d}{dr}[r^2J_{\omega_n}(\gamma, r)J_{\omega_n}(\gamma, r)] = 2rJ_{\omega_n}(\gamma, r)J_{\omega_n}(\gamma, r) - 2\omega_n rJ_{\omega_n}(\gamma, r)J_{\omega_n}(\gamma, r) + 2\gamma r^2J_{\omega_n}(\gamma, r)J_{\omega_n-1}(\gamma, r) \quad (D19)$$

This completes the Fourier-Bessel expansions given in (6.74) to (6.78).

### Curriculum Vitae of Xuexia W.F.J

Name Mr. Xneria WEL

**Current Status** Ph. D student, Department of Civil and Structural Engineering, The Hong Kong Polytechnic University, Hong Kong

### Education and Degree

1997-now Ph. D. student, Department of Civil and Structural Engineering, the Hong Kong Polytechnic University, Hung Hom, Hong Kong. (to be completed in June, 1999)  
Supervisors: Dr. Kam-tim CHAU, Dr. H. C. Wong  
Major: Civil Engineering

1989-1992 M. S. Department of Mechanics, Lanzhou University, China  
Supervisor: Prof. Tiande MIAO  
Major: Continuum Mechanics

1985-1989 B. S. Department of Mechanical Engineering, Xi'an Jiaotong University, China  
Major: Applied Mechanics

### Research Experience

1997-1999 Project: A theoretical and experimental study on point load strength test for rock cores, the research is supported by the Research Grant Council (RGC) Earmarked Grant No. PolyU 70/96E.

1993-1996 Project: Damage-mechanical study on relationship between microstructure and rheology of frozen soil, the research was supported by the National Science Foundation (NSF).

1990-1992 Project: Mechanical analysis of microstructure change and creep characteristic of frozen soil under complicated stress condition, which was supported by the State Key Laboratory of Frozen Soil Engineering, Chinese Academy of Science, Lanzhou, PRC.

1989-1990 Project: Mechanical analysis of hillslope in the Loess Plateau, the research was supported by Beijing Forestry University, P.R.C.

1990-1993 Visiting researcher of the State Key Laboratory of Frozen Soil Engineering, Chinese Academy of Science, P.R.C.

### Research Interests

Geotechnical Engineering, Applied Mechanics, Damage Mechanics, Elasticity, Continuum Mechanics, Dynamic response and failure of materials.

### Teaching Experience

1995-1997 Lecturer of Department of Mechanics, Lanzhou University, PRC

1992-1995 Assistant lecturer of Department of Mechanics, Lanzhou University, PRC

1997-1999 Teaching assistant: Soil Mechanics, Department of Civil and Structural Engineering, the Hong Kong Polytechnic University.

Modules which I have lectured to undergraduate student in Lanzhou University: Advanced Algebra; Theoretical Mechanics; Engineering Mechanics; Structural Mechanics; Steel and Cement Structure; Material Mechanics

#### *Honours and Awards*

1. The excellent thesis prize in Lanzhou University in 1992.
2. The youngest visiting researcher in the State-key Laboratory of Frozen Soil Engineering, Chinese Academy of Sciences, PRC, 1990-1993.

#### *Publications*

1. Chau K.T. and Wei X.X. (1999a), "Spherically isotropic, elastic spheres subject to diametral point load strength test", *International Journal of Solids and Structures*, 36(29), 4473-4496.
2. Wei X.X., Chau K.T. and Wong, R. H. C. (1999), "A new analytic solution for the axial point load strength test on solid circular cylinders", submitted to *Journal of Engineering Mechanics, ASCE* (accepted).
3. Chau K.T. and Wei X.X. (1999b), "A new analytic solution for the diametral point load strength test on finite solid circular cylinders", submitted to *International Journal of Solids and Structures*.
4. Chau K.T. and Wei X.X. (1999c), "Finite solid circular cylinders subjected to arbitrary surface loads: part I. analytic solution", submitted to *International Journal of Solids and Structures*.
5. Wei X.X. and Chau K.T. (1999a), "Finite solid circular cylinders subjected to arbitrary surface loads: part II. application to double-punch test", submitted to *International Journal of Solids and Structures*.
6. Wei X.X. and Chau K.T. (1999b), "Some new theoretical developments on point load strength test for rocks", *13th ASCE Engineering Mechanics Division Conference, Baltimore, June 13-16, 1999*.
7. Wei X.X. and Chau K.T. (1998a), "Spherically isotropic spheres subject to diametral point load test: analytic solutions", *International Journal of Rock Mechanics and Mining Science* 35: 4-5, paper No. 006.
8. Wei X.X. and Chau K.T. (1998b), "Analytic solution for the point load strength test on anisotropic rocks", *International Conference on Geomechanics/ Ground Control in Mining and Underground Construction*, 1, 147-156.
9. Wei X.X. and Chau K.T. (1998c), "Similarities of tensile stress concentrations in solid cylinders and spheres under Point Load Strength Test (PLST): a new theoretical basis for testing irregular rock specimens using PLST", *Sixth Pan American Congress of Applied Mechanics PACAM VI*, January, 1998.
10. Miao T., Wei X. X.(1994), "A damage theory on relationships between the microstructure of frozen soil and its mechanical property", *Science in China*, 25(3), 309-317, 1994.
11. Zhang C., Wei X. X. Miao T.(1994), "Microstructure damage behavior and change characteristic in frozen soil creep process", *Proc. of the 7th Int. Symp. on Ground Freezing*, PP163-167, 1994.
12. Wei X. X., Miao T., Zhang C.(1993), "A microstructure damage theory on creep of frozen soil", *7th International Conference on Permafrost Proceedings*, 2(7), 2125-2132.
13. Wei X. X. (1992), "A Experimental and theoretical study on the microstructure of frozen soil during creep process", M. S. thesis, Lanzhou University, 1992.
14. Gao X., Wei X. X.(1991), "An exact elasto-plastic solution for thick-walled spherical shell of a strain hardening material", *ASME Pressure vessel & piping conference proceedings*, 1991.
15. Wang Z., Wei X. X., Gao X.(1991), "Solution of the plane stress problem of strain hardening material described by power-law using the complex pseudo stress function, *Applied Mathematics and Mechanics*, 12, 481-492.